
Long-Term Irradiation Studies of Large-Area Micromegas Detectors for the ATLAS NSW Upgrade

Fabian Vogel



München 2023

Long-Term Irradiation Studies of Large-Area Micromegas Detectors for the ATLAS NSW Upgrade

Fabian Vogel

Dissertation
an der Fakultät für Physik
der Ludwig-Maximilians-Universität
München

vorgelegt von
Fabian Vogel
aus Mühldorf am Inn

München, den 20.12.2023

Erstgutachter: Prof. Dr. Otmar Biebel
Zweitgutachter: Prof. Dr. Wolfgang Dünneweber
Tag der mündlichen Prüfung: 20.02.2024

Zusammenfassung

Im Zuge des geplanten Upgrades des Large Hadron Colliders am CERN zu höheren Interaktionsraten werden Detektoren und Elektronik der dort angesiedelten Experimente ausgetauscht und durch leistungsfähigere Komponenten ersetzt. Eines dieser Experimente ist das ATLAS Experiment. Dieses erfuhr in der ersten Upgrade Periode (Phase 1) unter anderem eine Verbesserung des inneren, vorwärtsgerichteten Myonspektrometers. Das dort befindliche Small Wheel wurde durch das New Small Wheel (NSW) ersetzt. Das NSW besteht aus zwei Detektortechnologien, den small-strip Thin Gap Chambers (sTGCs) und den MICRO-MEsh Gaseous Structure (Micromegas) Detektoren.

Zentrales Thema dieser Arbeit sind Studien zu den großflächigen ($2\text{-}3\text{ m}^2$) Micromegas Detektoren. Diese zeigten ein instabiles Verhalten, welches zu Effizienzeinbußen oder Langzeitproblemen im Hinblick auf die Benutzung in den kommenden Jahren führen könnte. Die Verwendung des vorgesehenen Betriebsgases, einem Gemisch aus Argon und Kohlenstoffdioxid im Verhältnis 93:7 vol%, konnte die Anforderungen nicht zufriedenstellend erfüllen. Ein Wechsel zu einem dreigeteilten Gasgemisch aus Argon, Kohlenstoffdioxid und Isobutan im Verhältnis 93:5:2 vol% wurde in Betracht gezogen. Diese Beimischung eines Kohlenwasserstoff-Gases mündete in intensiven Untersuchungen in Bezug auf Langlebigkeit, Effizienz und Auflösung der Micromegas Detektoren die Teil dieser Arbeit sind. Mögliche Alterungsschäden in Folge des Beimischens von Isobutan werden diskutiert.

Ersatz Micromegas Detektoren, die baugleich zu den verbauten Serien Detektoren im NSW sind, werden in dieser Arbeit auf die vorher diskutierten Parameter untersucht. Zwei Einrichtungen zum Testen der Detektoren wurden ausgewählt. Die am CERN befindliche Gamma Irradiation Facility (GIF++) stellt eine 14 TBq Caesium Quelle zur Verfügung (662 keV Photonen). Mehrere Micromegas Detektoren werden dort mit dieser Quelle bestrahlt und akquirieren dabei Ladungen die äquivalent zu den zukünftig erwarteten Ladungsmengen im ATLAS Experiment sind. Des Weiteren bietet diese Einrichtung regelmäßige Strahlzeiten mit einem Myonenstrahl an. Bestrahlte Detektoren werden in regelmäßigen Abständen auf ihre Effizienz und Auflösung getestet. Diese Tests werden mit der finalen Ausleseelektronik des NSW getestet. Verschiedene Hintergrundstärken durch die Caesium Quelle werden durch Einsatz verschiedener Abschwächfilter in der GIF++ simuliert, um die Leistung der Detektoren und der Ausleseelektronik unter der zu erwartenden Strahlungsrate zu testen. Eine Kalibrierung der Strahlungsraten in der GIF++ im Hinblick auf die Rate im ATLAS Experiment ist notwendig und wird in dieser Arbeit durchgeführt. Grundlage dieser Kalibrierung sind aktuelle Messdaten die mit dem NSW im ATLAS Experiment aufgenommen wurden. Zusätzlich wurden in diesem Messaufbau die bisher besten Rekonstruktionsgenauigkeiten für schrägen Teilcheneinfall mit großflächigen Micromegas Detektoren erzielt.

In einem zweiten Langzeitaufbau wird ein weiterer Ersatz Micromegas Detektor mit einer Americium-Beryllium Neutronenquelle über einen Zeitraum von knapp drei Jahren bestrahlt. Ziel ist es hierbei, im Gegensatz zur Gammastrahlenbelastung in der GIF++, den Detektor auch hochionisierender hadronischer Strahlung auszusetzen. Langzeitstudien unter Verwendung des ursprünglichen Gasgemisches aus Argon und Kohlenstoffdioxid und mit dem dreigeteilten Gasgemisch werden durchgeführt und verglichen. Ausgangseffizienzen des Detektors werden mit Zwischenmessungen und einer abschließenden Messung nach Beendigung der Bestrahlung verglichen. Hierzu werden kosmische Myonen verwendet. Zusätzliche Untersuchungen mit der Neutronenquelle als Hintergrundstrahlung sowie eine Kalibrierung der Neutronenquelle werden durchgeführt.

Basierend auf den Ergebnissen dieser Arbeit, werden die Micromegas Detektoren bei ATLAS nun mit dem dreigeteilten Gas betrieben.

Abstract

In the course of the planned upgrade of the Large Hadron Collider at CERN to higher interaction rates, detectors and electronics of the experiments located there will also be exchanged and replaced by more powerful components. One of these experiments is the ATLAS experiment. This underwent, among other things, an upgrade of the inner forward muon spectrometer in the first upgrade period (Phase 1). The Small Wheel located there was replaced by the New Small Wheel (NSW). The New Small Wheel consists of two detector technologies: the small-strip Thin Gap Chambers (sTGCs) and the MICRO-MESh Gaseous Structure (Micromegas) detectors.

The central topics of this work are studies on large-area ($2\text{-}3\text{ m}^2$) Micromegas detectors. These showed unstable behavior, which could lead to efficiency losses or long-term problems concerning operations in the years to come. The use of the intended operating gas, a mixture of Argon and Carbon dioxide in a ratio of 93:7 vol%, could not satisfactorily meet the requirements. A change to a ternary gas mixture of Argon, Carbon dioxide, and Isobutane in a 93:5:2 vol% ratio was considered. This admixture of a hydrocarbon gas leads to intensive investigations in terms of longevity, efficiency, and resolution of the Micromegas detectors which are the topic of this thesis. Possible aging damages as a consequence of the admixture of isobutane are discussed.

Spare Micromegas detectors, identical to the series detectors installed in the NSW, are examined in this work for the parameters discussed previously. Two facilities were selected for testing the detectors. The Gamma Irradiation Facility (GIF++) at CERN provides a 14 TBq cesium source (662 keV photons). Several Micromegas detectors are irradiated with this source and acquire charges equivalent to the expected future amount in the ATLAS experiment. Furthermore, this facility offers regular beamtimes with a muon beam. Periodic tests are conducted to investigate the efficiency and precision of irradiated detectors. These tests are performed with the final readout electronics of the NSW. Different absorption filters are used in the GIF++ to simulate varying background intensities. This is done to test the expected irradiation rate's impact on detector performance and readout electronics. A calibration of the irradiation rates in the GIF++ is performed in this work to compare them with the rate in the ATLAS experiment. The basis of this calibration is data taken with the NSW at the ATLAS experiment. In addition, the best results are achieved for large-area Micromegas detectors concerning inclined particle incidents.

A second long-term setup is situated in Garching near Munich. Another spare Micromegas underwent irradiation from an Americium-Beryllium neutron source for nearly three years. In contrast to pure gamma radiation exposure in the GIF++, the aim here is to expose the detector additionally to highly ionizing hadronic radiation. Long-term studies compare the performance of the legacy (Ar:CO₂) and the ternary gas mixture. Benchmark efficiencies of the detector are compared with intermediate measurements and a final measurement after completion of the irradiation. Cosmic muons are used for this measurement. Additional investigations with the neutron source as background and a calibration of the neutron source are performed.

Based on the results of this work, the Micromegas detectors at ATLAS are now operated with the ternary gas mixture.

Contents

1	Introduction to ATLAS und the NSW Upgrade	1
1.1	LHC	1
1.2	ATLAS	2
1.3	Phase I Upgrade of the ATLAS Muon Spectrometer	7
2	Particle Detection	11
2.1	Particle-Matter Interaction	11
2.1.1	Heavy Charged Particles	11
2.1.2	Photons	13
2.1.3	Neutrons	15
2.2	Charge Separation and Amplification	18
2.2.1	Particle Drift in Gas	18
2.2.2	Gas Amplification	20
2.3	Resistive Strip Micromegas	22
2.3.1	Anode Signals	23
2.3.2	NSW Micromegas Modules	24
3	Counting Gas	27
3.1	Quenching Gas	27
3.2	Legacy Gas Problems	27
3.2.1	Adaptation of the Operating Gas	28
3.3	Comparison of Operating Gas Properties	30
3.3.1	Drift Voltage	30
3.3.2	Amplification Voltage	30
3.4	Observed Aging Effects	32
3.5	Long-Term Irradiation Studies for Aging Investigations in Gaseous Detectors	33
4	Data Acquisition Systems	35
4.1	The Scalable Readout System (SRS)	35
4.2	Signal Evaluation of the APV25 Hybrid	38

4.2.1	Signal Shape	38
4.2.2	Charge and Timing Determination	38
4.3	NSW Data Acquisition System	40
4.3.1	Reduced NSW Readout Chain for Standalone Micromegas Data Taking	41
4.4	VMM ASIC	42
4.4.1	VMM Charge and Timing Determination	43
4.4.2	Time Calibration	45
5	Position Reconstruction and Particle Tracking	49
5.1	Position Reconstruction Using Stereo Layers	49
5.2	Cluster Building	52
5.3	Particle Tracking	53
5.3.1	Reference Tracking	53
5.3.2	Detector Alignment	55
5.3.3	Detector Resolution	59
5.4	Inclined Particle Trajectories	60
5.4.1	μ TPC-Like Position Reconstruction	60
5.4.2	Charge-Weighted Time Correction of the Charge-Weighted Position Reconstruction	63
5.5	Detector Efficiency	66
6	Long-Term Irradiation in the CERN GIF++	67
6.1	The Gamma Irradiation Facility	67
6.2	Irradiation Setup	69
6.3	HL-LHC Equivalent Calibration	70
6.3.1	Particle Interaction Rate	70
6.3.2	Currents and Expected Accumulated Charges	72
6.3.3	Accumulated Charges of the Long-Term Irradiated Modules	75
7	Performance Studies of a Long-Term Irradiated Module	79
7.1	Measurement Setups	79
7.1.1	Setup 1	80
7.1.2	Setup 2	80
7.1.3	Setup 3	81
7.2	GIF++ Beamtime Using NSW VMMs	81
7.2.1	Event Selection	81
7.2.2	Results for Perpendicular Particle Incident	82
7.2.3	Results for 29° of Particle Incident	87

7.3	Investigations of the High-Background Issues Using APV25 Hybrids	90
7.4	Detector Performance with Increased Bias Current for the VMMs	91
7.4.1	Resolution	91
7.4.2	Efficiencies	93
7.5	Testbeam Conclusions	95
8	Long-Term Irradiation Using an Am-Be Source	97
8.1	Measurement Setups	97
8.1.1	Long-Term Irradiation Setup	97
8.1.2	CRF for Performance Tests	98
8.1.3	Final Test Cosmic Muon Setup after 3 Years of Irradiation	100
8.2	Source Characterization	101
8.2.1	Composition and Activity	101
8.2.2	Detector Sensitivity	102
8.2.3	Current Density Calibration	103
8.3	Detector Stability	106
8.3.1	Long-Term Current Behaviour Under Irradiation	106
8.3.2	Accumulated Charge	108
8.4	Detector Performance	109
8.4.1	Internal Tracking	109
8.4.2	Benchmark Performance Before Irradiation	110
8.4.3	Detector Performance After 1 Year of Irradiation	111
8.4.4	Detector Performance After Irradiation Using Ar:CO ₂ :iC ₄ H ₁₀	112
8.4.5	Detector Performance with the Am-Be Source as Background	116
8.5	Conclusion Neutron Irradiation Studies	120
9	Summary	121
	Bibliography	124
A	Simulated Electron Drift Velocity for Polluted Detector Gas	133
B	VMM Registers	135
C	Additional Beamtime Plots	137
D	Neutron Irradiation Studies	139
D.1	Neutron Interaction Cross-Sections	139
D.2	Asymmetric Irradiation	140

D.3 Environmental Dependent Current Fluctuations	140
--	-----

Chapter 1

Introduction to ATLAS und the NSW Upgrade

1.1 LHC

The Conseil Européen pour la Recherche Nucléaire (CERN) is situated in Meyrin (Switzerland) and is one of the biggest research institutions worldwide. The large particle accelerator complex situated there is the origin of many breakthroughs in nuclear and particle physics, like the discovery of the Z boson (Arnison et al. [1983b]) and W boson (Arnison et al. [1983a]). Both particles were measured at the Super Proton Synchrotron (SPS) (see figure 1.1). With the necessity for higher energies a larger accelerator was added to the complex utilizing the SPS as pre-accelerator, first the Large Electron-Positron Collider (LEP) and ultimately the Large Hadron Collider (LHC). In 2012 the last missing piece of the standard model of particle physics, the Higgs boson, was experimentally proven independently by the two detector experiments ATLAS (A Toroidal LHC ApparatuS) and CMS (Compact Muon Solenoid) situated at the LHC (CERN [2012]). These detector complexes are multi-purpose detectors specialized for collisions at the highest center-of-mass (CM) energies and very high luminosities, i.e. interaction rate per area. ALICE (A Large Ion Collider Experiment) is a third detector system at the LHC primarily investigating heavy ion collisions and the properties of the resulting quark-gluon plasma (CERN [2023a]). The fourth detector experiment, the LHCb (Large Hadron Collider beauty) focuses on interactions containing b quarks and corresponding hadronized particles (CERN [2023c]).

For the near future of the LHC (2029) an upgrade to higher luminosities is foreseen to accumulate more data targeting rare or suppressed processes (CERN [2023b]). An upgrade of the particle accelerator consequently results in an upgrade of the particle detectors to adapt to the new parameters. Such upgrades are performed in multiple steps containing software-based upgrades and the replacement of detectors and electronics. The topic of this thesis is part of an upgrade of the ATLAS forward muon spectrometer. A short introduction to the ATLAS detector complex including the different subsystems and upgrades is given in the following.

In general, the ATLAS experiment can be divided into two distinct regions, the barrel region, and the end-cap region situated in the forward direction parallel to the beam axis. This distinction can be described by the pseudorapidity (Workman et al. [2022]) given by

$$\eta = -\ln\left(\tan\left(\frac{\theta}{2}\right)\right) \quad (1.1)$$

with θ being the angle between the beam axis and particle momentum direction. Values of $\eta < 1$ represent the barrel region and larger values denote the end-cap region in the forward direction of the beam axis.

The detector is built onion-like concerning the different detector technologies with their specific purposes. Starting from the center, the experiment is built from high-precision tracking chambers and particle identification detectors surrounded by a magnetic field provided by a solenoid magnet (CERN [1997a]). An electromagnetic and a hadronic calorimeter follow this inner detector. At last, visible in pale blue in figure 1.2, the muon spectrometer concludes the detector. Within the muon spectrometer, toroidal magnets provide magnetic fields to bend the trajectory of charged muons. This thesis will focus on the forward ($\eta > 1$) muon spectrometer.

For completion, all subsystems are described shortly in the following.

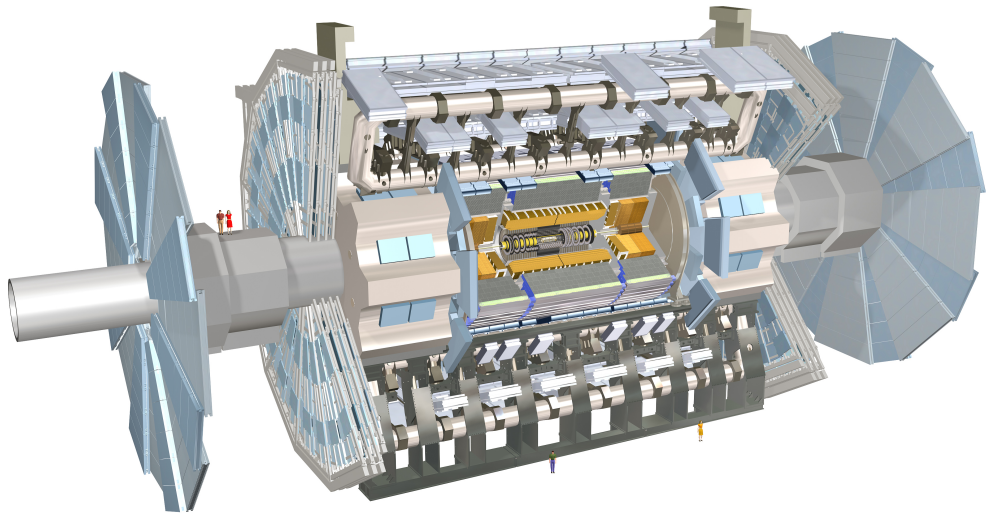


Figure 1.2: Computer-generated picture of the ATLAS experiment.

ATLAS is a symmetrically built multi-purpose detector complex. It consists of multiple layers designed for different tasks.

One distinguishes between the barrel and the end-cap detectors. Although containing different technologies, both follow the same structural order.

Starting from the inside closest to the beam pipe the inner detector is situated. This detector is enclosed by a solenoid magnet to bend the trajectories of charged particles. Up next are two different calorimeters (electromagnetic and hadronic) followed by the muon spectrometer (pale blue). Within the muon spectrometer are toroidal magnets bending the muon trajectories on their way through the spectrometer. A short explanation of the listed components will be given in this chapter.

Figure taken from Pequeno [2008c].

Inner Detector

The inner detector (CERN [1997a]) is situated closest to the beam pipe having the highest requirements on position resolution (see figure 1.3). Resolutions of $10\ \mu\text{m}$ are achieved using a high granularity silicon pixel detector system consisting of 92 million pixels. The pixel sizes are $50 \times 250\ \mu\text{m}^2$ and $50 \times 400\ \mu\text{m}^2$ for the innermost and external layers respectively. The innermost layer (Insertable B-Layer (IBL) Capeans et al. [2010]) was installed in 2014 as an additional layer of the pixel detector³. The main goal is to determine the location of the production vertex of the particle to assign multiple particles to a common origin.

Following the pixel detector the Semiconductor Tracker (SCT) is used for tracking the particles. The tracker is built from strips to account for the increasing area to be covered.

Transition Radiation Trackers (TRTs) form the next layers of the inner detector tracking the particles but also identifying the type of the particle by their emitted transition radiation. Opposing the other two technologies contained in the inner detector, the TRT is built from gas-filled straw tubes, hence not being a semiconductor detector. A niobium-titanium superconducting solenoid magnet providing a 2 T magnetic field surrounds the inner detector bending charged particle trajectories for momentum reconstruction and differentiation between particles and anti-particles.

In terms of the High-Luminosity LHC (HL-LHC) upgrade the inner detector will undergo improvements to cope with the increase in luminosity (see Technical Design Report (TDR) CERN [2017c] and CERN [2017b]).

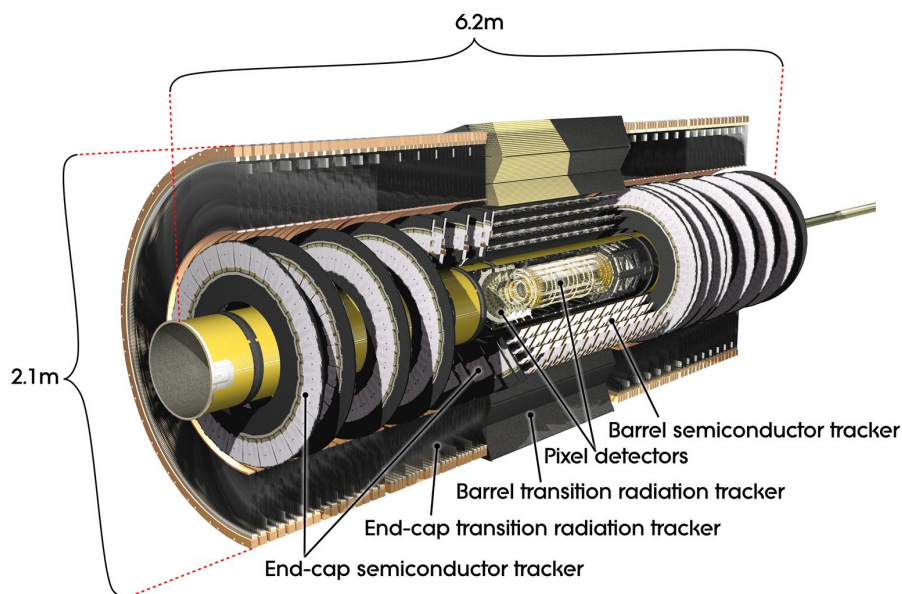


Figure 1.3: Computer-generated picture of the inner detector of the ATLAS experiment.

In total three different technologies are found within the inner detector. Closest to the beam pipe is a silicon pixel detector with 92 million pixels achieving position resolutions of $10\ \mu\text{m}$. The barrel and end-cap SCT form the next layer of detectors also made from silicon sensors. To cover the larger area strips are used instead of pixels resulting in a slightly worse position resolution of $25\ \mu\text{m}$. The main focus is also the track reconstruction of charged particles. Being the last layer of the inner detector the TRT uses a different detection technology. It is built from thin, gas-filled straw tubes where crossing particles ionize the gas creating a detectable signal. Additionally, transition radiation, hence the detector name, is emitted allowing for charged particle identification, i.e. differentiation between electrons and pions (CERN [1997a]).

Figure taken from Pequeno [2008b].

³see <https://atlas.cern/updates/news/new-sub-detector-atlas>

Calorimeter

The next layers of the ATLAS experiment contain the calorimeters used to determine particle energies when stopping them (see figure 1.4). Two different calorimeters are used to target particles interacting differently with matter.

The inner part is the electromagnetic calorimeter and as the name suggests is used to determine the energy of electromagnetically interacting particles like photons and electrons. For both, the barrel and the end-cap region, a liquid Argon (LAr) calorimeter is used (CERN [1996a]). It consists of multiple layers containing liquid argon and high-density converter materials like tungsten or lead. Particles interacting with the material create showers which are detected in the liquid argon parts of the system as a current. These solid layers are placed in an accordion-like structure to increase the amount of material to pass for the particles.

Such an LAr calorimeter is also used as a hadronic calorimeter in the forward, end-cap region. For the barrel region, a tile calorimeter (see CERN [1996b]) was chosen as a hadronic calorimeter for particles passing the electromagnetic calorimeter. It is built from steel as converter material for showers and tile plastic scintillators, hence the name, producing scintillation radiation which is then read out via photomultiplier tubes. Measured currents are proportional to the deposited energy.

Also, the calorimeter system will undergo upgrades as discussed in CERN [2017e] for the tile and CERN [2017a] for the LAr calorimeter.

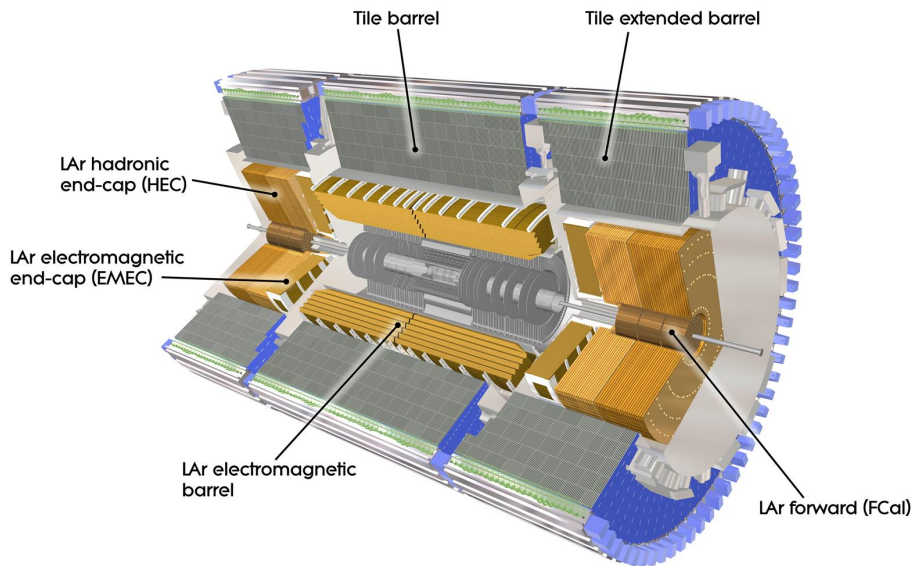


Figure 1.4: Computer-generated picture of the calorimeter complex of the ATLAS experiment. The calorimeter system can be divided into two purposes. First an electromagnetic calorimeter for detecting electrons, photons, and all other particles interacting via the eponymous electromagnetic force. Liquid argon combined with absorber material (e.g. tungsten or lead) is used. This detector type is also used in the end caps functioning as a hadronic calorimeter CERN [1996a]. The barrel region has a different type of hadronic calorimeter, namely the tile calorimeter. It has additional layers of steel combined with scintillator tiles with photomultiplier tubes for particle detection. Due to its structure, it is also referred to as sampling calorimeter CERN [1996b].

Figure taken from Pequeno [2008a].

Muon spectrometer

The last part of the ATLAS experiment is the muon spectrometer that is depicted in pale blue in figure 1.2. It consists of barrel and end-cap regions covered by different detector technologies discussed further down.

Within this muon spectrometer a second magnet system as shown in figure 1.5 is incorporated (see CERN [1997b]). The orange coils represent the barrel toroid magnet whereas the green part illustrates the end-cap toroid magnet. A second version of these end-cap toroids is situated on the other end of the barrel magnets not shown in the figure.

Part of the forward muon spectrometer lies between the end-cap toroid magnets and the central part of the detector with others being further outside as shown in figure 1.2. Since the detectors are assembled in a circular shape to cover the whole end-cap region they are referred to as wheels. The inner, with smaller diameter, are called Small Wheels whereas the larger, outer wheels are called Big Wheels.

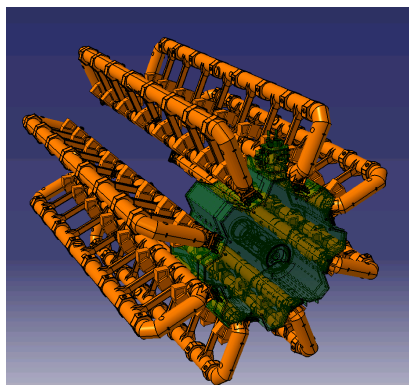


Figure 1.5: 3D computer-generated picture of the barrel and end-cap toroid magnet system.

In total three magnet systems are used to bend the trajectory of muons for determination of the momentum. The central magnet (orange) consists of eight individual coils surrounding the whole barrel region. End cap toroids (green, only one is illustrated with the second one being on the other end of the orange barrel) provide the magnetic field in the $\eta > 1$ region. Magnetic fields up to 3.5 T are achieved CERN [1997b].

Picture taken from Koulouris [2019].

Four different detector technologies were used in the muon spectrometer (see CERN [1997c]). The barrel region is built from three layers of Monitored Drift Tube (MDT) chambers and Resistive Plate Chambers (RPC). MDT chambers are gas-filled tubes assembled in multilayers providing precise track information of the muon ($\mathcal{O}(50\mu\text{m})$). Since the track is bent by the toroid magnet, the momentum information of the muon can be determined from the curvature of the track. The RPC detectors are also gas-filled detectors, compared to the MDTs they are built and operated such that they provide very precise timing information of traversing particles in the order of 2 ns at a moderate spatial resolution (Chiodini [2012]). For the end-cap region of the detector, three technologies were combined. MDTs are used in one of the Big Wheels and were used in the outer part of the Small Wheels for precise position reconstruction. The inner part for precision tracking of the Small Wheel was built from Cathode Strip Chambers (CSC). Additionally, layers of Thin Gap Chambers (TGC) provide good timing information in the forward direction for the Small Wheel. The second Big Wheel is also built from TGCs providing the trigger in the forward direction. This trigger information is included in the trigger scheme of the ATLAS experiment to pre-select interesting events and reduce the amount of data processing and storage.

Major upgrades of the muon system were and are foreseen with some of them already being in the finalizing stage. The reasons and first finished projects of this upgrade, the phase 1 upgrade, are discussed in detail in the following.

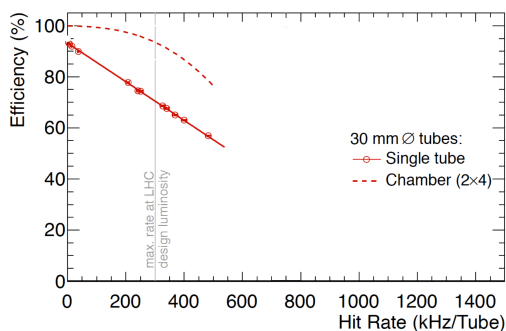
1.3 Phase I Upgrade of the ATLAS Muon Spectrometer

The continuous increase in luminosity and given the HL-LHC project, studies were carried out to test the limits of the installed components of the muon spectrometer.

Testbeam measurements have shown that MDTs in the Small Wheel suffer from high hit rates resulting in a performance decrease (see figure 1.6a). Already at the design luminosity of the LHC single tubes only provide 70 % efficiency. Due to the multilayer structure of the MDT chamber efficiencies $> 90\%$ are reachable. For increasing hit rates, resulting from the increase in luminosity, the chamber efficiency also decreases. HL-LHC is targeting a luminosity 7.5 times as high as the design luminosity. The efficiency of MDT chambers would decrease towards low efficiencies (Kawamoto et al. [2013]).

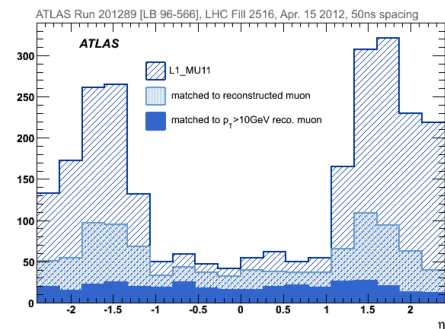
The agglomeration of additional detector hits that are not interesting for the analysis of physics processes, i.e. the background of certain processes, is called pile-up. This effect is most pronounced in the end-cap region at $\eta > 1$ as shown in figure 1.6b. Data shown in the figure is from the end of the Run-1 of the LHC at approximately 0.75 times the design luminosity. For the HL-LHC operation the luminosity will reach $7.5 \times 10^{34} \text{ cm}^{-2} \text{ s}^{-1}$.

To solve both of these issues the Small Wheel of the forward muon spectrometer was replaced in the phase 1 upgrade of the ATLAS muon spectrometer by the New Small Wheel (NSW). For completion, it is necessary to mention, that a second upgrade of other parts of the muon spectrometer will follow in the coming years as part of the phase 2 upgrade. The main topics of this upgrade are the replacement of readout electronics, upgrade of the trigger logic, and installation of new detectors in the high η region of the barrel muon spectrometer (see CERN [2017d]).



(a) MDT efficiency for different hit rates.

As the number of hits increases, the efficiency of both the single tube and the combined multilayer decreases. For the given design luminosity ($1 \times 10^{34} \text{ cm}^{-2} \text{ s}^{-1}$) the single tube efficiency only yields 70 %. The expected HL-LHC luminosity of $7.5 \times 10^{34} \text{ cm}^{-2} \text{ s}^{-1}$ results in an expected single tube hit rate of $\approx 2250 \text{ Hz}$, hence decreasing the performance further. Results shown are from testbeam measurements (Kawamoto et al. [2013]).



(b) Muon trigger candidates for different values of the pseudorapidity η .

The number of possible muon candidates allowed by the first stage selection (L1_MU11) is multiple times higher than the final (dark blue) reconstructed number of muons for large values of $\eta > 1$, i.e. the end cap region. The data shown are from 2012 at the end of the Run-1 before going into the first long shutdown. It is expected that the situation will be even worse for the operation at the HL-LHC. By introducing an additional trigger in the NSW and combining the information with the first stage selection process this high background should be controlled (Kawamoto et al. [2013]).

Figure 1.6: High-rate limitations of the Small Wheel.

To tackle the pile-up issue the NSW is going to be included in the trigger system supporting the rejection of fake hits. Figure 1.7 illustrates the working principle of the inclusion into the central trigger system. Initially, only the hit information and reconstructed trajectory of the muons provided by the first Big Wheel were considered in the trigger decision. This leads to no rejection for the trajectories B and C. Including the track information reconstructed by the NSW B and C are rejected as both do not originate from the interaction point in the center of the ATLAS experiment. Only track A will be further processed.

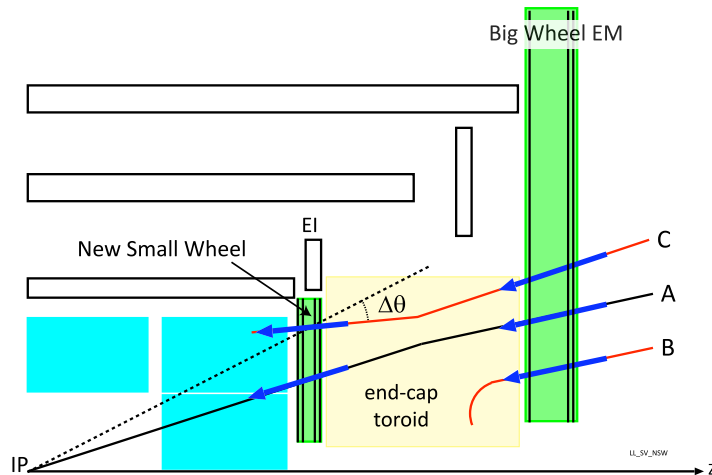


Figure 1.7: Schematic showing how the NSW is integrated into the ATLAS end-cap trigger system.

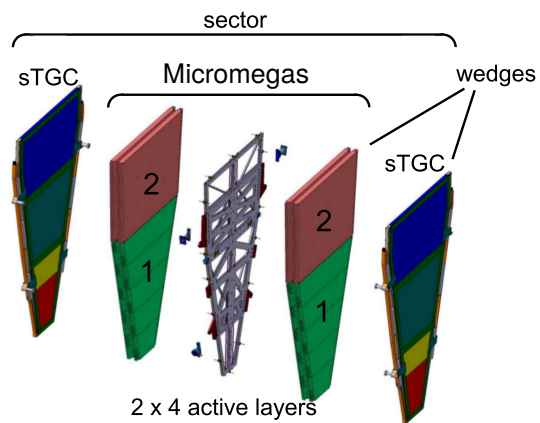
Candidate tracks provided by the Big Wheel are combined with the track information of the NSW to exclude false triggers not originating from the interaction point (IP). From the three tracks illustrated only track A is a valid candidate with the others being discarded.

Figure taken from Kawamoto et al. [2013].

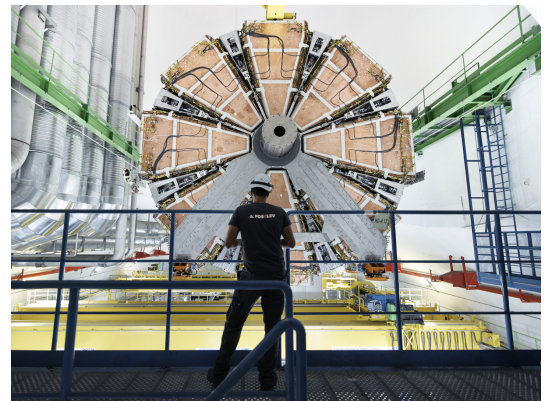
To cope with the increased rate different detector technologies were included in the NSW. Small-Strip Thin Gap Chambers (sTGCs) replace the TGC. They provide tracking information but are mainly used for trigger information. MICRO-MESH Gaseous Structure (Micromegas) detectors were chosen to replace both the MDTs and CSCs for precision tracking and to provide additional trigger information. To obtain a 360° coverage in the end-cap regions and for constructional reasons each NSW is built from 16 individual sectors. An exploded view of one sector is depicted in figure 1.8a. sTGCs and Micromegas detectors are assembled in a sandwich-like structure with two wedges being combined into a sector. Each of the wedges consists of four layers of sTGCs and Micromegas resulting in 16 layers of detectors for a sector. Exemplary for the Micromegas the splitting of the wedge into two smaller structures, labeled as 1 and 2, is shown. These parts were produced separately and assembled at a later stage before being mounted onto the NSW.

One fully assembled NSW is shown during its lowering process into the ATLAS cavern in 2021 in figure 1.8b. Visible are eight large sectors of the NSW. Not visible are eight small sectors placed behind the large sectors rotated by 22.5° to be centered between two large sectors to ensure overlap with the large sectors.

This thesis focuses on investigations of the Micromegas detectors. Although they are already included in the ATLAS experiment, there were performance problems with these detectors in terms of operational stability. Studies to investigate these problems were necessary. Proposed and accepted solutions including extensive tests concerning stability, efficiency, and resolution are performed and presented as the central topic of this thesis.



(a) Exploded representation of a NSW sector. Each sector consists of two wedges and a holding structure. Individual wedges are built from four active layers of Micromegas and sTGCs assembled as modules. Micromegas wedges are split into modules of type 1 and 2 for easier production. Figure adapted from Lösel [2017].



(b) Photo of one NSW being lowered down to the ATLAS experiment. Eight large sectors, part of the holding structure, and the opening for the beam pipe are visible. Figure taken from Brice and Ordan [2021].

Figure 1.8: Schematic of one NSW sector and photo of one fully assembled NSW.

Chapter 2

Particle Detection

The following chapter is dedicated to giving an overview of the particle-matter interactions important for detecting particles using gaseous detectors like Micromegas detectors. Charged particles are directly detectable. They interact electromagnetically. Neutral particles like photons and neutrons have to undergo primary interactions creating charged particles that are detectable (Kleinknecht [1992]).

Charge movement and amplification to create sufficiently high numbers of charges to be detectable are discussed in chapter 2.2.

An introduction to the resistive strip Micromegas detector and its structural specifications for the NSW upgrade will be discussed in chapter 2.3.

2.1 Particle-Matter Interaction

2.1.1 Heavy Charged Particles

As the Micromegas is part of the ATLAS muon spectrometer the interaction of muons with matter is the most important one to discuss. Muons are classified as heavy charged particles among others like protons and pions (Leo [1994]). The main interaction processes with matter are inelastic collisions with atomic electrons and elastic scattering with the nucleus. Other less common interactions are the emission of Cherenkov radiation, nuclear reactions, and bremsstrahlung (Leo [1994]).

The mean energy loss of particles traversing matter is described by the Bethe Bloch equation (Workman et al. [2022]):

$$\left\langle -\frac{dE}{dx} \right\rangle = 4\pi N_A r_e^2 m_e c^2 \frac{Z}{A} \frac{z^2}{\beta^2} \left[\frac{1}{2} \ln \left(\frac{2m_e c^2 \beta^2 \gamma^2 W_{\max}}{I^2} \right) - \beta^2 - \frac{\delta(\beta\gamma)}{2} \right] \quad (2.1)$$

Parameters of equation 2.1 are as follows: N_A Avogadro's number, r_e classical electron radius, m_e electron mass, Z atomic number of absorber, A atomic mass of absorber, z charge of incident particle, $\beta = v/c$ of incident particle, $\gamma = 1/\sqrt{1-\beta^2}$, W_{\max} maximum energy transfer per collision, I mean excitation energy, δ density correction.

The mass stopping power ($dE/d(\rho x)$) for muons in copper is shown in figure 2.1. A minimal amount of energy is transferred for $\beta\gamma \approx 4$. Typical values of energy loss in this region are 2-3 MeV cm² g⁻¹ (Kleinknecht [1992]). Particles of energies corresponding to this region are called Minimum Ionizing Particles (MIPs). Energies below the minimum are strongly dominated by the $1/\beta^2$ squared behavior. At $\beta\gamma \approx 0.1$ equation 2.1 breaks down and shell corrections including the atomic binding become non-negligible (Workman et al. [2022]).

At very high energies of $\beta\gamma > 1000$ radiative losses become more important. At the critical point $E_{\mu c}$ radiative losses and energy losses due to ionization are equal. Measurements for this thesis include cosmic muons of mean energies $\langle E \rangle = 4 \text{ GeV}$ (MIPs) (Workman et al. [2022]) and muons of energies up to 120 GeV ($\beta\gamma \approx 1000$). The energy loss distribution in thin media is not purely Gaussian. A shift to higher energies is visible originating from δ -electrons. These are electrons created by ionization having sufficiently high energies for secondary ionization processes (Kleinknecht [1992]).

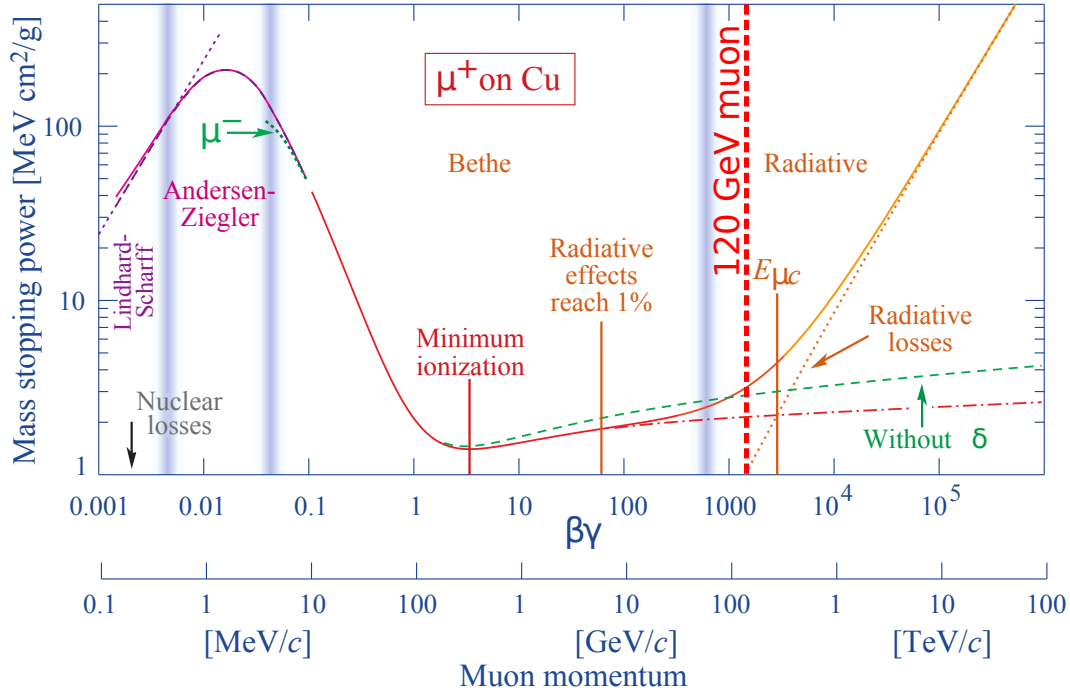


Figure 2.1: Mass stopping power for muons in copper against the muon momentum.

The minimum corresponds to values of $\beta\gamma = 4$. Particles located close to this value are called MIPs with cosmic muons being an example of such particles with a mean energy of $\approx 4 \text{ GeV}$ at sea level Workman et al. [2022]. For measurements in chapter 7 a muon beam of 120 GeV (vertical red line) is used as a test beam.

Figure adapted from Workman et al. [2022] and Jagfeld [2023].

Table 2.1 gives an overview of different gases highlighting key parameters for gaseous detectors like Micromegas. Compared to other materials noble gases offer high first ionization energies (E_I) resulting in resilience against undesired ionization processes induced by e.g. optical photons. A second desired property is a high number of (primary and total) electrons (N_p and N_T), with the reason being discussed in more detail in chapter 2.2.2.

Dedicated gases and compounds of gases are used depending on the application, economic, and ecological reasons.

Gas	ρ [mg cm ⁻³]	E_x [eV]	E_I [eV]	W_I [eV]	$dE/dx _{min}$ [keV cm ⁻¹]	N_P [cm ⁻¹]	N_T [cm ⁻¹]
He	0.179	19.8	24.6	41.3	0.32	3.5	8
Ne	0.839	16.7	21.6	37	1.45	13	40
Ar	1.66	11.6	15.7	26	2.53	25	97
Xe	5.495	8.4	12.1	22	6.87	41	312
CO ₂	1.84	7.0	13.8	34	3.35	35	100
CF ₄	3.78	10.0	16.0	35-52	6.38	52-63	120
iC ₄ H ₁₀	2.49	6.5	10.6	26	5.67	90	220

Table 2.1: Properties of different gases used in particle detectors.

ρ : density; E_x , E_I : first excitation, ionization energy; W_I : average energy for creation of an electron-ion pair; $dE/dx|_{min}$: differential energy loss; N_P , N_T : number of primary, total electron-ion pairs per cm for MIPs (extract from table 35.5 of Workman et al. [2022]).

2.1.2 Photons

The interaction of neutral particles like photons can not be described as done in the previous chapter 2.1.1. The photon intensity $I(d)$ after traversing a medium of thickness d with an attenuation coefficient μ and density ρ for a given initial intensity I_0 is given (Kleinknecht [1992]) as:

$$I(d) = I_0 e^{-\mu d / \rho} \quad (2.2)$$

The attenuation coefficient is strongly dependent on the photon energy (see figure 2.2 for Argon). Different interaction processes dominate over the photon energy range.

At low energies $E_\gamma < 100$ keV the Photoelectric Effect dominates. The photon is completely absorbed by a bound electron in the material. This electron is released from its shell with the final kinetic energy T given by (Einstein [1905])

$$T = E_\gamma - W \quad (2.3)$$

with W as the minimum energy needed to release the electron from its bound state. The sharp edge in figure 2.2 at $E_\gamma \approx 15$ keV corresponds to an energy high enough to release electrons from the K-shell (Leo [1994]).

For $E_\gamma \in [100 \text{ keV}, 10 \text{ MeV}]$ Compton Scattering dominates. Compton Scattering describes the scattering of a photon on quasi-free electrons. Bound electrons in matter can be approximated as free if the photon energy is high compared to the binding energy of the electron (Leo [1994]). The energy transfer to the electron is strongly dependent on the scattering angle Θ . Energies after the collision are given by equations 2.4 and 2.5 for the photon and electron respectively (Kleinknecht [1992]).

$$E'_\gamma = \frac{E_\gamma}{1 + \frac{E_\gamma}{m_e c^2} (1 - \cos(\Theta))} \quad (2.4)$$

$$T'_e = \frac{E_\gamma^2}{m_e c^2} \frac{1 - \cos(\Theta)}{1 + \frac{E_\gamma}{m_e c^2} (1 - \cos(\Theta))} \quad (2.5)$$

A minimum energy transfer occurs for $\Theta = 0$ resulting in $T'_e = 0$. This value increases up to a maximum energy transfer for $\Theta = \pi$. The sharp cut-off at the maximum is known as the Compton edge.

For $E_\gamma > 2m_e c^2$ photons can decay into an electron-positron pair. For momentum conservation, this process only occurs in the presence of a third body, typically the nucleus. As visible in figure 2.2 this effect becomes the dominating one for $E_\gamma > 10$ MeV in Argon.

Measurements performed in this thesis include photons with energies ranging from a few eV up to 5 MeV. Therefore all previously discussed interaction processes occur.

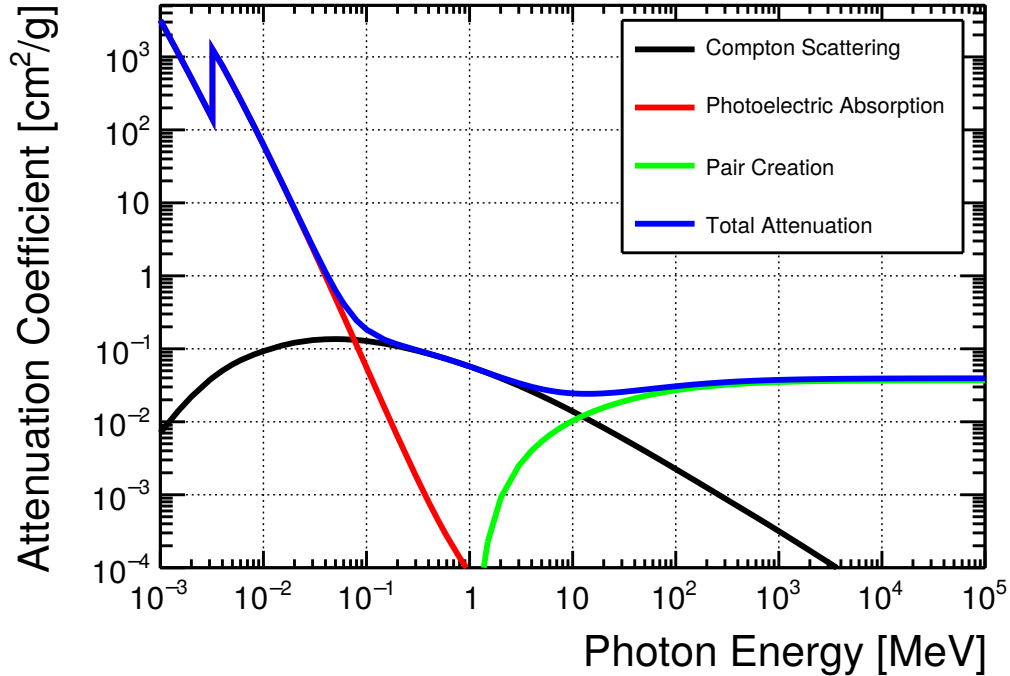


Figure 2.2: Total attenuation coefficient for different photon energies in Argon (blue line). Photoelectric Absorption (red), Compton Scattering (black), and Pair Creation (green) are drawn separately showing their dominating energy ranges. Data taken from Berger et al. [2010].

2.1.3 Neutrons

Neutrons are a second type of neutral particle interacting with matter. The total cross-section of neutrons interacting with other particles (see equation 2.6) is the sum of individual cross-sections discussed further down.

$$\sigma_{\text{Total}} = \sigma_{\text{elastic}} + \sigma_{\text{inelastic}} + \sigma_{\text{capture}} + \sigma_{\text{fission}} + \dots \quad (2.6)$$

Different cross-sections dominate at different neutron energies. The classification varies in the literature. This thesis uses the definitions from Kolanoski and Wermes [2016] listed in table 2.2. Neutrons of energies up to 11 MeV are used in measurements discussed in this thesis. The actual neutron energy spectrum will be presented in the dedicated chapter 8.

E_{kin}	Classification
< 2 meV	(Ultra-)cold neutrons
25 meV	Thermal neutrons
< 1 eV	Slow neutrons
~ 1 MeV	Fission neutrons ¹
< 20 MeV	Medium and fast neutrons
> 20 MeV	Relativistic neutrons

Table 2.2: Nomenclature for different neutron energies used in this thesis.

Elastic Scattering

The elastic scattering of a neutron with the nucleus of an atom can be described non-relativistically as being the dominant energy loss interaction in the MeV range. The starting point is a Galilean transformation of the velocities of the neutron and its scattering partner into the common CM frame (the concept is discussed in Galilei [1638] and described in Newton [1687]). The upcoming derivation of the energies and velocities partially follows Leo [1994]. The corresponding positions \vec{r}_i and velocities \vec{v}_i , as derivatives of the positions, transform as follows

$$\begin{aligned} \vec{r}_{i, \text{Lab}} &= \vec{r}_{i, \text{CM}} + \vec{V} \times t \\ \vec{v}_{i, \text{Lab}} &= \vec{v}_{i, \text{CM}} + \vec{V} \end{aligned} \quad (2.7)$$

with the CM velocity \vec{V} and time t .

From the definition of the CM frame, the sum of all momenta in this system must add up to 0. In the case of two scattering partners one obtains

$$\sum_i \vec{P}_{i, \text{CM}} = 0 = m_1 \times (\vec{v}_{1, \text{Lab}} - \vec{V}) + m_2 \times (\vec{v}_{2, \text{Lab}} - \vec{V}). \quad (2.8)$$

¹Value taken from Cranberg et al. [1956] for the nuclear fission of U^{235} . The neutron energy is continuously distributed between 0.18 MeV and ~ 12 MeV with a most probable value of 0.6 MeV.

Solving equation 2.8 for \vec{V} leads to

$$\vec{V} = \frac{m_1 \vec{v}_{1, \text{Lab}} + m_2 \vec{v}_{2, \text{Lab}}}{m_1 + m_2}. \quad (2.9)$$

Expressing the masses in terms of the atomic mass number A , the mass of the neutron and the target nucleus becomes $m_1 = 1$ and $m_2 = A$ respectively. The target nucleus is initially at rest, i.e. $\vec{v}_{2, \text{Lab}} = 0$. Substituting \vec{V} in equation 2.7 results in

$$\vec{v}_{1, \text{CM}} = \frac{A}{A+1} \vec{v}_{1, \text{Lab}} \quad (2.10)$$

$$\vec{v}_{2, \text{CM}} = -\frac{1}{A+1} \vec{v}_{1, \text{Lab}}. \quad (2.11)$$

With $\vec{v}_{i, \text{CM}} = \vec{v}'_{i, \text{CM}}$ being constant before and after (denoted with ') the collision only changing its direction, the quadratic velocity in the lab frame can be calculated as

$$\begin{aligned} |\vec{v}'_{1, \text{Lab}}|^2 &= (\vec{v}'_{1, \text{CM}} + \vec{V}) \times (\vec{v}'_{1, \text{CM}} + \vec{V}) = \\ &= |\vec{v}'_{1, \text{CM}}|^2 + |\vec{V}|^2 + 2\vec{v}'_{1, \text{CM}} \vec{V} \\ &= v'_{1, \text{CM}}{}^2 + V^2 + 2v'_{1, \text{CM}} V \cos(\Theta_{\text{CM}}) \end{aligned} \quad (2.12)$$

with Θ_{CM} being the scattering angle in the CM system (see figure 2.3). Substituting equations 2.9 and 2.10 into 2.12 follows for the kinetic energy ratio before and after scattering

$$\frac{|\vec{E}'_1|}{|\vec{E}_1|} = \frac{|\vec{v}'_{1, \text{Lab}}|^2}{|\vec{v}_{1, \text{Lab}}|^2} = \frac{A^2 + 1 + 2A \cos(\Theta_{\text{CM}})}{(A+1)^2} \quad (2.13)$$

resulting in a final kinetic energy for the neutron of

$$|\vec{E}'_1| = |\vec{E}_1| \frac{|\vec{v}'_{1, \text{Lab}}|^2}{|\vec{v}_{1, \text{Lab}}|^2} = |\vec{E}_1| \frac{A^2 + 1 + 2A \cos(\Theta_{\text{CM}})}{(A+1)^2}. \quad (2.14)$$

By conservation of kinetic energy $|\vec{E}_1| + |\vec{E}_2| = |\vec{E}'_1| + |\vec{E}'_2|$ in elastic collisions (note: $\vec{E}_2 = \frac{1}{2}A\vec{v}_{2, \text{Lab}} = 0$) the final energy of the nucleus is determined as

$$|\vec{E}'_2| = |\vec{E}_1| - |\vec{E}'_1| = |\vec{E}_1| \left(1 - \frac{A^2 + 1 + 2A \cos(\Theta_{\text{CM}})}{(A+1)^2} \right) = |\vec{E}_1| \frac{2A}{(A+1)^2} (1 - \cos(\Theta_{\text{CM}})). \quad (2.15)$$

From equations 2.14 and 2.15 trivially follows the maximum and minimum energy transfer for $\cos(\Theta_{\text{CM}}) = -1$ and $\cos(\Theta_{\text{CM}}) = +1$ respectively. A last thing to note is the maximizing effect for $A = 1$, resulting in a final energy range for the neutron of

$$0 \leq |\vec{E}'_1| \leq |\vec{E}_1|. \quad (2.16)$$

Hydrogen-rich materials like water and CH_2 (paraffin) are therefore excellent for slowing down neutrons.

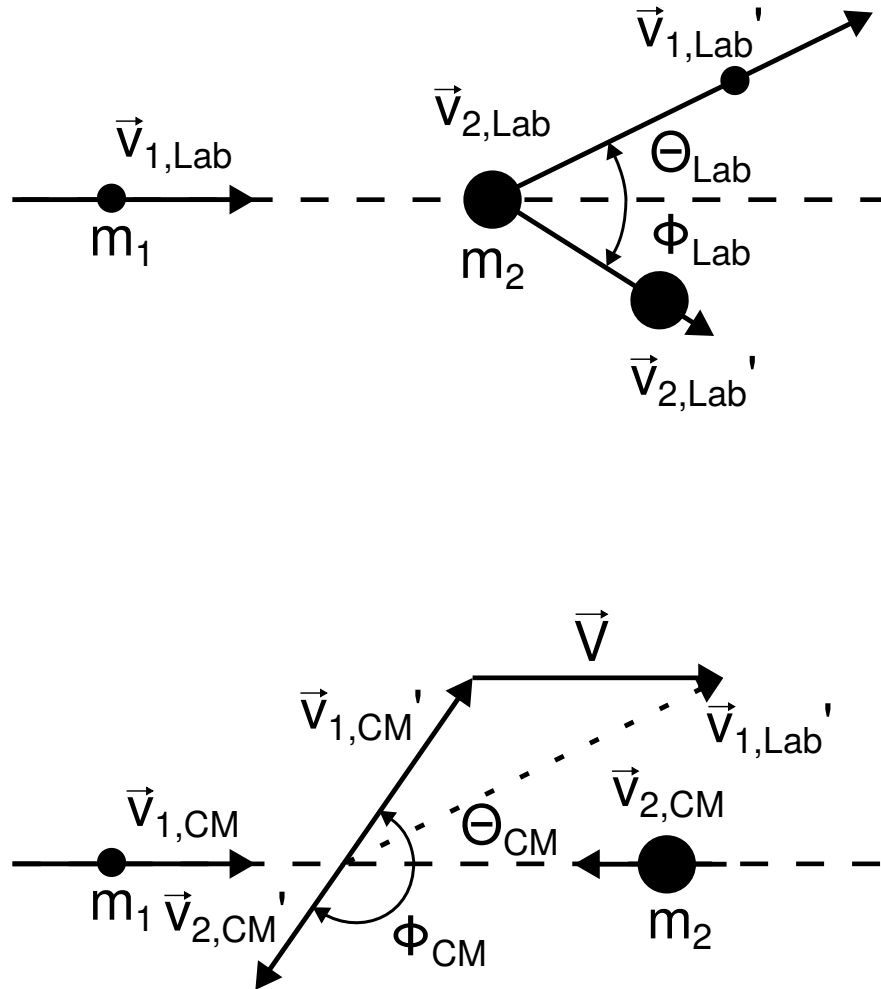


Figure 2.3: Elastic scattering of a particle with mass m_1 at a target at rest with mass m_2 . The upper figure depicts the collision in the lab frame, while the lower shows it in the CM frame. All velocities \vec{v} are before the collision, whilst \vec{v}' represents the velocities after the collision. Θ and Φ are the respective scattering angles and \vec{V} is the CM velocity.

Radiative Scattering

In comparison to elastic scattering, the kinetic energy of the system in inelastic scattering processes is not conserved. Hence it occurs only for sufficiently high, nucleus dependent, energies leaving the target in an excited state. Typically these energies are of $\mathcal{O}(1\text{ MeV})$. Examples for the inelastic cross-sections are given in appendix D for Argon (figure D.1) and Carbon (figure D.2). For Argon inelastic scattering becomes the dominant interaction process above 5.6 MeV, while for Carbon the elastic scattering remains the main contribution to the total cross-section. The excited nuclei decay then via radiative emission, e.g. by emitting a photon.

A rare inelastic-induced reaction is the dissociation of the target into multiple α particles. For $\text{C}^{12}(n, n')3\alpha$ this was investigated by Vasil'Ev et al. [1958] showing an energy dependent total cross-section of (100–400 mbarn) for neutron energies of 12.5 MeV and > 18 MeV respectively. The threshold energy for this reaction is 7.28 MeV, therefore contributing to the possible reactions induced by the neutron source discussed in chapter 8.

Another possibility is the release of additional neutrons in an $A(n, 2n')B^*$ interaction resulting in a different isotope. For sufficiently high energies also emission of charged particles is possible, e.g. ${}^3\text{He}(n, p){}^3\text{H}$ or ${}^{10}\text{B}(n, \alpha){}^7\text{Li}$ (Wirtz and Beckurts [1958]).

Since the cross-section for neutron capture processes follows roughly $1/v_{\text{Neutron}}$, slower ones are more likely to be captured by a target nucleus. Resulting in a $A(n,\gamma)A + 1$ reaction emitting a photon. For this reaction element dependent resonances may increase the cross-section for specific neutron energies.

The last interaction to be mentioned is the neutron-induced nuclear fission $A(n, f)B + C$. Here neutrons are captured providing sufficient high energy to overcome the strong force in the nucleus leading to a separation of the target into two smaller nuclei. These experience repulsion from the electromagnetic forces and split up. Additionally to the two nuclei, fast neutrons are emitted. There are two main types of creating a chain reaction. The usage of 'fissile' fuel, e.g. ^{235}U , where the emitted fast neutrons are moderated to thermal energies enhancing the capture cross-section. Alternatively, a 'fissionable' fuel, e.g. ^{238}U , is used utilizing unmoderated fast neutrons to overcome the strong coupling.

2.2 Charge Separation and Amplification

The energy of traversing particles in a detector is deposited in the form of creating a certain number of electron-ion pairs based on the particle type, energy, and detector material. The number of created electrons or ions is then measured in the form of charge signals. Electron-ion pairs created in matter without external influence will however recombine. To detect particles traversing a detector a charge separation is necessary. Additionally for the case of gas-filled detectors like the Micromegas detector (see chapter 2.3) primary electrons need to be multiplied to be detectable and distinguishable from electronic noise.

2.2.1 Particle Drift in Gas

Separation of electrons and ions is achieved by applying an electric field to the medium. Electrons will move to the positive anode and ions will travel to the negative cathode.

Electron Movement

Electrons are accelerated along the electric field lines within a free path length. On their path to the anode, they interact with atoms of the medium. For electric fields $|\vec{E}| \approx 1 \text{ kV/cm}$ as in detectors discussed in this thesis the acceleration and the elastic scattering of the electrons with the medium cancel without inducing further ionization, hence the electrons drift (Leo [1994]).

The cross-section for elastic scattering processes depending on the electron velocity is shown in figure 2.4. A minimum cross-section is visible for electron energies below 1 eV which is known as Ramsauer minimum (Ramsauer and Kollath [1929]). Electrons of energies close to this minimum follow the electric field lines most closely due to the decreased scattering probability. This effect is utilized in gas detectors and explained in more detail in chapter 3 with a detailed view on the properties of different operating gases.

High energy electrons like the previously discussed δ -electrons or electrons created by photons move more freely in the electric field. Energy loss of such electrons in matter can be described using the Continuous Slowing Down Approximation (CSDA) range. This range describes the distance in a given material until electrons are slowed down to an energy of approximately 10 eV. Flierl [2018] simulated this for Helium and Argon for electron energies up to 100 keV. Results depicted in figure 2.5 show electron ranges of a few cm for the highest energies. Photoelectrons of $T = 50 \text{ keV}$, which are important in chapter 8, travel up to 20 mm before having slowed down. A tracking simulation for various electron energies was performed in

Flierl [2014] also showing the electron-induced ionization processes along the track. Electrons of higher initial energies tend to follow a straight line whereas electrons with lower initial energy deposit their energy more clustered in a small volume.

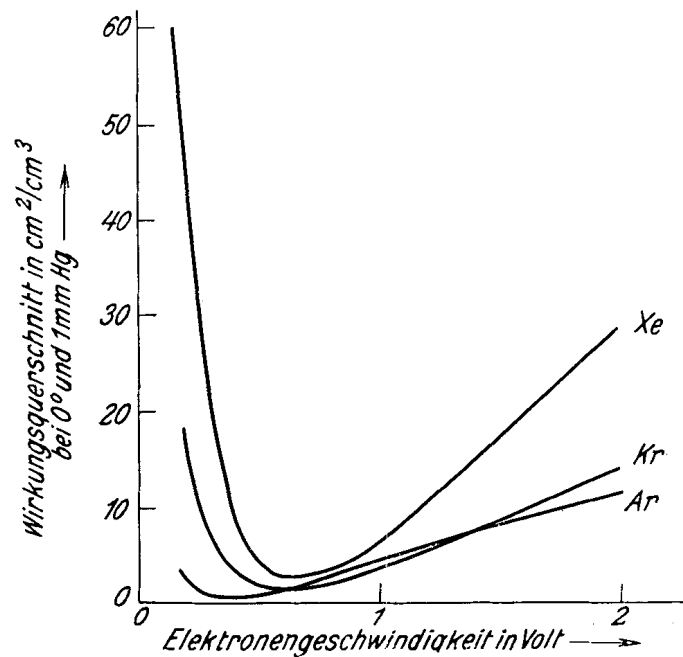


Figure 2.4: Energy dependency of the elastic scattering cross-section of electrons in different noble gases.

For the displayed gases and energy scale the elastic cross-section reflects the total cross-section due to the high excitation and ionization energies of inert gases ($\mathcal{O}(10\text{ eV})$). Graphic taken from Ramsauer and Kollath [1929].

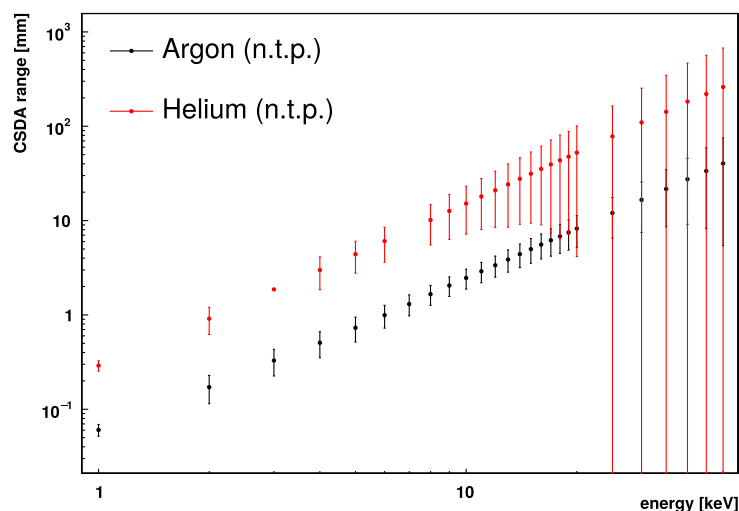


Figure 2.5: CSDA range for electrons in Argon and Helium plotted against the initial electron energy.

Photoelectrons with an energy of $\approx 50\text{ keV}$ have a CSDA range of 20 mm in Argon. Depending on the detector geometry only a fraction of the initial photon energy is detected. Figure taken from Flierl [2018].

Ion Mobility

Ions produced during the ionization processes experience the same electric field. Due to their much higher mass and smaller mean free path compared to electrons, ions accelerate less along their path. Additionally ions have a much smaller mobility (μ_{ion}) than electrons ($\mathcal{O}(10^2 - 10^3)$). The mean ion velocity (\vec{v}_{ion}) in an electric field \vec{E} at a gas pressure p is given by Kleinknecht [1992] as

$$\vec{v}_{\text{ion}} = \mu_{\text{ion}} \vec{E} \frac{p_0}{p} \quad (2.17)$$

with p_0 as normal pressure of 760 Torr. Mobilities for ions of type i (μ_i) in compound gas mixtures can be calculated using

$$\frac{1}{\mu_i} = \sum_{k=1}^n \frac{c_k}{\mu_{ik}} \quad (2.18)$$

with c_k being the concentration of a gas k and μ_{ik} being the mobility of the ions of type i in the gas of type k (Kleinknecht [1992]).

Typical ion mobilities for gases used in this thesis are given in table 2.3.

Gas	Ion	μ [$\text{cm}^2\text{V}^{-1}\text{s}^{-1}$]
Ar	Ar^+	1.7
Ar	$\text{iC}_4\text{H}_{10}^+$	1.56
Ar	CO_2^+	1.72
iC_4H_{10}	$\text{iC}_4\text{H}_{10}^+$	0.61
CO_2	CO_2^+	1.09

Table 2.3: Ion mobilities in various gases (extract from table 6 of Kleinknecht [1992]).

2.2.2 Gas Amplification

For sufficiently high electric fields electrons gain enough energy between collisions to ionize further atoms creating additional electron-ion pairs. This process will repeat for the new secondary electron subsequently producing electrons forming an electron avalanche (Kleinknecht [1992]). Due to the higher mobility of the electrons compared to the ions a drop-like structure as shown in figure 2.6 is created. This charge multiplication is necessary to provide a sufficiently high number of electrons that is resolvable by the readout electronics.

Townsend [1910] described the number of electrons N in dependence of the drift distance x by the following differential equation

$$dN(x) = \alpha (|\vec{E}(x)|) N(x) dx \quad (2.19)$$

with α being the first Townsend coefficient.

Solving equation 2.19 for the total number of electrons $N(x)$ gives for an initial number of electrons N_0 :

$$\begin{aligned} N(x) &= N_0 e^{\int \alpha(x) dx} \\ N(x) &= N_0 G \end{aligned} \quad (2.20)$$

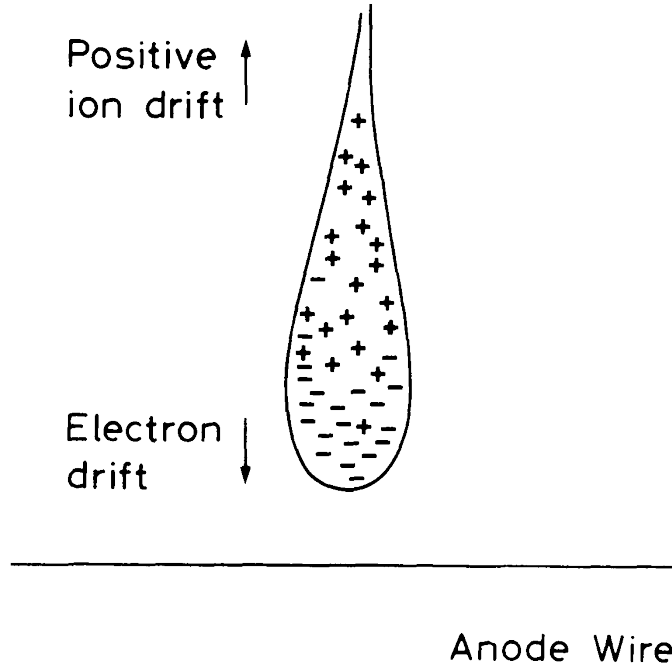


Figure 2.6: Avalanche formation in an electric field. The drop-like structure originates from the higher electron mobility compared to the ions up to factors of $10^2 - 10^3$ Kleinknecht [1992]. Figure taken from Leo [1994].

G is the achieved gain factor in the given electric field and gas conditions. α can be expressed in terms of the mean free path λ as described in Kleinknecht [1992]:

$$\alpha(|\vec{E}|) = \frac{1}{\lambda(|\vec{E}|)} \quad (2.21)$$

A theoretical model described by Korff [1946] proposes equation 2.22 for the determination of the Townsend coefficient with p and T being the pressure and temperature respectively. A and B are gas and detector-dependent constants that need to be determined experimentally as done in Lippert [2012] for the Micromegas detectors. For a gas mixture of Ar:CO₂ 93:7 vol% values of $A = (111.2 \pm 0.6) \text{ K bar}^{-1} \mu\text{m}^{-1}$ and $B = (2196 \pm 7) \text{ K V bar}^{-1} \mu\text{m}^{-1}$ were measured.

$$\alpha(|\vec{E}|) = \frac{Ap}{T} \exp\left(-\frac{Bp}{|\vec{E}|T}\right) \quad (2.22)$$

For the gain follows, therefore:

$$G = \exp\left[\frac{Ap}{T} \exp\left(-\frac{Bp}{|\vec{E}|T}\right) x\right] \quad (2.23)$$

Important to note is an upper limit of the gain of $G < 10^8$ (Leo [1994]) known as Raether limit (Raether [1964]). For higher values voltage breakdowns occur. Such voltage breakdowns are observed as discharges resulting in a change of the electric potential.

2.3 Resistive Strip Micromegas

The upcoming chapter is dedicated to explaining the working principle of a resistive strip Micromegas detector ([Alexopoulos et al., 2011]) a further developed variant of the original Micromegas detector (Giomataris et al. [1996]). Since all Micromegas detectors used in this thesis are of the resistive strip type, Micromegas detectors denote resistive strip Micromegas detectors if not stated differently.

Micromegas detectors are gas-filled detectors operated typically with a gas mixture of Ar:CO₂. A gas ratio of 93:7 vol% was originally chosen for the NSW Micromegas detectors (Kawamoto et al. [2013]). A detailed discussion on the operating gas follows in the next chapter 3.

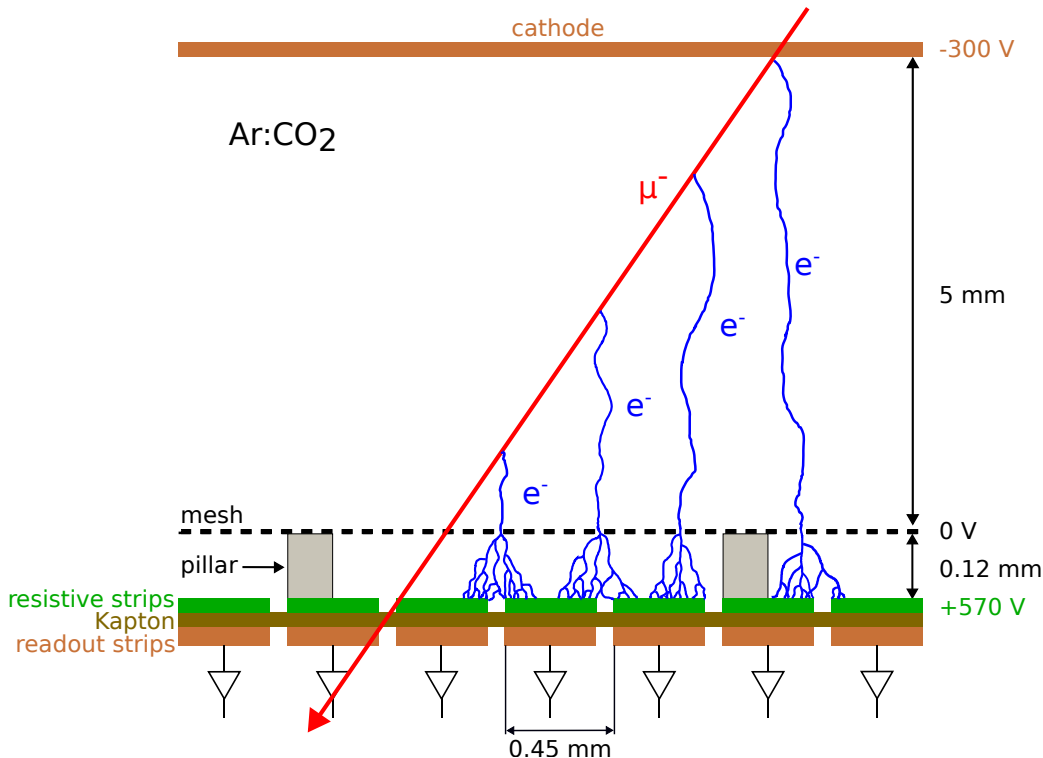


Figure 2.7: Working principle of a resistive strip Micromegas detector.

A Micromegas detector consists of three parallel planar structures: a copper cathode, a stainless-steel micro-mesh, and an anode. Ionizing particles create electron-ion pairs in the gas-filled (e.g. Ar:CO₂) detector. A weak electric field ($\mathcal{O}(< 1 \text{ keV/cm})$) between the cathode and the micro-mesh separates the charges with the electrons drifting towards the mesh. This region is called drift region. The electric field between the mesh and the resistive anode is in the order of $\mathcal{O}(40 - 50 \text{ keV/cm})$. This strong increase in the electric field strength in the vicinity of the mesh leads to a funneling of the electrons through the mesh achieving a transparency close to 100%. The region between the mesh and the resistive anode is called amplification region. Electrons in this region are accelerated resulting in charge multiplication via Townsend avalanches (see chapter 2.2.2). Electrons are collected on resistive anode strips. The signal is coupled to the readout strips beneath. Strip pitches in the NSW Micromegas detectors are 0.425 and 0.450 mm. The distance between the mesh and the anode is defined by an insulating pillar structure on the anode.

Micromegas detectors consist of three planar structures as shown in figure 2.7: A copper cathode, a grounded stainless-steel micro-mesh, and a resistive anode. The micro-mesh divides the detector into two areas. Between the cathode and the micro-mesh is the drift region where a weak electric field ($\mathcal{O}(< 1 \text{ keV/cm})$) is applied. Typical for a Micromegas detector is the large drift volume compared to the total volume of the detector. Exemplary for the used Micromegas (see figure 2.7), 5 mm of the total height of 5.12 mm are part of the drift gap.

The large volume increases the ionization probability of traversing particles like muons and hence the number of primary electrons (see table 2.1). Created electrons drift toward the micro-mesh.

Between the micro-mesh and the resistive strips on the anode a strong electric field ($\mathcal{O}(40 - 50 \text{ keV/cm})$) is applied. This region is called the amplification gap. The large difference in electric field strength results in the creation of funnels above the micro-mesh increasing the electron mesh transparency close to 100% (Kuger [2017]). Insulating pillars with a height of $h_{\text{pillar}} \approx 0.12 \text{ mm}$ are used to ensure a homogeneous electric field by fixing the distance between the anode and the micro-mesh. The micro-mesh is electrostatically pressed onto the top of the pillars. Electrons reaching the amplification gap are strongly accelerated towards the anode creating Townsend avalanches (see chapter 2.2.2). In the 0.12 mm amplification gap a gain of typically $G = 10000$ is achieved². Electrons are collected on the resistive strips. The copper readout strips that are separated from the resistive strips by an insulating layer, e.g. Kapton (Dupont [2023]) are connected to readout electronics (see chapters 4.2 and 4.3). Signals induced by the electrons and the ion movement (see Shockley-Ramo Theorem Shockley [2004] and Ramo [1939]) couple through the insulating layer to the copper strips.

Copper and resistive strip pitches of 0.425 mm and 0.450 mm are used in the NSW Micromegas detectors. The resistive strips are screen-printed using a resistive paste on a 50 μm thick Kapton foil and then glued on top of the copper strips. A good alignment of the resistive strips and the readout strips is crucial to ensure a good detector performance (Alexopoulos et al. [2011]).

The main advantage of the resistive strip Micromegas detector compared to the standard Micromegas detector is the improved discharge quenching. Given a too-high charge density in the amplification gap, a discharge between the mesh and the anode can be created resulting in a current flow. If the anode is built from copper strips as proposed in Giomataris et al. [1996] discharges will lead to a voltage breakdown of the full detector as there is almost no resistance along the anode copper strips. The discharge is quenched after voltage equilibrium between anode and mesh and the high-voltage power supply has to recharge the high-voltage plane. Long periods of inefficient operation are the consequence.

In the case of high resistive strips $R = \mathcal{O}(\text{M}\Omega/\text{cm})$ charges can not flow fast enough to the discharge position resulting only in a local voltage decrease (Alexopoulos et al. [2011]).

2.3.1 Anode Signals

Electrons and ions contribute to the signal on the anode. Flierl [2018] calculated the individual contributions. Results are shown in figure 2.8 for the electron (blue) and ion (red) components. About half of the electrons and ions are created in the last amplification stage of the avalanche close to the anode. This and the high electron mobility result in a very fast signal $\mathcal{O}(< 5 \text{ ns})$. Ion movement away from the anode towards the mesh contributes to a signal of the same polarity. Due to their smaller mobility and the fact that they have to traverse the whole amplification gap the ion signal is much longer $\mathcal{O}(100 \text{ ns})$. This slow ion movement limits locally ($\mathcal{O}(1 \text{ mm}^2)$) the detection rate as the space charge moving towards the mesh influences the electric field and thus the amplification. A typical timescale of this local inefficiency is $\mathcal{O}(100 \text{ ns})$ for the Micromegas detector as shown in figure 2.8. The rest of the detector remains unaffected and thus high-rate capability is ensured.

²An overview of the measured gain for different gas compositions and amplification voltages can be found in Vandenbroucke [2019].

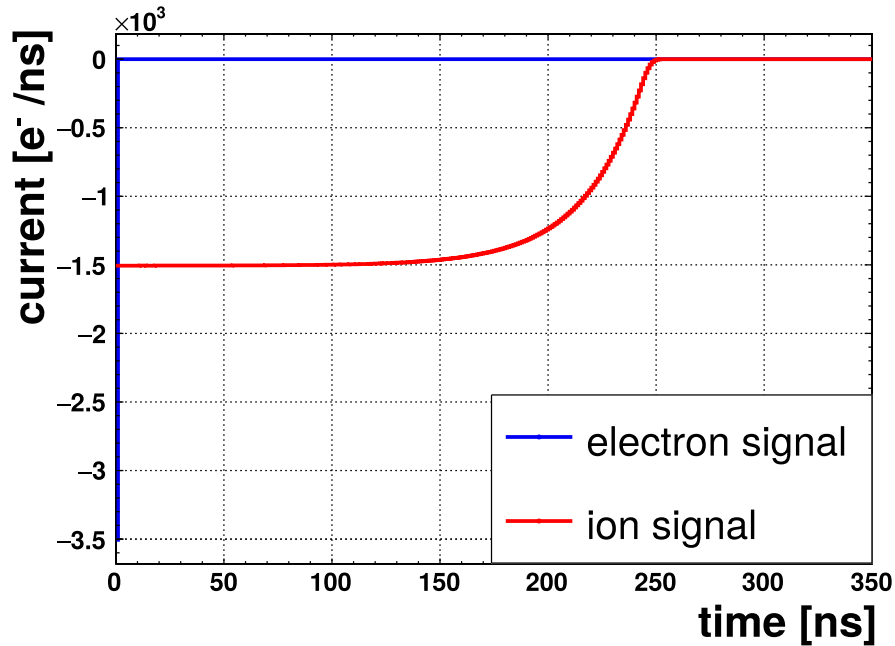


Figure 2.8: Calculated signal components for a Micromegas detector. The signal consists of a fast electron component (blue) and much slower ($\mathcal{O}(100\text{ ns})$) ion tail (red) induced by the ion movement towards the mesh. Due to the movement away from the anode but with the opposite charge, the signal polarity induced by ions is identical to the electron signal polarity. Figure taken from Flierl [2018].

2.3.2 NSW Micromegas Modules

The upcoming chapter is a summary of the necessary key information regarding the NSW Micromegas detector layouts from the NSW TDR (Kawamoto et al. [2013]).

To provide a full 360° coverage of the NSW in ATLAS the wheel structure was divided into 16 sectors per wheel (see figure 1.8a). Eight large and eight small sectors are built and assembled with overlap to introduce alignment capabilities, redundancy and to prevent the passing of muons undetected.

Sector Layout

Sectors themselves are split into two wedges mounted on a common spacer frame. Two individual subparts in the case of the Micromegas detectors build a wedge as shown in figure 2.9 for small (left) and large (right) sectors. The four differently sized detectors Small Module 1 (SM1), Small Module 2 (SM2), Large Module 1 (LM1) and Large Module 2 (LM2) were built and assembled in Italy, Germany, France, and in a collaborative effort of CERN, Greece and Russia respectively. Besides their dimensions, small and large modules differ by their strip pitch which is 0.425 mm for the small and 0.450 mm for the large modules. Individual modules are built from multiple Printed Circuit Board (PCB)s that are glued together (see Herrmann [2019]). Type 1 modules are made from five rather narrow PCBs while type 2 modules consist of three rather wide PCBs. The production of the PCBs was limited in one dimension by construction and chosen thus to 450 mm. Therefore this splitting was necessary. Module and PCB names throughout the thesis refer to the naming scheme given in figure 2.9.

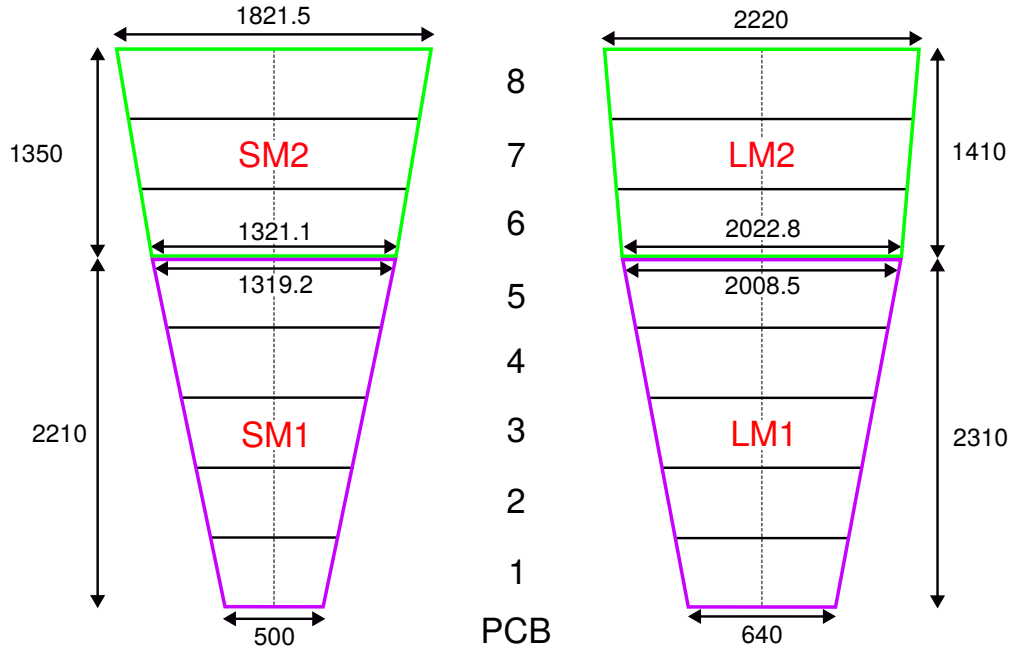


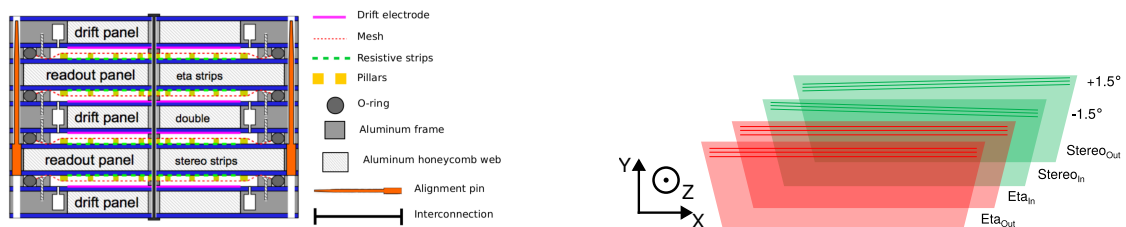
Figure 2.9: Dimensions of the four different NSW Micromegas sizes given in mm. Left: Small Wedge. Right: Large Wedge.

A sector is built from two wedges, separated by a spacer frame. For constructional reasons, the sectors of the NSW were split into four quadruplets, being assembled into wedges at CERN. The differently sized detectors were built in Italy (SM1), Germany (SM2), France (LM1) and in Greece, Russia and at CERN (LM2). For the NSW a total of 32 each were necessary with additional spares being built.

The labeling used throughout this thesis follows e.g. SM2 M03 being series module 3 of SM2, where module refers to a fully assembled quadruplet of four active layers (see figure 2.10). The strip pitches of small modules are 0.425 mm whereas large modules have strip pitches of 0.450 mm. The high-voltage supply of the anode is split in the center of the PCB and can be set individually (dotted line). During operation in the NSW both halves of the PCB are powered by the same high-voltage line.

Quadruplet Layout

Individual modules of the sectors consist of multiple active readout layers. For redundancy and to provide high efficiency each of the modules contains four individual Micromegas detectors as explained in chapter 2.3. The four anodes of a quadruplet are built onto two readout panels that are sandwiched between three drift panels as sketched in figure 2.10a. O-rings at the edges of the panels provide gas tightness. Blow-up protection is ensured by introducing interconnections between the different layers (Lösel [2017]). NSW Micromegas detectors are one-dimensional strip detectors with strips parallel to the parallel sides of the trapezoid. These strips are shown as Eta strips in figure 2.10b. Due to the magnetic field configuration (see chapter 1.2) and cylindric geometry of the ATLAS experiment the precision requirement to achieve a good momentum reconstruction is perpendicular to the Eta strips. However, by introducing two Stereo layers that have readout strips rotated by $\pm 1.5^\circ$ concerning the Eta strips coarse position information ($\mathcal{O}(\text{mm})$) along the readout strips is reconstructible. The position reconstruction using Stereo layers is discussed in chapter 5.1. In this thesis, the direction perpendicular to the Eta strips is called precision direction whereas non-precision direction denotes position information along the readout strips.



(a) Assembly structure of the four active layers of the NSW Micromegas module.

It consists of three drift panels (two outer and one central double drift) containing the cathodes and the floating meshes. Two readout panels with two anode structures each are sandwiched between the drift panels. Pillars on the readout anode define the distance between the micromesh and the anode. O-rings are used for gas tightness whereas the interconnection provides blow-up protection for too high gas pressures (Lösel [2017]).

Figure taken from Sidiropoulou [2018].

(b) Anode geometries and nomenclature:

The two readout panels used in a single module are the Eta and Stereo panels. Eta panels consist of two identical readout anodes having readout strips parallel to the long and short sides of the characteristic trapezoidal shape. Stereo anode strips are rotated by $\pm 1.5^\circ$ concerning the Eta strips providing position information along the strips by combining hit positions of both layers (see equation 5.14 in chapter 5.1).

Figure 2.10: NSW Micromegas layout.

Chapter 3

Counting Gas

Micromegas detectors for the NSW upgrade were foreseen to be operated with a gas mixture of Ar:CO₂ 93:7 vol%. Noble gases like Argon are favorable for proportional counters. Due to their high first ionization energies (see table 2.1) unwanted ionization by optical or UV-photons is prevented. A stable amplification can be formed for relatively low electric fields. High excitation energies of pure Argon give rise to photon emission by de-excitation that leads to ionization processes in the detector material, e.g. the Copper cathode (Leo [1994]). Neutralization processes of Argon ions at the cathode result also in the emission of photons (Kolanoski and Vermes [2016]). This results in unwanted, uncontrollable secondary processes affecting the detector's performance and stability. Due to the nature of a single atomic gas like Argon low energy photons can not be captured to prevent this.

3.1 Quenching Gas

Quenching gases like CO₂, CF₄, CH₄ or iC₄H₁₀ are added to the noble gas mixture to absorb low energy photons. Due to their molecular structure, these gases provide additional vibrational degrees of freedom that are excited by the absorbed photons and de-excite non-radiatively. Additionally, due to lower excitation levels electrons traveling through the compound mixture lose energy. The electrons are slowed down to the Ramsauer minimum (see figure 2.4). Due to the less frequent scattering interactions, the mean drift velocity of the electrons rises.

3.2 Legacy Gas Problems

The exact mixing ratio of the gases concerning the operation in ATLAS had multiple reasons. Economically a reuse of the installed gas system at ATLAS is favoured since the previously installed MDTs also used Argon and CO₂ as operating gas.

The gas system for the ATLAS NSW Micromegas detectors operates with an open-end exhaust (Kawamoto et al. [2013]). For ecological reasons reducing the amount of greenhouse gas emission prefers mixtures with low CO₂ content. Alexopoulos et al. [2011] showed a better discharge resilience of small 10 × 10 cm² Micromegas detectors under neutron irradiation for the Ar:CO₂ 93:7 vol% operating gas compared to gas mixtures containing larger amounts of CO₂. Neutrons are one of the main backgrounds passing the inner forward muon spectrometer in ATLAS possibly inducing radiation damage. Consequently, the decision was made for the Ar:CO₂ 93:7 vol% gas mixture (Kawamoto et al. [2013]).

Throughout this thesis, this mixing ratio of Argon and CO₂ is called legacy gas mixture.

Herrmann [2019] has shown during the series production of the SM2 that higher gains are achievable for mixing ratios of e.g. Ar:CO₂ 80:20 vol%. This is only possible by increasing the amplification voltage (U_{Amp}) applied to the anode and the drift voltage (U_{Drift}) applied to the cathode.

The scaling of the small $10 \times 10 \text{ cm}^2$ Micromegas detectors, operating stably with the legacy gas mixture, to large area detectors for the NSW project showed large problems regarding the discharge stability of the detector. The applied amplification voltage and the current development over time are shown for an exemplaric sector of an SM2 detector in figure 3.1. A constantly spiking current of up to $0.5 \mu\text{A}$ is observed, meaning continuous discharging is happening in the detector between the anode and the mesh. For nonresistive strip Micromegas this would result in a visible voltage drop (see Alexopoulos et al. [2011]). With the locally restricted discharging and fast quenching this is prevented. However, discharges tend to introduce surface damage on the anode (Vogel [2021]) destroying the resistive layer of the detector. This damage is irreversible and in the case of a foreseen installation of the detectors into the ATLAS experiment replacement of damaged detectors is not easily feasible. Detectors can only be replaced in long shutdown periods as a disassembling of the NSW would be necessary.

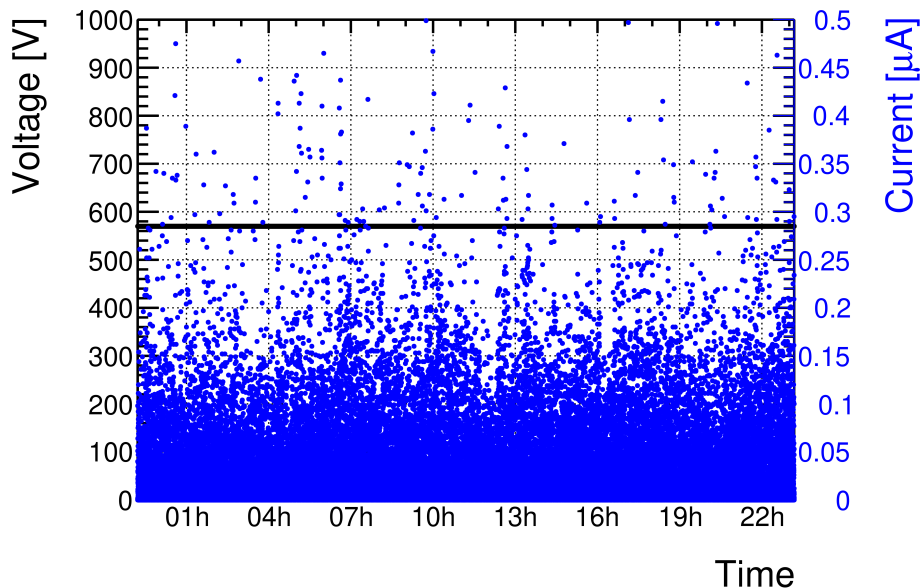


Figure 3.1: Discharging HV sector of SM2 M03 under Ar:CO₂ at $U_{\text{Amp}} = 570 \text{ V}$ (black line). A high rate of current spikes (blue) up to $0.5 \mu\text{A}$ is visible. Such discharges may induce surface damage to the resistive strip anode resulting in a worse detector performance. The displayed timeframe is one day.

3.2.1 Adaptation of the Operating Gas

Besides the adaptations of the gas mixing ratios studied in Herrmann [2019] adding a third gas with even better quenching capabilities than CO₂ is an approach to improve the detector stability. Concerning the feasibility within the ATLAS experiment the selection of possible additions is limited. Economical and ecological restrictions have to be taken into account. Historically hydrocarbons were used in Micromegas detectors for quenching (Giomataris et al. [1996]). Within the NSW upgrade project the decision to test the detector performance replacing 2% of the CO₂ with Isobutane (iC₄H₁₀) to form a new ternary gas mixture of

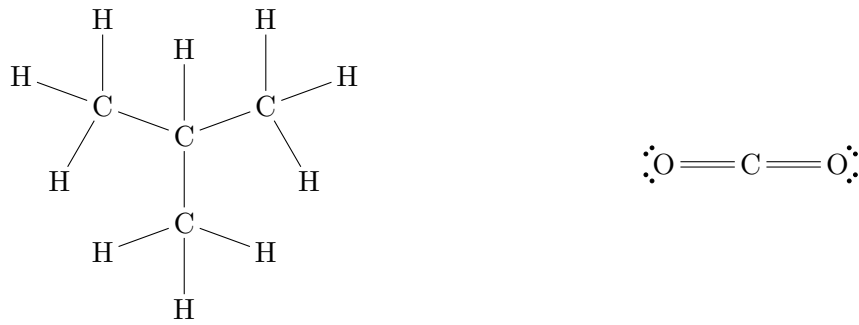


Figure 3.2: Molecular formulae for iC_4H_{10} and CO_2 . The number of vibrational degrees of freedom scales with the number of atoms and the structure of the molecule². For iC_4H_{10} there are $N_{DOF} = 36$. The linear CO_2 has only $N_{DOF} = 4$.

Ar: CO_2 : iC_4H_{10} 93:5:2 vol% was taken. This admixture of isobutane is the maximum amount allowed within the ATLAS cavern ensuring the flammability limit in case of leakage is never reached¹.

Being a larger molecule than CO_2 (see figure 3.2) Isobutane provides more rotational and vibrational degrees of freedom hence better quenching. As a rule of thumb: the quenching capabilities of a gas improve with the number of atoms in a molecule (Kolanoski and Wermes [2016]). The improvement in the detector stability is visible in figure 3.3 displaying the former discharging sector from figure 3.1 operated with the ternary gas mixture of Ar: CO_2 : iC_4H_{10} 93:5:2 vol%. No discharges are observed for the displayed time window of one day. The detector was hereby operated at a higher gas gain than in the case of the Ar: CO_2 gas mixture.

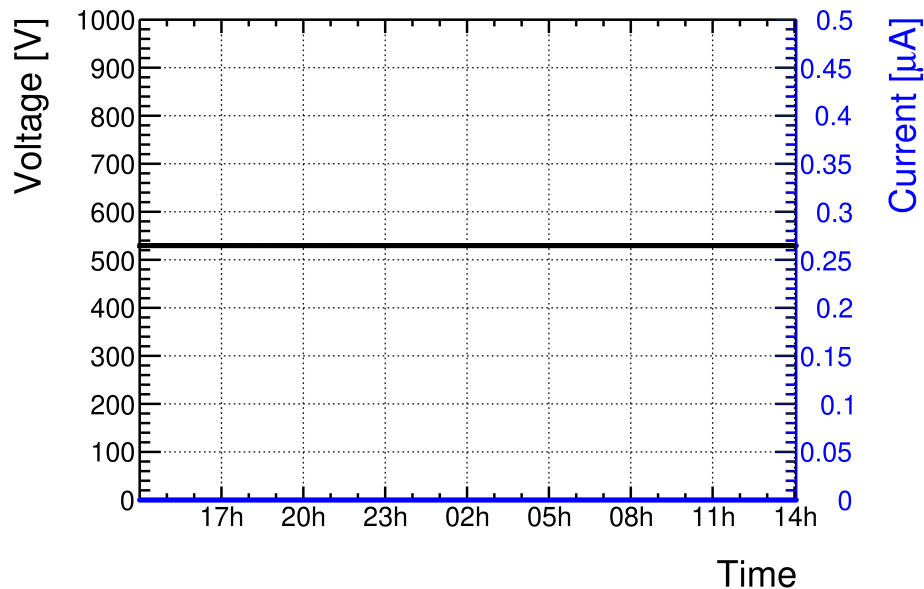


Figure 3.3: HV sector of SM2 M03 under Ar: CO_2 : iC_4H_{10} at $U_{Amp} = 530$ V showing no discharges at all. The sector shown is the same as in figure 3.1. The displayed timeframe is one day.

¹The flammability limits for isobutane are given e.g. in https://produkte.linde-gas.at/sdb_konform/R600_10021773DE.pdf with a lower limit of 1.5% and an upper limit of 9.5% pure isobutane in air.

²Linear molecules have $3N-5$ vibrational degrees of freedom, while non-linear molecules have $3N-6$ (Landau and Lifshitz [1977]).

3.3 Comparison of Operating Gas Properties

For the new gas composition Ar:CO₂:iC₄H₁₀ 93:5:2 vol% amplification and drift voltage have to be adapted which is the topic of this section of the chapter.

3.3.1 Drift Voltage

A MAGBOLTZ (Biagi [2023]) simulation in Garfield++ (Veenhof [2010]) for varying drift fields was performed investigating the electron drift velocity (left) and the transverse diffusion (right) for the two previously discussed gas mixtures with results shown in figure 3.4. Both gas mixtures behave similarly regarding the electron drift velocity with the ternary gas mixture curve (green) being shifted by $\approx 60 \text{ V cm}^{-1}$ towards lower electric fields. Maximum values for a drift gap of 5 mm (see figure 2.7) are achieved for $U_{\text{Drift}} = 250 \text{ V}$ and $U_{\text{Drift}} = 280 \text{ V}$ for the ternary and legacy gas mixture (brown) respectively. The maximum electron drift velocity of the legacy gas mixture of $4.7 \text{ cm } \mu\text{s}^{-1}$ is $0.1 \text{ cm } \mu\text{s}^{-1}$ faster. The transverse diffusion of the electrons decreases for both gas mixtures up to a minimum value at $\approx 150 - 200 \text{ V cm}^{-1}$. A small value is preferred for better position reconstruction (see chapter 5.2). As the maximum drift velocity under Ar:CO₂:iC₄H₁₀ is achieved at smaller U_{Drift} lower transverse diffusion is achievable compared to the Ar:CO₂ gas mixture. Additional test measurements by Fallavollita and Iengo [2022] concerning the mesh transparency for electrons and ions also favor smaller values of U_{Drift} for the ternary gas. At ATLAS an operating voltage of $U_{\text{Drift}} = 300 \text{ V}$ for the legacy gas mixture is chosen. The ternary gas mixture uses $U_{\text{Drift}} = 240 \text{ V}$.

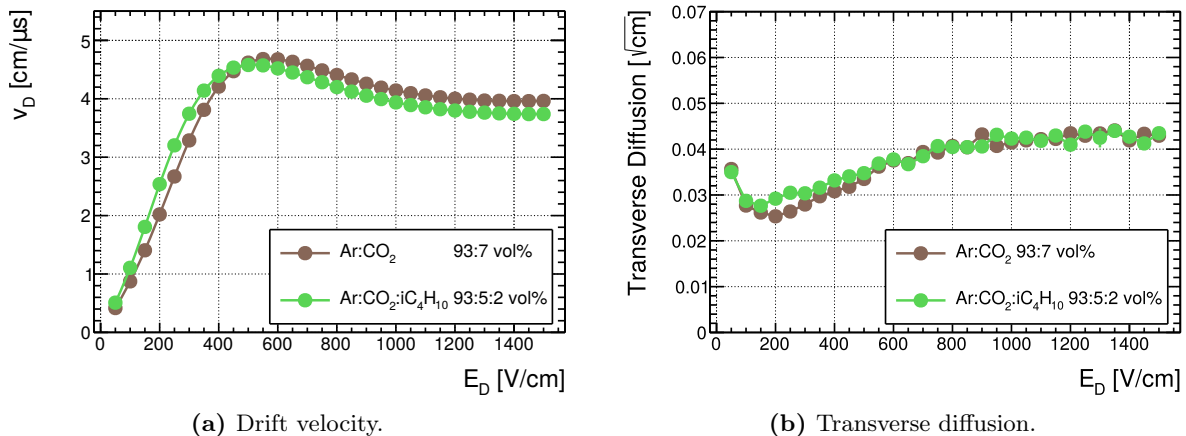


Figure 3.4: MAGBOLTZ (Biagi [2023]) simulation in Garfield++ (Veenhof [2010]) of electron movement parameters in Ar:CO₂ and Ar:CO₂:iC₄H₁₀ for various electric fields³. The ternary gas mixture shows similar drift velocities as the legacy gas mixture shifted slightly to lower electric fields (left). Operating the detector at lower electric fields leads to less transverse diffusion (right) up to an inflection point at $\approx 150 - 200 \text{ V cm}^{-1}$.

3.3.2 Amplification Voltage

The decision on the amplification voltage depends on the detector stability regarding discharges and the achievable gas gain. To compare the gain of the two gas mixtures the detector was irradiated by a radioactive source. The source used for this measurement is an Americium-Beryllium (Am-Be) source which will be the topic in chapter 8. Anode currents drawn by the detector for varying amplification voltages are compared. Since the current is

³The errors of the displayed data points are smaller than the marker size. This also holds for figure 3.5.

proportional to the number of charges on the resistive strips, which themselves are proportional to the gain this is a suitable parameter to compare the gains of the operating gases. Results of amplification scans for the two gas mixtures are shown in figure 3.5. Values for the legacy gas mixture (brown) are shifted by -50 V matching the values of the ternary gas mixture (green) for better comparison. Comparing the current drawn for $U_{\text{Amp}} = 570\text{ V}$ of the legacy gas mixture with the curve of the ternary gas mixture an equal gain at $U_{\text{Amp}} = 512\text{ V}$ is achieved (green line). For amplification voltages of $U_{\text{Amp}} = (520 - 530)\text{ V}$ a higher gain as for $\text{Ar}:\text{CO}_2$ 93:7 vol% is achieved. Discharges under the $\text{Ar}:\text{CO}_2:\text{iC}_4\text{H}_{10}$ operating gas start to occur for $U_{\text{Amp}} \geq 540\text{ V}$ (see figure 3.6).

In conclusion, a nominal amplification voltage of $U_{\text{Amp}} = 520\text{ V}$ for subsequent measurements discussed in this thesis is chosen for the ternary gas mixture. A detailed comparison regarding detector efficiencies and resolutions is done in chapter 8.

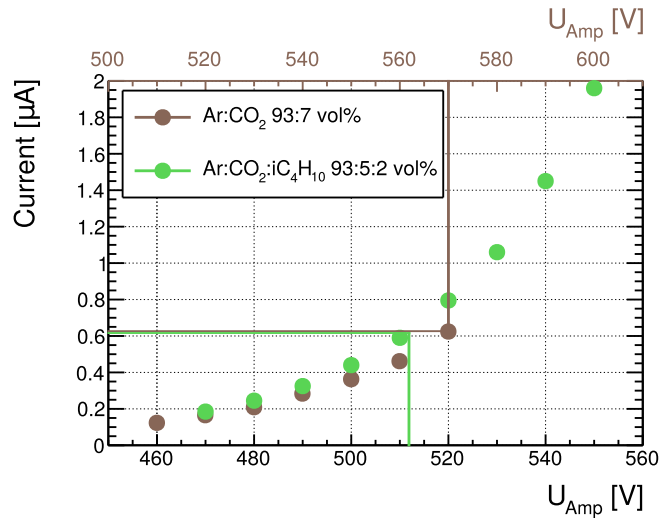


Figure 3.5: Comparison of the measured current under constant irradiation for the two gas mixtures $\text{Ar}:\text{CO}_2:\text{iC}_4\text{H}_{10}$ (93:5:2 vol%) and $\text{Ar}:\text{CO}_2$ (93:7 vol%).

For a better comparison, the values of the $\text{Ar}:\text{CO}_2$ measurements have been shifted by -50 V . Actual values for $\text{Ar}:\text{CO}_2$ follow the upper x-axis with the brown line guiding the eye for comparison of the two curves. An equality point for the measured current is visible for 570 V ($\text{Ar}:\text{CO}_2$) and $\approx 512\text{ V}$ under $\text{Ar}:\text{CO}_2:\text{iC}_4\text{H}_{10}$ (green line).

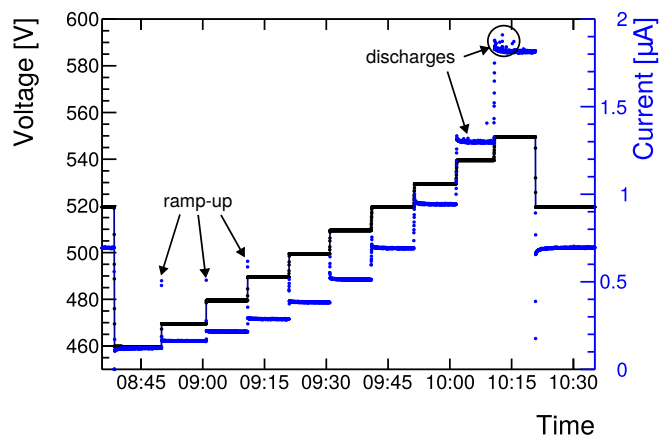


Figure 3.6: Ramp-up scan under $\text{Ar}:\text{CO}_2:\text{iC}_4\text{H}_{10}$ (93:5:2 vol%) of a sector under constant irradiation.

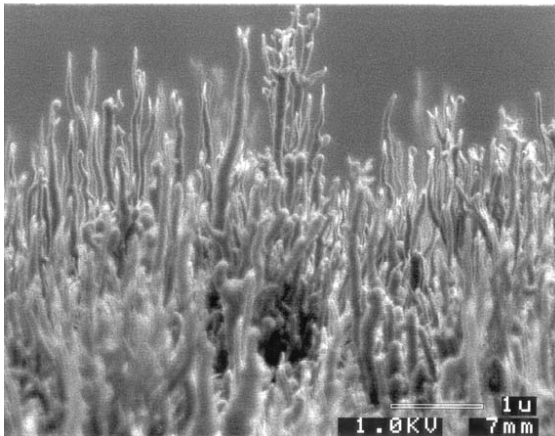
At amplification voltages $U_{\text{Amp}} \geq 540\text{ V}$ discharges start to occur, hinting for unstable operation. Single higher currents result from the high-voltage ramping.

3.4 Observed Aging Effects

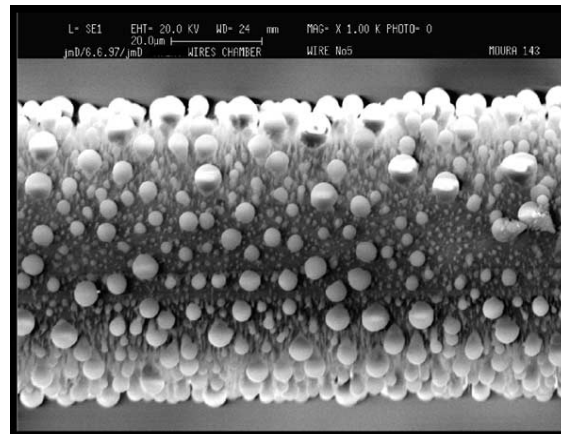
The major drawback of introducing hydrocarbons to the operating gas mixture is the possibility of detector aging. Titov [2004] gives an overview of observed aging effects in gas-filled detectors and the most important information will be summarized in this chapter. Main aging effects result from chemical reactions induced by the avalanche plasma close to the electrode. Free radicals are produced during this process. These radicals either recombine with their initial partners or form new molecules and polymerize. In the presence of fluorines or silicates whiskers or other solids are formed that are deposited on the electrodes. Exemplary pictures for drift chambers in the Collider Detector at Fermilab (CDF) experiment at Fermilab (left) and CMS CSC (right) are shown in figure 3.7. Both depositions visible are based on silicon originating from lubricants, rubber, gas impurities, and many more. Also, hints of polymerization chains solely based on hydrocarbons like CH_4 are discussed.

Deposits on the anode influence the electric field reducing the gain and consequently the performance of the detector. Conducting whisker structures may introduce a connection between the micro-mesh and the anode resulting in a current flow and breakdown of the electric field. Also, an increase of dark currents is possible (Titov [2004]).

An extensive test of the new operating gas mixture of $\text{Ar}:\text{CO}_2:\text{iC}_4\text{H}_{10}$ not only concerning its performance but also on the longevity of the detectors and the possibility of aging is crucial.



(a) Silicon oxide whiskers found in the drift chambers of the CDF experiment that were operated using a gas mixture of $\text{Ar}:\text{C}_2\text{H}_6$ (50:50 vol%) with a slight admixture of alcohol. Also, long polymers of hydrocarbons have been observed (Binkley et al. [2003]).



(b) Silicon bubble deposits on a CMS CSC under $\text{Ar}:\text{CO}_2$ (70:30 vol%). An x-ray emission spectroscopy showed prominent peaks for silicon, carbon, and oxygen (Ferguson et al. [2002]).

Figure 3.7: Deposits on anode structures of different gas-filled detectors.

3.5 Long-Term Irradiation Studies for Aging Investigations in Gaseous Detectors

One of the central parameters to describe the "age" of a detector is the accumulated charge. This accumulated charge represents the charge deposited in the detector over its expected operational time. Simulations and extrapolations to estimated particle backgrounds in future environments, like the HL-LHC, provide values for these expected accumulated charges (see chapter 6). For test cases, detectors are irradiated by radioactive sources to accumulate charges.

Sauli [2023] emphasizes on the compatability of these long-term irradiation studies to the actual working conditions of the detectors. Amongst others, this includes: the same type and size of the detector, operation of the detectors at the working point (gain, gas flux, ...), similar particle type/energy, identical irradiation strengths/particle flux, and identical services. It was shown, that an acceleration beyond one order of magnitude higher than the actual operating conditions leads to different results concerning the observed aging rate (Sauli [2023])⁴. Following this guideline, different irradiation studies on the new ternary gas mixture are performed⁵. This includes two distinct setups utilizing different particle types for irradiation. Studies concerning highly ionizing particles like neutrons are discussed in chapter 8. The energy spectrum of the provided neutrons covers a part of the expected neutron energies in the NSW at ATLAS⁶.

Accumulated charges in a slightly accelerated environment ($< \times 5$) using photons and concluding performance studies including these photons as particle background are the topic of the chapters 6 and 7 respectively.

If no deterioration is observed for conditions comparable to the foreseen operation in the NSW the ternary gas mixture of Ar:CO₂:iC₄H₁₀ 93:5:2 vol% will be an excellent candidate for the long-term operation of the Micromegas detectors at ATLAS.

⁴Such an acceleration can be achieved by increased gas gain, a higher irradiation intensity or a combination of both.

⁵Irradiated detectors are spare detector modules of the NSW Micromegas series production.

⁶An interactive map concerning the expected irradiation strength, particle energy and particle type is found online: https://twiki.cern.ch/twiki/pub/AtlasPublic/RadiationSimulationPublicResults/WebRadMaps_Full_R2_public.html. The NSW is situated at $|z| \approx 700$ cm and $r = (100 - 450)$ cm.

Chapter 4

Data Acquisition Systems

Two different types of readout systems are utilized within this thesis and both of them will be introduced in this chapter. The focus is going to be on the electronics setup, their specialties, and (dis-)advantages. Lastly, the determination of the parameters for particle detection, like charge and timing information, is going to be discussed.

4.1 The Scalable Readout System (SRS)

The first measurement setup uses the APV25 Application Specific Integrated Circuit (ASIC) on hybrid boards as part of the Scalable Readout System (SRS) Martoiu et al. [2013]. This system consists of multiple parts as depicted in figure 4.1:

- APV25 ASIC front-end electronic on the detector
- Analog to Digital Converter (ADC) card
- Front-End Concentrator (FEC) card
- Scalable Readout Unit (SRU)
- Data Acquisition (DAQ) PC

Originally designed for the CMS silicon tracker (Jones et al. [1999]) the APV25 was further developed and implemented into the SRS as a key component. The APV25 hybrids are directly mounted on the detector and connected via 130-pin Panasonic connectors¹ to the readout strips. Each APV25 hybrid has 128 readout channels.

Charge deposited on the strips is guided through discharge protection circuits to the ASIC for further processing. The signal arriving on the chip is shaped and amplified in a maximum time window of 27×25 ns bins. Operation in shorter data-taking windows, e.g. 24×25 ns bins, is possible and used in this thesis (see figure 4.3).

Two hybrid boards can be connected via flatband cable to operate in a master-slave configuration. In this configuration a single HDMI cable (black lines in figure 4.1) transmits the data and configuration to the ADC card.

The ADC card digitizes the arriving data. Additionally, 5 V of power is supplied to the APV25 via the HDMI cables coming from the ADC card as described by Martoiu et al. [2013]. Connected by PCIe to the ADC card is the FEC card for controlling the front-end electronic and

¹AXK5SA3277YG and AXK6SA3677YG

as the interface to the DAQ PC. Setting the configurations of the front-end chips and processing the trigger signal for correct readout are two of the functions used. This card is connected via ethernet to the DAQ PC where the data taking is initialized and where measured data is stored.

The setup of this thesis differs from the originally designed SRS in that sense, that the SRU as an optional tool for synchronizing multiple FEC cards, is not connected to the FEC cards, but directly connected to the DAQ PC. The synchronization process is implemented via software during data taking.

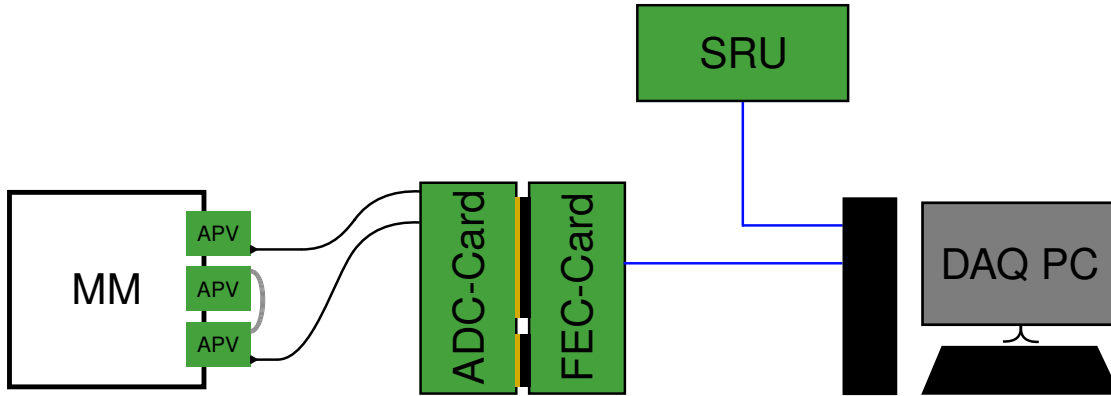


Figure 4.1: Altered SRS used for data taking in this thesis.

Front-end electronic ASICs (APV25 hybrids) are connected to the detector via Panasonic plugs AXK5SA3277YG and AXK6SA3677YG.

The powering of the APV25 and the data transfer happens via HDMI cables (black) plugged into an ADC card. This card is connected via PCIe to the FEC card. This card complex is situated in a crate with a power supply.

The FEC card is connected via ethernet (blue) to a DAQ PC controlling the data taking and configuration of the readout system.

Lastly, an optional SRU can be connected to the DAQ machine that synchronizes multiple FEC cards via software and trigger distribution (see figure 4.2).

Up to eight HDMI cables can be connected to a single ADC-FEC combination resulting in up to 16 APV25 hybrids in the master-slave configuration where two hybrids are connected via flatband cable (grey).

To initialize the readout sequence a trigger has to be provided to the FEC card. A simple schematic of the trigger determination is shown in figure 4.2. All trigger configurations used in this thesis are based on the same basic setup utilizing scintillators with photomultipliers attached as fast response triggers. Typically two or more of such trigger detectors are combined. The initial signal provided by the photomultipliers is sent via Nuclear Instrumentation Standard (NIM) cable (red lines in figure 4.2) to a discriminator with a tunable threshold². If a signal of sufficient height is detected a NIM pulse of set length is forwarded to a coincidence logic unit. Only if all scintillators provide a signal in the same time frame a trigger signal is created and sent to a dual timer.

By using the dual timer two different modi for further processing of the trigger signal are available. In the first case, the signal length of the dual timer is set to a fixed length $t_{\text{Dual_Timer}}$ resulting in maximum data taking rate $R \leq 1/t_{\text{Dual_Timer}}$. The resulting trigger signal is then sent to the FEC card. This mode of operation is used in single FEC card setups in low-rate environments.

For higher trigger rates it has to be ensured no data are lost and in the case of multiple FEC cards that the data are synchronized correctly. The pulse length provided by the dual timer $t_{\text{Dual_Timer}}$ is set to "infinity". After an initial trigger, no further triggers are allowed until

²NIM electronic modules provide fast analog logic signals in a standardized way optimal for the described application in a trigger environment Costrell et al. [1990].

the signal is reset. The reset signal is sent from an Arduino connected to the DAQ PC when the data processing has been completed. Operating multiple FEC cards together with a SRU requires individual trigger signals for all cards and the SRU.

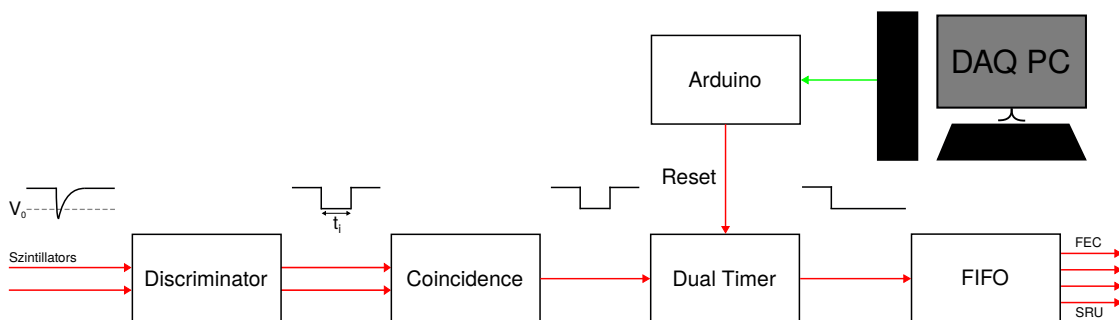


Figure 4.2: Sketch of the trigger processing and trigger distribution using external scintillator triggers.

Signals created in scintillators and readout via photomultiplier tubes are sent to a discriminator via NIM cables (red). High enough signals surpassing a set discriminator level (V_0) are further processed to a coincidence logic unit. If all trigger scintillators (typically two or three) deliver a signal in the same time window, i.e. their discriminator signal durations t_i overlap, a NIM signal is sent to a dual timer. This component is used for limiting the trigger rate by sending a signal of adjusted length before resetting. A signal length of 1 ms would result in a maximum trigger rate of 1 kHz. Too high rates may result in data loss or other unwanted side effects. The signal from the dual timer is then sent to the FEC card.

For synchronized readout of multiple FEC cards using an SRU a different trigger mode is used. The signal length of the dual timer is set to "infinity" allowing no further triggers until it is reset. Resetting this signal and therefore allowing for a new trigger is done by the DAQ PC combined with an Arduino. This Arduino sends a NIM signal to the dual timer after the data processing is finished.

Additionally, the trigger signal from the dual timer has to be multiplied and distributed to the SRU and all FEC cards. A logic Fan-In Fan-Out (FIFO) is the component of choice.

4.2 Signal Evaluation of the APV25 Hybrid

4.2.1 Signal Shape

Following figure 2.8 the signal on the readout strips consists of two components, the fast electron and slow ion part. Both of these are measured and processed by the APV25 front-end electronic. An exemplary signal of the output of an APV25 channel is shown in figure 4.3. In comparison to figure 2.8 the shown signal is modified by the response function of the APV25 chip and it has been already inverted. The very fast electron signal convoluted with the ion signal leads to a fast rise of the distribution. The maximum detectable pulse height is typically in the range of 1600-1800 ADC Counts. The exact value varies between different channels. If higher charges create saturation at the APV25 this maximum value will be processed and the correct charge information is lost.

After a signal is processed it takes a certain time for the chip to discharge completely and restore its baseline ($\mathcal{O}(250)$ ns). This is visible by the slower decrease after the maximum. If an additional signal arrives before the baseline is restored the data quality decreases since the correct charge information of the signal is altered. The issue of multiple overlapping signals is addressed in chapter 7.3.

4.2.2 Charge and Timing Determination

To obtain the correct charge and timing information from the signal distributions given in figure 4.3 two different methods are used. Both methods have specific areas of application in which they outperform the other method. The first method is based on an inverse fermi fit of the signal rise for a responding strip given by:

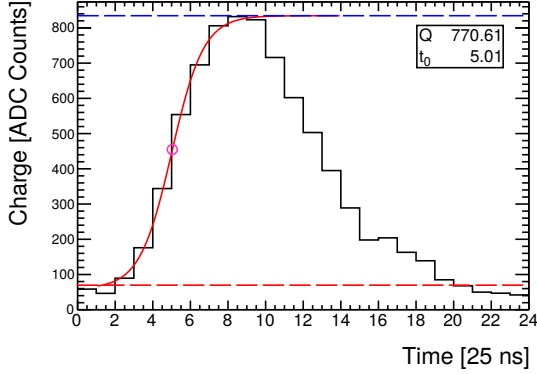
$$q(t) = \frac{Q}{1 + \exp\left(\frac{t_0-t}{t_{\text{Rise}}}\right)} + q_0 \quad (4.1)$$

The height of the fermi fit (Q) determines the charge induced on the specific readout strip. For the case in figure 4.3a a deposited charge of 770.61 ADC Counts is derived. q_0 is a charge offset of the fermi function. This charge offset originates from baseline fluctuations of the APV25 and is not part of the actual deposited charge of a particle. Additionally, timing information better than the sampling of 25 ns of the APV25 is achievable using this method. The inflection point of the fit is chosen as strip timing. This timing information is crucial for reconstruction algorithms for particles passing the detector under an angle (chapter 5.4). Perpendicular incident requires no timing information relying purely on the charge information. The exact process is described in the next chapter 5.2. One major disadvantage of the parameter determination using an inverse Fermi fit is the computational time of the analysis³. Especially for large area detectors in a heavy background environment like in chapter 7 this slows down the performance of analysis algorithms unnecessarily.

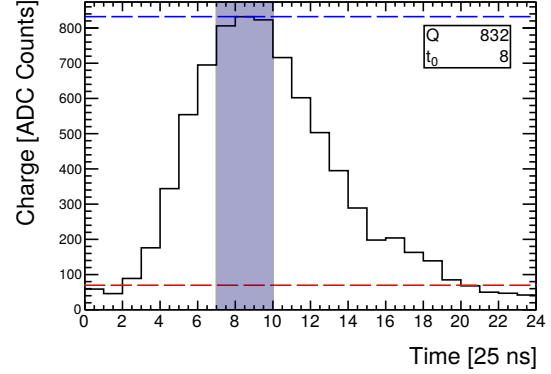
Utilizing the fact that the charge is single information for a perpendicular incident a second method is introduced. The "sliding template" method iterates over the whole distribution in an array of three consecutive bins searching for the highest (see figure 4.3b). A union of three bins is chosen for distinguishing from noisy strips. Performing no fit the charge information is influenced by a constant baseline signal resulting in a bias. Such a bias can be corrected by utilizing the bins not being part of the actual signal (e.g. bins 22-24 in figure 4.3b). The timing information is based on the 25 ns sampling of the APV25 and is chosen as the bin containing

³Each strip sending a signal (including noisy strips) requires the filling of a histogram and processing of a fit.

the highest charge, for the given case this results in $t_0 = 8$. This method performs orders of magnitude faster⁴. The performance of the two algorithms for perpendicular incidents is compared in chapter 5.3.3. Signals below a minimum charge of 64 ADC Counts (dashed red lines in figure 4.3) are discarded to reject noisy strips with small charges.



(a) Charge and timing determination using an inverse fermi fit function (see equation 4.1). The charge is the height of the fermi function (770.61 ADC Counts) above the baseline fluctuations and the signal timing is the inflection point of the fit (5.01×25 ns).



(b) Charge and timing determination using the "sliding template" technique.

Three consecutive bins scan through the full width of the distribution finding the maximum. The charge value is the content of the highest bin (832 ADC Counts) and the signal timing is the corresponding x-value (8×25 ns). Disadvantages of this method are the worse timing resolution (only in steps of 25 ns) and possible errors in the charge information since any offset is included. The major advantage is a speed up of multiple orders of magnitude in the computing time skipping histogram filling and fitting⁵. A comparison of the performance compared to the fitting method is done in chapter 5.3.3.

Figure 4.3: Methods used to determine the charge and timing information readout via the SRS using APV25 hybrids (see chapter 4.1). Signals below a minimum charge threshold of 64 ADC Counts, indicated as dashed red line, are discarded.

⁴No histogram filling is needed and the figure is purely for visualization purposes.

⁵See footnote 3.

4.3 NSW Data Acquisition System

This and the upcoming part of this chapter are dedicated to the DAQ system used in the ATLAS NSW. A second topic focuses on a scaled-down system for a measurement setup used during some of the testbeams discussed in chapter 7. A complete overview of the NSW DAQ system can be found in Iakovidis et al. [2023], which is also taken as the primary source for the information discussed throughout the remainder of this chapter.

Figure 4.4 depicts the whole NSW DAQ system. Both detector technologies, the Micromegas and the sTGCs are read out by the same front-end electronics mounted directly on the detector, the VMM chip. A detailed introduction to the VMM ASIC will follow later in this chapter.

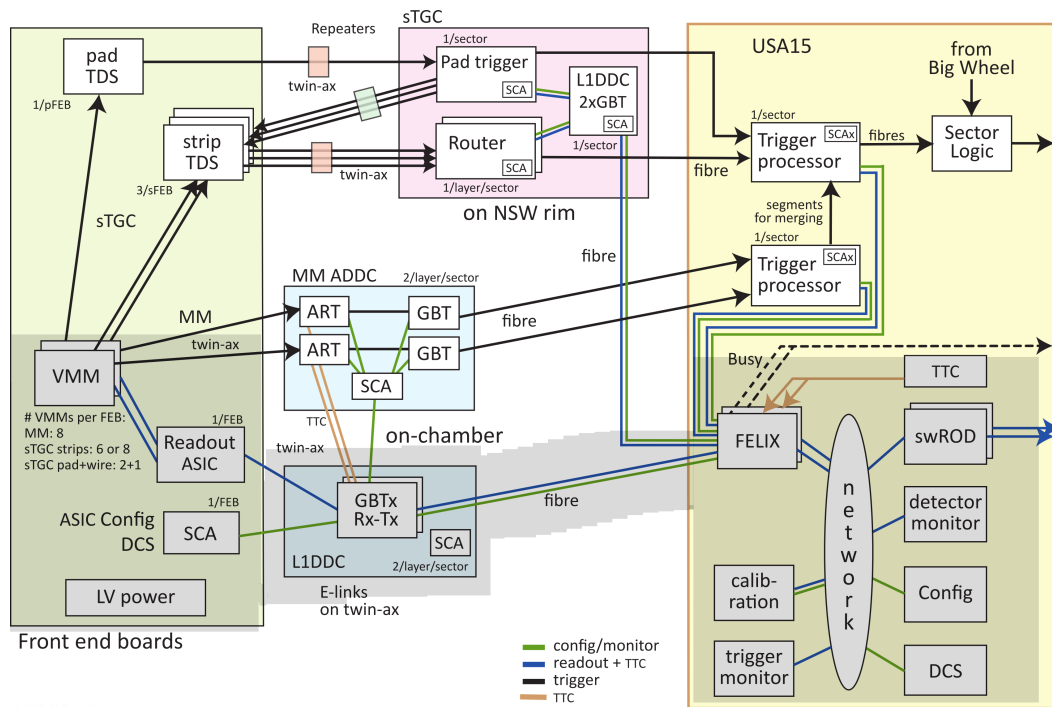


Figure 4.4: NSW readout and trigger chain.

The grey shaded area contains everything for a reduced standalone Micromegas data-taking system used in testbeam measurements as in chapter 7. This minimal setup consists of front-end electronics mounted on the detector (MicroMegas Front-End with 8 VMM's (MMFE8), green), a trigger distributor and data collector card (Level 1 Data Driver Card (L1DDC)), a Timing, Trigger and Control (TTC) Field-Programmable Gate Array (FPGA) and PCs for data acquisition, configuration and readout controlling (Front End Link eXchange (FELIX) + SoftWare ReadOut Driver (swROD)). The individual components will be discussed later in this chapter.

Adapted from Iakovidis et al. [2023].

4.3.1 Reduced NSW Readout Chain for Standalone Micromegas Data Taking

For test setups using only Micromegas detectors, the large and complex system can be scaled down. The whole upper part of figure 4.4 can be dismissed, being necessary for the sTGCs only. The trigger information of the Micromegas that is processed via the Address in Real Time Data Driver Card (ADDC) linkage to the central ATLAS trigger is not used in testbeam measurements either.

For the minimal readout system only the parts in the grey-shaded area of figure 4.4 are needed. From right to left the DAQ chain starts from the storage of the data on a filesystem (swROD) up to the front-end ASICs mounted on the detector (VMM).

DAQ PC

The readout system is controlled and monitored by multiple PCs connected through a network. There are dedicated machines for storage and operation (swROD) including all the individual parts connected to the network bubble in figure 4.4 except FELIX.

FELIX is the interface used to transform optical data arriving from the detector readout to ethernet and vice versa for configuration settings from the DAQ PC to the front-end electronics (Iakovidis et al. [2023]). It is also used for TTC distribution.

For the minimal setup used in chapter 7 the trigger is provided by scintillators following the trigger chain explained in figure 4.2 up to the coincidence which is then providing a trigger signal to the TTC in figure 4.4.

L1DDC

Connected to FELIX is the L1DDC, a trigger distributor and data collector card. The L1DDC is the interface converting the data from twin-ax cables to optical fibers. It is also used for programming the front-end electronic boards and distributing the external trigger signal.

MMFE8

The last part of the NSW data acquisition system is the MMFE8 (see figure 4.5) that is directly mounted on the detector. On this front-end board are eight VMM ASICs providing 64 readout channels each (red squares). In total a single MMFE8 board provides 512 readout channels. The Read-Out Controller (ROC) (blue square) distributes the TTC signal sent by the L1DDC through the left twin-ax connector (green square) to the VMMs. Measured data is sent through the same connection from the front-end board to the L1DDC and ultimately to the DAQ PC. Configuration parameters for the individual chips and even channels are set via the Slow Control Adapter (SCA) (pink square). The second twin-ax connector (right green square) is used for communication with the ADDC sending information to the ATLAS trigger system. It is not used in the minimal setup.

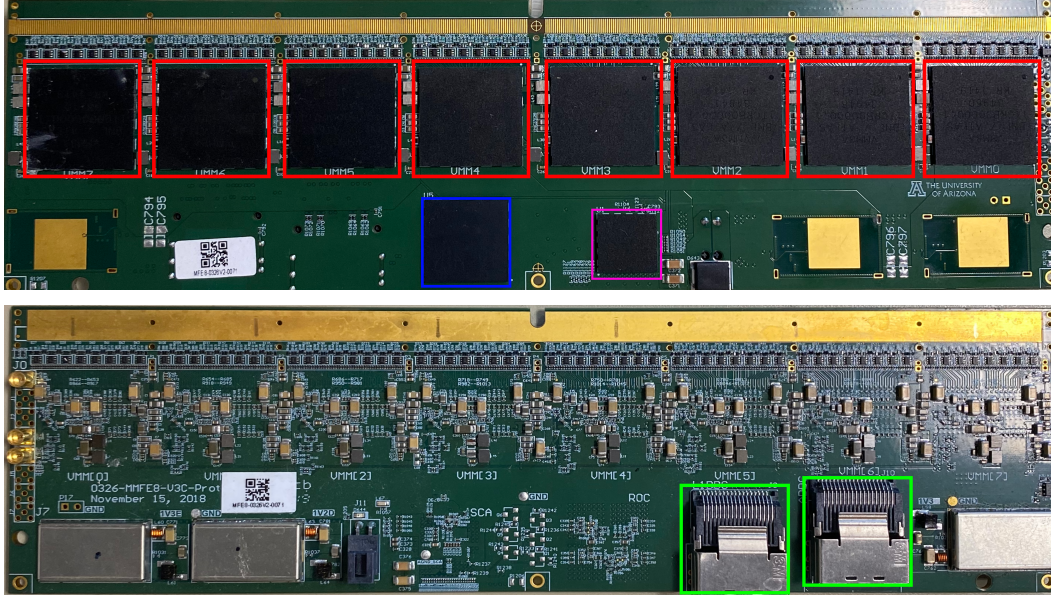


Figure 4.5: The MMFE8 are directly mounted to the Micromegas detectors for readout. The eight VMM ASICs (red squares) provide 64 readout channels each resulting in 512 channels per MMFE8. TTC signals are sent to the MMFE8 (left green square) from the L1DDC. Measured data is sent through this connection back to the L1DDC. The TTC signal is distributed via the ROC ASIC (blue square) to the VMMS. The second connector (right green square) is used for communication with the ADDC which is not used for the measurements discussed in this thesis. Configuration parameters are read and set by the SCA (pink square)⁶.

4.4 VMM ASIC

The VMM ASIC is the new front-end chip specifically developed for the NSW upgrade project (Iakovidis et al. [2023]). Following the blockchain depicted in figure 4.6 from the left incoming charges are passing a Charge Amplifier (CA) and a shaper. The CA offers a programmable gain in the range of 0.5-16 mV/fC. Within the shaper a peaking time p_t of values 25, 50, 100, and 200 ns can be set defining the charge integration time. Longer integration times yield higher detected charges.

The next region contains the discriminator (step symbol left of the logic box) with a channel-specific tunable threshold (5-b trim). The threshold is given in multiples of the standard deviation of the baseline fluctuation of the channel⁷. Signals surpassing the threshold are processed by a peak and timing detection instance. The working principle of these is discussed in the next section of this chapter.

Charge and timing information is then digitized by different ADCs. Different readout modes of the VMM are offered to utilize different types of ADCs (6-bit or 10-bit for the charge information with the latter one being more precise). The 10-bit ADC used for the NSW DAQ is the main rate-limiting factor introducing a per channel deadtime of 250 ns per conversion (Iakovidis et al. [2023]).

After conversion the data is buffered in a so-called latency FIFO and given the size of the FIFO (64-deep) and the deadtime of 250 ns a total of 16 μ s of storage per channel is available (Iakovidis et al. [2023]).

To utilize the information collected on the VMM directly in the trigger scheme of the ATLAS

⁶Picture courtesy: Internal Communication Alexander Naip Tuna, CERN.

⁷Given is a channel with a constant baseline signal of 20 ADC Counts and a fluctuation of $\sigma = 4$ ADC Counts. A typical threshold of $VMM_{RMS} = 9\sigma$ would correspond to $(20 + 9 \times 4)$ ADC Counts = 56 ADC Counts.

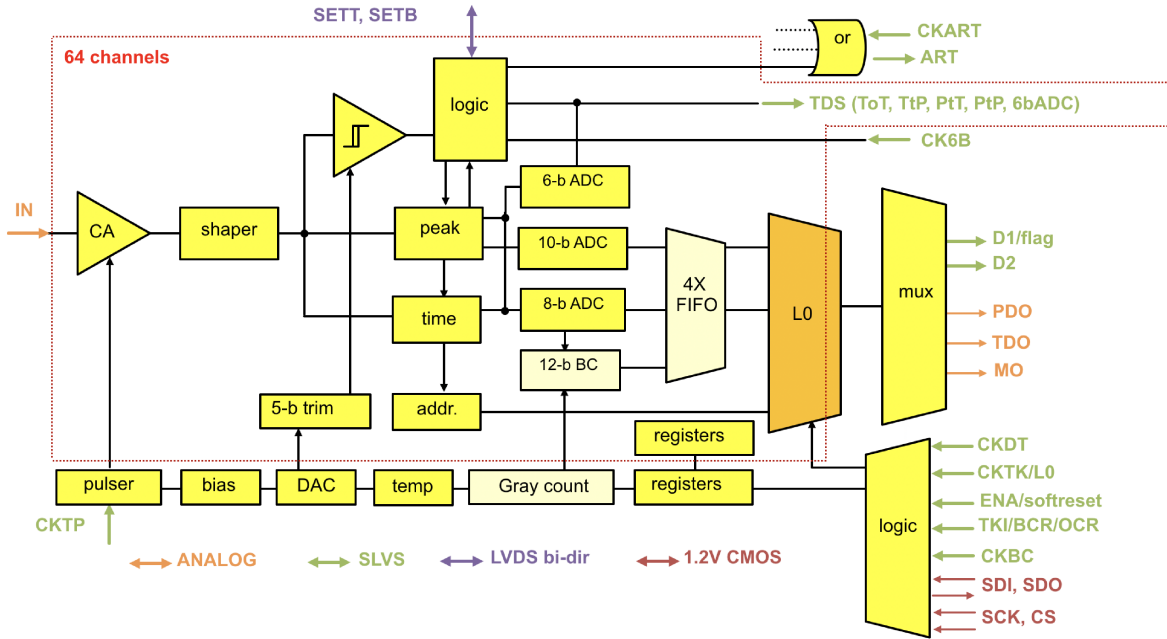


Figure 4.6: Blockchain of the VMM readout chip.

Incoming signals are amplified by a CA and shaped. The CA is programmable with adjustable gain ranging from 0.5-16 mV/fC. For the shaper a programmable peaking time p_t with values of 25, 50, 100, and 200 ns is available. Next up is the discrimination (step symbol left of the logic box), peak, and timing detection measurements followed by different ADCs for different readout modes.

Collected data is stored in the FIFO with a maximum amount of data stored corresponding to 16 μ s of continuous data taking. The VMM provides standalone trigger information (so-called Level-0) that will be exploited in ATLAS to cope with the increased rate of fake triggers (see chapter 1.3).

Taken from Iakovidis et al. [2023].

detector an internal Level 0 (L0) selector circuit searches within the latency FIFO for an L0 trigger accept and copies them to its L0 channel FIFO. The L0 trigger information is sent out to be further processed in the ATLAS trigger selection. For the testbeam setup, this information is not used.

4.4.1 VMM Charge and Timing Determination

As discussed in the previous section the VMM features a peak and timing detection scheme. The general working principle is demonstrated in figure 4.7. Signals surpassing the discriminator level (V_A) initiate the peak detector starting to integrate up to the first peak determined by a peak finding algorithm. The height of the peak (Peak Detector Output (PDO)) represents the detected charge. A typical PDO distribution is shown in figure 4.8. The distinct peaking structure is a well-known artifact produced by the VMM. The last peak at PDO= 1023 ADC Counts corresponds to the saturation of the 10-bit ADC⁸.

Simultaneously a Time-to-Amplitude Converter (TAC) starts to ramp up. Depending on the settings the ramp-up starts after the crossing of the threshold or at peak timing. During the data taking a clock is running in steps of 25 ns (CKBC). This clock is synchronized to the bunch crossing in the LHC for operation in the ATLAS detector. The first rising edge of this clock arms the ramp-up system of the TAC, meaning from this time on the ramping will stop

⁸A 10-bit ADC allows for $2^{10} = 1024$ different values. Including the 0 as the first value the highest value equals 1023.

at the next falling edge of the clock. Therefore a rising edge followed by a falling edge in the clock is always necessary for the ramp-up to stop. The height of amplitude combined with the TAC slope provides timing information finer than the 25 ns from the CKBC. This readout-channel specific slope and offset value t_0 (see figure 4.7) can be determined by an internal pulser of the VMM chip. For the measurements performed in chapter 7 such calibration has not been performed resulting in the necessity of a post-measurement, data-driven calibration.

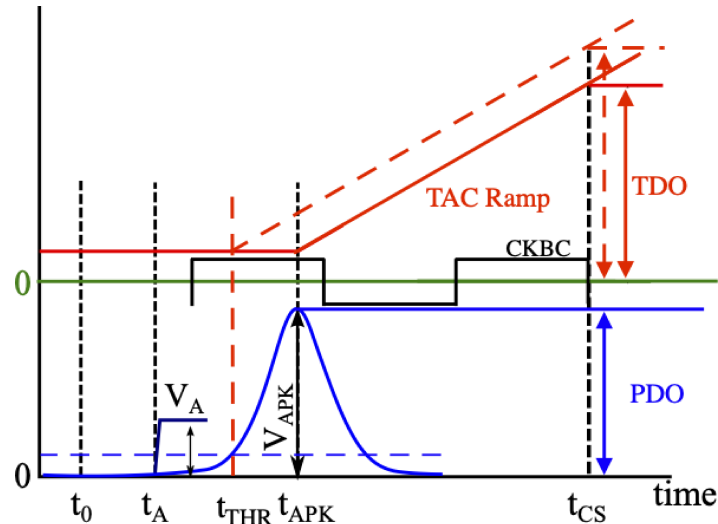


Figure 4.7: Sketch illustrating the determination of the charge and timing information in the VMM ASIC.

If a signal surpasses the discriminator level (V_A) the peak detector starts integrating charge up to the first detected peak. Either at threshold or peak, the TAC starts ramping up. Starting from the next rising edge of the clock (CKBC) the system is armed awaiting the next falling edge. The ramped-up value at that time (Time Detector Output (TDO)) is sent out for further processing. Calibrating the TAC slope provides a better than 25 ns timing information given by the clock (see chapter 4.4.2). t_0 describes a channel-specific time offset that also needs to be calibrated.

Taken from de Geronimo et al. [2022]

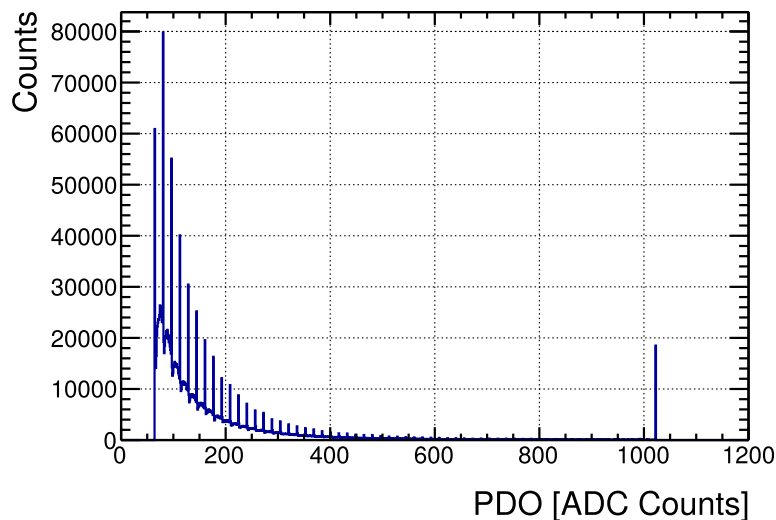


Figure 4.8: Exemplary PDO distribution acquired with a VMM3a on a MMFE8.

The distinct peaking structure is a well-known feature of the VMM resulting from the value determination process. The peak at PDO = 1023 ADC Counts is the saturation maximum of the PDO.

4.4.2 Time Calibration

Measurements without timing calibration can be processed using a data-driven timing calibration. The global LHC bunch crossing clock and the clock (CKBC) on the VMM shown in figure 4.7 are synchronized. The relative bunch crossing ID (rel_{BCID}) is the number of clock cycles of the CKBC relative to the global trigger⁹.

The strip time is calculated by the rough timing information provided by the rel_{BCID} ¹⁰ and the fine timing information (t_{fine}) derived from the TDO and is given by¹¹:

$$t_{\text{Strip}} = (\text{rel}_{\text{BCID}} + 1) \times 25 \text{ ns} - t_{\text{fine}} - t_{0,\text{Strip}} - t_{\text{trigger}} \quad (4.2)$$

t_{fine} and $t_{0,\text{Strip}}$ have to be derived during the data-driven calibration. They differ for each readout channel. t_{trigger} is an event-wise timestamp applied to synchronize all events in time being provided externally.

The fine timing t_{fine} is given by:

$$t_{\text{fine}} = \frac{\text{TDO} - \text{TAC}_{\text{offset}}}{\text{TAC}_{\text{slope}}} = \frac{\text{TDO} - p_1}{p_3 - p_1} \times 25 \text{ ns} \quad (4.3)$$

with the TAC ramp-up slope and offset from figure 4.7. Parameters p_1 and p_3 are determined from the TDO distribution.

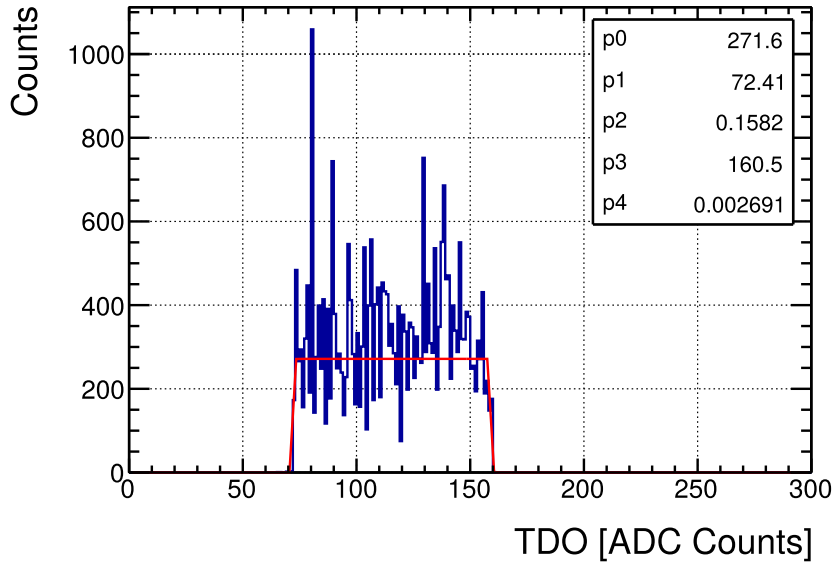


Figure 4.9: Measured TDO for a single strip fitted with a double fermi function (see equation 4.4) to extract the parameters p_1 and p_3 . The slope of the TAC is described by the width of the distribution. p_1 is the $\text{TAC}_{\text{offset}}$ from figure 4.7.

The TDO distribution measured for a single readout channel is shown in figure 4.9. The full width of the distribution correlates to a time of 25 ns. Dividing the width by this time results in the $\text{TAC}_{\text{slope}}$ for equation 4.3.

⁹For the DAQ in the NSW the system is calibrated to arrive within the first eight cycles after the trigger. This time window is kept short, and therefore the data package is small for further fast data processing (Iakovidis et al. [2023]).

¹⁰Since the fine timing corresponds to the falling edge of the clock after a rising edge one clock cycle after the charge maximum as shown in figure 4.7, the actual rel_{BCID} value has to be increased by 1 clock cycle (25 ns). It is accounted for by the +1 in equation 4.2.

¹¹Internal communication, Valerio D'Amico.

The width itself is determined by a double-fermi fit as the difference of the inflection points p_1 and p_3 :

$$f(t) = \frac{P_0}{1 + \exp\left(-\frac{t-p_1}{P_2}\right)} \times \frac{1}{1 + \exp\left(\frac{t-p_3}{P_4}\right)} \quad (4.4)$$

The TAC_{offset} of equation 4.3 is equal to p_1 .

$t_{0,\text{Strip}}$ of equation 4.2 is chosen for each strip individually such that all strips of the detector are calibrated to a common time¹². The strip time spectrum before calibration for all strips of a Micromegas detector is shown in figure 4.10a. A broad, non-rectangular, peaking distribution with soft edges is observed, differing from the expected box-like distribution. As the ionization process is statistically distributed in the detector all strip timings within the maximum drifttime should be measured equally often. Small strip timings correspond to ionization processes close to the micro-mesh and large strip timings to ionizations close to the cathode. Electrons created in the latter case have to traverse the whole drift region of 5 mm. Applying the calibration results in the strip time distribution shown in figure 4.10b. This calibrated distribution is very close to the expected box shape. A drift velocity of $v_D = 4.63 \pm 0.69 \text{ cm } \mu\text{s}^{-1}$ is obtained given the width of 108 ns and a 5 mm drift region¹³. This is in agreement with the simulated drift velocity of $v_D \approx 4.58 \text{ cm } \mu\text{s}^{-1}$ in figure 3.4a for 480 V cm^{-1} and the ternary gas mixture.

A second illustration of the strip timing calibration is given in figure 4.11. Here the strip time is plotted against the position. In the uncalibrated distribution (figure 4.11a) distinct bunches of 64 strips are visible representing individual VMM chips. Within the bunches, additional fluctuations can be observed. After the calibration (figure 4.11b) none of these effects remains.

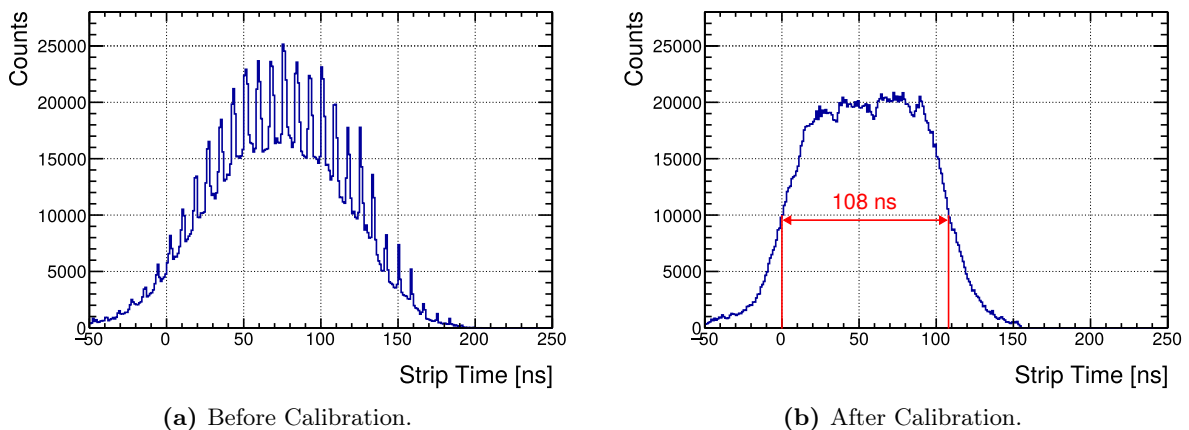


Figure 4.10: Strip timing spectra of all strips of a Micromegas detector for a testbeam measurement (see chapter 7) with 120 GeV muons under 29° of inclination.

Left shows a very distinct peaking structure that vanishes after applying the correct timing calibration (right) from equation 4.2.

¹²Within the NSW community it was agreed on a strip time of zero for the first inflection point of the strip time distribution as a common time stamp for all strips.

¹³For the estimation of the error, a time resolution of $\sigma_{\text{time}} = 16.22 \text{ ns}$ (see chapter 7) and no error of the drift height of 5 mm are assumed.

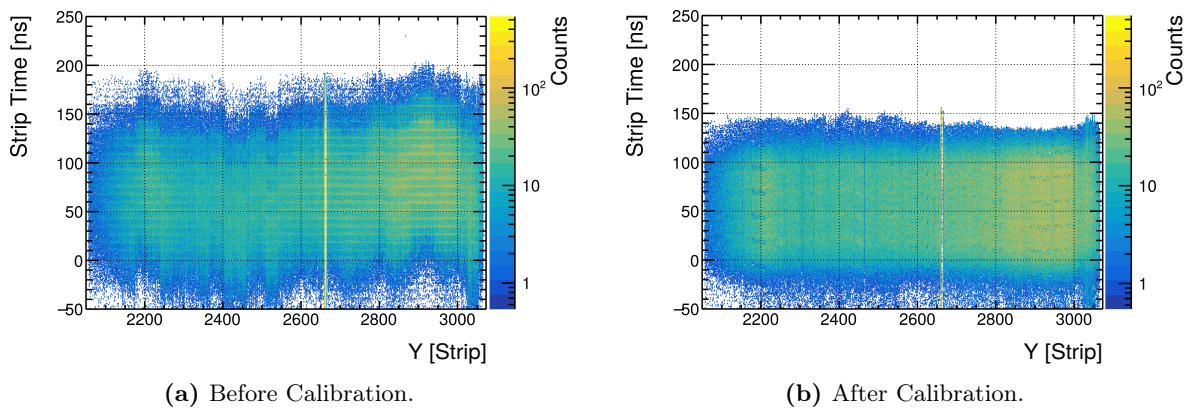


Figure 4.11: Strip timing spectra of a Micromegas detector for a testbeam measurement (see chapter 7) with 120 GeV muons under 29° of inclination as a function of the strip number.

Before the calibration (left) strong variations in the strip time are visible. Distinct bunches of 64 consecutive strips represent individual VMMs showing different $t_{0,\text{Strip}}$ offset values. Also, the peaking structure from figure 4.10a is still visible. The effect of the timing calibration from 4.2 is shown in the figure on the right with a much smoother and homogeneous strip time distribution over all strips.

Chapter 5

Position Reconstruction and Particle Tracking

The position determination of a traversing particle and the reconstruction of particle tracks are performed identically for both readout electronics discussed in the previous chapter 4. The starting point for the position reconstruction is the hit position (strip number), the measured charge, and the reconstructed timing.

Differences in the position reconstruction using Eta and Stereo strips are going to be discussed in this chapter. Algorithms and methods for particle tracking including the alignment of detectors in the scope of a testbeam setup consisting of multiple Micromegas detectors will be explained. Lastly, central parameters for performance investigations, like position resolution and detection efficiencies are going to be introduced focusing additionally on the differences between perpendicular and inclined particle incidents.

5.1 Position Reconstruction Using Stereo Layers

The position determination using Eta layers is straightforward having parallel strips to the short and long edge of the trapezoidal shape of the detector. Given a signal on a strip, the position perpendicular to the strips is given by

$$Y_{\text{Strip}} = N_{\text{Strip}} \times p \quad (5.1)$$

with N_{Strip} and p the strip number and the strip pitch respectively.

Throughout this thesis, the direction of precision (Y) is defined to be perpendicular to the Eta readout strips and the readout strips are always parallel to the X-axis.

For Stereo layers, having rotated strips, additional steps are necessary to determine the actual position in Y (denoted as x in figure 5.1)¹. Following Flierl [2018] and Alexopoulos et al. [2015] a summary is given discussing this in a NSW sector using the information provided by four rotated Stereo layers. This method is crucial for the internal tracking discussed in chapter 8.4.1. For measurements with additional tracking chambers as in chapter 7 the Stereo layers can be rotated and treated as Eta layers. The rotation and other alignment corrections are explained later in this chapter.

¹For an easier understanding following the sketch in figure 5.1 the orientation of the coordinate systems given there is kept although being different to the standard nomenclature used in this thesis with X being along the Eta strips and Y perpendicular to them. For a correct mapping to the nomenclature the x and y in equations 5.12 - 5.15 have to be changed to Y and X respectively.

Given are four readout planes with parallel readout strips that are rotated by $\pm\varphi$ concerning a standard cartesian coordinate system (X, Y) ². The hit positions in the cartesian coordinate system can be calculated by the positions of the rotated system (U, V) (Flierl [2018]).

$$x_1 = \frac{u_1 + v_1}{2 \cos \varphi} \quad (5.2)$$

$$x_2 = \frac{u_2 + v_2}{2 \cos \varphi} \quad (5.3)$$

$$y_1 = \frac{u_1 - v_1}{2 \sin \varphi} \quad (5.4)$$

$$y_2 = \frac{u_2 - v_2}{2 \sin \varphi} \quad (5.5)$$

Each of the four readout planes offers one coordinate u_1 , u_2 , v_1 or v_2 (see figure 5.1)³. u_1 and v_1 are assumed to be at the same Z position. This holds also for u_2 and v_2 at a different common Z . The two origins are placed at a distance ΔZ .

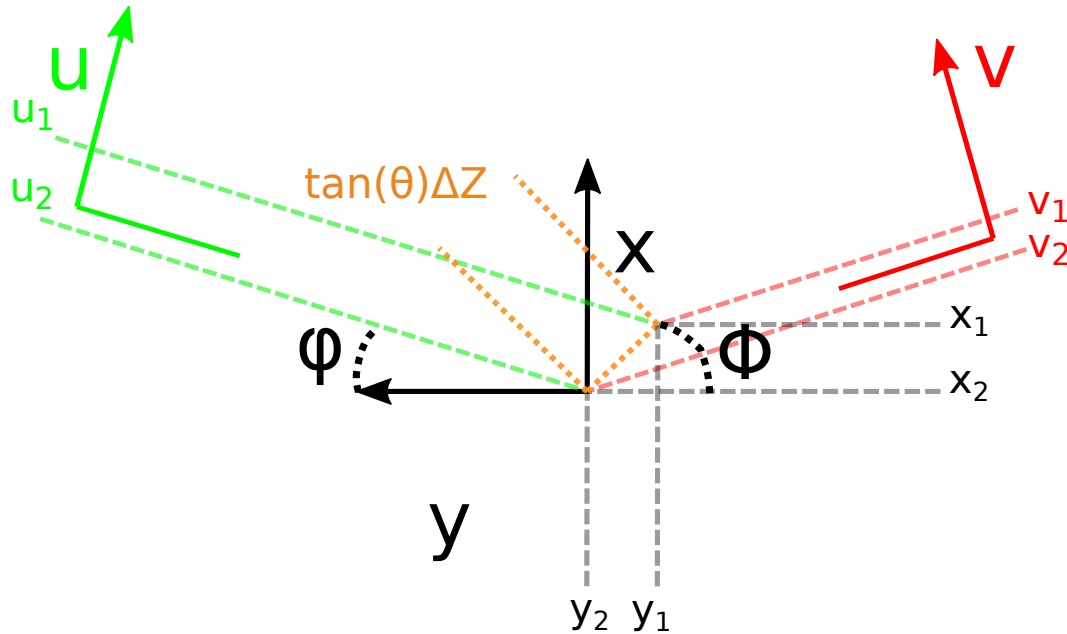


Figure 5.1: Schematic of the reconstruction of the position through four parallel readout layers that are rotated by $\pm\varphi$ concerning a cartesian coordinate system (X, Y) . Each of the readout layers offers one of the four coordinates u_1 , u_2 , v_1 or v_2 .

Two readout layers at a common Z position form one (U, V) coordinate system. A second (U, V) coordinate system is given by the other two readout layers.

The two coordinate systems are placed parallel to each other at a distance ΔZ . A track through both coordinate systems is given by the position (x_1, y_1) and the polar and azimuthal angle θ and Φ .

These four layers represent the four Stereo layers of a NSW sector (see figures 1.8a and 2.10b.) Figure taken from Flierl [2018].

²For the specific case of $\varphi = 1.5^\circ$ this corresponds to the four Stereo layers of a NSW sector. The readout strips of two Stereo layers are rotated by $+1.5^\circ$ concerning the Eta strips, while for the other two Stereo layers, the strips are rotated by -1.5° .

³Concerning a NSW sector, u_1 and v_1 are given by the two Stereo layers of one module and u_2 and v_2 are given by the Stereo layers of the second module of the sector.

The differences of the individual positions in the tilted coordinate system are then given by

$$\Delta u = u_1 - u_2 = \tan(\theta)\Delta Z \sin(\Phi + \varphi) \quad (5.6)$$

$$\Delta v = v_1 - v_2 = \tan(\theta)\Delta Z \sin(\Phi - \varphi) \quad (5.7)$$

with the azimuthal and polar angle Φ and θ (Flierl [2018])⁴.

The intersection of the track with an auxiliary plane centered between the two coordinate systems (U_1, V_1) and (U_2, V_2), can be calculated by:

$$x = x_1 - \frac{x_1 - x_2}{2} \quad (5.8)$$

$$y = y_1 + \frac{y_1 - y_2}{2} \quad (5.9)$$

Inserting now equations 5.2-5.5 and solving equations 5.6 and 5.7 for u_2 and v_1 respectively

$$u_2 = u_1 - \tan(\theta)\Delta Z \sin(\Phi + \varphi) \quad (5.10)$$

$$v_1 = v_2 + \tan(\theta)\Delta Z \sin(\Phi - \varphi) \quad (5.11)$$

are the positions in the auxiliary plane described by:

$$x = \frac{u_1 + v_2}{2 \cos \varphi} - \frac{\tan(\theta)\Delta Z \cos(\Phi) \tan(\varphi)}{2} \quad (5.12)$$

$$y = \frac{u_1 - v_2}{2 \sin \varphi} - \frac{\tan(\theta)\Delta Z \sin(\Phi)}{2 \tan(\varphi)} \quad (5.13)$$

For the case of only two readout layers in the same plane, the position in the (X, Y) coordinate system is given by⁵:

$$x = \frac{u + v}{2 \cos(\varphi)} \quad (5.14)$$

$$y = \frac{u - v}{2 \sin(\varphi)} \quad (5.15)$$

⁴The angle θ would correspond to a particle traversing the NSW sector under an angle in the direction of the pseudorapidity η (see equation 1.1).

⁵These equations hold for a single Micromegas module with two Stereo layers. The common plane is assumed to be located between the two readout anodes.

5.2 Cluster Building

Signals induced by an ionizing particle are not restricted to single strips. Due to transverse diffusion during the electron drift (see figure 3.4b) and broadening during amplification as a result of the repulsive force between the electrons the charge will be distributed over multiple, neighboring strips. A Gaussian distribution of the charge around a central position is observed (see e.g. Jagfeld [2023]). Capacitive coupling between neighboring readout strips (see Lösel [2017]) leads to an additional increase of strips measuring a charge signal.

Figure 5.2 shows the raw signals from the APV25 hybrids for adjacent strips in the case of a perpendicular muon incident. To acquire the total charge and correct position information of the particle passing the detector neighboring strips are combined into a cluster.

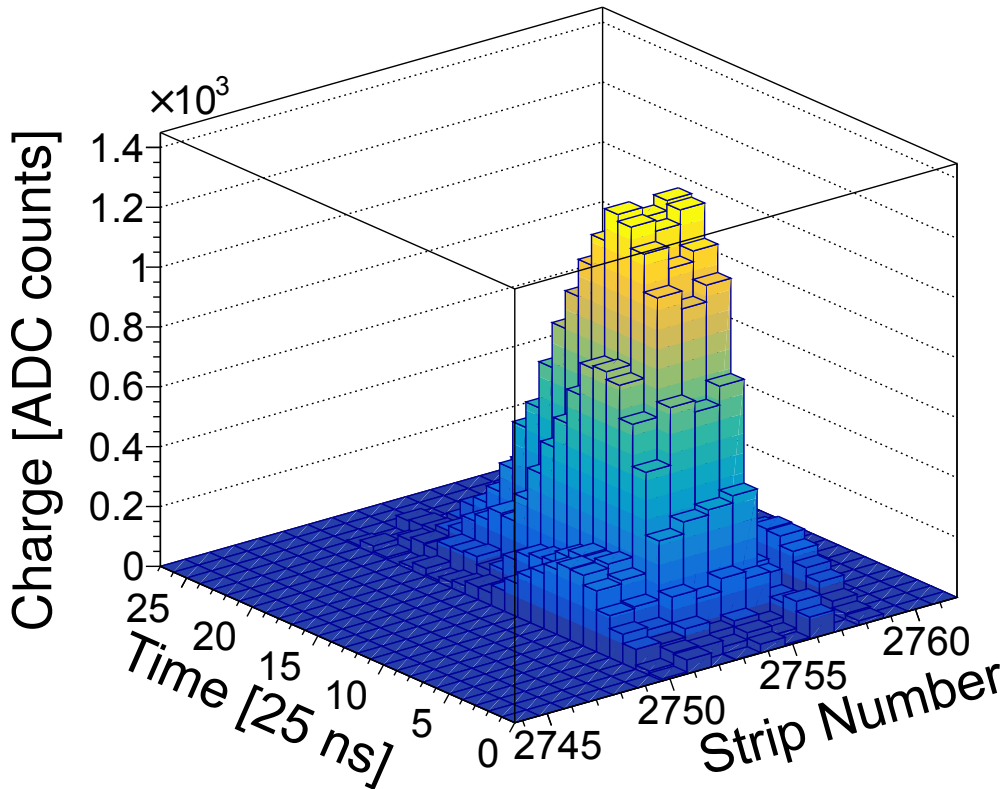


Figure 5.2: Signals of multiple consecutive strips that are conglomerated to a cluster for perpendicular muon incident.

Due to transverse diffusion in the detector and capacitive coupling between readout strips (see Lösel [2017]) more than one strip experiences a signal. Additionally, the amplification process yields a Gaussian distribution of the charge due to the repulsion of the increasing number of electrons in the avalanche.

Analogously to the distinguishing of noisy strips from the signal, cuts are applied to the cluster-building process. A minimum number of two consecutive strips is necessary to form a cluster with a single missing strip between two strips with signals being allowed. Only one of such gaps is allowed per cluster.

Figure 5.3 illustrates this cluster building allowing for a single missing strip between two strips per cluster. Cluster building is performed in ascending strip numbers, i.e. missing strip restrictions are applied towards higher strip numbers. Following the previously discussed cuts strips 1-4 build a cluster with strip 6 being discarded. Strips 24-27 build no cluster due to two consecutively missing strips. This strong restriction is necessary due to the high background rates resulting in high occupancies enlarging clusters performed in chapters 7 and 8.

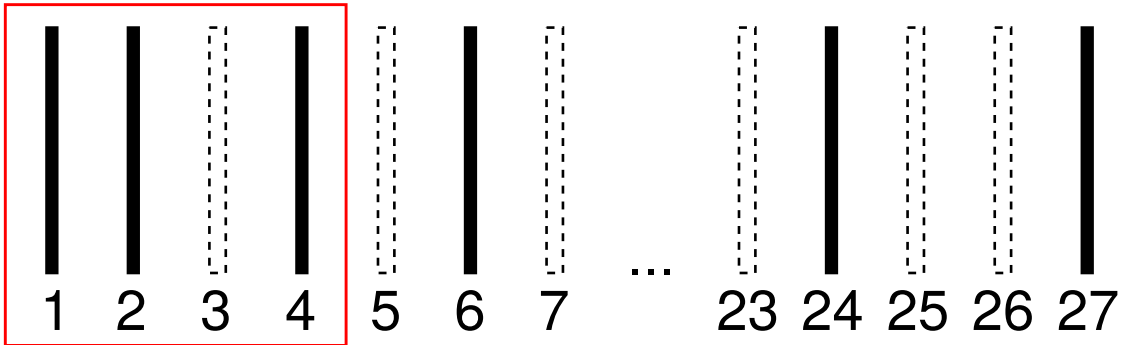


Figure 5.3: Sketch of the clustering process demonstrating applied restrictions. Strips 1,2 and 4 are grouped into a cluster since a single strip missing in between is allowed. Strip 6 is not assigned to the cluster being separated from the cluster by a second single missing strip (5). From 24 onwards no cluster is built due to two consecutively missing strips.

The determination of the position, where the particle passed the detector, is calculated using

$$Y_{\text{Cluster}} = \frac{\sum_{\text{Strips}} (Q_{\text{Strip}} \times Y_{\text{Strip}})}{\sum_{\text{Strips}} Q_{\text{Strip}}} \quad (5.16)$$

with Q_{Strip} and Y_{Strip} as strip charge and position respectively.

A charge-weighted mean (centroid) over all strips contained in a cluster is derived providing a position determination more precise than the strip pitch. This method performs best for perpendicular particle incidents. For inclined tracks a different approach is necessary. An overview of these methods is given later in chapter 5.4.

5.3 Particle Tracking

5.3.1 Reference Tracking

To investigate the resolution of the Micromegas detectors a reference track determined by a tracking hodoscope perpendicular to the beam is utilized. The reconstructed particle trajectory by the hodoscope is compared to the measured position in the detector under investigation.

The reference track is determined using a linear χ^2 minimization of the centroid positions of the tracking chambers along the particle track following Klitzner [2019]. For a successful track formation, at least one cluster is required in each reference detector.

The resolution of the reference detectors has to be taken into account for the precision of the reference track. A track extrapolation error σ_{Track} for a set of n reference detectors is given by Horvat [2005] as

$$\sigma_{\text{Track}}^2 = \frac{\Lambda_{22} - 2Z\Lambda_{12} + Z^2\Lambda_{11}}{\Lambda_{11}\Lambda_{22} - \Lambda_{12}^2} \quad (5.17)$$

with Z being the position along the particle track and Λ_{ij} given by Z and the individual detector resolutions of the reference trackers σ_i as:

$$(\Lambda_{11}, \Lambda_{12}, \Lambda_{22}) = \sum_{i=1}^n \frac{(1, Z_i, Z_i^2)}{\sigma_i^2} \quad (5.18)$$

The detector resolution of the reference chambers is determined by the geometric mean as described in Carnegie et al. [2005]. For the case of similar resolutions for all reference detectors follows for the resolution of one reference detector:

$$\sigma_i = \sqrt{\sigma_{\text{Incl}}\sigma_{\text{Excl}}} \quad (5.19)$$

The calculation of the detector resolution using the residual between the track prediction and the detector hit position is explained in chapter 5.3.3. σ_{Incl} and σ_{Excl} correspond to the resolutions of the detector under investigation included and excluded from the track building. Calculating the tracking error using equation 5.17 for an exemplary setup from chapter 7 the dependency on Z is visible (see figure 5.4). In this setup, three reference detectors (BLY⁶) were used as reference trackers in Y. BLX provides only information in X and is not included in the track building. The tracking error at the position of the investigated detectors (vertical red lines) is better than the individual detector resolutions of the tracking chambers $\sigma_i \approx 75 \mu\text{m}$.

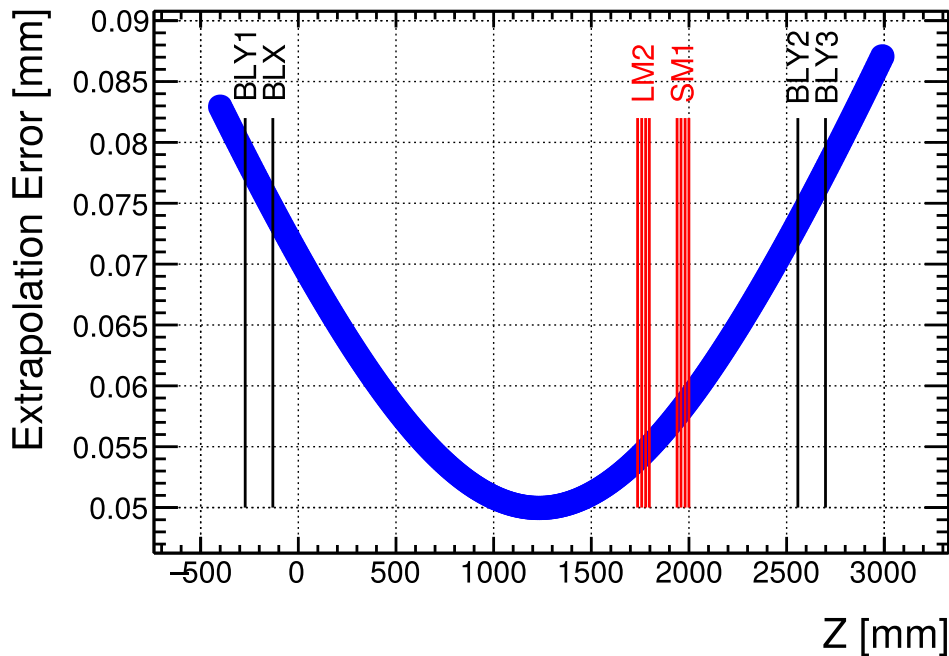


Figure 5.4: Exemplary track extrapolation error along Z for a measurement setup used in chapter 7.

Three tracking chambers (BLY) were used to determine the reference track in Y. The tracking error between multiple tracking chambers is better than the resolution of individual tracking chambers $\sigma_i \approx 75 \mu\text{m}$. Vertical red lines indicate the position of several investigated test detectors not contributing to the reference track. BLX is a chamber providing information along the Y axis and is not included in the track building in the Y direction.

⁶BL is the name of these reference chambers referring to "Beamline". X and Y denote their direction of precision, since these detectors provide only information in one coordinate.

5.3.2 Detector Alignment

To obtain high-precision tracking and the correct resolutions of tested detectors a precise alignment is required. Besides a coarse hardware alignment ($\mathcal{O}(< 1 \text{ cm})$) when setting up the detectors, a fine data-driven software alignment is performed.

This alignment is based on the residual (Y_{res}) given by equation 5.20. The residual is the difference between the reference position provided by the tracking chambers extrapolated into this detector ($Y_{\text{Extrapolated}}$) and the reconstructed position in the detector under investigation (Y_{Cluster}). The detector under investigation is excluded from the track building.

Misalignments of the detector result in dependencies of the residual on other parameters discussed further down in this chapter. These dependencies are accounted for in the alignment procedure following Jagfeld [2023].

$$Y_{\text{res}} = Y_{\text{Extrapolated}} - Y_{\text{Cluster}} \quad (5.20)$$

Detector Shifts

The most simple misalignment is a constant shift of the detector resulting in a residual not centered around zero as illustrated in figure 5.5. For Y being the precision direction of the detectors this constant shift concerning the reference track is added to the position Y :

$$Y_{\text{corr}} = Y + \Delta Y \quad (5.21)$$

The provided reference track and the detectors under investigation are sensitive in the Y direction. Shifts in X direction can not be resolved but are also not affecting the residual in Y .

A shift along the beam axis (Z direction) can be determined only by inclined particle tracks. Perpendicular tracks are not sensitive to such a shift (see figure 5.6b). It is resolved by a correlation between the residual and the reconstructed track slope as depicted in figure 5.6a. The distribution is fit by a polynomial of first order with p_1 as the slope of the linear equation, p_0 being an offset and "Slope" the track slope variable:

$$\Delta Y = p_1 \times \text{Slope} + p_0. \quad (5.22)$$

With "Slope" = $\frac{\Delta Y}{\Delta Z}$ (see figure 5.6b) and $p_0 = 0$ equation 5.22 becomes

$$\Delta Z = p_1 \times \frac{\Delta Y}{\Delta Y} = p_1 \quad (5.23)$$

The shift⁷ in Z is equal to the slope of the fit, which is for the given example in figure 5.6a 395.5 mm/mrad and thus:

$$Z_{\text{corr}} = Z + \Delta Z = Z + p_1 \quad (5.24)$$

⁷For visualization purposes the misalignment has been worsened artificially. This holds for all corrections discussed in this chapter.

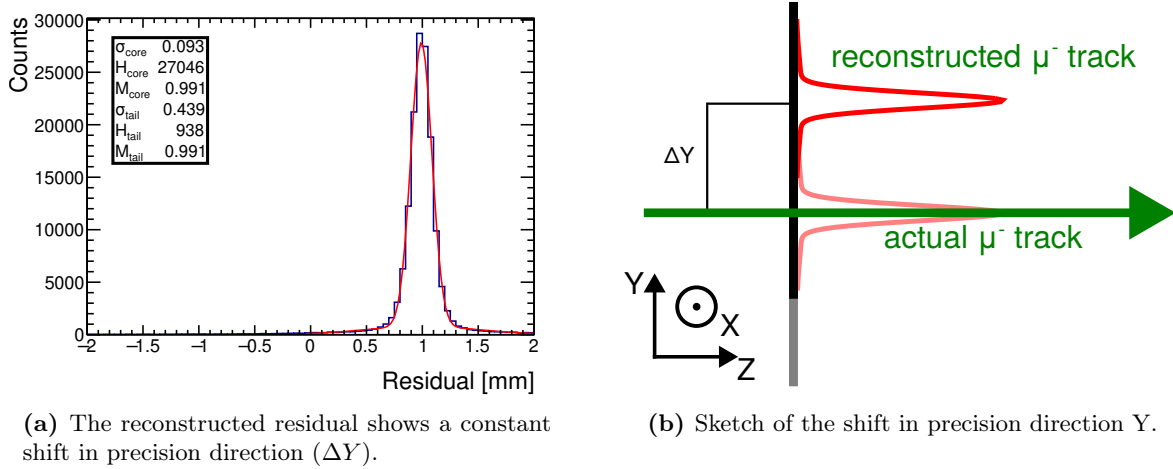
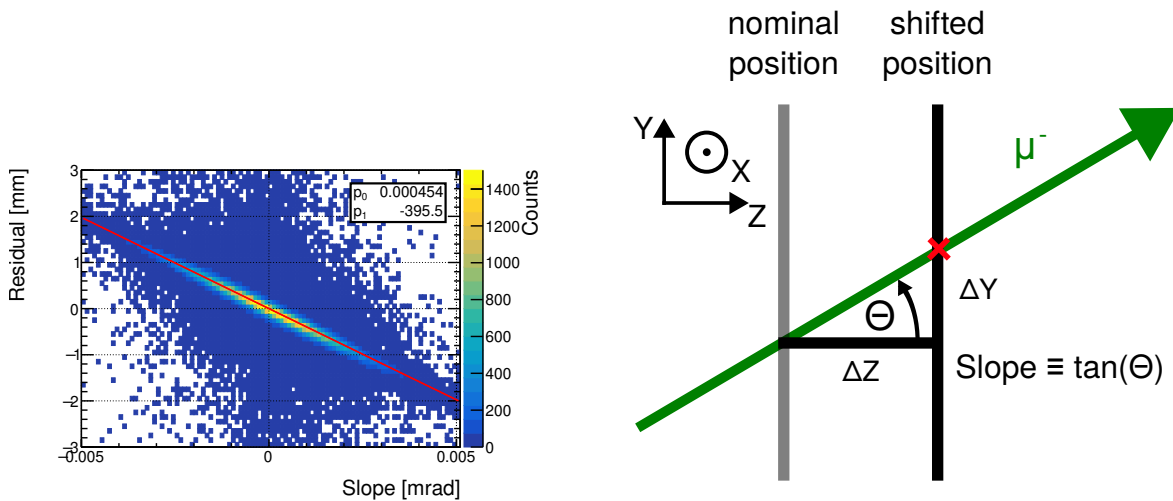


Figure 5.5: Constant shifts in the precision direction of the detector concerning the tracking chambers are visible with the residual distribution not being centered around zero. It is corrected as described in equation 5.21.



(a) Shifts along the beam axis in the Z direction are visible as a correlation between the track slope and the residual Y_{res} . Perpendicular tracks ("Slope" = 0) are insensitive to this shift. The distribution is horizontal for well-aligned detectors.

(b) Sketch of the shift along the beam axis.

Figure 5.6: Constant shift along the beam in the Z direction. The correction value ΔZ is determined by a linear fit of the correlation plot (equation 5.22) with the fit slope p_1 corresponding to the shift in mm (equation 5.23).

Detector Rotations

In addition to constant shifts of the detector rotations also affect the residual. Detector rotations around the Y-axis are not resolved but also do not influence the residual. Rotations of the detector are corrected similarly to the shift along the beam axis using a linear fit and applying corrections depending on specific fit parameters.

A rotation of the detector around the X-axis leads to a correlation between the reconstructed cluster position Y and the residual Y_{res} (figure 5.7). A linear fit of the distribution with p_1 as slope and p_0 being an offset is applied:

$$\Delta Y = p_1 \times Y + p_0 \quad (5.25)$$

To account for the rotation it is sufficient to correct only for the slope (p_1) of the correlation shown in figure 5.7a. All remaining constants (p_0) are included in equation 5.21⁸. Thus follows for the rotation angle Θ

$$\cos(\Theta) = \frac{Y}{Y + \Delta Y} = \frac{1}{1 + p_1} \quad (5.26)$$

and for the corrected position

$$Y_{\text{corr}} = Y + \Delta Y = Y + \frac{Y}{\cos(\Theta)} - Y = \frac{Y}{\cos(\Theta)} \quad (5.27)$$

Rotations around the beam axis Z result in dependencies between the residual in one direction (Y_{res}) and the position in the second coordinate X (see figure 5.8). Analogously to the previous corrections, this distribution is fit linearly and the constant p_0 is absorbed in the constant shift corrected by equation 5.21.

$$\Delta Y = p_1 \times X + p_0. \quad (5.28)$$

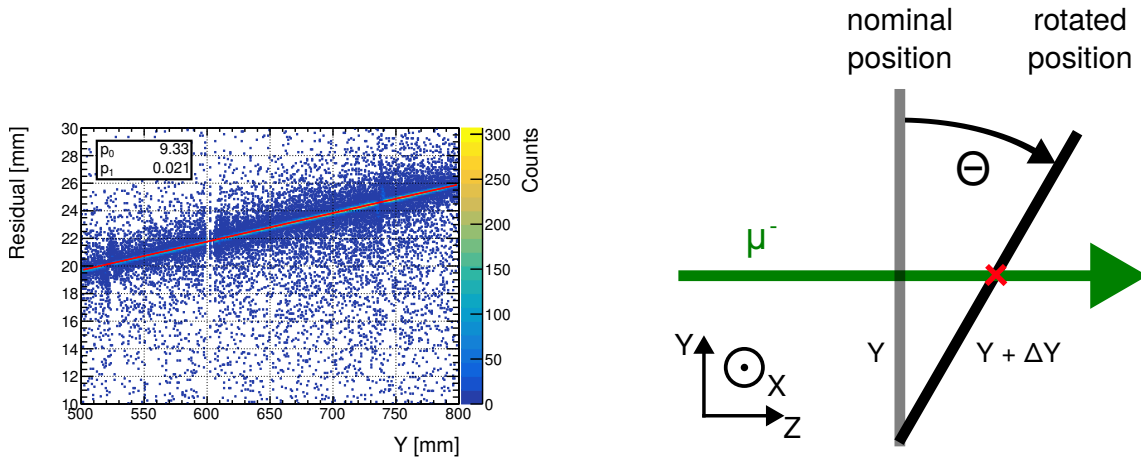
For the resulting angle of rotation, Θ follows

$$\tan(\Theta) = \frac{\Delta Y}{X} = p_1 \quad (5.29)$$

The corrected position is then given by:

$$Y_{\text{corr}} = Y + \Delta Y = Y + X \times \tan(\Theta) \quad (5.30)$$

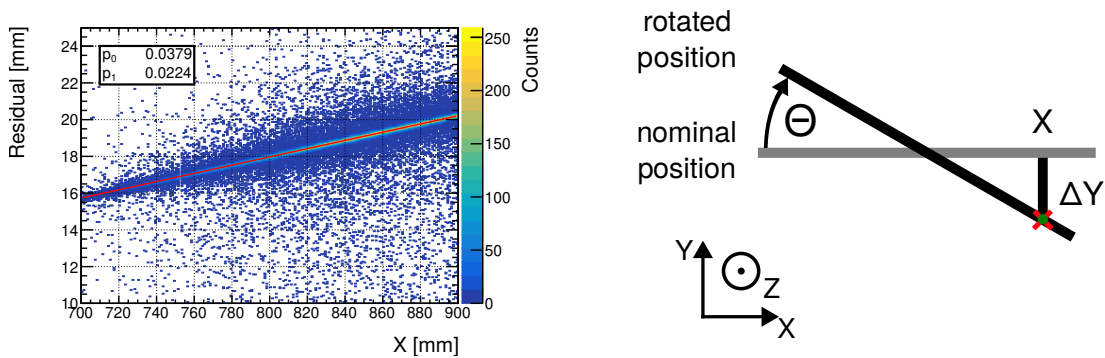
⁸This shift in precision direction is typically the last step in the software alignment, accounting for all the constants at once.



(a) Rotations around the X-axis lead to correlations between the hit position Y and the residual Y_{res} . The distribution is horizontal for well-aligned detectors.

(b) Sketch of the rotation around the X-axis.

Figure 5.7: The rotation angle Θ of a rotation around the X-axis is determined by a fit of the correlation distribution in figure 5.7a using equation 5.26.



(a) Rotations around the Z axis show correlations between the hit position along the strips (X) and the residual in precision direction (Y_{res}). The distribution is horizontal for well-aligned detectors.

(b) Sketch illustrating the rotation around the Z axis.

Figure 5.8: The rotation angle Θ of a rotation around the Z-axis is determined by a fit of the correlation distribution in figure 5.8a using equation 5.29.

5.3.3 Detector Resolution

The resolution of the detectors inside a tracking hodoscope is derived from the width of the residual distribution as shown in figure 5.9. The two residual distributions correspond to the two different methods to determine the strip charge as discussed in chapter 4.2.2, the inverse fermi fit (figure 5.9a), and the "sliding template" technique (figure 5.9b). Obtained residual distributions are fit with a sum of two Gaussians:

$$f(x) = a \times e^{-\frac{(x-b)^2}{2\sigma_{\text{core}}^2}} + c \times e^{-\frac{(x-d)^2}{2\sigma_{\text{tail}}^2}} \quad (5.31)$$

a, c, and b, d being free parameters defining the height and the offset of the Gaussians from zero respectively. σ_{core} is a measure of the width of the narrower Gaussian (green) while σ_{tail} defines the broader, blue Gaussian.

The inner fit represents the internal resolution of the detector while the outer distribution takes into account secondary effects originating from scattering inside the detector, particle showers, or δ -electrons.

Starting from this, two different residuals are used for the resolution calculation. The inner core residual (σ_{core}) and a weighted residual (σ_{weighted}) taking into account all the previously mentioned effects:

$$\sigma_{\text{weighted}} = \frac{\int a \times e^{-\frac{(x-b)^2}{2\sigma_{\text{core}}^2}} dx \times \sigma_{\text{core}} + \int c \times e^{-\frac{(x-d)^2}{2\sigma_{\text{weighted}}^2}} dx \times \sigma_{\text{weighted}}}{\int a \times e^{-\frac{(x-b)^2}{2\sigma_{\text{core}}^2}} dx + \int c \times e^{-\frac{(x-d)^2}{2\sigma_{\text{weighted}}^2}} dx} \quad (5.32)$$

Comparing the inverse fermi fit (figure 5.9a) and the "sliding template" method (figure 5.9b) results in close to equal residuals⁹. Both methods reconstruct a $\sigma_{\text{weighted}} = 0.124$ mm. From this, it is shown that for perpendicular incidents the methods perform equally well.

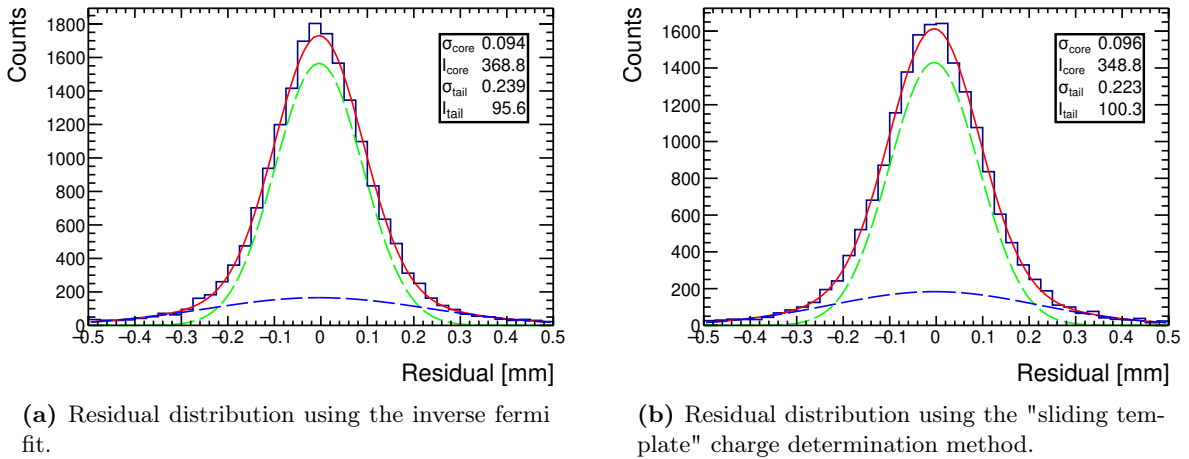


Figure 5.9: Comparison of the residual distributions obtained with the inverse fermi fitting and "sliding template" method showing close to equal core residuals with 0.094 mm and 0.096 mm respectively.

The track extrapolation error has to be subtracted quadratically from $\sigma_{\text{core/weighted}}$ to obtain the core and weighted detector resolution respectively:

$$\sigma_{\text{res}} = \sqrt{\sigma_{\text{core/weighted}}^2 - \sigma_{\text{track}}^2} \quad (5.33)$$

⁹Inverse fermi fit: $\sigma_{\text{core}} = 0.094$ mm; "sliding template": $\sigma_{\text{core}} = 0.096$ mm.

5.4 Inclined Particle Trajectories

Particles traversing the detector under an angle are more complicated to reconstruct with similar precision. The main reason for the previously introduced centroid position reconstruction (see chapter 5.2) to perform worse is the inhomogeneous ionization process of the minimum ionizing muon along the particle track as depicted in figure 5.10. Shown is a simulation of a 120 GeV muon passing the drift region of 5 mm under 29° of inclination in Garfield++ (Veenhof [2010]). An asymmetry of deposited charge along the anode strips is established in agreement with the Landau-shaped energy loss of MIPs in thin gaseous detectors, shifting the charge-weighted cluster position to the right (Y_{CW}). As a consequence, the charge-weighted timing (t_{CW}) distribution is altered similarly. The charge-weighted timing is derived in the same way as the charge-weighted position (see equation 5.39 in chapter 5.4.2).

The correct position (Y_{True}) is defined at the center of the drift region ($Z = 0.25$ cm). Different methods utilizing the timing information are introduced to improve the position reconstruction for inclined tracks. This will be the subject of this chapter.

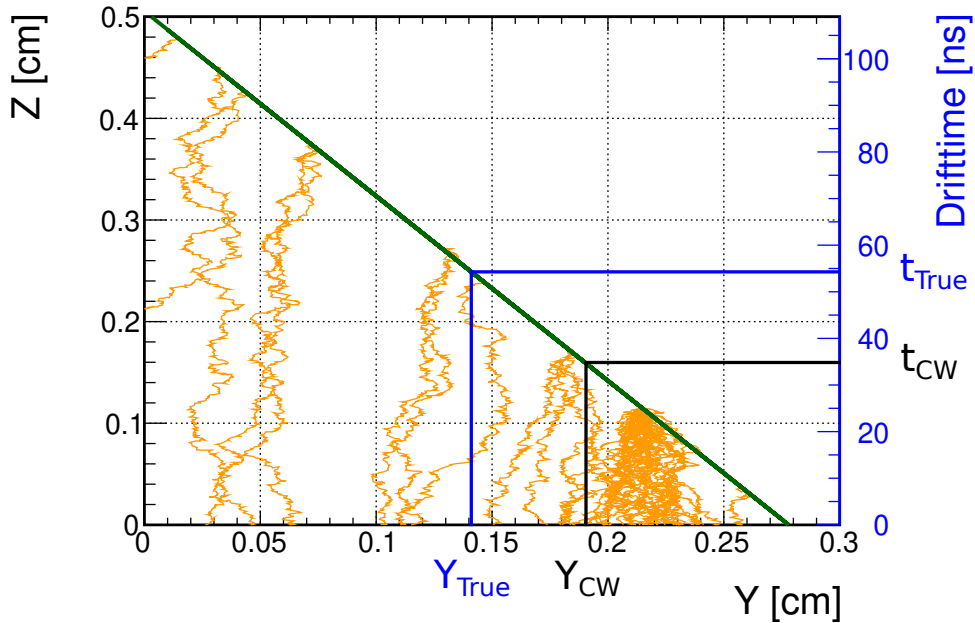


Figure 5.10: Inhomogeneous ionization by a 120 GeV muon in Ar:CO₂:iC₄H₁₀ (93:5:2 vol%) over a 5 mm drift gap simulated in Garfield++ (Veenhof [2010]). The increasing number of primary electrons to the right part of the figure shifts the charge-weighted position (Y_{CW}) away from the actual position (Y_{True}) of the particle reconstructed at the center of the drift gap. For the charge-weighted cluster timing (t_{CW}), this follows accordingly. As a result, a decrease in resolution for inclined tracks using the centroid position reconstruction method is observed (see figure 5.15a).

5.4.1 μ TPC-Like Position Reconstruction

The first alternative method to be discussed is based on the algorithms used in Time Projection Chambers (TPCs) hence its name μ TPC-like reconstruction (Iakovidis [2014]). For each strip of a cluster, the position of the primary electron within the drift gap is calculated by

$$Z_{Strip} = v_D \times t_{Strip} \quad (5.34)$$

with v_D being the electron drift velocity. Values of the drift velocity are taken from simulation for the corresponding applied drift fields E_D as shown in figure 3.4a.

The derived 2D (y_i, z_i) data points are fit analytically by χ^2 minimization of the linear fit function following Klitzner [2019]. This process is visualized in figure 5.11. The particle position is derived by evaluating the linear fit at the center of the drift gap. Different errors in the Z direction for the different strips of the cluster are visible. Each point has an initial error corresponding to the time resolution (e.g. figure 7.11) of the detector assigned. This error is scaled as follows: Strips with $Q < 100$ ADC Counts by a factor of 10; strips with $100 < Q < 200$ ADC Counts by a factor of 3; saturated strips $Q > 1020$ ADC Counts and $Q > 1800$ ADC Counts for VMM (see chapter 4.4) and APV25 readout (see chapter 4.2) respectively by a factor of 10. For fit results of $\chi^2/ndf > 3$ a Hough Transformation (Hough [1959]) is applied to determine outlying particles and to correctly scale the errors. If the fit result remains worse than $\chi^2/ndf > 3$, the μ TPC position reconstruction is marked as failed and this cluster is discarded.

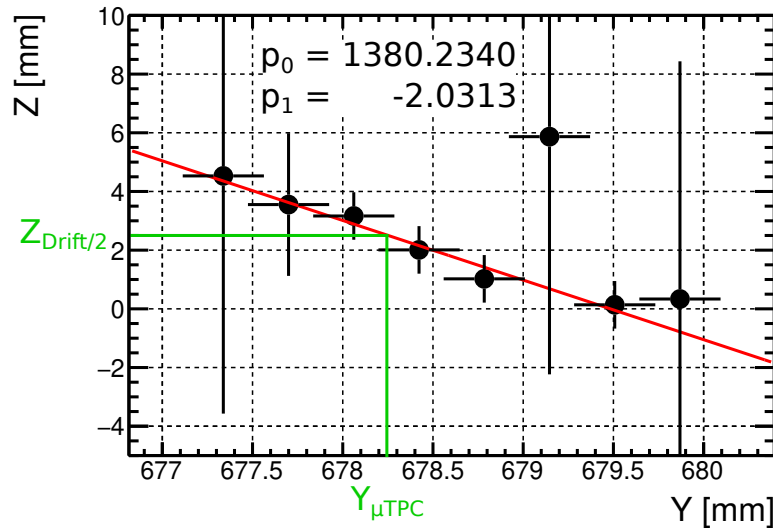


Figure 5.11: Each strip in a cluster is filled into a graph with the strip position y_i on the X-axis and the position in the drift gap $z_i = v_D \times t_i$ (see equation 5.34), where the primary electron was created. A linear fit of the points evaluated at the center of the drift region provides the μ TPC position $Y_{\mu\text{TPC}}$.

Errors of strips with small charges (< 100 ADC Counts), saturated strips (> 1020 ADC Counts and > 1800 ADC Counts for VMM and APV25 readout respectively) or strips that have been found off track via a Hough transformation (see figure 5.12) are scaled by a factor of ten in Z.

Hough Transformation

The Hough Transformation is an analytical method to detect straight lines (Hough [1959]). Points in the original space are represented by lines in the Hough space. The transformation uses a family of lines through each of the data points in Hesse normal form (Hesse [1865]). The normal vector \vec{n} is then given by

$$\vec{n} = \begin{pmatrix} \cos(\alpha) \\ \sin(\alpha) \end{pmatrix} \quad (5.35)$$

with α being the angle between the X-axis and the normal vector.

Each point $P(Y, Z)$ in figure 5.11 is transformed to the Hough space by parametrization using

$$d(\alpha) = Y \cos(\alpha) + Z \sin(\alpha) \quad (5.36)$$

$d(\alpha)$ is then by definition the shortest distance of the normal line from the origin.

Points that lie on a straight line in the original space will accumulate at the same point in the Hough space because of identical α and $d(\alpha)$. The result of the transformation of all points in figure 5.11 to the Hough space is depicted in figure 5.12. A common point for $d(\alpha) \approx 2$ mm and an angle of 0.46 rad is found. The single line not crossing the common point can be easily identified in the Hough space. This line corresponds to the outlier at $Y = 679.15$ mm. Positional errors in Z of such strips are scaled by an additional factor of ten before the χ^2 minimization of the linear fit is redone.

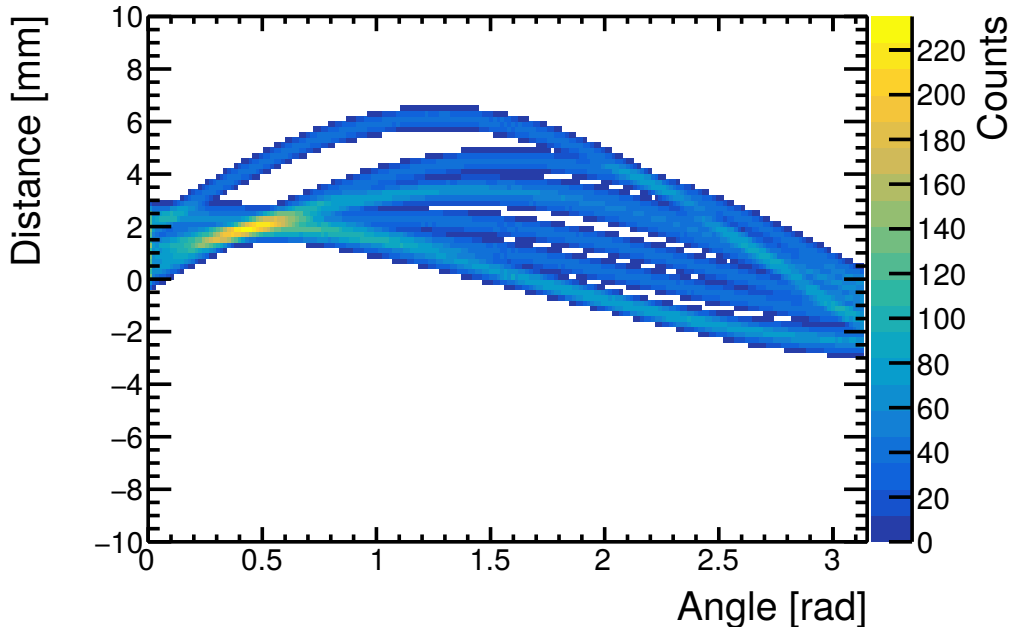


Figure 5.12: Hough transformation of the strips shown in figure 5.11.

The line not crossing the common intersection point corresponds to the strip at $Y = 679.15$ mm. This outlier is easily identified in the Hough space.

The positional error in Z (see figure 5.11) of such strips is scaled by a factor of ten before the χ^2 minimization of the linear fit to determine the μ TPC position is repeated.

Reconstructed Angle of Inclination

The slope of the fit function determining the μ TPC position ($m_{\mu\text{TPC}}$) is directly correlated to the angle of track inclination (Θ) relative to the perpendicular incident. It is described by equation 5.37 with the drift velocity v_D and the strip pitch p .

$$\Theta = 90^\circ - \tan^{-1}\left(\frac{v_D}{m_{\mu\text{TPC}} \times p}\right) \quad (5.37)$$

The reconstructed angle of inclination for a set angle of $(29 \pm 1)^\circ$ is shown in figure 5.13¹⁰. With the angle reconstruction directly depending on the drift velocity v_D deviations due to humidity or air in the detector change the reconstructed angle. An overview of the effect of different contents of those on v_D is given in appendix A.

¹⁰Variable binning on the X-axis has to be applied resulting from the non-linear transformation of the track slope to the angle. This is described in detail in Bortfeldt [2014].

To obtain the asymmetric angular resolution ($\sigma_{<,>}$) the peak of the distribution is fit with a piecewise-defined Gaussian function given by

$$f(\Theta) = a \times \exp\left(-\left(\frac{\Theta - \Theta_{\text{Max}}}{\sigma_{<}}\right)^2\right) \quad \text{for } \Theta \leq \Theta_{\text{Max}} \quad (5.38)$$

$$f(\Theta) = a \times \exp\left(-\left(\frac{\Theta - \Theta_{\text{Max}}}{\sigma_{>}}\right)^2\right) \quad \text{for } \Theta > \Theta_{\text{Max}}$$

with a being the height of the distribution (Bortfeldt [2014]).

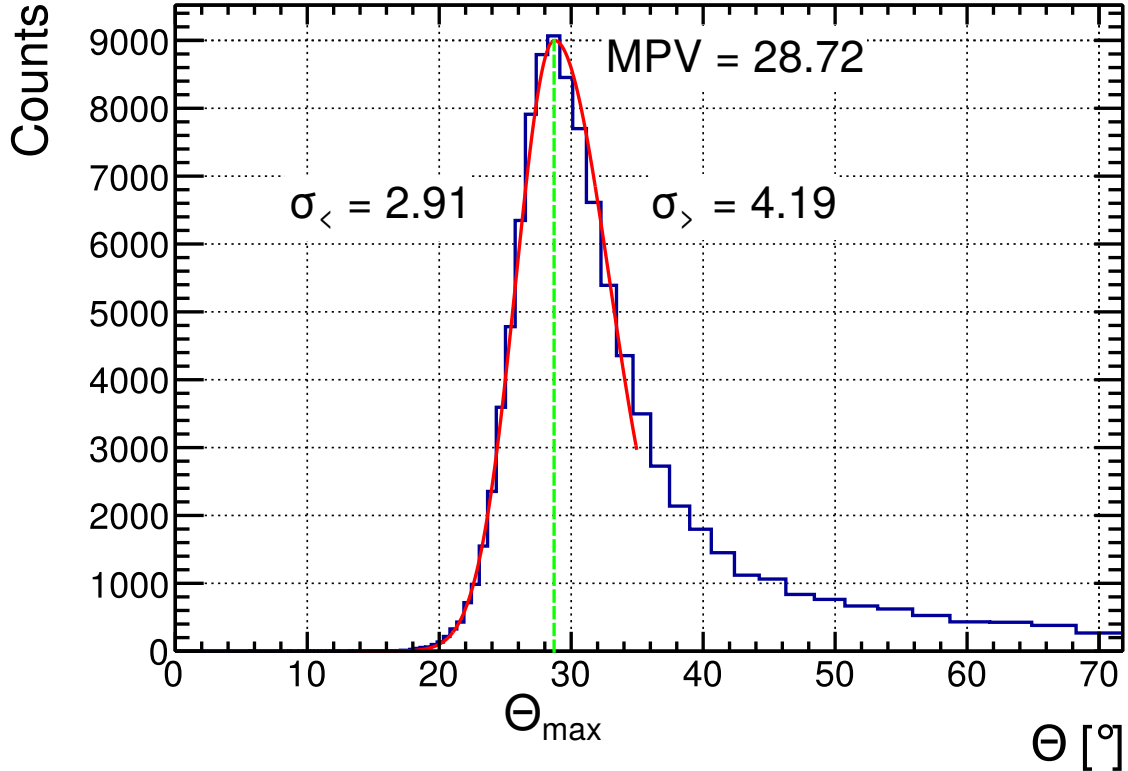


Figure 5.13: Reconstructed inclination for an inclination angle of $(29 \pm 1)^\circ$.

The distribution is fit with a piecewise-defined Gaussian function (see equation 5.38) centered around the most probable value Θ_{max} of $(28.72^{+4.19}_{-2.91})^\circ$. Being directly dependent on the drift velocity, deviations due to impurities in the gas mixture, like water vapor or air, result in different reconstructed angles. Figure A.1 in the appendix provides an overview of the effect of these impurities on v_D .

5.4.2 Charge-Weighted Time Correction of the Charge-Weighted Position Reconstruction

Another method to determine the position of inclined particle tracks was introduced by Flierl [2018]. A correction depending on the charge-weighted cluster time t_{CW} , given by equation 5.39, is applied to the reconstructed charge-weighted position derived in equation 5.16.

$$t_{\text{CW}} = \frac{\sum_{\text{Strips}} (Q_{\text{Strip}} \times t_{\text{Strip}})}{\sum_{\text{Strips}} Q_{\text{Strip}}} \quad (5.39)$$

The shift of the centroid position Y_{CW} in figure 5.10 directly correlates with the shift of the charge-weighted cluster timing t_{CW} . Plotting the residuals determined by the centroid position against the cluster time proves this linear correlation (see figure 5.14). This correlation can be corrected analogously to the corrections performed on the detector position and rotation alignment described in chapter 5.3.2:

$$\Delta Y = \Delta t \times v_D \tan(\Theta) \quad (5.40)$$

with $\Delta t = t_{\text{True}} - t_{CW}$ (see figure 5.10).

To utilize equation 5.40 the angle of inclination (Θ) has to be known¹¹.

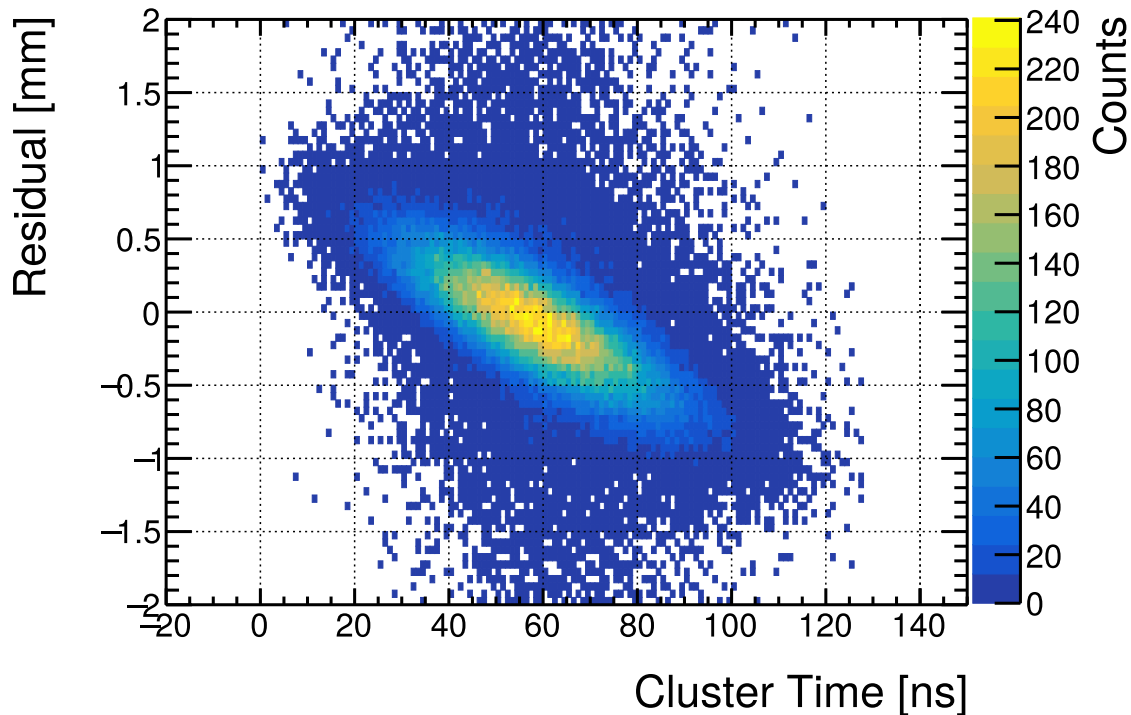


Figure 5.14: As shown in figure 5.10 the charge-weighted timing (t_{CW}) is shifted from the true timing t_{True} in the same manner as the position Y_{CW} . The correlation between the residual determined using the charge-weighted position reconstruction and the charge-weighted cluster timing allows for a correction of the prior by equation 5.40 resulting in improved resolutions (see figure 5.15c).

A comparison of the residuals determined using the previously discussed methods, centroid, μ TPC-like and time corrected centroid, are shown in figure 5.15 for 120 GeV muons under $(29 \pm 1)^\circ$ of inclination. As expected the reconstructed residuals using the centroid method without corrections (top left) shows the worst results with a $\sigma_{\text{core}} = 0.379$ mm. Applying the μ TPC-like position reconstruction algorithm an improvement of more than 120 μm compared to the previous method with a $\sigma_{\text{core}} = 0.164$ mm is achieved. This method is surpassed by the time correction of the centroid position providing a $\sigma_{\text{core}} = 0.138$ mm. A huge improvement is visible by applying these methods. Yet residuals as determined for perpendicular particle incident of $< 100 \mu\text{m}$ (see figure 5.9) could not yet be achieved. One of the major limiting factors is the timing resolution provided by the detector and readout electronics.

¹¹Flierl [2018] states that a coarse angular information is sufficient.

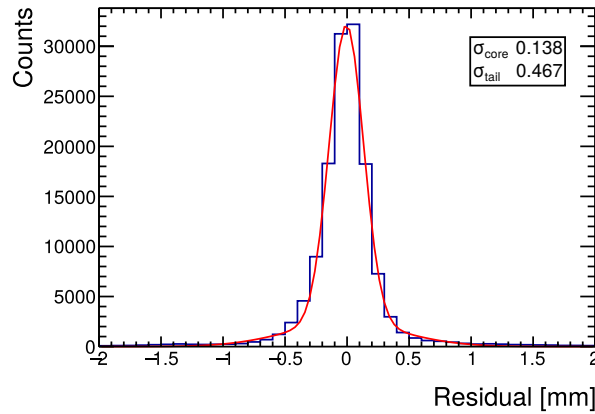
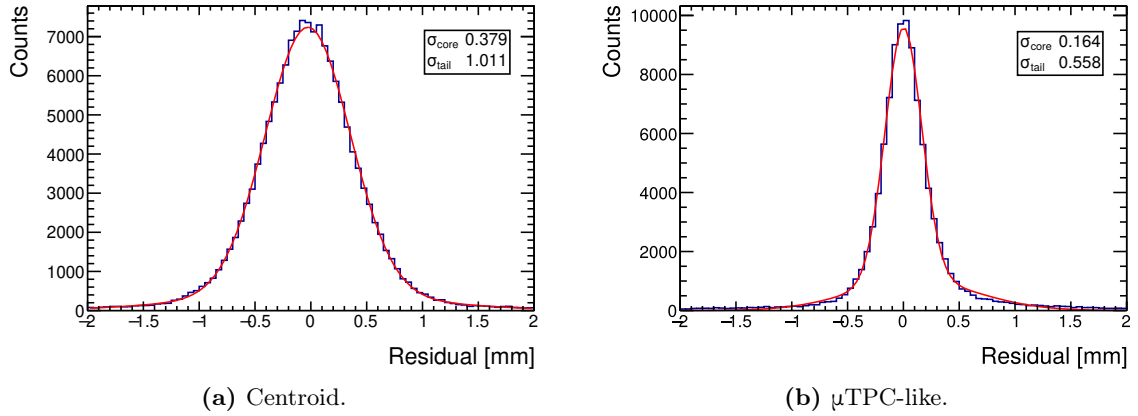


Figure 5.15: Comparison of the residuals determined using different position reconstruction methods for 120 GeV muons at an angle of inclination of $(29 \pm 1)^\circ$ (see chapter 7).

For particles passing the detector the charge-weighted method suffers from the inhomogeneous ionization (see figure 5.10) resulting in a bad $\sigma_{\text{core}} = 0.379$ mm. The μ TPC-like method shows improvement with a $\sigma_{\text{core}} = 0.164$ mm. Correcting the centroid position by the charge weighted cluster time using equation 5.40 surpasses the μ TPC-like method showing a $\sigma_{\text{core}} = 0.138$ mm.

For all the residuals shown here, the track extrapolation error has not been subtracted yet.

5.5 Detector Efficiency

Given a successful track building as described in 5.3.1 the residual of the detector under investigation is determined. If it is within an efficiency window of ± 2 mm the event is counted as efficient (see figure 5.16). For a reconstructed residual outside the window or no reconstructed cluster at all, the event is declared as inefficient¹². The efficiency is determined by dividing the number of efficient events ($N_{\text{Total}} - N_{\text{Inefficiencies}}$) by the total number of reconstructed tracks (N_{Total})¹³:

$$\epsilon = \frac{N_{\text{Total}} - N_{\text{Inefficiencies}}}{N_{\text{Total}}} \quad (5.41)$$

The size of the efficiency window (± 2 mm) is set accordingly to the internally decided limits by the NSW Micromegas community and kept for this thesis¹⁴.

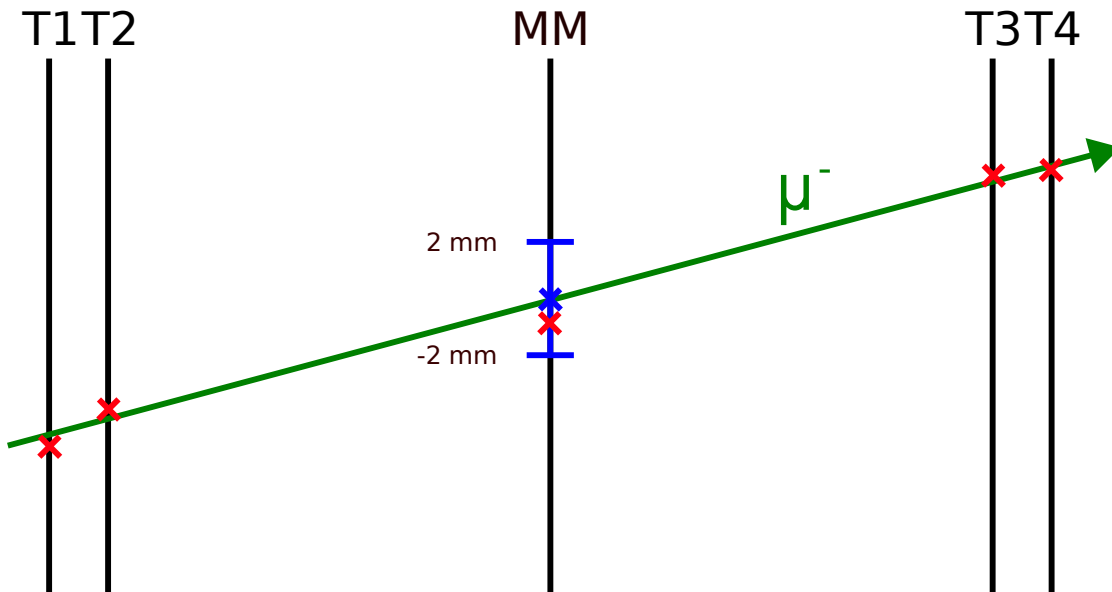


Figure 5.16: A reconstructed hit in a tested detector (MM, red cross) is counted as efficient if it lays within a window of ± 2 mm around the extrapolated value (blue cross) provided by reference tracking chambers (Ti). The number of efficient hits is divided by the total number of events where a reference track was built successfully.

¹²If multiple clusters reside inside the window, the cluster closest to the extrapolated position is taken into account preventing overcounting.

¹³Although the possibility of multiple tracks occurring for the same trigger only a single track is reconstructed per event. The selection criteria depend on the given setup. The main cut is on the known track slope.

¹⁴This window is adapted in chapter 8 since a different tracking without reference detectors is performed. This will be discussed in detail in that chapter.

Chapter 6

Long-Term Irradiation in the CERN GIF++

The long-term irradiation tests of the ATLAS NSW Micromegas detectors are carried out at two different facilities. The central topics of these tests are the longevity and performance of the detector under and after irradiation. One facility, located close to Munich, is the Maier-Leibnitz-Laboratorium (MLL) and the corresponding setup will be discussed in chapter 8. There, one detector is irradiated with an Am-Be radioactive source delivering photons and neutrons.

The second irradiation facility is situated at CERN being the Gamma Irradiation Facility++ (GIF++) built for high-intensity gamma fluxes. This chapter introduces this facility and the long-term irradiation setup. Additionally, the provided irradiation is calibrated for comparison with the expected irradiation levels the detectors will face during operation in the ATLAS experiment at HL-LHC.

6.1 The Gamma Irradiation Facility

The key component of the facility is a very strong ^{137}Cs gamma source with an initial activity of 14 TBq (Jaekel et al. [2015]). Since the installation in 2015, the activity has decreased to ≈ 11.65 TBq in the year 2023:

$$N(t) = N_0 e^{-t \times \ln(2)/t_{1/2}} = 14 \text{ TBq } e^{-8 \text{ a} \times \ln(2)/30.17 \text{ a}} = 11.65 \text{ TBq} \quad (6.1)$$

Figure 6.1 shows a top view of the facility. The source position is indicated by the radiation hazard symbol. Placed inside a shielding aperture as sketched in figure 6.2a two regulated irradiation zones are provided (upstream and downstream¹). Additionally, two areas outside of the shielded facility are dedicated to setup preparation (Preparation area) and providing services like gas, HV, and electronics (Gas and Electronics). Since the facility is situated at the H4 extraction line of the SPS, detectors inside can be tested with muon beams created by the protons accelerated in the SPS, that are guided to targets situated at the very beginning of these beamlines. The muons enter the facility from the right in figure 6.1. A common trigger for all users of the GIF++ is provided by two $40 \times 40 \text{ cm}^2$ scintillators (pale blue) at the entrance and exit outside of the GIF++ along the muon beam.

¹The naming scheme of the irradiation zones follows their position concerning the location of the facility. Particle beams originating from the SPS pass the facility from right to left in figure 6.1. Hence the irradiation zone right of the source is called upstream and left of the source downstream.

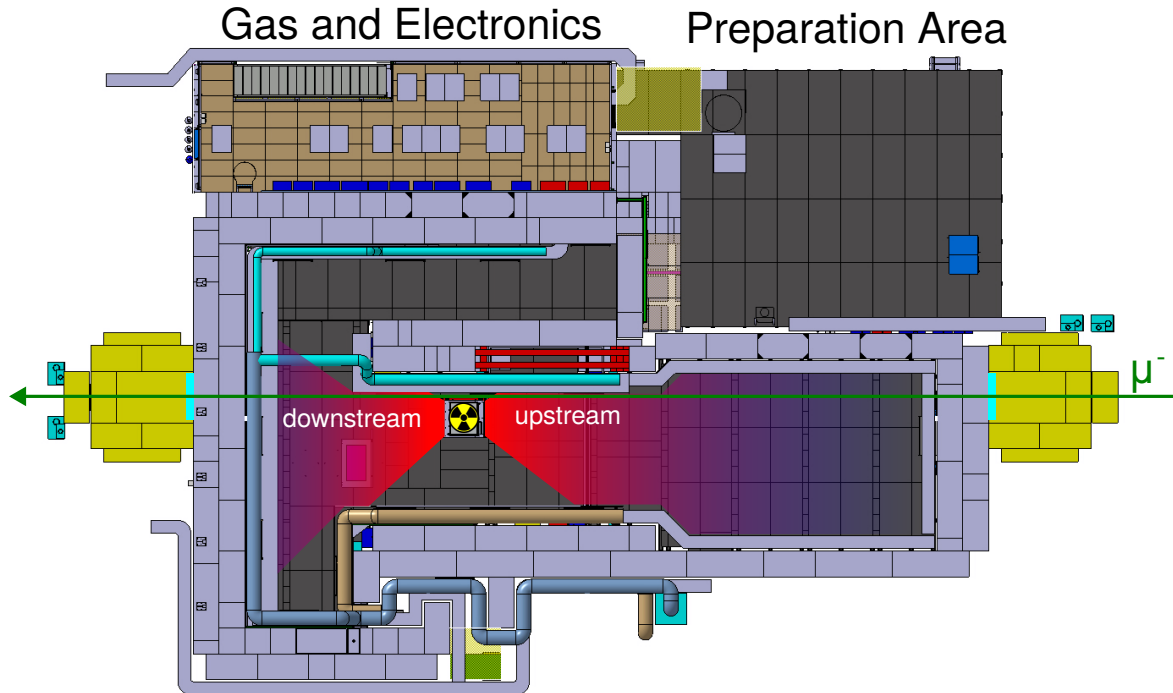


Figure 6.1: Layout of the GIF++ at CERN.

Originally the irradiator was a 14 TBq ^{137}Cs source. Since the installation in 2015, the activity reduced to approximately 11.65 TBq (see equation 6.1). The GIF++ offers two areas for irradiation with independent adjustment possibility of gamma flux configurations.

For beamtimes muons originating from a converter target hit by protons coming from the SPS are delivered into and through the facility (H4 beam). A pair of $40 \times 40\text{cm}^2$ scintillators positioned before and after the GIF++, shielded from the irradiator, at a distance of 25 m can be used as a coincidental trigger for the users (pale blue along muon track).

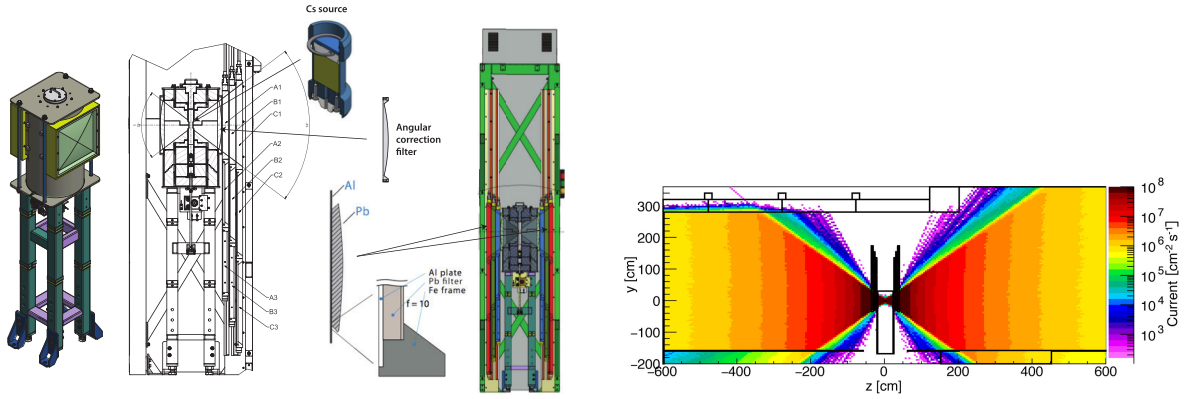
In front of the closed facility is a dedicated area for the preparation of setups as well as an area for gas supply and storing of electronics, e.g. power supplies or NIM electronics.

Figure adapted from <https://gif-irrad.web.cern.ch/Documents.html> (restricted access).

The photon intensity is controlled by a filter matrix system illustrated in figure 6.2a. A constant angular correction filter made from steel is situated closest to the source resulting in an intensity profile in dependence of the distance as depicted in figure 6.2b. The photon intensity is constant for a given distance in z in the form of vertical slices. The attenuation filter system consists of 3×3 filters (see table 6.1) providing 24 unique attenuation levels from 1 (no attenuation²) to 46415 (highest filter). The convex filters are made from steel and lead. Attenuation filters can be set independently for upstream and downstream. Additionally, the source can be "turned off" with the source being moved downwards into the garage position where the source is encapsulated in a tungsten block (see Pfeiffer et al. [2017] and Jaekel et al. [2015]).

As a shared facility with many other users, the applied intensity had to be coordinated. For the long-term irradiation studies almost exclusively the filter configuration A1, B1, C1 from table 6.1, i.e. no additional attenuation, was chosen to accumulate the maximum number of charges over time. For testbeam periods with a muon beam filter scans are performed to test the performance of the detectors for various background intensities (see chapter 7).

²No attenuation refers in this context to no additional attenuation filters. The angular correction filter still affects the photon flux and energies by Compton Scattering and Photoelectric Effect in the filter material.



(a) Sketch of the filter system controlling the gamma flux.

Taken from Jaekel et al. [2015].

(b) Simulation of the gamma flux versus the distance from the source.

Taken from Pfeiffer et al. [2017].

Figure 6.2: The angular correction filter provides identical irradiation strengths in vertical slices at a fixed distance from the source.

	1	2	3
A	1	10	100
B	1	1.47	100
C	1	2.15	4.64

Table 6.1: Attenuation filter settings in the GIF++.

One filter setting of A, B, and C has to be set. The values are combined multiplicatively leading to an attenuation factor of $F = A(i) \times B(j) \times C(k)$. This value ranges from $F=1$ (A1, B1, C1) up to $F=46415$ (A3, B3, C3) Pfeiffer et al. [2017]. The delivered fraction of the intensity is given by $I = I_0/F$, with I_0 being the full intensity.

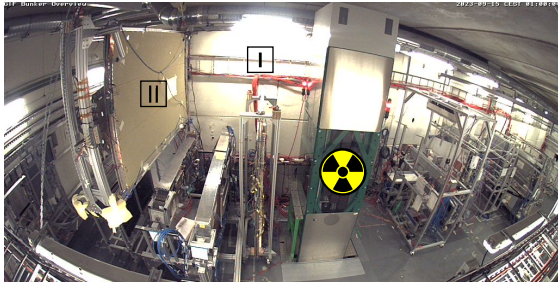
6.2 Irradiation Setup

The long-term irradiation setup offers the two positions depicted in figure 6.3. All four module types (SM1, SM2, LM1 and LM2) were tested (Vogel [2022]). An overview of the modules, their positioning in the facility, and the duration of irradiation are given in table 6.2. Position I is at a distance of about 1 m from the source, and position II resides at roughly 2.8 m. Due to the lack of space, not all modules were irradiated simultaneously but rather in consecutive measurement blocks. Detectors under investigation were operated with the ternary gas of Ar:CO₂:iC₄H₁₀ in a ratio of 93:5:2 vol%. A single reference module being constantly irradiated was tested under Ar:CO₂ (SM1 M35). The focus will be on the two modules SM1 M40 and LM2 M40 having accumulated the largest amount of charge. The accumulated charge is compared to the expected charge the detector will experience during operation at the ATLAS experiment.

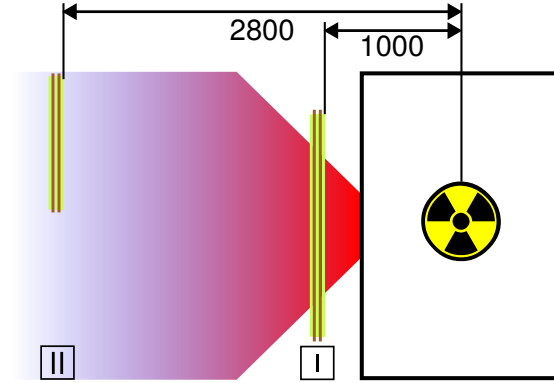
Both modules are spare modules and hence not built into the NSW. Two years of irradiation for both modules have been performed³. Despite being spare modules they fulfill all production standards and have passed the quality control.

Shown in figure 6.3b is the inhomogeneous irradiation of a single detector layer at 1 m distance. The lower PCB of SM1 M40 experiences next to no irradiation. This results in an inhomogeneous amount of charges accumulated over the detector. A discussion on this follows in chapter 6.3.3 with the actual measured accumulated charges.

³The irradiation of the detectors in the GIF++ is continuing in parallel to the operation of the NSWs at ATLAS to carefully monitor the longevity of the detectors.



(a) Picture of the long-term irradiation setup in the GIF++ (taken from <https://gif-irrad.web.cern.ch/> (restricted access, 15.09.2023)).



(b) Sketch of the long-term setup from 6.3a illustrating the inhomogeneous irradiation of detectors close to the source. Distances are given in mm.

Figure 6.3: Position of the detectors in the GIF++ for long-term irradiation tests. On the hanging trolley (II) up to three detectors were mounted simultaneously at a distance of ≈ 2.8 m. Position I is approximately 1 m from the source. Some areas experience next to no irradiation being outside of the irradiation cone.

Module	Position	Duration [months]	Gas
SM1 M31	II	2	Ar:CO ₂ :iC ₄ H ₁₀
SM1 M35	II	full time	Ar:CO ₂
SM1 M40	I	24	Ar:CO ₂ :iC ₄ H ₁₀
LM1 M07	II	5	Ar:CO ₂ :iC ₄ H ₁₀
LM1 M04	II	4	Ar:CO ₂ :iC ₄ H ₁₀
SM2 M33	I	0.5	Ar:CO ₂ :iC ₄ H ₁₀
LM2 M20	II	5	Ar:CO ₂ :iC ₄ H ₁₀
LM2 M40	II	24	Ar:CO ₂ :iC ₄ H ₁₀

Table 6.2: Overview of the NSW modules studied in the long-term irradiation measurements. All different types of modules assembled in the NSW were tested under Ar:CO₂:iC₄H₁₀. SM1 M35 was used as a reference chamber kept under the legacy gas for the whole irradiation period. The focus of this thesis is on SM1 M40 as the module with the highest charge accumulated (see figure 6.9) tested in various muon beam periods (see chapter 7).

6.3 HL-LHC Equivalent Calibration

For a scientific interpretation of the charges accumulated in the GIF++ or the photon rate provided by the source in the frame of a future HL-LHC a calibration is necessary. The particle rate and the currents for the calculation of the accumulated charge are calibrated independently. Basis of the calibration are measurements taken with the ATLAS detector at mean luminosities of $L=2.315 \times 10^{34} \text{cm}^{-2}\text{s}^{-1}$ and $L=2 \times 10^{34} \text{cm}^{-2}\text{s}^{-1}$ for the rate and current calibration respectively. Measurements are then extrapolated to the expected HL-LHC luminosity of $L_{\text{HL-LHC}} = 7.5 \times 10^{34} \text{cm}^{-2}\text{s}^{-1}$ (Aberle et al. [2020]).

6.3.1 Particle Interaction Rate

The starting point for the interaction rate calibration is the trigger rate measured by the sTGCs in the ATLAS detector at luminosities between $L = (2.15 - 2.48) \times 10^{34} \text{cm}^{-2}\text{s}^{-1}$ and a center-of-mass energy of $\sqrt{s} = 13.6 \text{ TeV}$. Measured rates depending on the distance from the

center of the wheel in radial distance are shown in figure 6.4. A steep decrease in the hit rate is visible. The points shown represent the mean rate recorded over one measurement at a mean luminosity⁴ of $\langle L \rangle = 2.315 \times 10^{34} \text{cm}^{-2} \text{s}^{-1}$. Following equation 6.2 a hit rate of 25.9kHz cm^{-2} for the innermost region is expected at HL-LHC. Important to notice is the particles detected in ATLAS range not only over a large energy spectrum but also all kinds of particles, e.g. muons, neutrons, protons, photons, etc. Everything contributes to the spectrum of figure 6.4 while the GIF++ only provides photons ($E = 662 \text{keV}$) and a muon test beam.

$$\text{Rate}_{\text{HL-LHC}} = \frac{L_{\text{HL-LHC}}}{\langle L \rangle} \times \text{sTGC}_{\text{Rate}} = \frac{7.5}{2.315} \times 8 \frac{\text{kHz}}{\text{cm}^2} = 25.9 \frac{\text{kHz}}{\text{cm}^2} \quad (6.2)$$

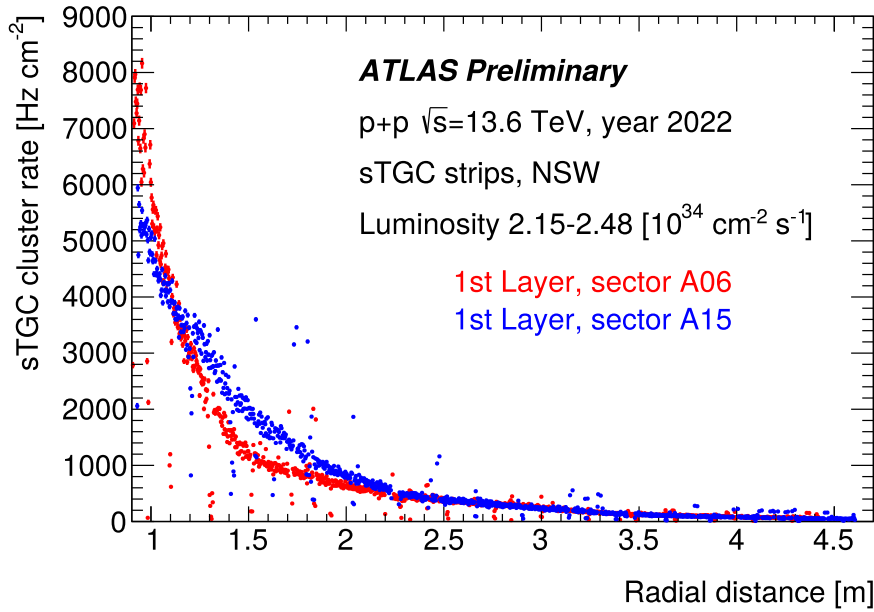


Figure 6.4: Measured sTGC cluster rate per area against the radial distance from the center. In red and blue the rate for two different sectors of the NSW are shown for luminosities between $L = (2.15 - 2.48) \times 10^{34} \text{cm}^{-2} \text{s}^{-1}$ at a center-of-mass energy of $\sqrt{s} = 13.6 \text{TeV}$. The highest measured rate is approximately 8kHz cm^{-2} assuming a mean luminosity of $L = 2.315 \times 10^{34} \text{cm}^{-2} \text{s}^{-1}$ (Iodice et al. [2023]). This translates to an expected maximum rate at $L_{\text{HL-LHC}} = 7.5 \times 10^{34} \text{cm}^{-2} \text{s}^{-1}$ of approximately 25.9kHz cm^{-2} .

To acquire the hit rate in the GIF++ the module SM1 M40 was placed at a distance of 1.82m from the source, and an artificial random trigger was set. Photons interact in the detector uncorrelated to the trigger. Hence the number of photons detected corresponds to the background hit rate times the data acquisition time after a trigger. The results of this measurement are shown in figure 6.5 with a mean number of reconstructed photon clusters of $N = 6.535$ per event.

$$\text{Rate}_{\text{GIF++}} = \frac{N}{t_{\text{RO}} \times A} = \frac{6.535}{200 \times 10^{-9} \text{s} \times 1334.7 \text{cm}^2} \approx 24.5 \frac{\text{kHz}}{\text{cm}^2} \quad (6.3)$$

Following equation 6.3 with a readout window of $t_{\text{RO}} = 200 \text{ns}$ and an active area of $A = 1334.7 \text{cm}^2$ this leads to a hit rate of 24.5kHz cm^{-2} . Comparison with equation 6.2 shows a

⁴This is only an approximation since at the beginning of a measurement run the luminosity is kept at the maximum for a certain time. Then the luminosity decreases exponentially. The calculated values are conservative, as the mean luminosity was probably slightly higher.

background rate of $0.95 \times \text{Rate}_{\text{HL-LHC}}$ at 1.82 m distance. As a result of the angular correction filter of the GIF++ the irradiation strength follows the $1/z^2$ law (Pfeiffer et al. [2017]). Measurements taken at different distances z from the source can be scaled by applying this power law⁵.

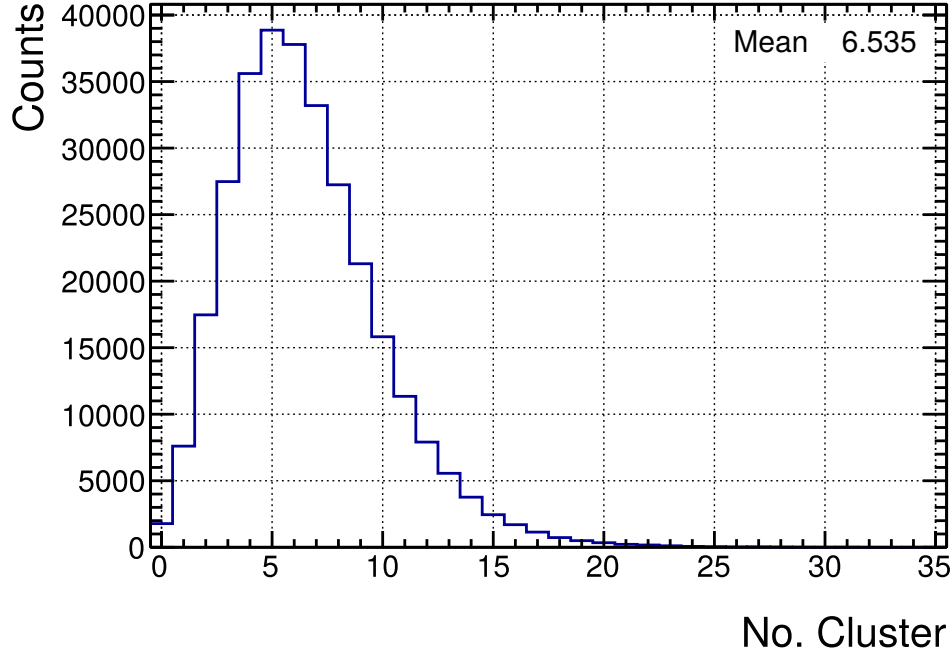


Figure 6.5: Number of clusters for a random trigger measurement with pure source background at attenuation factor 1.

With 6.535 clusters reconstructed, an active area of 1334.7 cm^2 , and 200 ns readout window this calculates to a hit rate of approximately 24.5 kHz cm^{-2} (see equation 6.3). Comparing this with the expected HL-LHC hit rate of 25.9 kHz cm^{-2} (see figure 6.4), $0.95 \times \text{Rate}_{\text{HL-LHC}}$ are delivered at 1.82 m distance from the source.

$$U_{\text{Amp}} = 520 \text{ V}, p_t = 100 \text{ ns}, \text{VMM}_{\text{RMS}} = 9\sigma.$$

6.3.2 Currents and Expected Accumulated Charges

To estimate the number of charges the detector will process during HL-LHC and to compare these values to the currents measured in GIF++ also here a calibration is needed. Compared to the previous segment concerning the hit rate the current calibration requires additional steps discussed in the following.

The starting point is again measurements obtained during operation in the ATLAS detector. HV scans were performed and the currents were measured for U_{Amp} from (500-515) V at a luminosity of $2 \times 10^{34} \text{ cm}^{-2} \text{ s}^{-1}$. Currents measured for the innermost PCB of an SM1 module are depicted in figure 6.6. To acquire the current for $U_{\text{Amp}} = 520 \text{ V}$ ⁶ the distribution is fit by the exponential function given in equation 6.4. An exponential increase is expected to result from the current increase by increasing the gain of the detector which follows an exponential function (see equation 2.23).

$$I(U_{\text{Amp}}) = \exp(p_0 + p_1 \times U_{\text{Amp}}) \quad (6.4)$$

⁵ $1 \times \text{Rate}_{\text{HL-LHC}}$ is reached at a distance of 1.75 m.

⁶During long-term irradiation the detectors are operated at this amplification voltage, being the proposed working point of the detectors.

For an amplification voltage of $U_{\text{Amp}} = 520 \text{ V}$ a current of 960 nA is expected for PCB 1 at a luminosity of $2 \times 10^{34} \text{ cm}^{-2} \text{ s}^{-1}$. This value represents the whole PCB, but as seen in figure 6.4 the hit rate and ultimately the charge deposited varies strongly even in the order of a single PCB of height $\approx 430 \text{ mm}$. To account for this decrease and to assign the individual strips

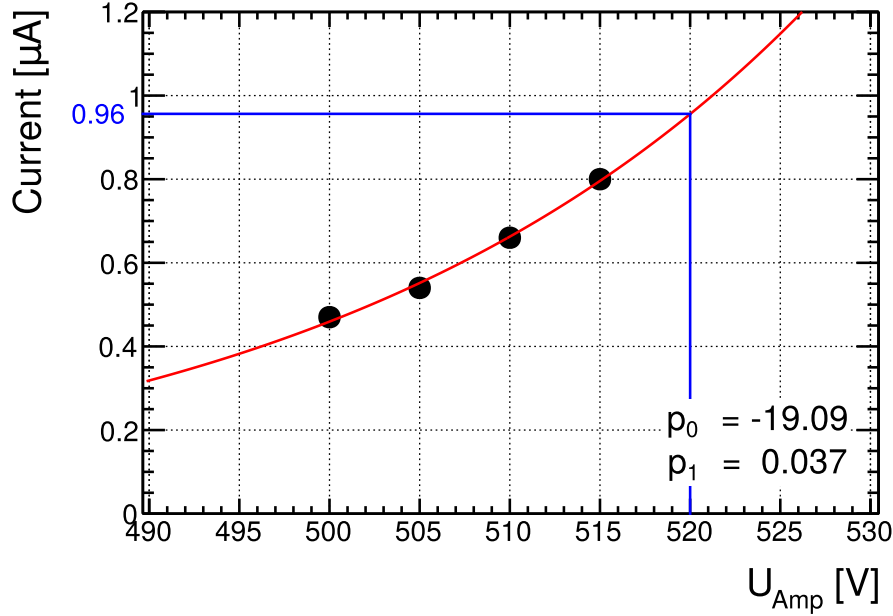


Figure 6.6: HV extrapolation of the measured currents at the ATLAS detector to 520 V ⁷. An exponential function (see equation 6.4) is fit on the four data points and then extrapolated to 520 V resulting in an expected current of 960 nA for the innermost PCB 1.

the correct expected currents the behavior along the PCBs has to be parametrized. The strip length and therefore area increase along a single PCB follows the same function as the area increase along the 5 PCBs of SM1 since the angles describing the trapezoidal shape of the individual PCBs remain the same over the first 5 boards. The extrapolation of the current to $U_{\text{Amp}} = 520 \text{ V}$ as shown in figure 6.6 is performed for all PCBs of a sector.

The resulting currents are then weighted by the area of the PCBs and plotted against the radius (r) of the wheel as shown in figure 6.7. A power law fit function (see equation 6.5) is applied to the first five points of the SM1 module. The last three points correspond to the SM2 module of the sector which has a slightly different strip length increase with r compared to SM1.

$$\frac{I}{A}(r) = \frac{p_0}{r^{p_1}} \quad (6.5)$$

As a result of the fit, the current density decreases with the radius following $\frac{1}{r^{2.42}}$. Distributing the current $I = 960 \text{ nA}$ for the innermost PCB (see figure 6.6) within this board using this decrease and accounting for the area of the individual strips (A_i) concerning the total area (A) of the module, strip i at a radius r_i of the module draws a current of:

$$I_i = \frac{A_i}{r_i^{2.42} \times A} \times I. \quad (6.6)$$

The resulting currents for the strips of PCB 1 are shown in figure 6.8.

⁷The errors of the displayed data points are smaller than the marker size. This also holds for figures 6.7 - 6.8.

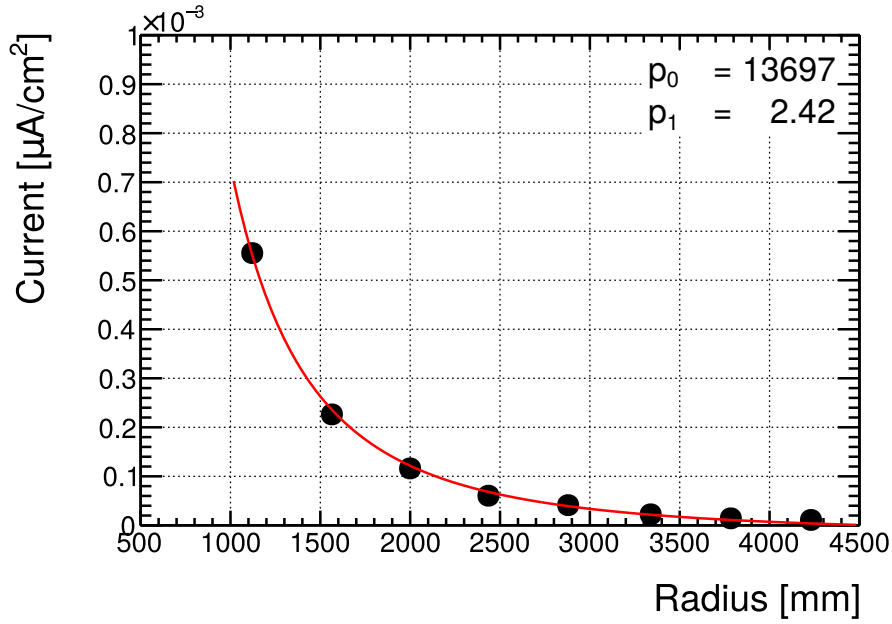


Figure 6.7: Current normalized to the area vs. radius to determine the current decrease along the NSW radius at 520 V.

The fit is performed using equation 6.5 on the first five data points belonging to SM1 up to $r \approx 2900$ mm. The exponent of the power p_1 describes the decrease along the module and within a PCB.

The expected charge accumulated per area and year (C_i) extrapolated to HL-LHC ($\times 3.75$ resulting from the increase in luminosity from $L = 2 \times 10^{34} \text{ cm}^{-2} \text{ s}^{-1}$ to $L_{\text{HL-LHC}} = 7.5 \times 10^{34} \text{ cm}^{-2} \text{ s}^{-1}$) is then given by

$$C_i = \frac{I_i}{A_i} \times t_{\text{Operation}} \times \frac{L_{\text{HL-LHC}}}{L} \quad (6.7)$$

The operation time ($t_{\text{Operation}}$) of the LHC is hereby defined as 200 days per year⁸ with 24 hours per day resulting in 17.28×10^6 s.

For the innermost strip at $U_{\text{Amp}} = 520$ V an accumulated charge per year of $0.068 \text{ C cm}^{-2} \text{ a}^{-1}$ is expected. The outermost strip of the PCB 1 already expects a reduced amount of accumulated charges of $0.029 \text{ C cm}^{-2} \text{ a}^{-1}$.

Scaling the calculations to the current operating voltage in ATLAS of $U_{\text{Amp}} = 505$ V, the innermost and outermost strip is expected to accumulate $0.039 \text{ C cm}^{-2} \text{ a}^{-1}$ and $0.017 \text{ C cm}^{-2} \text{ a}^{-1}$ respectively. Initially, it was foreseen to operate the innermost sectors of the NSW at $U_{\text{Amp}} 490$ V⁹. Some sectors operate currently at that amplification voltage¹⁰. For this, accumulated charges of $0.023 \text{ C cm}^{-2} \text{ a}^{-1}$ are expected for the innermost strip.

⁸200 days is a conservative approximation. Rossi and Brüning [2012] report on 150 days of proton-proton collisions for HL-LHC with the possibility to increase up to 180-200 days at the cost of heavy-ion collisions and maintenance periods.

⁹The particle track inclination in this region is small, hence the centroid position reconstruction works sufficiently well. Higher gain is only necessary for the reconstruction methods of inclined tracks, where the charge is spread over more strips, thus lowering the charge per strip.

¹⁰A performance comparison of the amplification voltages of 490 V and 505 V is ongoing. No final decision on the future operation voltage has been made yet.

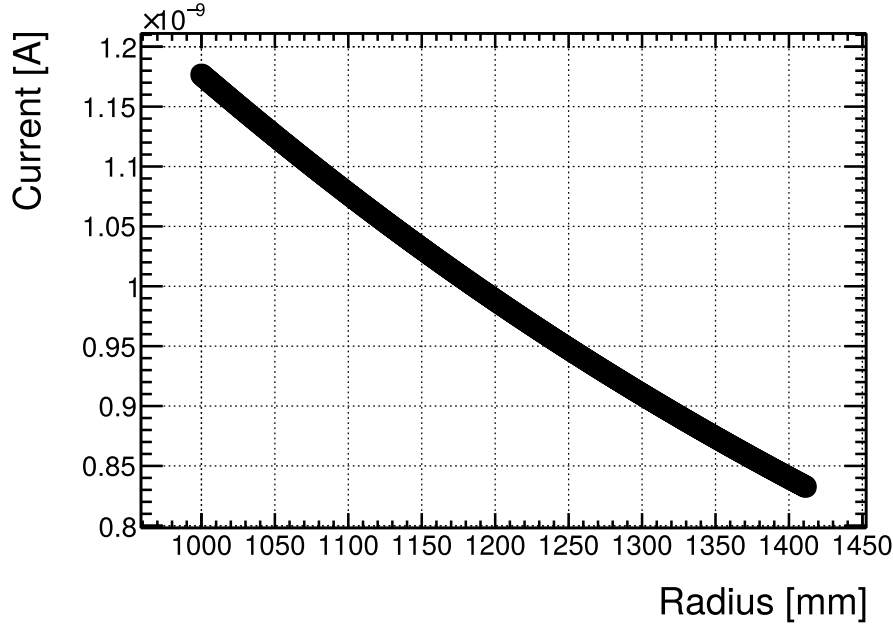


Figure 6.8: Current vs radius for PCB 1.

Data is obtained by multiplying the fit values from figure 6.7 with their actual strip sizes. Following this distribution the innermost strip at radius 1000 mm expects a current of 1.18 nA. For an increase in luminosity by a factor of 3.75 and 200 days of operation per year following equation 6.7 this yields $0.068 \text{ C cm}^{-2}\text{a}^{-1}$ for the innermost strip. The last strip of PCB 1 at radius 1412 mm expects $0.029 \text{ C cm}^{-2}\text{a}^{-1}$.

6.3.3 Accumulated Charges of the Long-Term Irradiated Modules

Given the calibrated values of chapter 6.3.2, the charges accumulated by the two long-term irradiated modules (SM1 M40 and LM2 M40) shall be discussed and compared to HL-LHC equivalents in terms of years of operation.

SM1 M40 has accumulated charges as shown in figure 6.9 with all 40 individual HV sectors depicted. The highest value accumulated surpasses 0.35 C cm^{-2} . The wide spread visible in this picture originates from the inhomogeneous irradiation as the module was positioned closely to the source (see figure 6.3b).

In terms of HL-LHC 0.34 C cm^{-2} are equivalent to 5 years of operation for the innermost strip of PCB 1 at $U_{\text{Amp}} = 520 \text{ V}$. The outermost strip of PCB 1 only receives $0.029 \text{ C cm}^{-2}\text{a}^{-1}$ resulting in more than 10 years of accumulated charges already reached. For the current operation setting at ATLAS of $U_{\text{Amp}} = 505 \text{ V}$ 9 years of operation would correspond to 0.351 C cm^{-2} in accumulated charges for the innermost strip.

Layer 4 sectors have accumulated more charges than comparable sectors in other layers despite being furthest away from the source. This layer drew higher currents from the start of the irradiation period possibly originating from a different amplification gap¹¹. Higher cluster charges are observed compared to the other layers (see figure C.1 in the appendix). Flat periods in the graph correspond to technical shutdowns of the facility or preparation periods for beamtimes in which the module was removed from the facility.

Dedicated performance studies of the SM1 M40 during the long-term irradiation concerning efficiency and resolution are the topic of the upcoming chapter 7.

¹¹Variations of the pillar height, which defines the amplification gap, of up to $10 \mu\text{m}$ have been observed (Herrmann [2019]). He states the gain dependency on the pillar heights d as $G(d) = \exp(a \times d_0 \times e^{-b \times d_0}) + a \times (1 - b \times d_0) \times \exp(-b \times d_0 + a \times d_0 \times e^{-b \times d_0}) \times (d - d_0) + \mathcal{O}((d - d_0)^2)$ with $a = \frac{A \times p}{T}$ and $b = \frac{B \times p}{T \times U}$. A and B are the gas parameters (see chapter 2.2.2), p and T are environmental pressure and temperature respectively, U is the amplification voltage, and $d_0 = 120 \mu\text{m}$ is the nominal pillar height.

LM2 M40 being situated further outside in the NSW and hence experiencing considerably less irradiation, accumulated 40 years of HL–LHC equivalent of 0.048 C cm^{-2} for the innermost strip of the PCB 6 (see figure 6.10).

No high-voltage instabilities or any types of degradations were observed.

No detector will face aging-related problems going into the HL–LHC era using the ternary gas mixture of Ar:CO₂:iC₄H₁₀ 93:5:2 vol%.

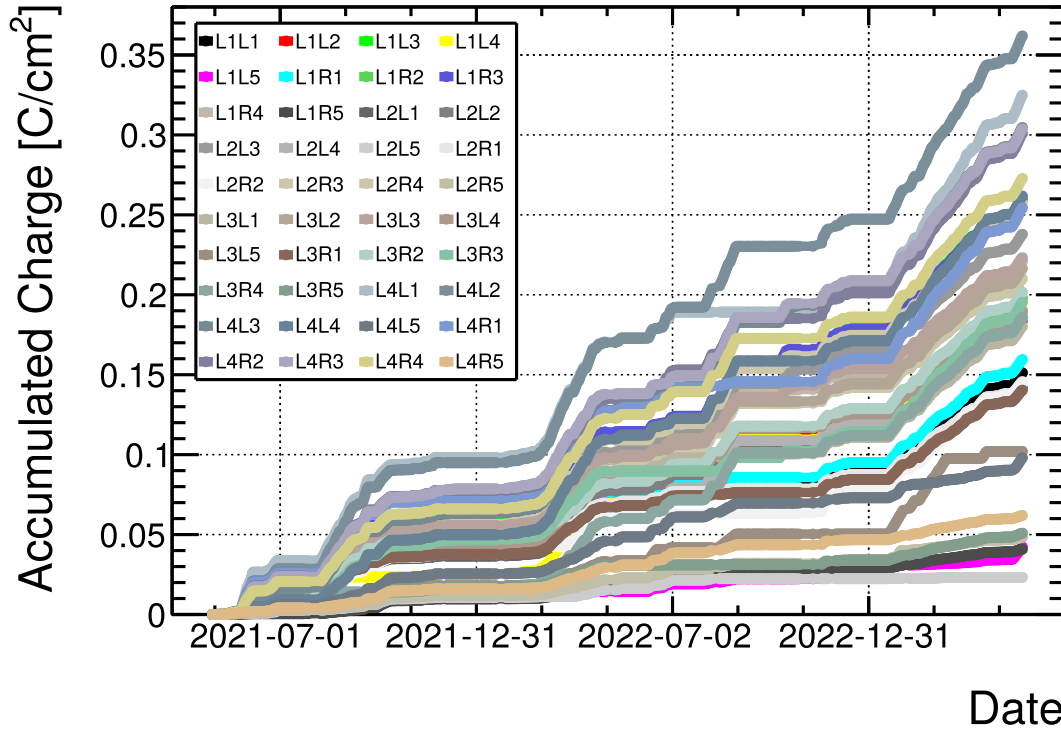


Figure 6.9: Accumulated charge for all 40 HV sectors of SM1 M40 at a distance of 1 m from the source.

The large spread results from inhomogeneous irradiation. With SM1 M40 being very close to the source (position I in figure 6.3b) some sectors are irradiated less than others.

From the start of the irradiation, sectors of layer 4 have shown higher currents than all other three layers. A possible reason is smaller pillar heights resulting in stronger gas amplification due to the higher electric field.

Sector L4 of layer 4 surpassed 5 years of HL–LHC equivalent to the innermost strip of PCB 1 at $U_{\text{Amp}} = 520 \text{ V}$ (0.34 C cm^{-2}) whereas for an operation at $U_{\text{Amp}} = 505 \text{ V}$, the current setting in ATLAS, 9 years of irradiation are reached (0.351 C cm^{-2}).

Flat periods in the graph correspond to technical shutdowns of the facility or preparation periods for beamtimes when the module was removed from the facility.

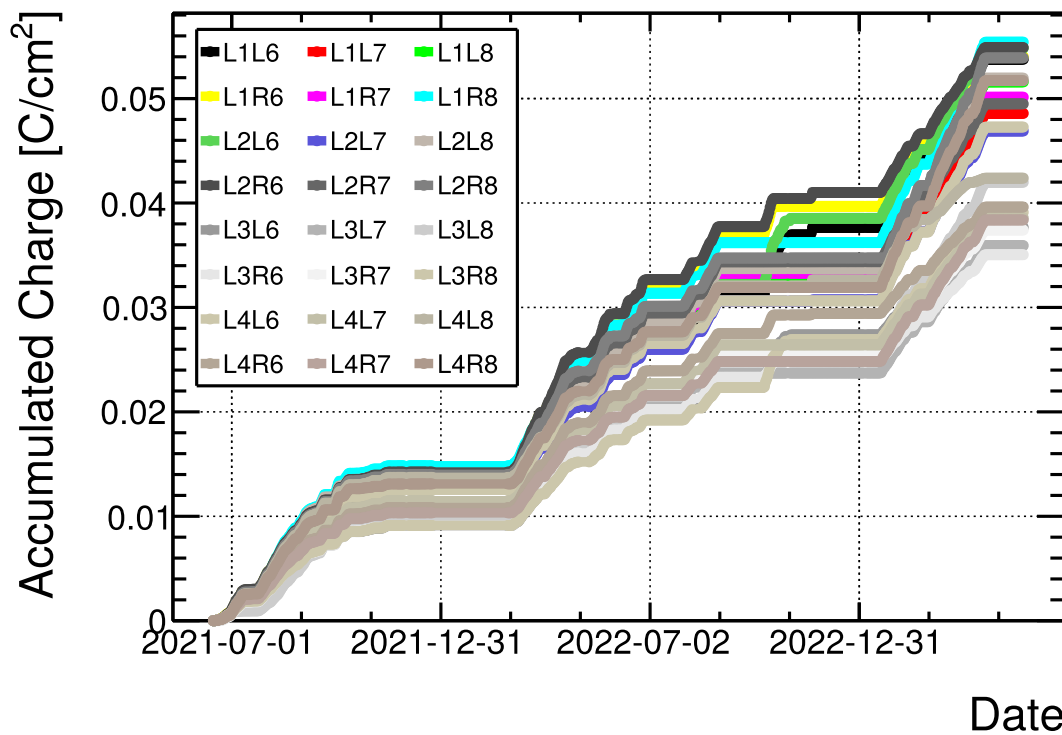


Figure 6.10: Accumulated charge for all 24 HV sectors of LM2 M40 at a distance of 2.8 m from the source.

With LM2 being on the outer part of the NSW the expected irradiation decreases strongly (see figure 6.7). Thus following the calibration for the innermost sector $0.0012 \text{ C cm}^{-2} \text{ a}^{-1}$ are to be expected. Many of the 24 sectors have already accumulated charges equivalent to more than 40 years of HL-LHC operation (0.048 C cm^{-2}).

Flat periods in the graph correspond to technical shutdowns of the facility or preparation periods for beamtimes when the module was removed from the facility.

No degradation due to aging is expected for the outer type 2 quadruplets.

Chapter 7

Performance Studies of a Long-Term Irradiated Module

As described in figure 6.1 the GIF++ is situated at an extraction line of the SPS. Muon beams ranging up to energies of 120 GeV are delivered into the irradiation area¹. Multiple measurement periods have been carried out and will be the topic of this chapter. The central aspect is the resolution and the efficiency of module SM1 M40 during the long-term irradiation.

7.1 Measurement Setups

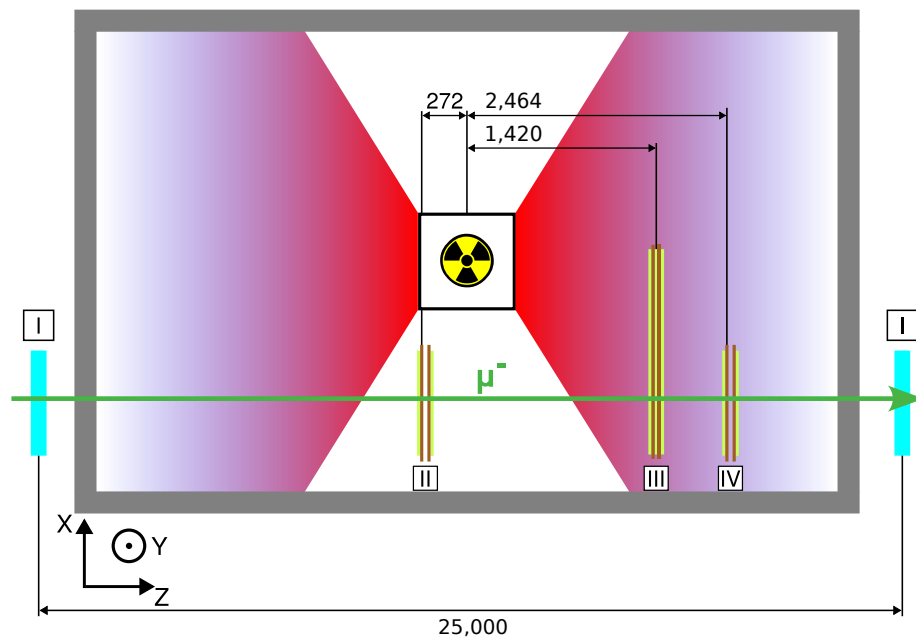


Figure 7.1: Irradiation setup at the GIF++ in the H4 beamline of the SPS. Distances are given in mm and are exemplary for setup 1 listed in table 7.1. Indicated with I are $40 \times 40 \text{ cm}^2$ scintillators providing trigger information. At positions II and IV tracking chambers are positioned to provide tracking information of muons traversing the setup. The reference chambers at II sit in the shadow of the source and experience a strongly reduced gamma background. Lastly, positioned at III is the SM1 M40 module under test. Indicated with the radiation hazard symbol is the ^{137}Cs gamma source.

¹Information provided by the facility operators.

The muon tracking setup is sketched in figure 7.1 in a top-down perspective and is similar for all measurement periods.

$40 \times 40 \text{ cm}^2$ GIF++ scintillators (pale blue, I) are used in coincidence as triggers. The scintillators are outside of the facility and experience no gamma irradiation from the source. Reference detectors providing track information are situated at positions II and IV. Detectors next to the source (II) experience no direct irradiation from the source and are only affected by backscattered photons. These detectors are utilized to provide clear position information as the starting point for track building and alignment (see chapter 5.3.2). Information in precision direction and parallel to the strips is provided by these detectors.

The SM1 M40 under investigation is placed at position III.

7.1.1 Setup 1

For the first test measurement the SM1 M40 was placed at a distance of 1420 mm from the source (see 7.1). There it faces photon rates equivalent to $1.56 \times \text{HL-LHC}$ hit rate (see chapter 6.3.1). For all setups described the Eta_{Out} layer was facing the source.

For reference tracking three 1D, $40 \times 40 \text{ cm}^2$ beamline (BL) Micromegas chambers were used. These are one-dimensional Micromegas detectors. The X and Y in 7.1 denote their precision direction. The X and one Y chamber were placed at position II for a clear tagging of the muon with a strongly reduced background. A second Y chamber is situated at position IV. The reference track for performance tests is built from the two Y chambers. Alignment of the SM1 M40 (see chapter 5.3.2) utilizes the information in X from the BLX chamber.

For readout VMM front-end electronics (see chapter 4.3.1) is used for both, the SM1 M40 and the BL chambers. The trigger is provided by the fast coincidence of the two scintillators (I). In this setup, the module was tested under perpendicular muon incident and a fixed angle of 29° .

The muon beam passes the detector through PCB 3. To mimic the active area of a PCB 1, which faces the harshest radiation at ATLAS (see chapter 6.3), only one half of the PCB 3 is under high-voltage (see figure 6.3). With this, the hit rate a readout strip experiences is reduced by a factor of 2 compared to the full PCB under high-voltage².

7.1.2 Setup 2

In the second measurement setup the AVP25/SRS DAQ was used (see chapter 4.2). The goal of this setup was to investigate the high-rate environment and its influence on the readout electronics. Therefore the analog output of the APV25 was chosen³.

Detector under investigation was SM1 M40 at position III at a distance of 2030 mm from the source⁴. An equivalence of $0.76 \times \text{HL-LHC}$ is expected as photon rate at this distance.

As reference detectors two 2D, $10 \times 10 \text{ cm}^2$ Micromegas detectors (TMM) were used. One was positioned at location II. The second one and a 1D $10 \times 10 \text{ cm}^2$ were placed at position IV.

An additional $9 \times 9 \text{ cm}^2$ scintillator was mounted in front of the reference detector at position II to form a triple coincidence with the two GIF++ scintillators (I).

²Only the high-voltage supply is divided in the center of the PCB. The readout strip ranges over the full width of the PCB.

³The VMM offers only an analog monitoring output not suitable for data-taking.

⁴As mentioned in chapter 6, the facility is occupied by multiple setups and the experimental positions during testbeams were under high demand. Therefore the SM1 M40 was positioned at different distances over the different beamtime periods. Also additional material in the form of other detector setups was introduced between the source and the SM1 M40 altering the gamma spectrum.

7.1.3 Setup 3

Setup 3 was dedicated to optimize the performance of the VMM under high background rates and to investigate the performance of the detector after further irradiation. This was the latest beamtime, performed in July 2023, with charges accumulated as shown in figure 6.9⁵.

SM1 M40 was the detector under investigation at position III at a distance of 1820 mm. In this setup the full PCB 3 was powered. With this the hit rate per strip is doubled, resulting in an equivalent of 1.90×HL-LHC.

The remainder of the setup, concerning electronics, trigger and reference detectors is identical to setup 1 (see chapter 7.1.1).

An additional BLY chamber was introduced at position IV. The reference track is built from the three BLY chambers (1 at position II, 2 at position IV). The BLX at position II was kept for alignment.

Setup No.	Readout	Tracker	Trigger	d_{Source}	HL-LHC eq.
1	MMFE8/VMM	1 BLX + 2BLY	GIF++	1420	1.56
2	SRS/APV25	2 TMM + TZ	Triple	2030	0.76
3	MMFE8/VMM	1 BLX + 3 BLY	GIF++	1820	0.95 ⁶

Table 7.1: Overview of the different measurement setups in the GIF++. The HL-LHC equivalent is based on an attenuation factor of 1 for the given setups as determined in chapter 6.3.1 for the innermost strip of the PCB 1.

7.2 GIF++ Beamtime Using NSW VMMS

Starting with setup number 1 this section of the chapter is dedicated to giving an overview of the overall performance of the module after having acquired approximately 0.2 C cm^{-2} for some sectors (October 2022 in figure 6.9). The detector performance under different levels of background is also evaluated.

7.2.1 Event Selection

Additionally to the condition for the cluster building (see chapter 5.2), necessary cuts for the track building will be discussed in the following. Figures 7.2a and 7.2b show cutflows for the two scenarios of no background irradiation and full source intensity respectively. The first column gives information on the total number of triggers.

Initially, a cut is done on requiring exactly one cluster in the reference trackers at position II of figure 7.1. In both cases, the statistical sample after this cut is sufficient for a relevant analysis. For both diagrams in figure 7.2 this is the major event selection cut. Measurements including the source discard more events due to additional clusters induced by backscattered photons.

⁵The figure only shows the values up to June 2023. The detector was removed then to be prepared for the beamtime. This includes the equipping of the readout electronics and the mounting of the detector on a dedicated holding structure. No further charge was accumulated until the start of the testbeam measurement.

⁶This value holds for measurements with only one side of the PCB under HV. Measurements taken in this setup have both sides of the PCB under HV. Strips ranging over both sides are exposed to twice the photon current. The HL-LHC equivalent value has to be doubled for this case.

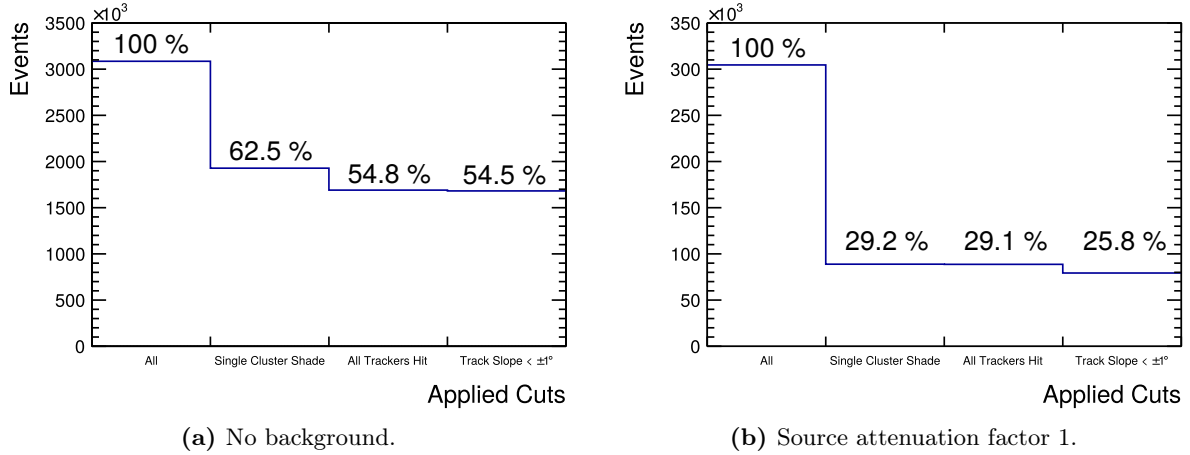


Figure 7.2: Cutflow histograms for two different background irradiation levels.

The first column represents the number of measured events. From left to right the cuts are: "Single Cluster Shade", being a cut requiring exactly one cluster in the two reference trackers in the shadow of the irradiation (see figure 7.1). Despite this being the major cut for both diagrams, the analysis sample is still sufficiently large in statistics. It is necessary to tag the muon in precision direction and apply misalignment corrections using the information of BLX along the SM1 readout strips. The cut is harsher for attenuation 1 measurements with backscattered photons creating additional signals in these detectors.

Cut on the "All Trackers Hit" refers to a cut on the trackers, not in the shadow. It is required to have at least a single cluster in both detectors. Multiple clusters are allowed.

The last cut is on the track slope, discarding particle tracks exceeding the geometrically allowed limit of $\pm 1^\circ$. No cuts on the tested detectors are performed besides those discussed in the cluster building in chapter 5.2.

$$U_{\text{Amp}} = 520 \text{ V}, p_t = 200 \text{ ns}, \text{VMM}_{\text{RMS}} = 9\sigma.$$

Secondly, a cut requiring at least a single cluster in the reference trackers at position IV is applied. Multiple clusters are allowed in these chambers. As expected almost no events are cut for the measurements with source due to the photon clusters. This may result in a wrong track reconstruction.

Therefore a last cut on the track slope is performed. The trigger scintillators⁷ define this to $\pm 1^\circ$. For very clear signals without background, this cut results in close to no events being discarded (see figure 7.2a). The influence on the measurement with the source included is more pronounced. Overall more than 50% of the triggers are used for measurements with no background, and approximately one quarter of the events are used in runs with the highest photon flux.

All cuts only concern the tracking detectors. No cuts in the event selection were performed based on SM1 M40.

7.2.2 Results for Perpendicular Particle Incident

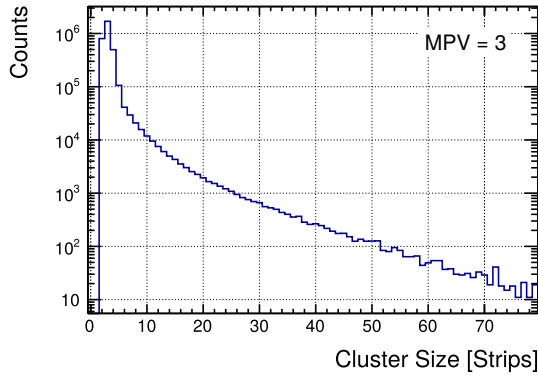
As discussed in chapter 5.2 the muon signal spreads over multiple strips. The Most Probable Value (MPV) of the reconstructed cluster size is three strips for perpendicular tracks (see figure 7.3a) with a very long tail to huge cluster sizes above 70 strips. Those large clusters are very rare and result from readout electronics effects.

Values shown correspond to $U_{\text{Amp}} = 520 \text{ V}$, $p_t = 200 \text{ ns}$, $\text{VMM}_{\text{RMS}} = 9\sigma$ and refer to readout layer Eta_{Out} ⁸. The cluster charge distribution shown in figure 7.3b is as expected for minimum

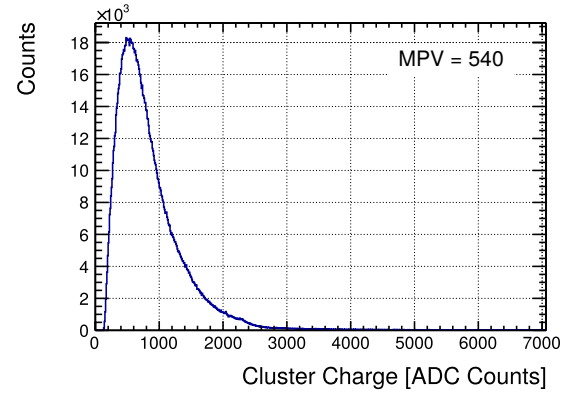
⁷For the $40 \times 40 \text{ cm}^2$ GIF++ scintillators at a distance of 25 m follows geometrically for the allowed track angle $\Theta_{\text{track}} = \tan^{-1}\left(\frac{0.4}{25}\right) = 0.92^\circ$.

⁸Reminder: p_t is the set peaking time of the VMM shaper and VMM_{RMS} is a signal threshold given in multiples of the baseline fluctuation level of the VMM (see chapter 4.4).

ionizing particles following a landau shape with an MPV of 540 ADC Counts. Deviations result from the high energy muons of up to 120 GeV not being situated in the minimum of the mass stopping power (see figure 2.1).



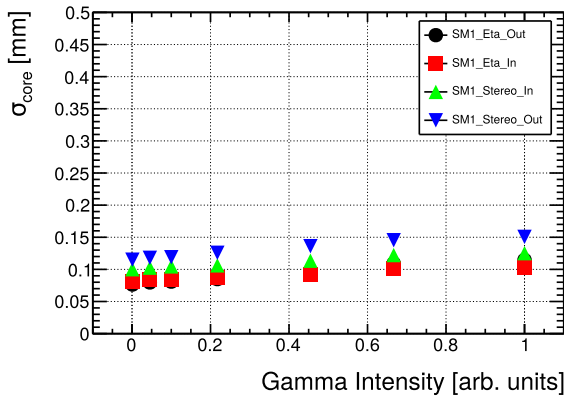
(a) Exemplary reconstructed cluster size for the perpendicular incident of muons without photon background in logarithmic scale. The most probable value is three strips. The long tail towards very large clusters can be explained by read-out electronics effects.



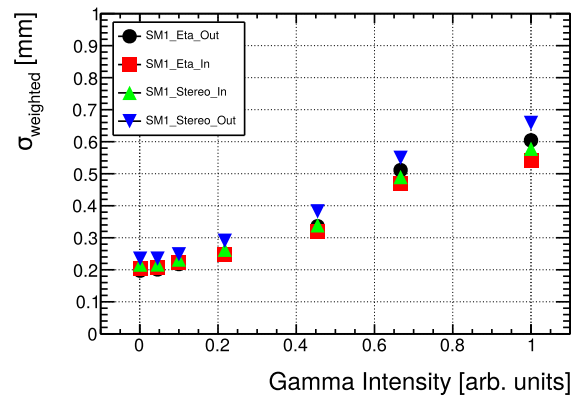
(b) Exemplary pulse height distribution of reconstructed clusters peaking at 540 ADC Counts. The distribution follows roughly a landau shape expected for minimum ionizing particles.

Figure 7.3: Cluster parameters for muon measurements without background.

$U_{\text{Amp}} = 520 \text{ V}$, $p_t = 200 \text{ ns}$, $VMM_{\text{RMS}} = 9\sigma$, Eta_{Out} .



(a) Core residuals.



(b) Weighted residuals.

Figure 7.4: Charge-weighted residuals for different gamma intensities⁹.

Core resolutions of $\sigma_{\text{core}} < 80 \mu\text{m}$ are achieved in both Eta layers becoming only slightly worse for high background activities with $\sigma_{\text{core}} \approx 100 \mu\text{m}$. The weighted residual becomes worse as expected taking into account the larger tails originating from the photons. Stereo_{Out} shows a slightly worse performance than the other three layers.

$U_{\text{Amp}} = 520 \text{ V}$, $p_t = 200 \text{ ns}$, $VMM_{\text{RMS}} = 9\sigma$.

Figure 7.4 depicts the resolution determined following the methods described in chapter 5.3 against the gamma intensity provided by the source. A gamma intensity of 0.65 represents an HL-LHC equivalent hit rate. Spatial resolutions of $\sigma_{\text{core}} < 80 \mu\text{m}$ are achieved. The values worsen to around $100 \mu\text{m}$ for HL-LHC equivalent background rates and above. Stereo_{Out} performs worse in resolution compared to the other three layers, possibly resulting from the saturation of strips due to the higher gain observed in this layer (see figure C.1). The increased gamma intensity is more pronounced in the σ_{weighted} distribution resulting in a decrease from

⁹The errors of the displayed data points are smaller than the marker size. This also holds for figures 7.6, 7.7, 7.8, 7.12, 7.13, 7.15, 7.16, 7.17, 7.18, 7.19 and 7.20.

$\approx 200\ \mu\text{m}$ to $\approx 600\ \mu\text{m}$ for no and maximum background respectively. Photons influence the cluster position if signals are induced close to the muon cluster increasing the number of consecutive strips hit. This issue is sketched in figure 7.5.

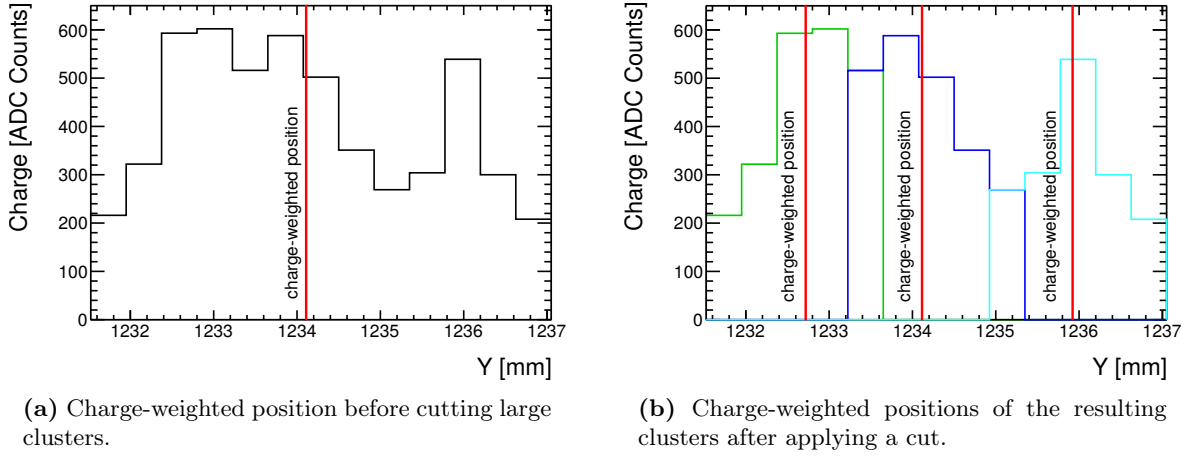


Figure 7.5: For higher background rates photon clusters overlap with the muon signal worsening the charge-weighted centroid position reconstruction.

Cutting large clusters (>5 strips) into multiple smaller clusters and reevaluating their properties leads to slightly improved residuals (see figure 7.6b). The cut is performed by searching for strip charge minima since a Gaussian-like charge spread is expected. As shown in figure 7.3a cluster sizes around three strips are expected for muons. This cut is only applied for perpendicular tracks.

Figure 7.5a shows the reconstructed cluster position with full intensity gamma background applying the centroid method (see chapter 5.2). In total 13 strips are combined into a single cluster. As a result from figure 7.3a around three strips are expected per muon cluster, hinting at an artificial enhancement of the cluster caused by photons. Still visible in figure 7.5a is the Gaussian-like charge spread in a cluster. Such large clusters of size > 5 strips are tested by a simple algorithm checking for minima in the charge versus position distributions and applying a positional cut at such points. The result of applying this algorithm to the distribution in figure 7.5a is shown in figure 7.5b with the corresponding new cluster positions again determined using the centroid method. With this method, noisy strips with large signals at the edges of a cluster can also be cut. One major problem resulting from the implementation is the wrong handling of missing strips always cutting the clusters at these positions.

The effect of implementing this cluster cutting into the analysis is shown in figure 7.6 containing the same raw data as used for figure 7.4. The core residuals show no difference between the two analyses, as expected. For the very strong backgrounds towards gamma intensities of 1, no real improvement is observed. Seemingly such high intensities deteriorate the charge position relation for cluster building not solvable by cutting the cluster into smaller pieces. The positive and negative effects on the position reconstruction even out for high enough statistics. For low gamma intensities a small improvement of $\mathcal{O}(20\ \mu\text{m})$ is visible with the prior weighted resolution of $\approx 200\ \mu\text{m}$ in figure 7.4b being improved to $\approx 180\ \mu\text{m}$ in figure 7.6b. Here the cut removes strips with larger signals at the edges of a cluster, that may originate from noisy strips.

As a result, this cut is included in the analysis for all subsequent measurements discussed in this chapter. This cut is only applicable for perpendicular tracks where the charge distribution is assumed to be Gaussian-shaped. For inclined tracks with inhomogeneous ionization, this is not granted (see chapter 5.4).

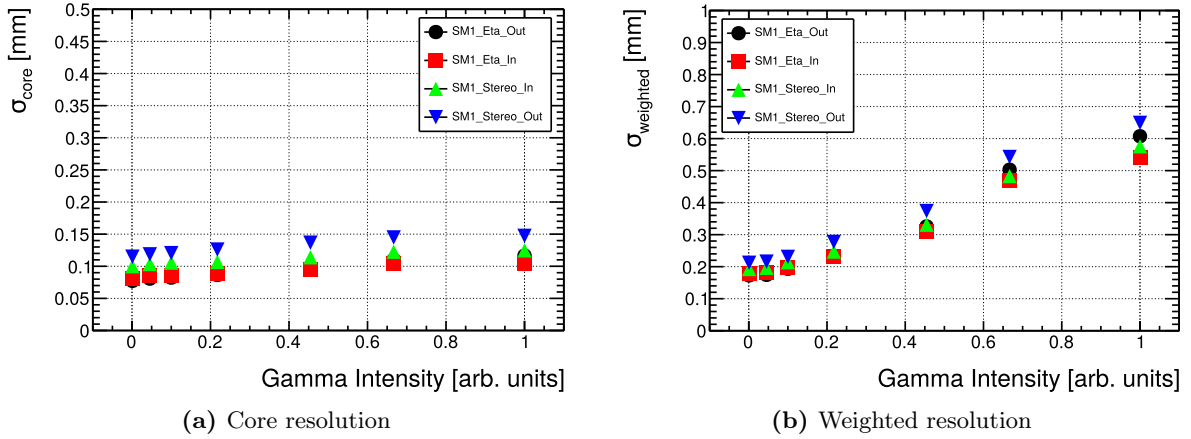


Figure 7.6: Resolutions after cutting large clusters into smaller ones.

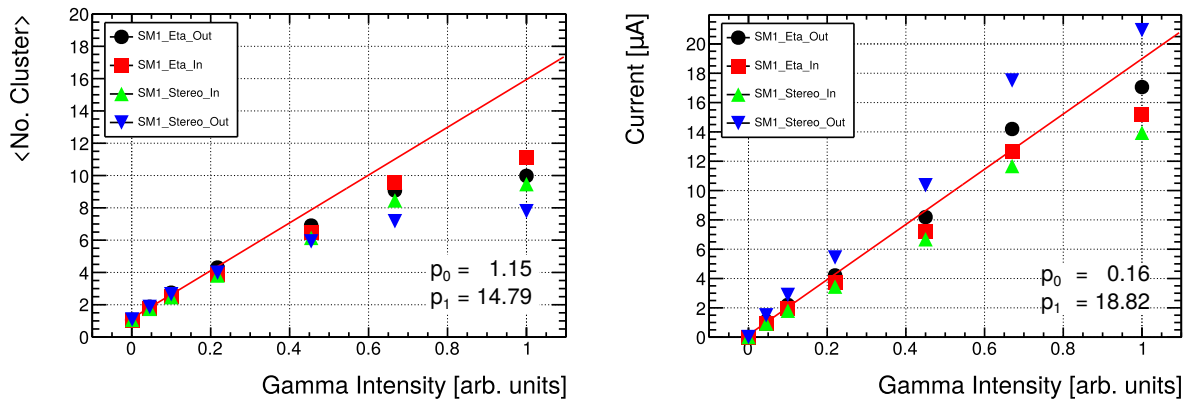
No difference in resolution for the σ_{core} is observed. The desired effect of improvement at high background rates does not occur. Although at low background an improvement of $\mathcal{O}(20\mu\text{m})$ for the weighted residuals is visible, dropping below $200\mu\text{m}$ in resolution. The cut is applied for all subsequent measurements including perpendicular particle incident.

$U_{\text{Amp}} = 520\text{ V}$, $p_t = 200\text{ ns}$, $\text{VMM}_{\text{RMS}} = 9\sigma$.

Another reason for the worse performance at high levels of background is demonstrated in figure 7.7. The current drawn by the detector is proportional to the number of particles creating primary electron-ion pairs. Since the photon flux scales exponentially, a linear correlation between the current and the photon flux, given in units of attenuation, is expected.

This is visible in figure 7.7b. Intensities up to 0.22 for Eta_{Out} are included in the fit followed by an extrapolation to the highest values. At an intensity of 1 only a small saturation is visible. This saturation is also visible for measurements at a larger distance from the source at considerably lower numbers of photons for the same attenuation factor (see figure C.2 in the appendix for measurements at a distance of 1.8 m from the source). Concluding from this the stronger differences observed at intensities 0.67 and 1 can be attributed to non-perfect attenuation filters.

This linear increase is also expected for the number of reconstructed clusters, yet an early saturation starting at gamma intensity values of > 0.4 is observed as depicted in figure 7.7a. From the linear current behavior, it is clear the detector itself is capable of detecting and amplifying such high particle fluxes. The saturation in reconstructed clusters at higher backgrounds directly translates into the worse resolution but also in a decrease of detector efficiency, which is shown in figure 7.8. For low background intensities, 90% single layer efficiency is achieved, yet at higher values, the efficiency decreases to $< 40\%$ for some layers. This drop in efficiency or possible signal loss is investigated in detail using the APV25 hybrids in chapter 7.3.



(a) Mean number of clusters vs. the gamma intensity.

(b) Current drawn by the detector vs. the gamma intensity. Intensity 0.67 shows higher currents for all layers than expected.

Figure 7.7: The mean number of reconstructed clusters shows a saturation effect starting at a source intensity of 0.44.

The cluster cutting discussed previously is applied. The measured current shows almost no saturation effect hinting at saturation effects in the readout electronics or problems in the cluster reconstruction at high rates.

For gamma intensities above 0.6, the current values differ from the fit. This is observed independent of the distance from the source (see figure C.2 in appendix C). Non-perfect attenuation filters controlling the gamma intensity explain this behavior. The linear fit is performed on the first four data points up to an intensity of 0.22 for Eta_{Out} .

$$U_{\text{Amp}} = 520 \text{ V}, p_t = 200 \text{ ns}, \text{VMM}_{\text{RMS}} = 9\sigma.$$

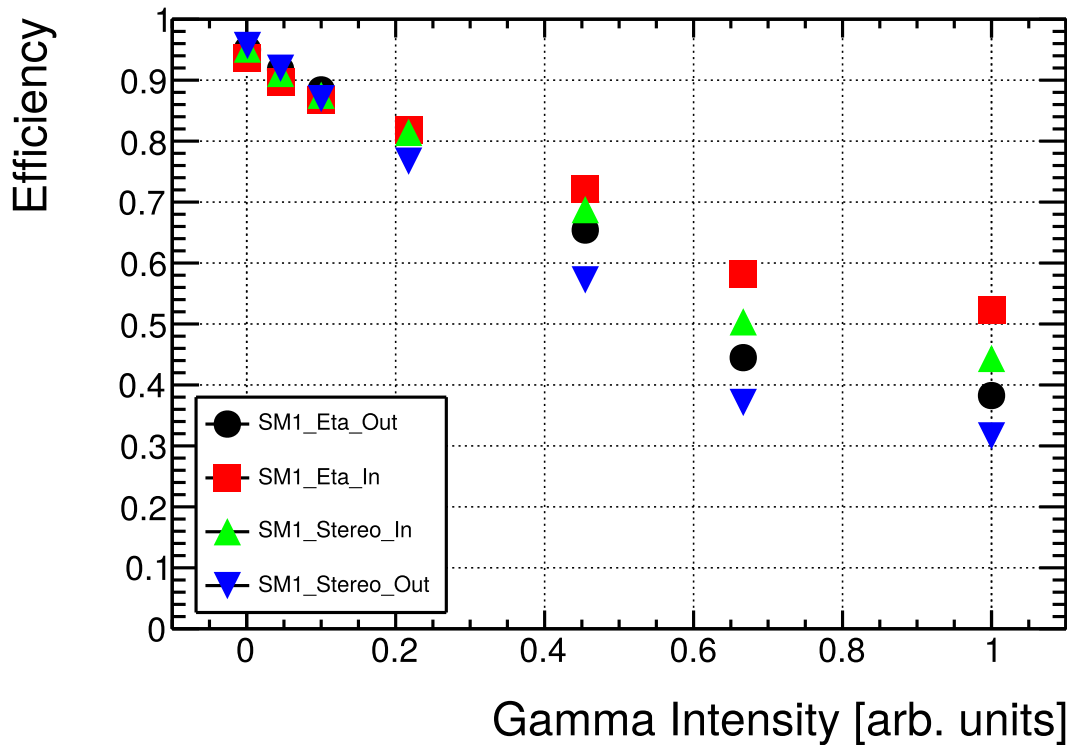


Figure 7.8: Reconstructed ± 2 mm efficiencies for the four detector layers of SM1 M40 vs. the gamma intensity.

A drop for increasing background is visible. This is expected due to the loss in reconstructed clusters.

$$U_{\text{Amp}} = 520 \text{ V}, p_t = 200 \text{ ns}, \text{VMM}_{\text{RMS}} = 9\sigma.$$

7.2.3 Results for 29° of Particle Incident

All setups used in the beamtimes offered the possibility to rotate SM1 M40 around the x-axis as defined in figure 7.1. An angle of inclination of 29° was set for the module and thus for the muon track, while keeping the reference trackers perpendicular to the muon beam. This was done to investigate the detector resolution for inclined tracks. Integrated into the ATLAS experiment detectors expect particle trajectories between (7 – 30.5)° for the innermost part of PCB 1 to the outermost part of PCB 8 respectively.

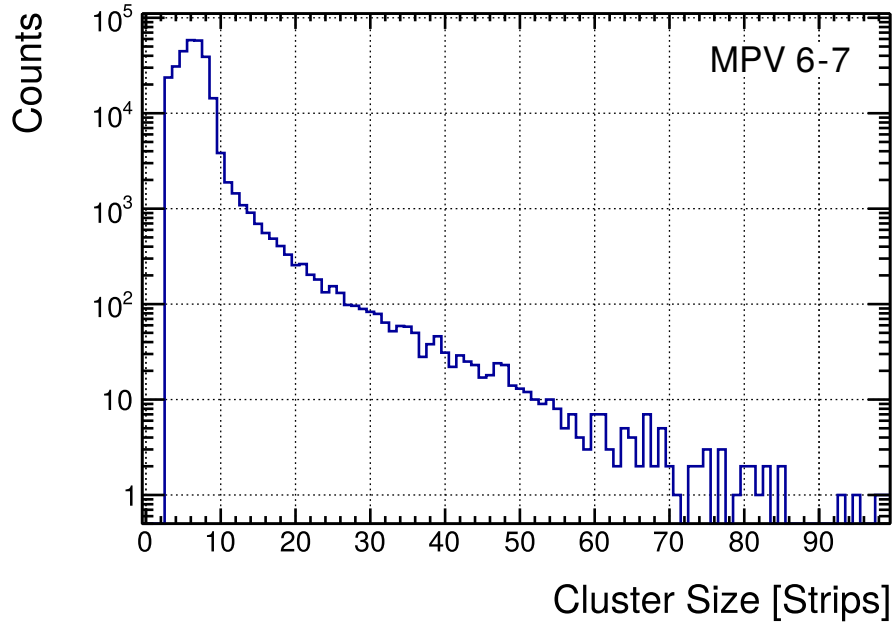


Figure 7.9: Reconstructed charge-weighted cluster size for 29° of track inclination. The most probable values of the distribution are 6-7 strips. For the 29° of inclination 6.52 strips are expected (see equation 7.1).
 $U_{\text{Amp}} = 520 \text{ V}$, $p_t = 200 \text{ ns}$, $VMM_{\text{RMS}} = 9\sigma$.

For a track inclination of $\Theta = 29^\circ$, a drift gap of $Z_{\text{Drift}} = 5 \text{ mm}$, and a strip pitch $p = 0.425 \text{ mm}$, the number of expected strips forming a cluster can be calculated as

$$N_{\text{Strips}} = \tan(\Theta) \times \frac{Z_{\text{Drift}}}{p} = \tan(29^\circ) \times \frac{5 \text{ mm}}{0.425 \text{ mm}} = 6.52 \quad (7.1)$$

The actual reconstructed cluster size is shown in figure 7.9 reproducing the expected value with an MPV of 6-7 strips.

Timing Resolution

An estimate of the timing resolution of the detector is determined using inclined tracks. Assuming the particles pass the detector at the speed of light the difference between the first signals detected as depicted in figure 7.10 gives information on the time resolution. Signals created at the mesh have no drift time and given equal electric fields in the amplification region these signals should arrive at the same time. The resulting time difference distribution is shown in figure 7.11. To determine the time resolution the distribution is fit with a Gaussian function. The obtained width $\sigma_{\text{gauss}} = 22.94 \text{ ns}$ needs to be divided by $\sqrt{2}$ due to the independent measurements resulting in a time resolution of $\sigma_t = 16.22 \text{ ns}$. This timing resolution was determined for $U_{\text{Amp}} = 530 \text{ V}$ and $p_t = 100 \text{ ns}$ producing the best results.

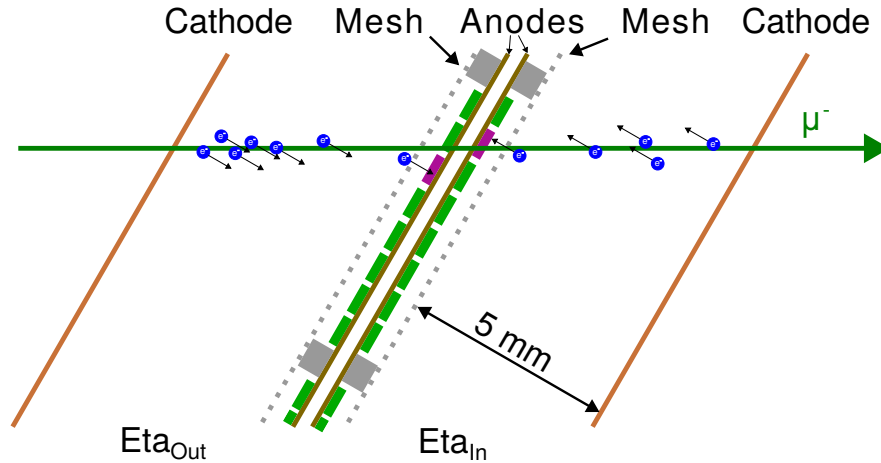


Figure 7.10: Sketch of the ionization process happening for an inclined muon incident in two of the four detector layers of SM1.

The electrons drift parallel to the electrodes inducing signals on multiple strips. Since the muon is traversing the detector close to the speed of light, the ionization happens well within 3 ns along the track. Electrons created very closely to the mesh have next to no drift time. For ionization exactly at the mesh and perfect readout electronics the time difference of the first responding strips of the two layers should be 0 ns. The actual measured difference is a measure of the time resolution of the system.

Sketch is not to scale.

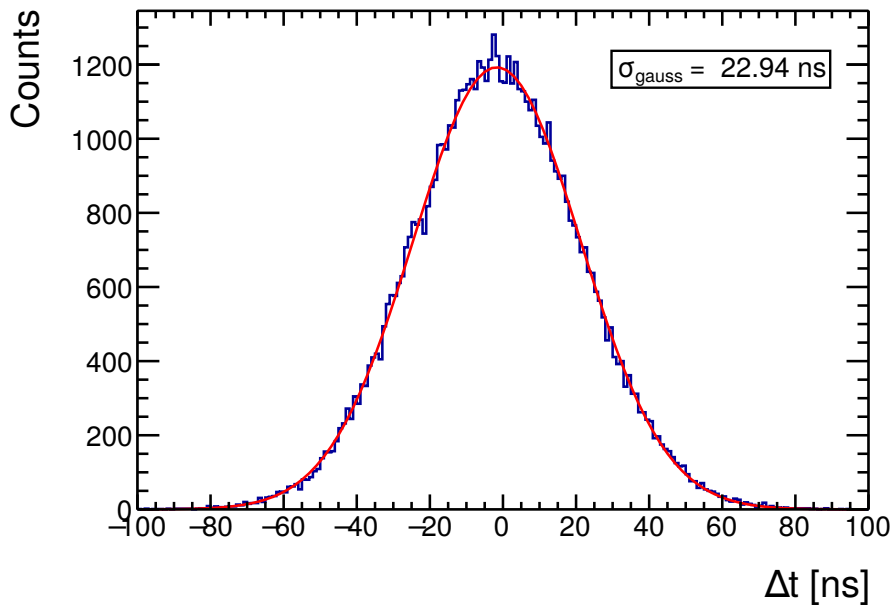


Figure 7.11: The difference between the fastest strip of the two Eta layers of SM1 for 29° inclined particle tracks is a measure for the time resolution of the detector and readout electronics.

The actual time resolution is obtained by fitting the Gaussian distribution and dividing the σ_{gauss} by $\sqrt{2}$ resulting in 16.22 ns time resolution.

$U_{\text{Amp}} = 530$ V, $p_t = 100$ ns, $VMM_{\text{RMS}} = 9\sigma$.

Spatial Resolution

For the spatial resolution of inclined particle tracks the μ TPC-like and the time correction of the centroid position as described in 5.4 are used. Core resolutions of both methods for all four layers of the detector dependent on the gamma intensity are compared in figure 7.12 with the μ TPC-like method depicted on the left and the time-corrected centroid method on the right.

As expected a worsening of the resolution with increasing background intensity is observed. With the μ TPC-like reconstruction method resolutions $\sigma_{\text{core}} < 200 \mu\text{m}$ are achieved whereas the second method shows results of $\sigma_{\text{core}} < 150 \mu\text{m}$ for Eta_{Out} . An increase in the gain is expected to be necessary to improve the results. Since the charge created by the muon is spread across more strips, smaller charges may be cut in the clustering process, although providing meaningful μ TPC information. In addition a reduction of the peaking time p_t to 100 ns is applied showing the best timing resolution. For this peaking time and $U_{\text{Amp}} = 530 \text{ V}$ the results are shown in figure 7.13. The resolution is improved for both methods by $\approx 30 - 40 \mu\text{m}$ compared to the longer peaking time of 200 ns. With the μ TPC-like reconstruction method $150 \mu\text{m}$ in core resolution is achieved. Here best resolutions are obtained using the time correction of the centroid position for the Eta_{Out} layer with $\sigma_{\text{core}} = 126 \mu\text{m}$. At the highest gamma irradiation intensities a $\sigma_{\text{core}} \approx 150 \mu\text{m}$ is reconstructed using this method.

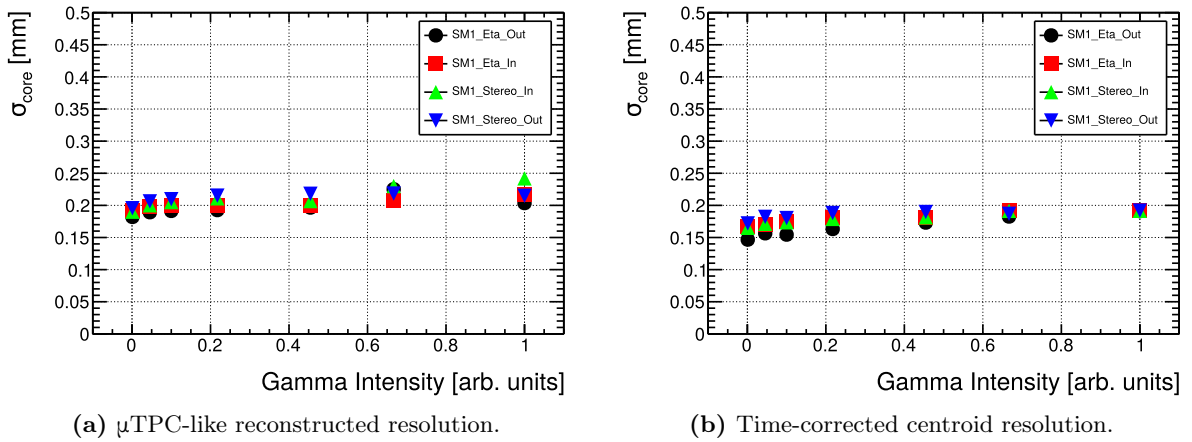


Figure 7.12: Comparison of the core resolutions for the two methods developed for inclined tracks for different source intensities.

μ TPC-like position reconstruction shows resolutions $< 200 \mu\text{m}$ for all layers at no background, worsening to $210 - 240 \mu\text{m}$ for attenuation factor 1. Best spatial resolutions are obtained using the time-corrected centroid position with $\sigma_{\text{core}} \approx 150 \mu\text{m}$ and $\sigma_{\text{core}} \approx 190 \mu\text{m}$ for no background and attenuation 1 respectively.

$U_{\text{Amp}} = 520 \text{ V}$, $p_t = 200 \text{ ns}$, $\text{VMM}_{\text{RMS}} = 9\sigma$.

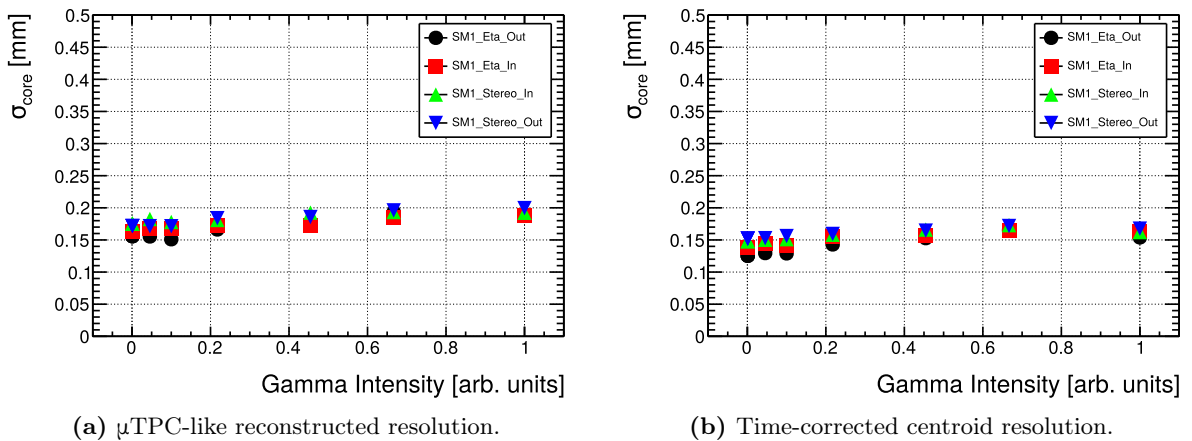


Figure 7.13: Comparison of the core resolutions for the two methods developed for inclined tracks for different source intensities at a shorter peaking time of $p_t = 100 \text{ ns}$ and higher $U_{\text{Amp}} = 530 \text{ V}$.

Additional resolution improvements are reached by reducing the peaking time of $p_t = 200 \text{ ns}$ (figure 7.12) and increasing the amplification voltage. Both methods improve by $30 - 40 \mu\text{m}$.

$U_{\text{Amp}} = 530 \text{ V}$, $p_t = 100 \text{ ns}$, $\text{VMM}_{\text{RMS}} = 9\sigma$.

7.3 Investigations of the High-Background Issues Using APV25 Hybrids

The decrease in performance of the detector system for high background rates is investigated in detail in this chapter. For this, the APV25 hybrids of the SRS system were chosen. The advantage over the VMM readout is the data output with the charge information being sampled in 24×25 ns bins (see figure 4.3) instead of being directly integrated on the chip providing charge peak information only. This allows for a precise analysis of the signal shape at high rates. The measurement setup is number 2 in table 7.1. Attenuation factor 1 of the source equals here to $0.76 \times \text{HL-LHC}$ in hit rate.

Figure 7.14 shows two exemplary situations happening at this gamma intensity at an $U_{\text{Amp}} = 520$ V. The system and the trigger are set up such that the muon signal should arrive at bins 6 – 10. As shown in figure 7.14a the muon signal is observed at the expected time. A second signal starting at 14×25 ns is detected. This signal originates from a photon creating a signal on the same readout strip within the readout window. Such a case is separable using the APVs. Since the VMM integrates the charges up to the first maximum correct values for the charge and timing will be obtained in this case as well.

However, the readout is going to fail in situations similar to figure 7.14b. The muon signal is hidden inside the large photon signal. The timestamp of such an early signal will not match the expected trigger timestamp and the signal is discarded. Only two cases are shown here with many more possible as the photon signal is arriving uncorrelated in time. To acquire the correct charge and timing information the readout electronics need to discharge and recover their baseline level. If a constant photon or particle flux (in the case of ATLAS) induces signals uncorrelated to the trigger, strips may be masked due to signals being in the period of baseline recovery. Muon signals are lost or altered in time and charge information resulting in decreased efficiency and resolution as observed in section 7.2 of this chapter. The VMM offers a faster baseline recovery by increasing the bias current enabled by the *slh* register (see figure B.1 in the appendix B).

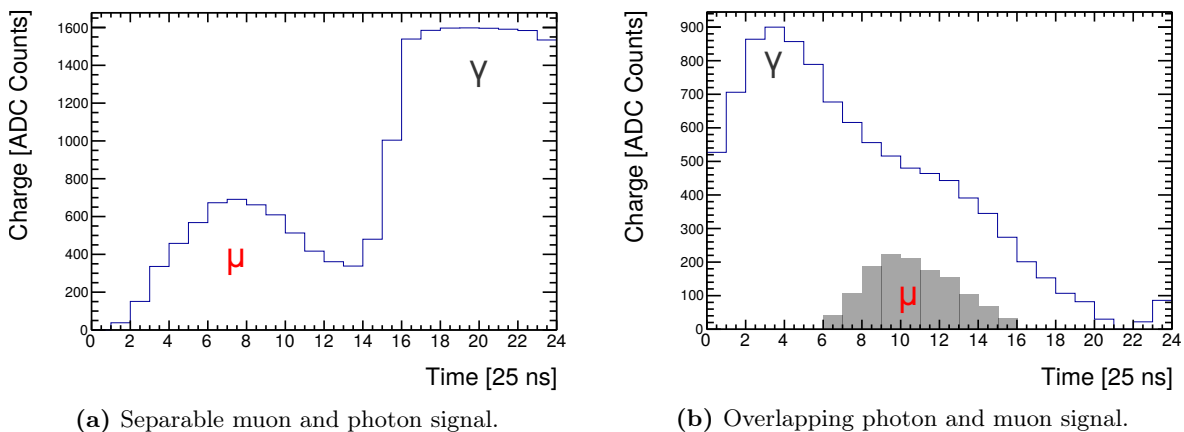


Figure 7.14: Analog signal output of a single readout strip measurement performed with APV25 hybrids at attenuation 1 and $U_{\text{Amp}} = 520$ V. The X-axis is given in bins of 25 ns.

Photon signals overlap with muon signals. The muon signal is to be expected at bins 6 – 10. For the left case, the photon signal arrives at a later stage leading to no issue for the signal selection. The peakfinder of the VMM should be able to correctly identify this signal searching for the first peak after threshold (see figure 4.7).

The photon signal on the right fully overlaps with the muon signal (grey) preventing a correct reconstruction. The muon signal drawn is just an estimate of the actual muon signal. In this case, the VMM identifies the photon signal wrongly as the muon signal being the first peak after the threshold. The photon signal is not correlated in time with the trigger and it can appear anywhere in the shown time window.

7.4 Detector Performance with Increased Bias Current for the VMMS

First tests utilizing this increased bias current have been performed without a muon beam using an accidental trigger. Investigations concerning the cluster number saturation as shown in figure 7.7 were carried out by Kolitsi et al. [2023]. A recovery in the number of detected clusters was shown, with a smaller remaining saturation at very high gamma intensities. This increase in performance is investigated in this chapter using setup 3 of table 7.1 comparing obtainable spatial resolutions and efficiencies with this VMM register disabled ($slh = 0$) and enabled ($slh = 1$). Measurements were taken with the full PCB under high-voltage, resulting in an increase of the area by a factor of two and a $1.9 \times \text{HL-LHC}$ equivalent background rate at attenuation factor 1 (maximum gamma intensity).

The mean number of reconstructed clusters for the different gamma intensities is shown in figure 7.15. With the slh register disabled (left), the expected saturation is visible. By enabling the higher bias current more clusters are reconstructed (right). The effect is most pronounced for Eta_{Out} and $\text{Stereo}_{\text{Out}}$. A remaining saturation is still observed at the highest values of gamma intensity at $1.9 \times \text{HL-LHC}$ equivalent background rate. The predicted increased number of reconstructed clusters by Kolitsi et al. [2023] is also visible using a muon beam setup.

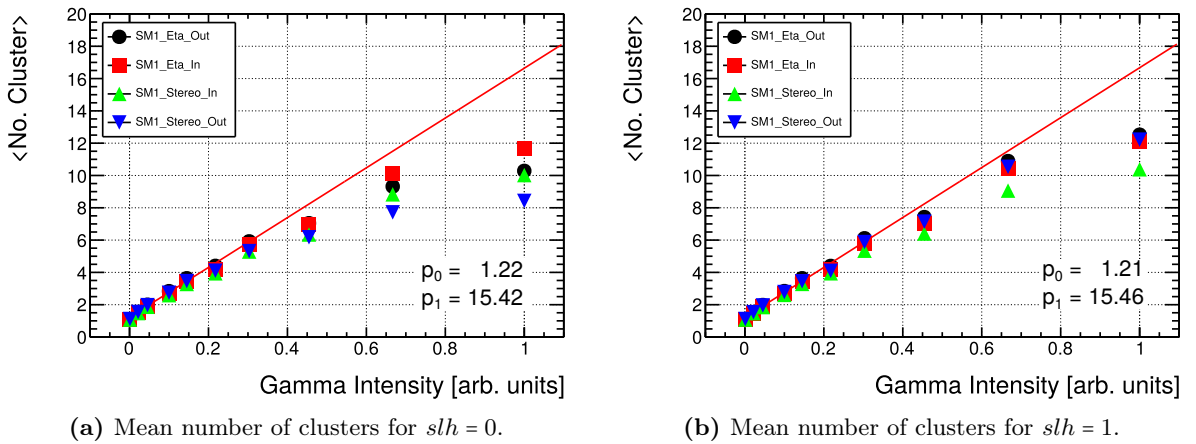


Figure 7.15: Comparison of the mean number of reconstructed clusters for different gamma intensities and values of the VMM slh register controlling the baseline recovery. HL-LHC equivalent background rates correspond to a gamma intensity of 0.53.

For the standard baseline recovery of $slh = 0$ (left), a clear saturation effect in the number of reconstructed clusters at higher gamma intensities (> 0.4) is visible. Enabling this register ($slh = 1$) results in a faster recovery of the VMM and weakens the saturation effect (right). For the highest gamma intensities, the saturation is still visible, but it is strongly reduced. At HL-LHC equivalent background intensities the effect is negligible. Some gamma intensity values do not follow the trend of the curves hinting at non-perfect filters (as already discussed in figure 7.7).

$U_{\text{Amp}} = 520 \text{ V}$, $p_t = 200 \text{ ns}$, $\text{VMM}_{\text{RMS}} = 9\sigma$.

7.4.1 Resolution

Additionally to the performance of the detector at different levels of background irradiation, high-voltage scans are performed for better compatibility to the current ATLAS settings of $U_{\text{Amp}} = 505 \text{ V}$ for the inner PCBs 1-5. The core and weighted centroid resolutions depending on the applied amplification voltage are shown in figure 7.16. Both are almost constant over the whole investigated amplification voltage window. The best core resolution is obtained for $U_{\text{Amp}} = 520 \text{ V}$. At higher amplifications saturated strips affect the resolution negatively.

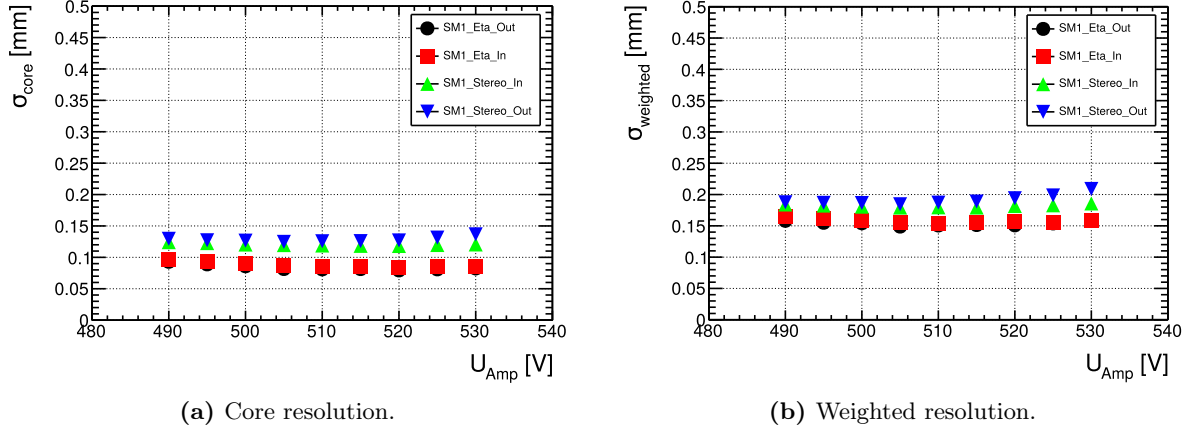


Figure 7.16: Detector resolution for perpendicular incident using the charge-weighted centroid reconstruction for different amplification voltages and no background.

For both, the core and the weighted resolution, the values remain fairly constant showing a slight improvement towards 515-520 V. For higher voltages, the resolution worsens due to strip saturation effects resulting in wrongly assumed strip charges affecting the charge-weighted position algorithm. The Stereo layers show worse performance than the Eta layers.

$p_t = 200$ ns, $VMM_{\text{RMS}} = 9\sigma$, $slh = 1$.

The effect of the enabled slh register on the core spatial resolution is visible in figure 7.17. At low gamma intensities, the effect is as expected minimal, while for higher intensities up to $20\ \mu\text{m}$ of improvement are achieved, e.g. for Eta_{Out} and Stereo_{Out}. This improvement correlates to the increased number of reconstructed clusters also having a bigger effect on these two layers (see figure 7.15). For the comparison of the weighted resolutions with the slh register disabled (left) and enabled (right) in figure 7.18 a more pronounced result is observed. Both layers acquire a meaningful improvement of up to $100\ \mu\text{m}$ showing the huge effect of the increased bias current resulting in a decrease of the long residual tails. The weighted residuals at the highest intensity are a factor of 3 worse than those with no background. The expected results for the innermost strip at HL-LHC correspond to an intensity of $1/1.9 = 0.53$, situated between the two data points at 0.44 and 0.66.

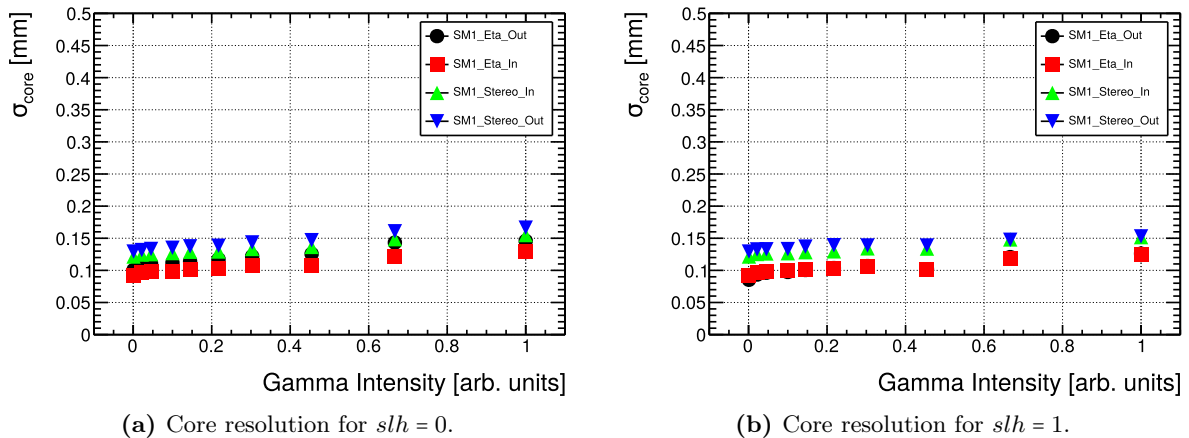


Figure 7.17: Comparison of the core resolutions with the slh register 0 and 1 for perpendicular muon incident.

As expected no major difference is visible at low gamma intensities for the register disabled (left) or enabled (right). For stronger background an improvement of up to $10 - 20\ \mu\text{m}$ is achievable for Eta_{Out} and Stereo_{Out}.

$U_{\text{Amp}} = 520$ V, $p_t = 200$ ns, $VMM_{\text{RMS}} = 9\sigma$.

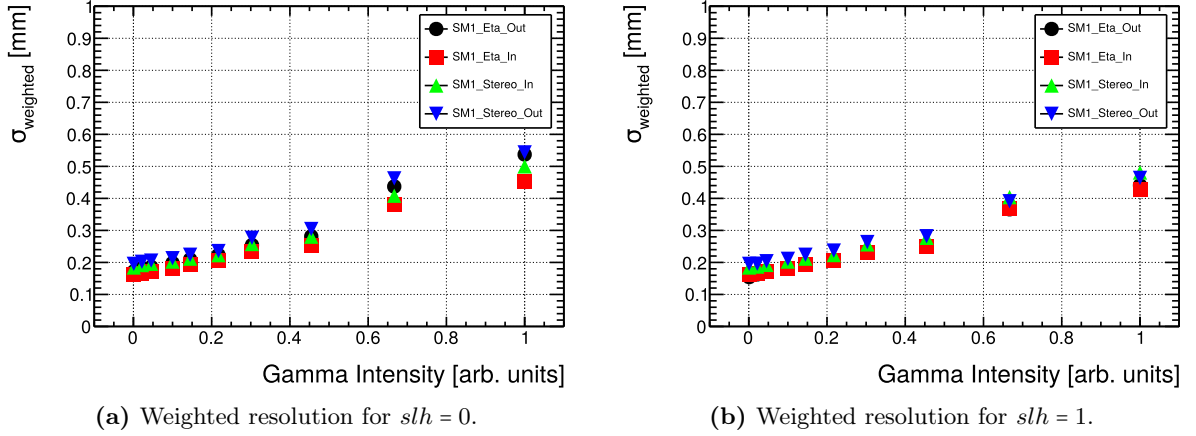


Figure 7.18: Comparison of the weighted resolutions with and without the slh register activated for perpendicular muon incident.

The effect of enabling the slh parameter (right) is more pronounced for the weighted resolution than for the core resolution (figure 7.17). The influence of the photons on the tails of the residuals is bigger than on the inner core Gaussian creating this difference. At very high gamma intensities improvements of 50 – 100 μm are observed (e.g. Eta_{Out}).

$U_{\text{Amp}} = 520 \text{ V}$, $p_t = 200 \text{ ns}$, $\text{VMM}_{\text{RMS}} = 9\sigma$.

7.4.2 Efficiencies

Besides the effect on the resolution the efficiency of the detector using this new VMM configuration is a topic of interest. Following the same ideas as for the resolution the efficiency for different values of U_{Amp} was investigated. Results of the measurements are depicted in figure 7.19 reproducing the expected increase in efficiency for higher voltages. At $U_{\text{Amp}} > 500 \text{ V}$ 90% of single layer efficiency is achieved for all layers with a further increase of U_{Amp} reaching a plateau of 98% starting from 510 V for Stereo_{Out}. This is the layer with the highest reconstructed cluster charges (see figure C.1 in the appendix). Efficiency values of 100% are not achievable due to passive areas in the detector like pillar structures.

The enabling of the increased bias current results in an increased detector efficiency as depicted in figure 7.20b. Compared to the $slh = 0$ (figure 7.20a) 15-20% of efficiency could be recovered for Eta_{Out} and Stereo_{Out} respectively. The bad performance of Stereo_{In} with no significant improvement visible for the enabled slh register is still an object of investigation. Possibly the wrong configuration was loaded to the VMMS of this layer and the legacy $slh = 0$ was used throughout all measurements.

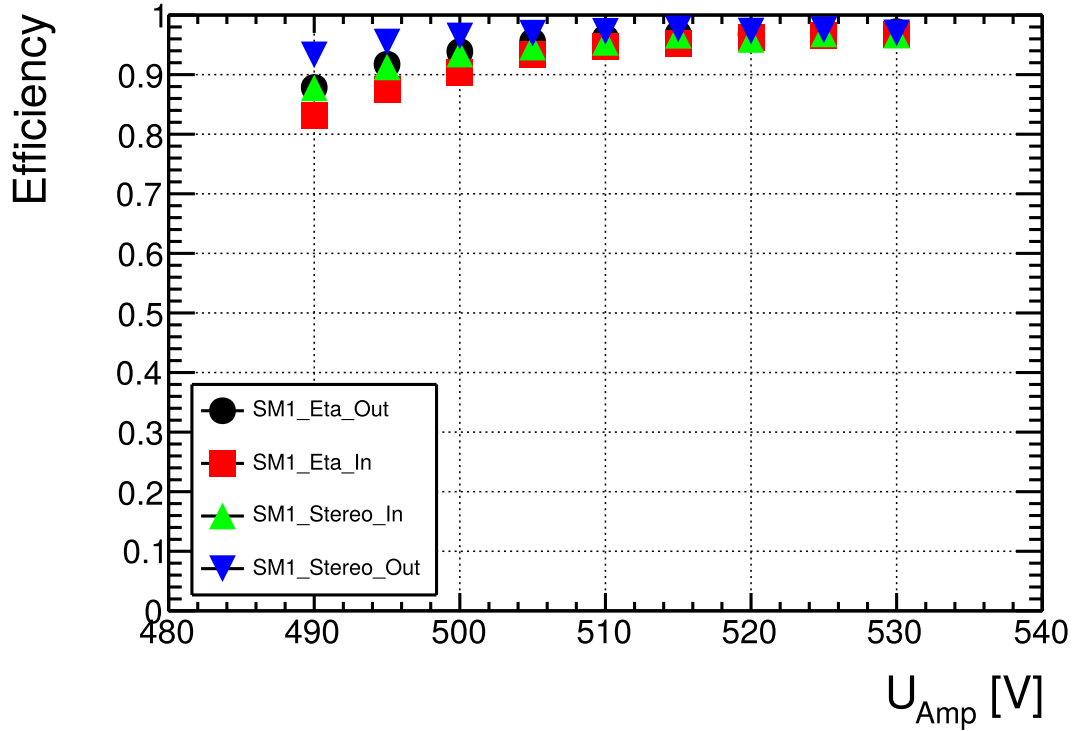


Figure 7.19: Reconstructed ± 2 mm efficiencies for the four detector layers of SM1 M40 vs. the applied anode voltage without gamma background.

An increase for higher amplification voltages is visible reaching a plateau at 98%. A 100% efficiency is not reachable due to passive areas like pillars. 95% of efficiency are reached at an amplification voltage $U_{\text{Amp}} \approx 505$ V.

$p_t = 200$ ns, $VMM_{\text{RMS}} = 9\sigma$, $slh = 1$.

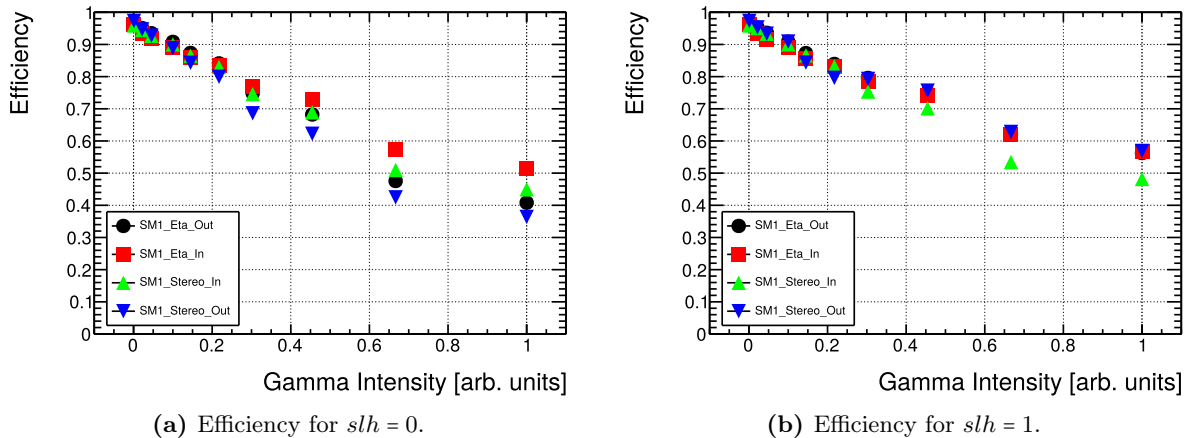


Figure 7.20: Reconstructed ± 2 mm efficiencies for the slh parameter turned off (left) and on (right) for different gamma intensities.

The HL-LHC equivalent background rate is at an gamma intensity of 0.53.

As expected many efficient events can be recovered at high gamma intensities (e.g. +15% for Eta_{Out}) using $slh = 1$. The next to none improvement for $\text{Stereo}_{\text{In}}$ is still an object of investigation.

$U_{\text{Amp}} = 520$ V, $p_t = 200$ ns, $VMM_{\text{RMS}} = 9\sigma$.

7.5 Testbeam Conclusions

Studies evaluating the performance of the long-term irradiated detector modules show excellent behavior of the detectors even after accumulating 5-10 a of HL-LHC equivalent charges. No aging-related effects concerning detection efficiency or spatial resolution are observed.

For perpendicular particle incident core resolutions of $\sigma_{\text{core}} < 80 \mu\text{m}$ are achieved for measurements without gamma background. For backgrounds equivalent to the expected HL-LHC rate, a core resolution of $\sigma_{\text{core}} \approx 100 \mu\text{m}$ is reconstructed.

Detection efficiencies of $> 95\%$ are reached for no gamma background. The efficiency loss at high background intensities can be partially recovered by increasing the bias current of the VMM ($slh = 1$) resulting in single-layer detection efficiencies of $> 75\%$ for HL-LHC equivalent rates. This efficiency corresponds to the innermost strips of the NSW and strongly increases with radial distance from the beam pipe¹⁰, reaching about 90% at PCB 2. As a result, is the $slh = 1$ parameter now used at ATLAS.

For track inclinations of 29° detector resolutions of $\sigma_{\text{core}} \approx 150 \mu\text{m}$ and $\sigma_{\text{core}} \approx 125 \mu\text{m}$ are achieved using the μTPC -like method and the time-corrected centroid position reconstruction method respectively. These are the best results obtained with large-area Micromegas modules for inclined particle tracks so far.

Optimized charge and timing calibration methods were established improving the spatial resolution and detection efficiency of the detector. These methods are now slowly implemented in the ATLAS NSW reconstruction algorithms.

These results illustrate the significance of test experiments with series detectors¹¹, final read-out electronics, and operational conditions¹² acquiring large statistics to develop methods, that can then be utilized in the analysis of a large experiment, such as the NSW at ATLAS.

¹⁰At PCB 2 the hit rate is already decreased by a factor of 5 (see figure 6.4 at $r \approx 1.5 \text{ m}$). With this the HL-LHC background rate for PCB 2 would correspond to a gamma intensity of 0.1 in figure 7.20b.

¹¹In this case the detectors were spare modules, which are identical to the series modules in the NSW.

¹²This includes, among others, the operating voltage, the gas flux, and the background hit rate.

Chapter 8

Long-Term Irradiation Using an Am-Be Source

The particle flux expected for the NSW in the ATLAS experiment at LHC is naturally not made of pure muons with a photon background as in the GIF++. It will also contain protons, neutrons, pions, and various other particles. Neutrons typically have smaller interaction cross-sections (see chapter 8.2.2) than photons. However, the elastic scattering of neutrons might lead to recoil nuclei that are strongly ionizing. Such particles may induce huge charges and lead to detector instabilities, dead-time, or induce aging effects.

To study the effects of neutrons on the newly chosen operating gas mixture containing iC_4H_{10} a long-term irradiation setup using an Am-Be neutron source has been built-up at the MLL¹ in Garching (Vogel et al. [2023]). Multiple years of HL-LHC equivalent in charges are accumulated in the irradiated area and performance tests using cosmic muons to investigate this irradiated area have been carried out.

The module under test is the ATLAS NSW series detector SM2 M03.

8.1 Measurement Setups

Throughout the irradiation period, multiple intermediate performance tests were carried out in different setups. The upcoming section is dedicated to introducing the various setups used over this timeframe.

8.1.1 Long-Term Irradiation Setup

For the long-term irradiation using the Am-Be neutron source the module was placed in a vertical position with the source targeting a single high-voltage sector (see figure 8.1). Eta_{Out} was chosen to be the layer closest to the source. In total a constant irradiation of almost three years has been performed using both gas mixtures described in chapter 3, only stopped for intermediate performance measurement or maintenance periods. A side view of the irradiation setup is given in figure D.3 in the appendix.

¹The facility was formerly known as MP-tandem-laboratory.

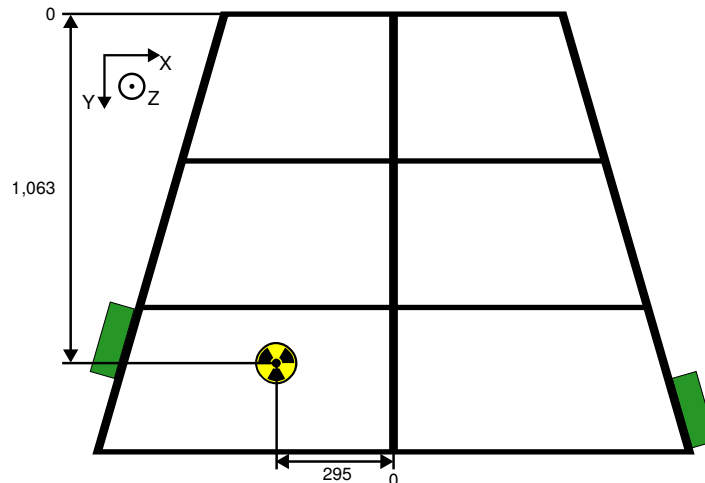


Figure 8.1: Sketch of the Am-Be source position in front of the SM2 M03 quadruplet. Distances are given in mm.

One half of PCB 8 is irradiated with the layer Eta_{Out} being closest to the source.

The detector module is kept in a vertical position. This setup was kept for almost three years testing the detector with the different gas mixtures discussed in chapter 3. The green squares indicate the position of the readout electronics boards.

8.1.2 CRF for Performance Tests

The performance of the detector before the start of the irradiation period was tested in the Cosmic Ray Facility (CRF) (see figure 8.2). This facility was used during the series production of the SM2 modules for quality control, strip position calibration, and performance tests as described in Herrmann [2019] utilizing cosmic muons. Intermediate tests after one year of irradiation have also been carried out in this facility.

The CRF consists of a trigger hodoscope (pale blue), a reference tracking setup built from MDTs², and an iron absorber to filter low energy muons ($E < 600 \text{ MeV}$) by cuts on multiple scattering. Test detectors are placed in between the two reference chambers. APV25 hybrids in combination with the SRS system as described in chapters 4.1 and 4.2 are used for data taking of the Micromegas detector. The trigger is provided by a fast coincidence between the upper and lower layers of the scintillator hodoscope. Initially, the performance of the detectors was tested using the reference chambers for tracking information. Due to the unavailability of the facility for the concluding tests discussed in chapter 8.4.4 internal tracking (see chapter 8.4.1) was performed additionally to enable compatibility between the setups. During internal tracking, only one of the four readout layers of a module is investigated. The other three layers provide the reference track.

Maximal angles of inclination of $\pm 38.5^\circ$ in precision direction (Y) are allowed following from the dimensions of the trigger scintillators in the CRF as shown in figure 8.2b³.

²The MDT chambers in this facility are identical to the BOS chambers installed in the ATLAS barrel muon spectrometer. A BOS chamber consists of six layers of MDTs split into two multilayers with three tube layers each.

³ $\Theta_{\text{track}} = \tan^{-1} \left(\frac{2200}{2766} \right) = 38.5^\circ$.

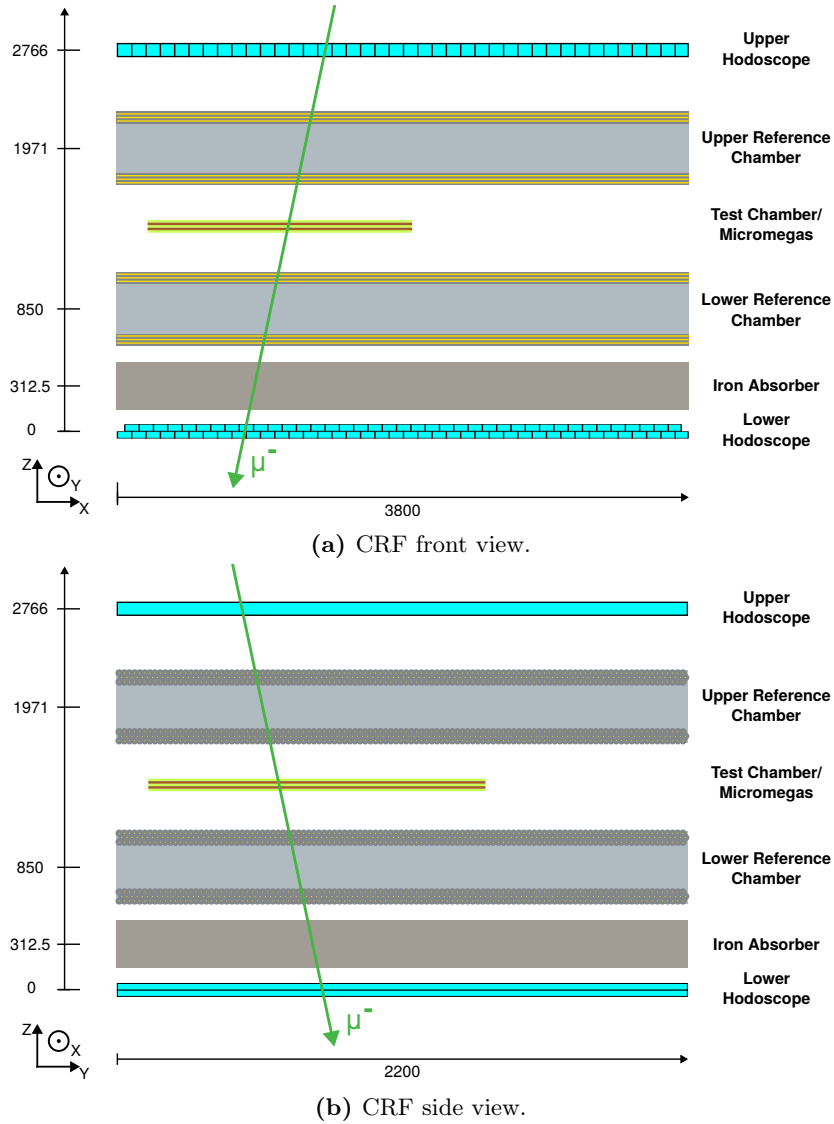


Figure 8.2: Sketch of the cosmic ray facility for the initial testing of the SM2 modules during the series production Herrmann [2019].

Readout of the Micromegas is triggered by a scintillator hodoscope (blue) if coinciding signals are measured. The scintillator hodoscope is segmented (in steps of 9 cm) providing coarse position information along X. The muon track angle is geometrically restricted to $\Theta_{\text{track}} \pm 38.5^\circ$.

Two reference MDT chambers can be utilized as reference tracking chambers providing a reference track in the Y direction. A thick iron absorber of ≈ 40 cm filters low energy muons (< 600 MeV) that are susceptible to multiple scattering.

8.1.3 Final Test Cosmic Muon Setup after 3 Years of Irradiation

The unavailability of the CRF resulted in the requirement of an additional setup to investigate the detector performance after concluding the long-term irradiation⁴.

Figure 8.3 depicts sketches of the front (left) and top (right) view of the test setup. Cosmic muons are used for the performance tests. As shown in the front view (figure 8.3a) two scintillators (pale blue) are used in coincidence to provide a trigger signal for the readout. SM2 M03 is placed between the scintillators on top of a beam dump built from plastic (light grey) and lead (dark grey).

Eta_{Out} is chosen as the lowest layer closest to the source. The module is placed such that the irradiated area (see figure 8.1) is centered within the beam dump. For safety reasons, a supporting structure is introduced to stabilize the detector.

In the center of the beam dump, a hole is available providing the option to introduce the Am-Be source beneath the detector. Measurements with and without the source have been performed and are discussed in chapters 8.4.4 and 8.4.5 respectively. Since no external tracking chambers were used only the internal tracking introduced in chapter 8.4.1 is applied. As shown in figure 8.3b the trigger scintillator paddles only cover one half of a PCB. The source position indicated with the radioactive hazard symbol is identical to the position shown in figure 8.1. For this setup, the APV25/SRS readout system was used. The geometrically allowed angle of acceptance in precision direction (Y) is $\pm 26.5^\circ$, given by the dimensions of the scintillators.

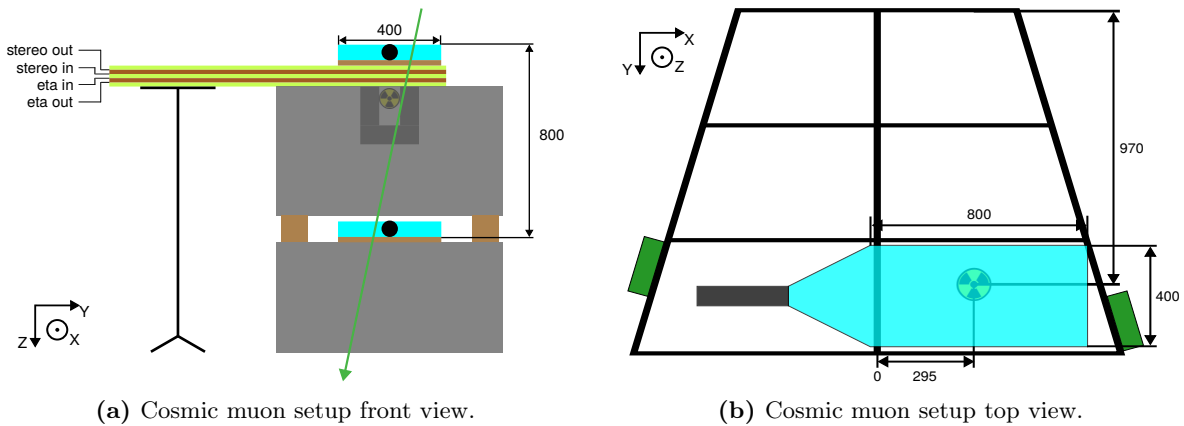


Figure 8.3: Cosmic muon setup after having concluded the long-term irradiation with distances given in mm.

The module was put in a horizontal position on a beam dump made from plastic (light grey) and lead (dark grey).

The beam dump has a central opening for the Am-Be source. Eta_{Out} was decided to be on the bottom for measurements including the source to keep the most strongly irradiated layer closest to the source.

Two large scintillator paddles are used for coincidence triggers on cosmic muons. The lower one is shielded from the neutron source.

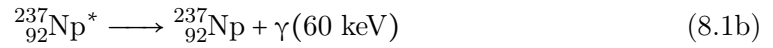
⁴The MDTs of the CRF are undergoing an electronics upgrade (Egli [2023]).

8.2 Source Characterization

Following the same order as done for the irradiation setup in the GIF++ a characterization of the source is performed. The source composition and the resulting particle yields are determined. The sensitivity of the Micromegas detectors on the particles and the irradiated area are simulated and measured. Lastly, the compatibility with HL-LHC is investigated to interpret the accumulated charge over the three years of irradiation.

8.2.1 Composition and Activity

An Am-Be source was chosen as a neutron source providing neutrons of energies up to 11 MeV (see figure 8.4). Sources with two different activities were used. A 3.7 GBq source could be replaced by a 10 GBq source after the first year of irradiation. The nuclear reactions producing the neutrons are listed in equations 8.1a-8.1c.



Americium decays via α -decay to an excited Neptunium. This Neptunium deexcites with 35.9% probability (Winberg and Garcia [1995]) by emission of a 60 keV photon (equation 8.1b). The α particle is captured by the Beryllium producing a Carbon nucleus and a neutron. The Carbon nucleus can be produced in its ground state or in one of its excited states emitting a photon of 4.4 MeV, if the carbon was excited in the first state (Marion and Fowler [1960]). Carbons in their first excited state are produced with a fraction of 0.591 ± 0.015 (Croft [1989]). A neutron yield of 0.594×10^5 per GBq is expected (Basiri and Tavakoli-Anbaran [2018]). For the 10 GBq source this results in an emission rate of 3.59×10^9 60 keV s^{-1} photons, 0.351×10^6 4.4 MeV s^{-1} photons and 0.594×10^6 neutrons per second with a neutron energy spectrum following figure 8.4.

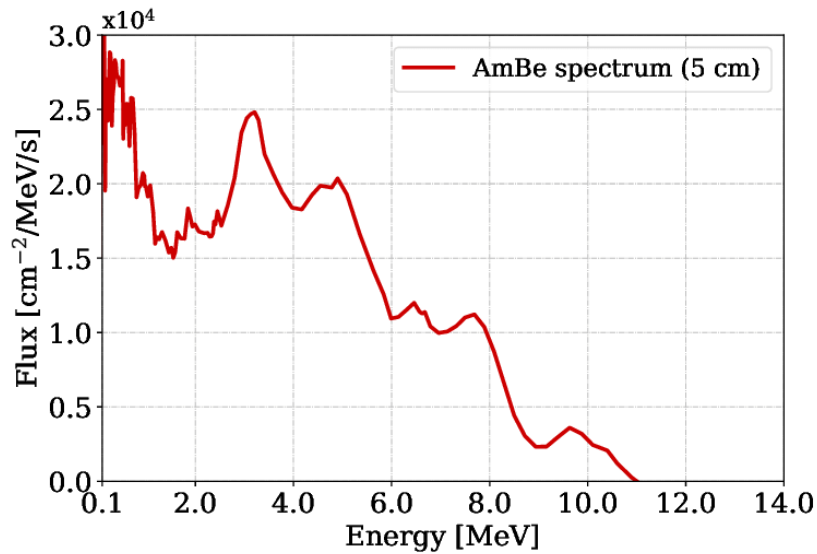


Figure 8.4: Emittted neutron energy spectrum.

Energies up to 11 MeV are observed. Additionally, slow and thermal neutrons are expected, as a result of the slowing down of the high-energy neutrons in the surroundings.

Figure taken from Cecchetto et al. [2021].

8.2.2 Detector Sensitivity

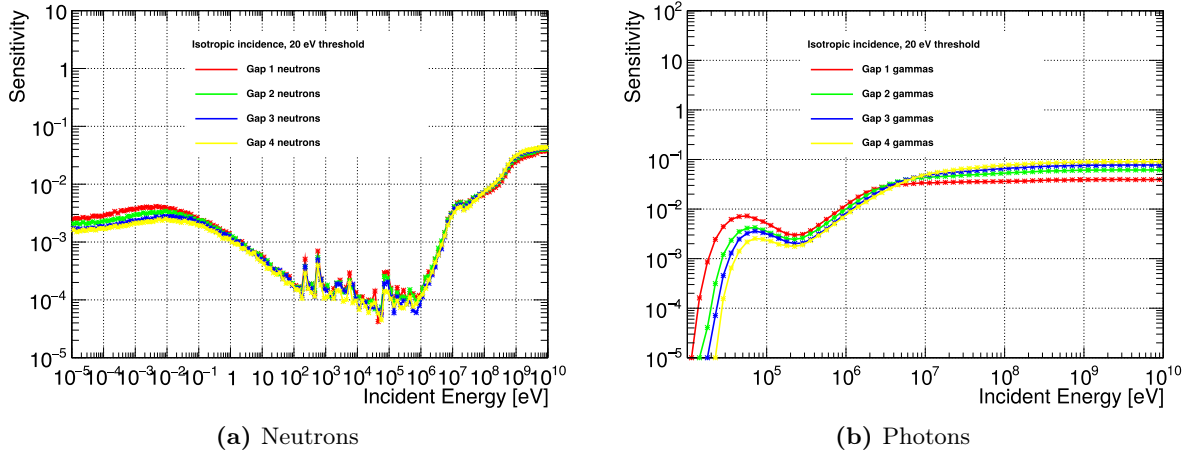


Figure 8.5: Simulated sensitivities of a four-layer Micromegas detector on isotropic neutron or photon incident⁵.

Ar:CO₂ (93:7 vol%) is used as operating gas. The peaking structure at 500 eV (chlorine), 2 keV (sodium), 5 keV (aluminum), 30 keV and 80 keV (both silicon) are neutron capture resonance peaks in the interaction cross-sections for the stated materials contained in the detector. The complete list of materials simulated with a more detailed discussion of the simulation process can be found in Cai et al. [2017].

For the Am-Be source sensitivities of $10^{-4} - 10^{-3}$ (MeV neutrons), 5×10^{-3} (60 keV photons) and 4×10^{-2} (4.4 MeV photons) can be deduced.

The figures are taken from Cai et al. [2017].

The interaction of the 10 GBq Am-Be source with a single layer Micromegas detector was studied in Kumar [2023] under my supervision and a brief summary of the results will be given in the following. To understand the composition and the energy spectrum leaving the neutron source different measurements and simulations were performed.

The photon contributions were disentangled using a high-purity Germanium detector. Real activities, i.e. the number of particles penetrating the source housing were used to scale the initial number of particles for the different energies and types used in a simulation investigating the interaction with the detector (Kumar [2023]).

The number of created electrons in the active volume of the Micromegas detector is taken as the basis for comparison of the simulation with measurements. This number of electrons is proportional to the current drawn by the Micromegas detector.

Different absorber materials were placed between the Am-Be source and the Micromegas detector. The change in measured current was in good agreement with the number of created electrons observed in the simulation, concerning neutron and high energy photon contributions. The simulation suggests however a much higher contribution from the 60 keV photons that is not yet fully understood (Kumar [2023]).

A second set of simulations has been performed by Cai et al. [2017] investigating the detector sensitivity for neutrons (figure 8.5a) and photons (figure 8.5b) of different energies. Results of the simulation are shown in figure 8.5 for neutrons and photons (right). Important sensitivity values are $10^{-4} - 10^{-3}$ for MeV neutrons, 5×10^{-3} for the 60 keV photons and 4×10^{-2} for the 4.4 MeV photons. The spiking behavior in the neutron spectrum represents neutron capture resonances of different materials of the detector, like chlorine (500 eV), aluminum (5 keV), or silicon (80 keV). Both simulations used Ar:CO₂ as operating gas.

⁵In the simulation each active volume of a Micromegas detector (drift + amplification region) is referred to as "gap".

8.2.3 Current Density Calibration

For comparison to the irradiation studies from GIF++ and to HL-LHC equivalences a current density calibration is performed. The irradiated PCB experiences inhomogeneous irradiation due to the small distance from the source. The irradiation strength of the Am-Be source follows the inverse square law (see equation 8.2). Therefore it delivers the highest particle flux at the center of the source decreasing for increasing distances. The measured current is distributed to areas of different radii around the center of the source, similarly to the strip current determination in figure 6.8.

$$I(\vec{r}) \propto \frac{1}{|\vec{r}|^2} \quad (8.2)$$

Important to note is that the source has a finite size and cannot be assumed to be point-like. The distance $|\vec{r}|^2$ depends on the starting point inside the source as sketched in figure 8.6a.

$$I(\vec{r}) \propto \frac{1}{|\vec{a}_i|^2 + |\vec{x}_i|^2} \quad (8.3)$$

Since the charges induce the current on discrete strips the induced current to a single strip at a vertical distance \vec{a}_i from the starting point (red dot in figure 8.6b) requires an integration along the strip (see equation 8.4). The integration limit x_i for strip i has to be chosen dependent on the area under investigation.

$$\begin{aligned} I(\vec{r}_i) &= \int_{-x_i}^{x_i} \frac{1}{|\vec{a}_i|^2 + |\vec{x}_i|^2} dx_{1,i} = 2 \int_0^{x_i} \frac{1}{|\vec{a}_i|^2 + |\vec{x}_i|^2} dx_{1,i} \\ &= \frac{2}{|\vec{a}_i|} \arctan\left(\frac{|\vec{x}_i|}{|\vec{a}_i|}\right) \Bigg|_0^{x_i} = \frac{2}{a_i} \arctan\left(\frac{x_i}{a_i}\right) \end{aligned} \quad (8.4)$$

All strips contributing to the investigated area have to be summed up to derive the total amount of current within the chosen limits using equation 8.5.

$$I_{\text{Total}}(r) = \sum_{i=0}^n I(\vec{r}_i) \quad (8.5)$$

To determine the effect on the whole PCB, i.e. to the total current, the strip length is chosen as integration limits and the sum ranges over all 1024 strips of the PCB. Results for this model on the whole PCB are shown as a red line in figure 8.7. The starting position of the particle was chosen randomly within the source dimensions with the center of the source situated at strip 570. In total 1 million particles emitted isotropically are simulated⁶. Blue points depict reconstructed hit positions using APV25 hybrids with a 1 kHz random trigger with the source irradiating the module in vertical position as sketched in figure 8.1. Measurements are in agreement with the expected intensity distribution provided by the integration model. For the smaller strip numbers (left leg of the distribution) a deviation is visible. It possibly originates from the slightly tilted module resulting in additional shielding for these strips and a small variation in the irradiation strength (see figure D.3 in the appendix). The two-dimensional intensity distribution in arbitrary units around the source center is depicted in figure 8.8.

⁶The simulation is performed purely geometrical.

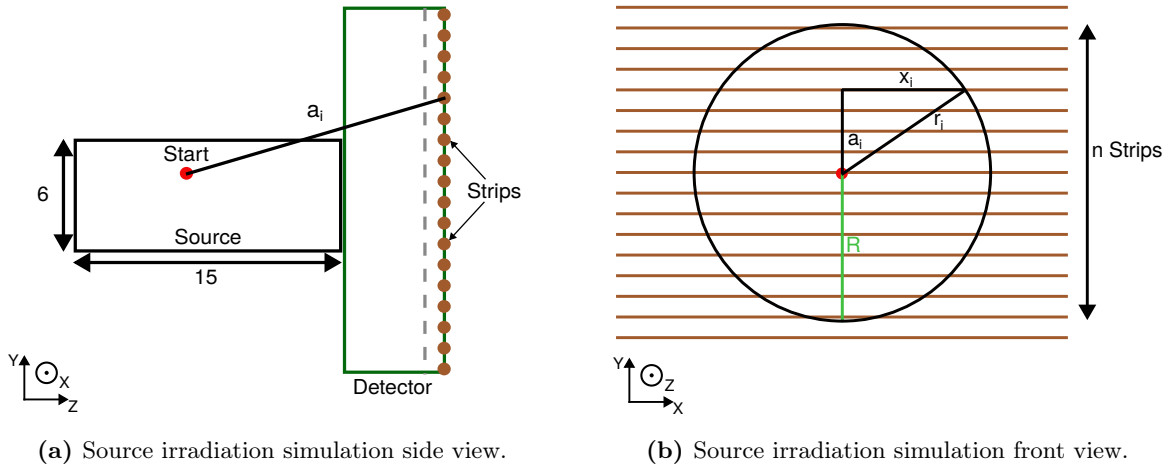


Figure 8.6: A simulation of the source intensity spectrum for variable radii around the center of the source has been performed.

The starting point (red dot) was chosen randomly within the source. From this starting position, the effect on each of the readout strips was calculated using the inverse square law (see equation 8.2).

To obtain the intensity or the fraction of the total integrated number of hits over the whole PCB the intensity along individual strips was integrated (equation 8.4) and then summed up (equation 8.5) both defined by the radius of the region of interest r_i and then being weighted with its area. The simulation of 1 million events leads to the intensity distribution shown in figure 8.7 (red line).

The calculation of the mean current density $I(r)$ of an area defined by the radius \bar{r} , around the center of the source is given by equation 8.6. The intensity in such an area, $I_{\text{Total}}(r)$, is derived using equation 8.5 with adapted integration and summation limits depending on the chosen radius \bar{r} (see figure 8.6b). To obtain the fraction of the current in this area this value is normalized by the total intensity derived for the PCB, $I_{\text{Total}}(\text{PCB})$. This fractional part is multiplied with the measured current I_{PCB} and weighted by its area $A(r)$ to derive the mean current density of the given area for a certain measured current.

$$I(r) = \frac{1}{A(r)} \frac{I_{\text{Total}}(r)}{I_{\text{Total}}(\text{PCB})} \times I_{\text{PCB}} \quad (8.6)$$

An overview of the calculated current densities for various radii with the corresponding equivalences to HL-LHC is given in table 8.1. The stated HL-LHC equivalences are taken from the values derived in chapter 6.3.2. In a circle of radius 50 mm HL-LHC equivalents of mean current density are expected.

Radius [mm]	Mean Current Density [nA/cm ²]	HL-LHC Equivalent
5	10.9	2.8
50	4.07	1.04
100	1.78	0.46
250	0.45	0.11
PCB ⁷	0.37	0.09

Table 8.1: Overview of the different current densities during irradiation with the Am-Be source. For an area of radius 50 mm around the center of the source HL-LHC equivalent mean current densities are expected. As reference current drawn by the whole PCB 900 nA was used. Current fluctuations between (800 - 1000) nA due to environmental effects are observed (see figures 8.10 and 8.11).

⁷The area of PCB 8 equals 2444.4 cm².

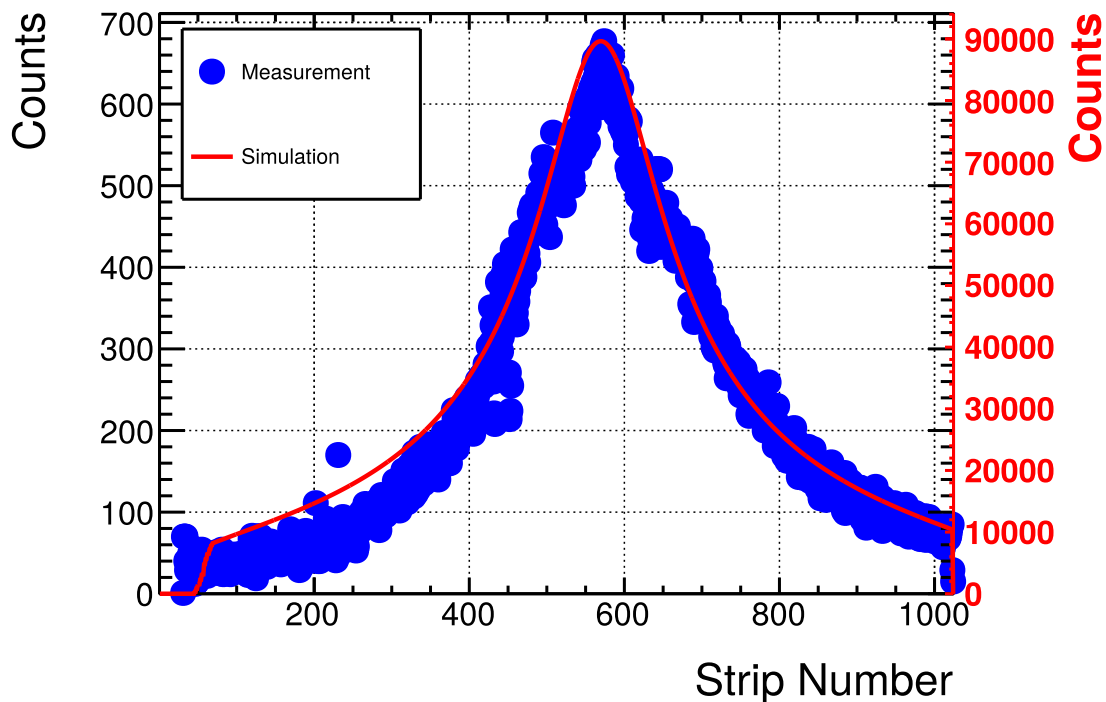


Figure 8.7: Reconstructed cluster position of a random trigger measurement of SM2 M03 irradiated by the Am-Be source.

The red line is the simulated hit distribution using equation 8.5. A good agreement is visible. For smaller strip numbers measurement and simulation differ as a result of a slight tilting of the module (see figure D.3). The strip numbering for this measurement starts from 0 on the long edge of the trapezoid and strip 1023 on the edge of PCB 8 to PCB 7.

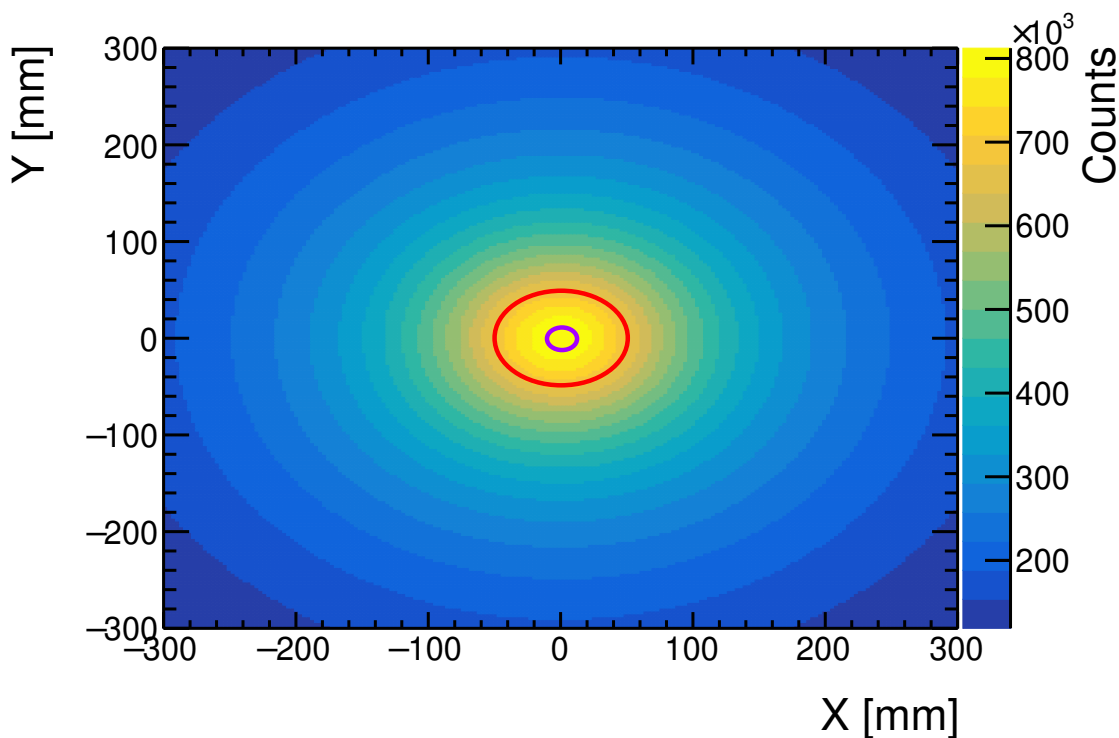


Figure 8.8: Simulated 2D irradiation strength of the Am-Be source.

The encircled areas correspond to HL-LHC equivalent irradiation strengths of $1\times$ HL-LHC (red circle of $r=50$ mm) and $2.8\times$ HL-LHC (purple circle of $r=5$ mm). A more detailed comparison of the irradiation strength for different areas of irradiation is given in table 8.1.

8.3 Detector Stability

This section is dedicated to investigating the detector stability under neutron and photon irradiation operated with the two different gas mixtures Ar:CO₂ (93:7 vol%) and Ar:CO₂:iC₄H₁₀ (93:5:2 vol%). The focus is going to be on the high-voltage stability and discussion of the induced currents. Performance tests regarding efficiency and resolution are the topic of the next chapter 8.4.

8.3.1 Long-Term Current Behaviour Under Irradiation

The center of the investigation is the sector of Eta_{Out} most strongly irradiated by the source (see figure 8.1). The benchmark of the comparison is the stability of this sector without irradiation and under heavy irradiation using a 3.7 GBq source.

Figure 8.9 shows the current behavior over one year, containing periods with and without irradiation. Additional intermediate test periods in the CRF paused the irradiation phase as marked in the figure. Discharging behavior occurs independently from the source. The current increases for higher amplification voltages as expected. A relatively wide spread of the current values (80 nA) is observed. Besides this small constant discharging effects the detector operated stably without high-voltage trips.

The irradiation period using the ternary gas mixture took place over 18 months. Figure 8.10 shows the measured current of the same sector discussed previously. A much narrower current distribution (30 nA) compared to the legacy gas is observed. This results from the better quenching capabilities of the isobutane compared to the CO₂.

During the irradiation period the 3.7 GBq source was replaced by a stronger 10 GBq source (dashed violet line). No discharges or high-voltage trips are observed. Very high current values (single points) correspond to high-voltage ramp-up scans to higher amplification voltages due to capacitor loading. Current values of 0 μA in figure 8.10 correlate to facility maintenance periods, periods without irradiation or gas outage.

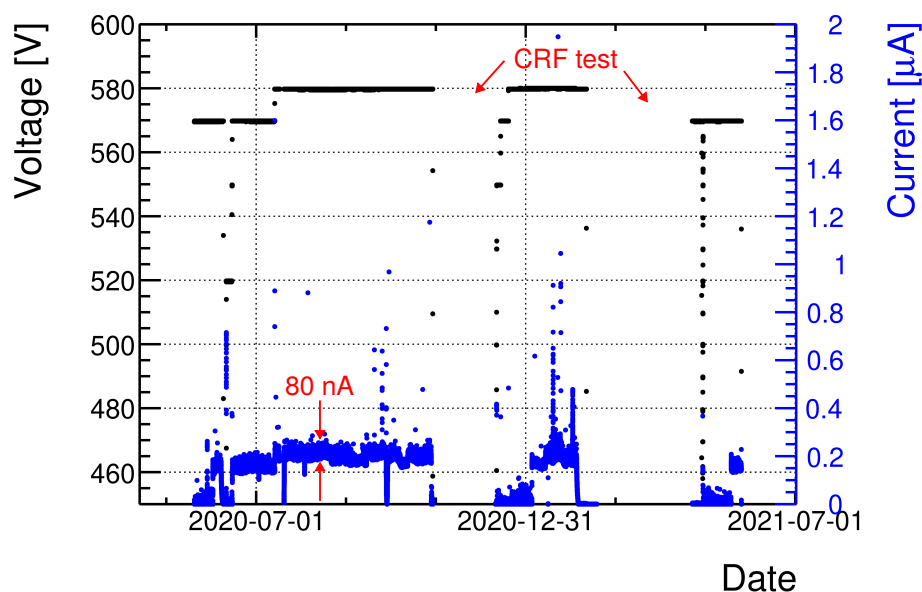


Figure 8.9: One year of irradiation of sector L1L8 of SM2 M03 under Ar:CO₂.

A wide current spread of ± 40 nA originating from the neutron interaction in the detector and its corresponding secondary processes is visible.

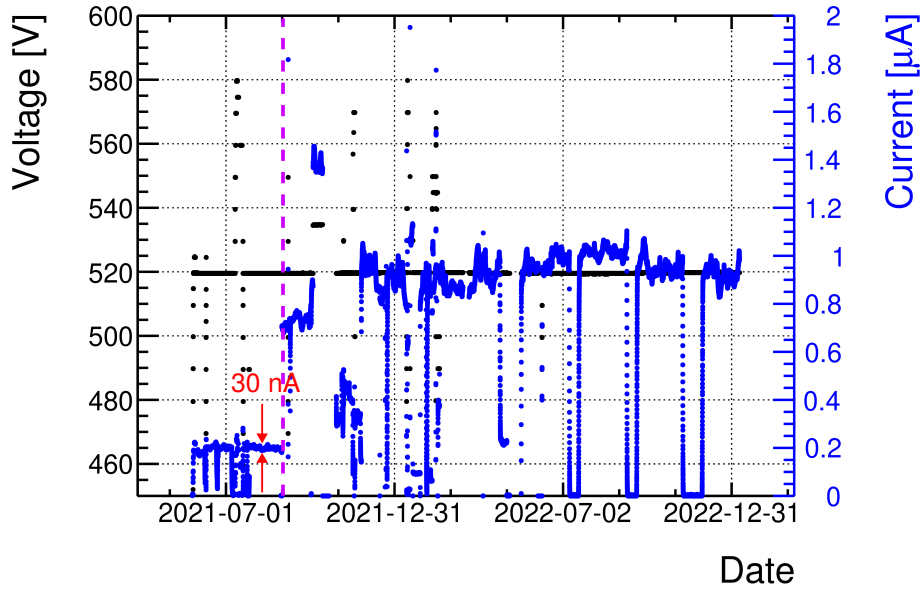


Figure 8.10: 18 months of irradiation of sector L1L8 of SM2 M03 using Ar:CO₂:iC₄H₁₀.

The current fluctuations (± 15 nA) are much narrower compared to figure 8.9. This effect is best visible for the starting period where the 3.7 GBq Am-Be source was used. No trips of the detector or a clear decreasing trend hinting for less amplification due to aging is visible.

The dips in the current are correlated to periods with no irradiation and periods where the gas was empty. The fluctuations in the current can be described by environmental fluctuations like pressure variations (see figure 8.11). A slow fluctuation with a frequency of $f = \mathcal{O}(1 \text{ a})$ corresponds to seasonal temperature fluctuations between summer and winter.

Current spikes, e.g. in January 2022 correspond to HV scans and not discharges.

The fluctuations in current are induced by environmental effects. With the gas gain being dependent on the pressure (see equation 2.23) a correction of the fluctuation follows the linear approximation given by equation 8.7. It is applied to the measured current (I_{meas}).

$$I_{\text{corr}} = I_{\text{meas}} - \frac{p_0 - p}{m} \quad (8.7)$$

For the given small pressure fluctuations a linear dependency is approximated⁸. The correlation factor m is determined analogously to the correlation corrections including linear fits discussed in chapter 5.3.2. As reference pressure $p_0 = 960$ mbar is chosen. In figure 8.11 the effect of this correction and the proportionality of the current (blue) to the pressure (red) is visible resulting in a constant current (green) proving the validity of the linear approximation. A remaining slow fluctuation within the last year of irradiation visible in figure 8.10 with a maximum in the summer and lower currents in the winter season correspond to temperature fluctuations affecting the gain (see equation 2.23)⁹. The temperature was controlled via an air conditioning system, however, seasonal trends remain as the facility is not fully thermally isolated.

Over the duration of irradiation, no constant decrease in the current is observed. Such a decrease would hint at aging, e.g. due to deposits on the anode lowering the electric field by creating an insulating area. Besides that, the remaining small fluctuations of the current, when already corrected for, hint at irregularities in the amplification process.

⁸The actual dependence of the gain on the environmental pressure is not linear (see equation 2.23).

⁹A zoomed in version of the last year of irradiation can be found in figure D.4 in the appendix D.3 for better illustration.

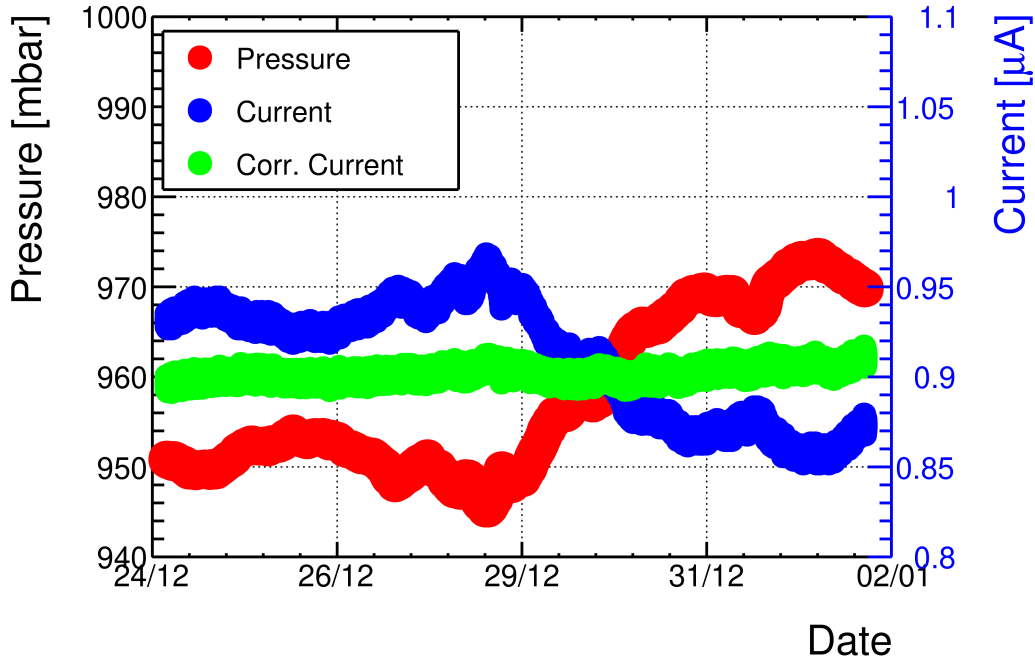


Figure 8.11: Environmental short-term pressure-current correlations:

The measured current in the detector (blue) is inversely proportional to the environmental pressure (red). The fluctuations of the current visible in figure 8.10 can be easily corrected by equation 8.7 resulting in a flat corrected current (green).

The correction was applied to a nominal pressure p_0 of 960 mbar.

8.3.2 Accumulated Charge

The results on accumulated charge of the previous chapter are put into perspective to the HL-LHC analogously to chapter 6.3.3. Figure 8.12 shows the accumulated charge of the irradiated sector of Eta_{Out} . Indicated by the two colored areas are periods using the legacy gas (brown) and the ternary gas (green). A steeper rise starts when the source is exchanged to the 10 GBq one. In total $> 0.011 \text{ C cm}^{-2}$ are accumulated on the PCB. Due to the strongly inhomogeneous irradiation of the PCB this value has to be scaled accordingly following the values given in table 8.1. Exemplary for the area given by a radius of 50 mm experiencing HL-LHC equivalent mean currents the accumulated charge equals

$$C(A) = C(\text{PCB}) \times \frac{I(A)}{I(\text{PCB})} = 0.011 \text{ C cm}^{-2} \times \frac{4.07}{0.37} = 0.121 \text{ C cm}^{-2} \quad (8.8)$$

This corresponds to approximately two years of HL-LHC. For the central area of radius 5 mm around the source center 0.324 C cm^{-2} are accumulated corresponding to roughly five years equivalent to the innermost strip of PCB 1.

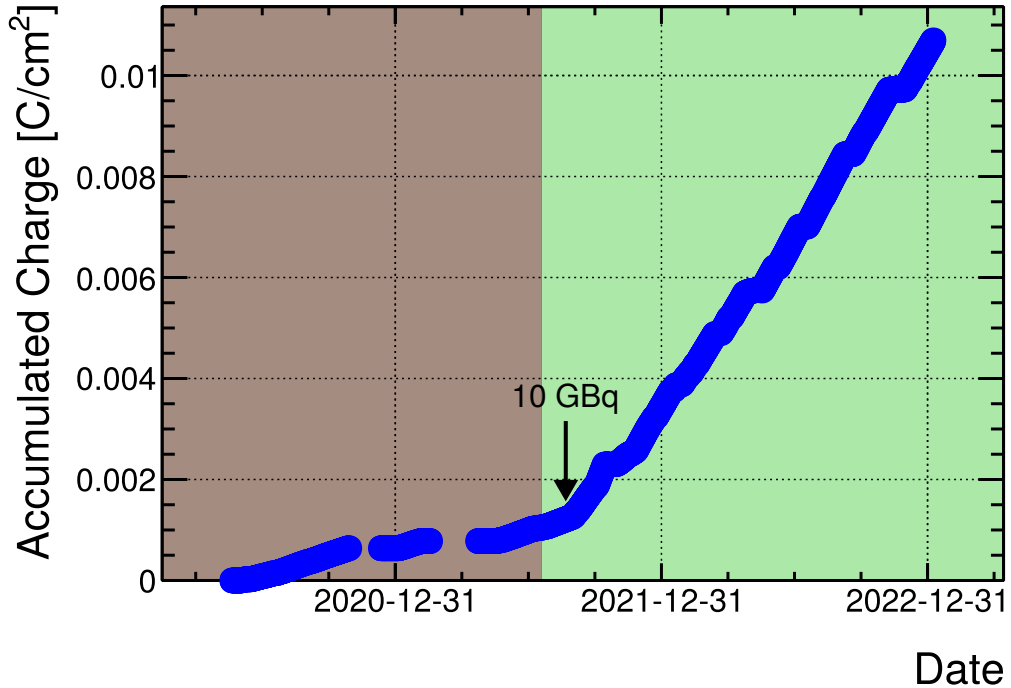


Figure 8.12: Accumulated charge on the HV sector under irradiation.

The two colored areas represent the different operating gases, the legacy gas mixture in brown and the ternary gas mixture in green. Indicated by the black arrow is the switch from the 3.7 GBq to the 10 GBq source resulting in a much steeper rise of the accumulated charge. The value shown represents the whole PCB of an area of 2444.4 cm^2 . This has to be scaled accordingly for areas around the source center as shown in figure 8.8. Scaling factors given in table 8.1 have to be applied accordingly.

8.4 Detector Performance

To investigate the possible effects of the irradiation on the detector performance regular tests are performed. An initial benchmark test before the irradiation and intermediate test measurements were done in the CRF using cosmic muons as sketched in figure 8.2. The final performance test measurements used a different setup shown in figure 8.3 due to an ongoing electronics upgrade of the CRF discussed in Egli [2023].

8.4.1 Internal Tracking

Since the final setup does not include reference trackers the multilayer structure of the Micromegas quadruplet is utilized as tracker. This method is called internal tracking. One of the four detector layers is under investigation with the remaining layers being utilized to build a reference track. It is exemplarily sketched in figure 8.13 for the Eta_{In} layer.

For the Eta_{Out} layer the following description of the method works analogously. Reconstructed hit positions in the two Stereo layers are combined to virtual points positioned at the center between the two readout layers following the calculations described in chapter 5.1. From the virtual point and the reconstructed hit position in Eta_{Out} a track is built and interpolated to Eta_{In} . Detector efficiencies and resolutions of Eta_{In} are then determined identically to the methods using external reference tracking chambers.

Due to the track interpolation to Eta_{In} a better position resolution compared to the Eta_{Out} is expected, where the track is extrapolated.

Additionally, the efficiency window discussed in chapter 5.5 is extended to $\pm 5 \text{ mm}$ following again internally decided standards for internal tracking.

The focus of the performance investigations is set on the two Eta layers that experienced higher irradiation than the Stereo layers. For all test measurements internal tracking is used for performance investigations to ensure a compatibility independent on the track provided by the reference chambers of the CRF.

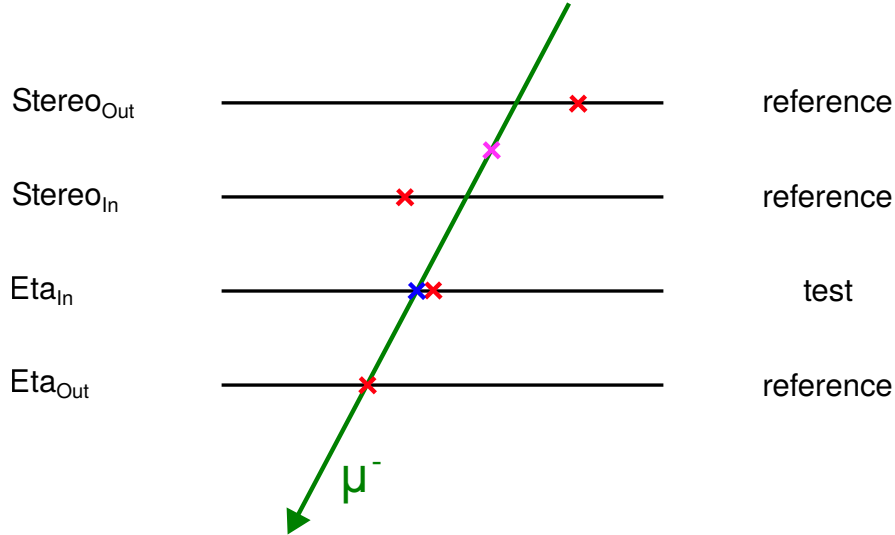


Figure 8.13: Illustration of the working principle of the internal tracking used to determine spatial resolution and efficiency.

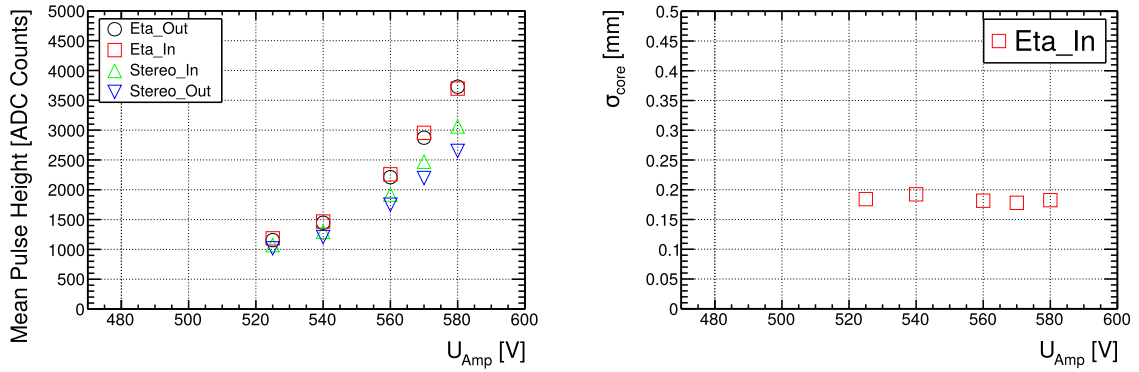
If used as reference trackers, the position information of the two stereo layers is combined to a data point in the precision direction on a virtual layer centered between them (pink cross). Red crosses show the reconstructed hits and the blue cross is the interpolated reference hit from a reference track built from the virtual layer and the Eta_{Out} layer. The residual is then determined in analogy to equation 5.20. An efficiency window around the extrapolated position of ± 5 mm is chosen for cosmic muons.

8.4.2 Benchmark Performance Before Irradiation

Before the irradiation of the detector, a reference measurement to set the starting efficiency and spatial resolution of the detector has been performed. Tests used a gas mixture of Ar:CO₂ (93:7 vol%), and shown results concern the performance of PCB 8 only. Figure 8.14 shows the mean pulse heights (figure 8.14a) and the spatial resolution (figure 8.14b) of the detector. The expected exponential increase of the pulse height with increasing U_{Amp} is observed. Eta layers show higher pulse heights than Stereo layers for the highest amplification voltages. Following the discussion of the previous section only the resolution of Eta_{In} is investigated showing the best performance using internal tracking. A constant $\sigma_{\text{core}} < 200 \mu\text{m}$ is observed for all amplification voltages. Important to note is the wide angular acceptance of up to 30° . Independent from the track angle the centroid method (see chapter 5.2) was used for position reconstruction that performs worse for inclined tracks (see figure 5.15). Thus the observed spatial resolution is limited to $\approx 200 \mu\text{m}$.

With higher amplification voltages the efficiency¹⁰ of the layers increases until the beginning of saturation at $U_{\text{Amp}} = 580 \text{ V}$ (see figure 8.14c). Efficiencies above 90 % are achieved for amplification voltages $> 570 \text{ V}$ for both Eta layers.

¹⁰Reconstruction efficiencies are derived as described in chapter 5.5 for an efficiency window of ± 5 mm.



(a) Mean pulse height.

(b) Core resolution.

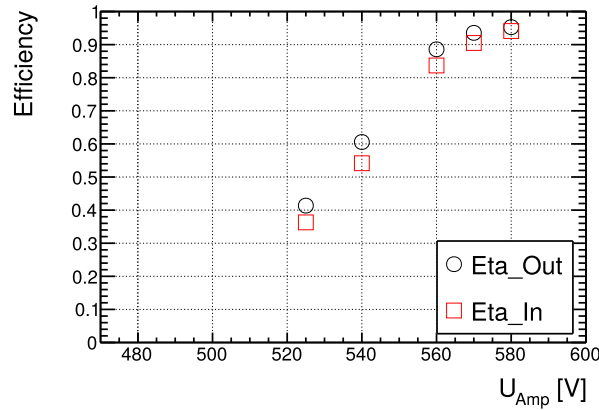
(c) ± 5 mm detection efficiency.

Figure 8.14: Benchmark detector performance before irradiation. Results shown were obtained in the CRF¹¹.

An exponential rise of the pulse height for increasing U_{Amp} is visible, as expected.

The residual was determined using the internal tracking explained in figure 8.13. A core resolution of 180 – 190 μm for all amplification voltages is achieved allowing all angles of inclination that are geometrically possible. For position reconstruction, the centroid method was used. Thus follows a spatial resolution limitation of $\approx 200 \mu\text{m}$.

An expected rise in the efficiency at higher amplification is visible. For the highest U_{Amp} efficiency saturation at 95% starts to occur. Ar:CO₂ 93:7 vol%.

8.4.3 Detector Performance After 1 Year of Irradiation

An intermediate performance test was performed after approximately one year of irradiation (second test period marked in figure 8.9). At that time the irradiation was performed using the weaker 3.7 GBq neutron source with the detector being operated under Ar:CO₂ 93:7 vol% for the whole period. The mean pulse height, the core resolution, and the efficiency of the detector after the irradiation (see figure 8.15) are used for comparison with the results of the previous chapter. Three of the four detector layers show slightly higher mean pulse heights, only Stereo_{In} remaining constant compared to the benchmark performance. The common increase is explained by different environmental conditions affecting the gain. A possible reason for the difference in Stereo_{In} is a change of the readout APV25 hybrids¹². Both measurements used the same technology. However, individual hybrids saturate at different

¹¹The errors of the displayed data points are smaller than the marker size. This also holds for figures 8.15, 8.16, 8.17, 8.18, 8.22, 8.23 and 8.24.

¹²The constant replacement of APV25 hybrids in the scope of the series testing during module production as discussed in Herrmann [2019] also leads to fluctuations in the performance.

values affecting the pulse height for large gains reaching the limits of the dynamic range of the APV25. The exponential increase for increasing amplification voltages is observed for all four layers. Compared to the benchmark resolution shown in figure 8.14b no differences are observed after the first year of irradiation, reconstructing $\sigma_{\text{core}} < 200 \mu\text{m}$ for all amplification voltages (see figure 8.15b).

Higher detector efficiencies are achieved for the two Eta layers (see figure 8.15c) concerning the starting efficiencies shown in figure 8.14c. This follows from the higher mean pulse height resulting in more strips passing the charge cuts.

Efficiencies well above 90% are achieved after one year of irradiation.

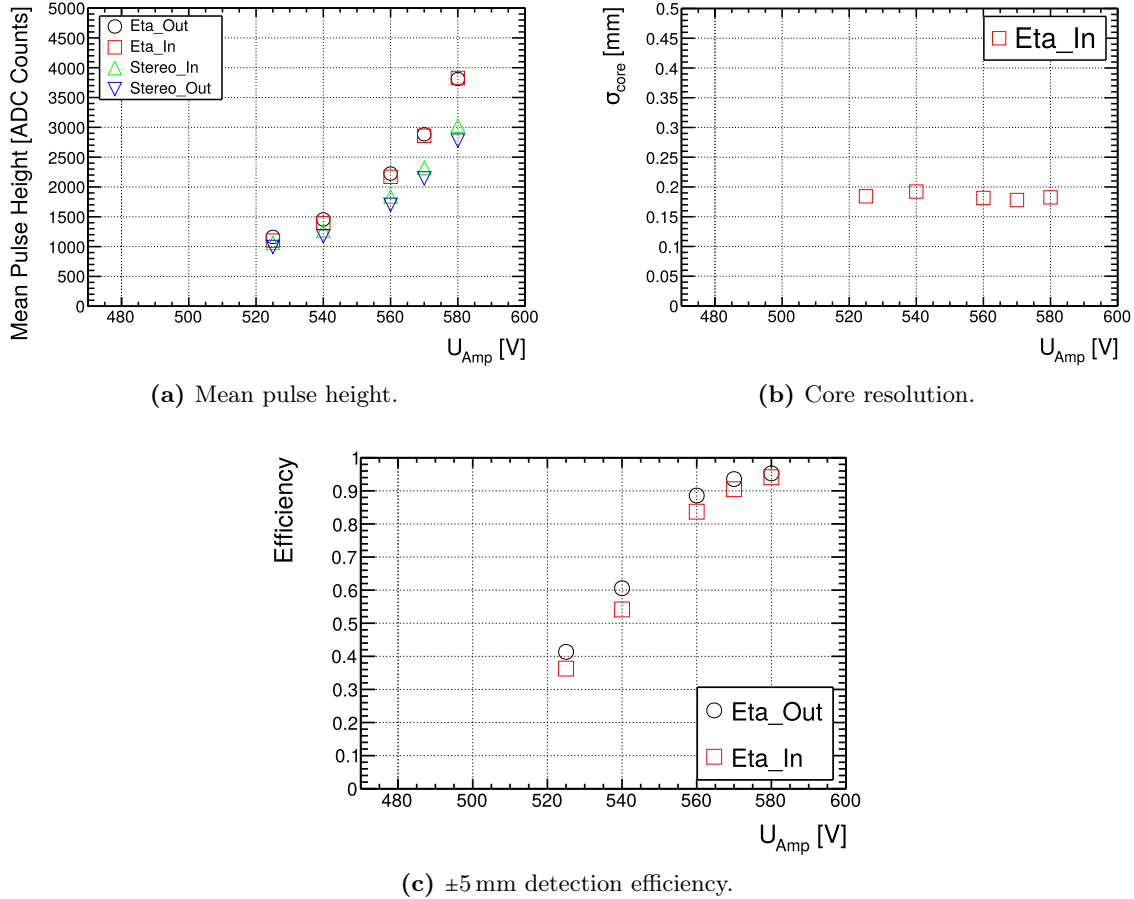


Figure 8.15: Cosmic muon performance measurements of the tested detector after one year of irradiation.

The obtained results are close to identical to the measurements before irradiation (figure 8.14).

For some layers at certain voltages, even higher pulse heights have been observed. The pulse height is analogous to the current inverse proportional to the environmental pressure that may differ for the two measurement periods before and after one year of irradiation.

Possible reasons for the slightly higher efficiencies are the observed higher pulse height resulting from different environmental conditions and the exchange of no longer badly performing APV25 hybrids in the CRF during the series testing discussed in Herrmann [2019].

Ar:CO₂ 93:7 vol%.

8.4.4 Detector Performance After Irradiation Using Ar:CO₂:iC₄H₁₀

As a disclaimer, the upcoming discussed results are based on measurements taken in collaboration with Kumar [2023] as part of a master thesis project. With the basic analysis framework being identical, final results may still differ due to individual fine-tuning being applied to the analysis algorithms.

After 18 months of irradiation and operation using the ternary gas mixture a final performance test was carried out in the setup described in figure 8.3. Both the legacy gas mixture and the new gas mixture are investigated. Additionally, cosmic muon tests including the Am-Be as constant particle background are performed.

The mean pulse height for both of the gas mixtures and all four layers of the detector are shown in figure 8.16. Values obtained for the ternary gas mixture are represented with filled markers, those with the legacy gas mixture are depicted by empty markers following the scheme used throughout this chapter.

Independent from the gas the exponential increase for higher amplification voltages is observed. An equality value in pulse height is observed for approximately 515 V and 570 V for Ar:CO₂:iC₄H₁₀ and Ar:CO₂ respectively agreeing with the current equality discussed in chapter 3.3.2. A small deviation from the values is expected due to environmental fluctuations as the measurement duration of each amplification voltage value is one day and the switch between gases adds an additional day. In total, the measurement time of the values shown in figure 8.16 was two weeks, whereas the current values from chapter 3.3.2 were obtained within a few days.

Different APV25 hybrids were used compared to the measurements performed in the CRF, resulting in different values for the mean pulse height. Only up to a certain extent, the absolute values of the pulse height are comparable.

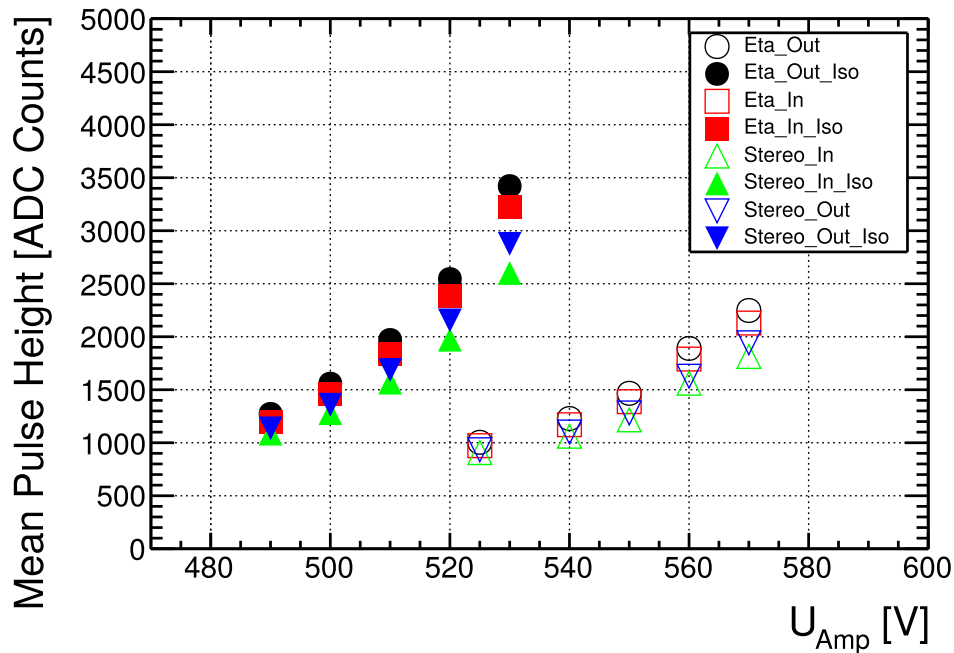


Figure 8.16: Mean pulse height after concluding the irradiation of SM2 M03.

For both gas mixtures (legacy gas: empty markers, ternary gas: filled markers) the exponential rise for increasing amplification voltages is visible for all readout layers. The pulse height at 515 V using Ar:CO₂:iC₄H₁₀ equals the pulse height at 570 V for Ar:CO₂.

The spatial resolution of the detector is displayed in figure 8.17 for the two gas mixtures. Both the core (left) and weighted (right) resolutions improve for higher amplification voltages. This is observed independently from the gas mixture. For the highest test amplification voltage of $U_{\text{Amp}} = 570 \text{ V}$ for Ar:CO₂ a $\sigma_{\text{core}} = 150 \mu\text{m}$ is achieved, $\approx 30 \mu\text{m}$ better than the benchmark and intermediate performance measurements.

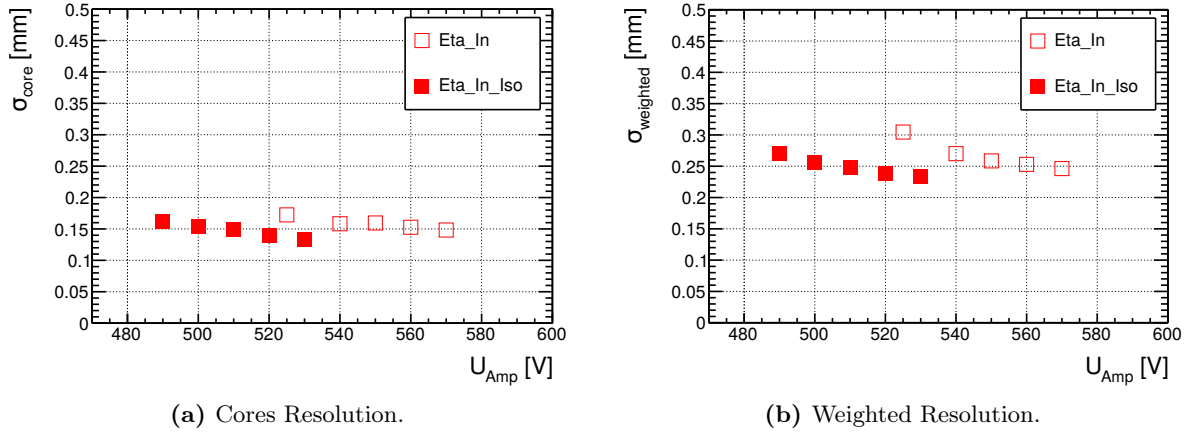


Figure 8.17: Spatial resolutions of Eta_{In} obtained using the setup depicted in figure 8.3 and the internal tracking algorithm.

Core resolutions of $< 140 \mu\text{m}$ are achieved with the ternary gas mixture. For the legacy gas mixture $\approx 150 \mu\text{m}$ are reached for $U_{\text{Amp}} = 570 \text{ V}$. Weighted resolutions of $< 250 \mu\text{m}$ could be obtained for both gas mixtures with the ternary gas mixture again performing slightly better.

A comparison with the starting point before irradiation (see figure 8.14b) or the test measurement after one year (figure 8.15b) shows better performance for the final measurement after the irradiation. A possible reason is the different restrictions on the muon angle and different environmental conditions.

A change of the gas mixture and the application of amplification voltages of higher gain, e.g. $U_{\text{Amp}} = 530 \text{ V}$ in figure 8.16 results in further improvements in spatial resolution. The reason for the improvement is the angle of acceptance, which is smaller in the final setup ($\pm 26.6^\circ$) than for the CRF ($\pm 38.5^\circ$) in the precision direction. As the position and ultimately the detector resolution are reconstructed using the charge-weighted centroid method a worse performance for the larger angle of acceptance is expected.

The reconstructed efficiencies for the two gas mixtures are shown in figure 8.18. Both surpass the 90% threshold. Comparing the values for the $\text{Ar}:\text{CO}_2$ gas mixture with the previous measurements (comparing figures 8.16 and 8.14a) identical efficiencies are obtained despite the smaller pulse heights. Following the trend of the detector resolution, due to the higher gain higher efficiencies up to 98% are achieved using the ternary gas mixture.

As the depicted efficiency is averaged over the active measured area restricted by the trigger scintillators as shown in figure 8.3 the position-dependent efficiency is also investigated for Eta_{Out} shown in figure 8.19. The black cross indicates the location of the center of the source during the irradiation period. If there would be aging-induced effects a decrease in performance in circular shapes around this point is expected following the intensity distribution of the irradiation in figure 8.8. A homogeneous efficiency over the whole PCB is observed leaving no hint for deteriorations.

The lower efficient part at $X = 0 - 100 \text{ mm}$, and $Y = 900 - 970 \text{ mm}$ corresponds to the location of the interconnection (see figure 2.10a) and a passivation of the surrounding area. This is by definition an insensitive area and thus this behavior is expected. On the lower left part of the figure, irregularities are visible following edge effects as this area corresponds to the rim of the PCB. Dark yellow lines ranging over the whole width correspond to readout electronics issues like dead or noisy channels. The darker line above the black cross is the edge between the two readout boards (see figure 8.1).

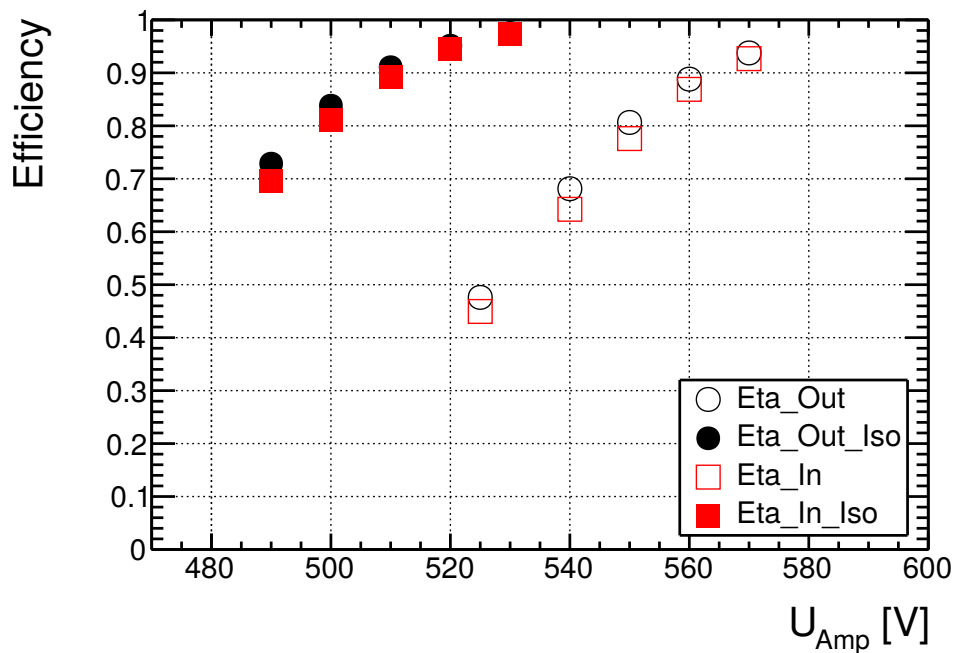


Figure 8.18: ± 5 mm efficiency of the detector after the neutron irradiation under the ternary gas mixture.

Cosmic muon measurements have been performed in the setup depicted in figure 8.3. Both the legacy gas (empty markers) and the new Ar:CO₂:iC₄H₁₀ (filled markers) were tested.

The overall performance for both gas mixtures is up to the specifications of > 90% with a slightly better performance of the ternary gas. Comparing the efficiencies under the legacy gas with the benchmark measurements in figure 8.14c an equally good performance is observed.

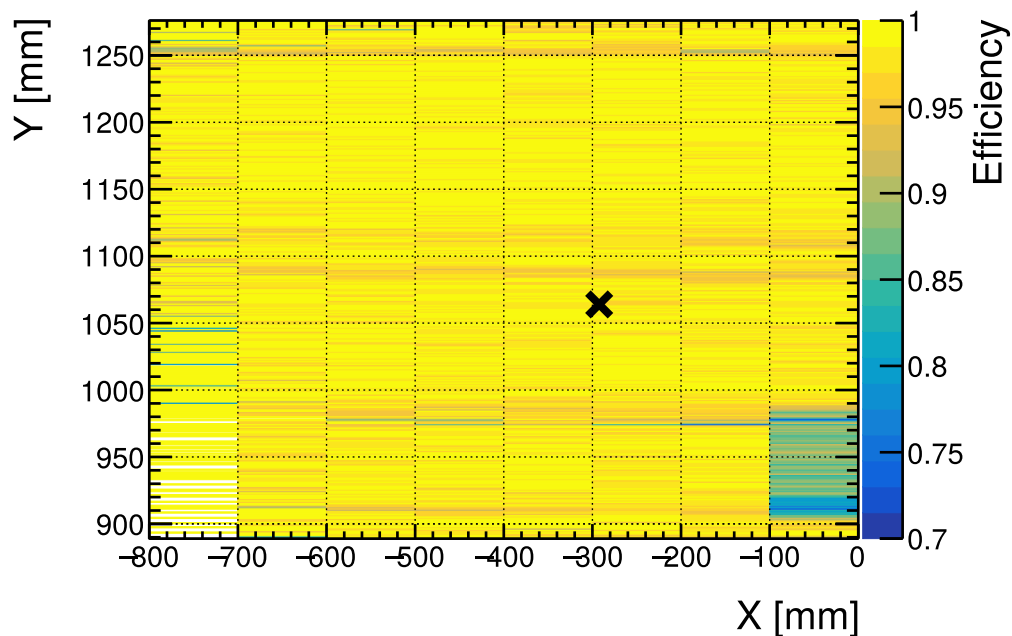


Figure 8.19: 2D efficiency distribution of Eta_{Out} after concluding the long-term irradiation.

The black cross indicates the position of the source center. An overall homogeneous efficiency > 95 % is visible with no decrease around the source position. Horizontal lines of lower efficiency originate from imperfect APV25 channels. The drop in efficiency close to X=0 mm and Y < 990 mm results from a passivated area around the interconnection situated at that position.

U_{Amp} = 530 V, Ar:CO₂:iC₄H₁₀ 93:5:2 vol%.

8.4.5 Detector Performance with the Am-Be Source as Background

Given the setup shown in figure 8.3 the detector performance can be tested under irradiation as well. The neutron source is placed beneath the Micromegas module with Eta_{Out} chosen to be closest to the source.

The reconstructed blue hit distribution without source in figure 8.20 is close to constant over the whole PCB in precision direction only decreasing towards the edges. Spiky behavior corresponds to noisy readout channels. This behavior is visible for measurements with and without the source.

An increased amount of reconstructed clusters centered around $Y = 970$ mm is visible, being the position of the source center.

Since both measurements were taken for an equal amount of time, subtracting both histograms leads to the actual source-induced clusters. The source cluster position distribution shows an asymmetry around the source center. The source center is located at the edge between two APV25 master-slave pairs, which could explain this slightly different number of reconstructed clusters.

For the last 54.4 mm ($Y > 1250$ mm) no events were recorded for measurements with the source. This width equals 128×0.425 mm corresponding to one malfunctioning APV25.

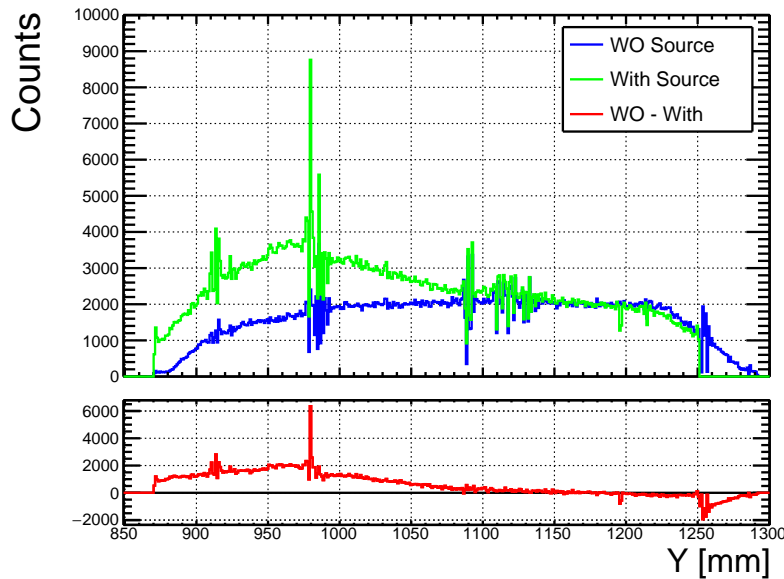


Figure 8.20: Comparison of the reconstructed cluster position with and without the Am-Be source.

The source is centered around $Y = 960$ mm. The duration of data taking was identical for both measurements.

Most of the strong fluctuations are equally pronounced in both measurements originating from noisy readout channels of the APV25 readout electronics. Subtracting the two distributions from each other (red) removes most of the spiking behavior.

Above $Y = 1250$ mm no clusters were reconstructed for the measurement with the installed source hinting for a malfunctioning APV25 hybrid. The width of the inefficient area is approximately equal to 54.4 mm corresponding to the 128 strips of an APV25 with a 0.425 mm detector strip pitch.

$U_{\text{Amp}} = 520$ V, Eta_{Out} , Ar:CO₂:iC₄H₁₀ 93:5:2 vol%.

The influence of the source on the strip and cluster charges (see figure 8.21) is obvious in both distributions.

For the strip charge, an increased amount of saturated strips is visible with an overall increase of the strip charge. Saturations occur for densely, heavy ionizing particles where many pri-

many electrons are created in a small volume. Both neutrons and photons can induce such ionization. Elastically scattered neutrons create heavily ionizing particles like protons or ions. Photons interacting via photoeffect (e.g. the 60 keV photons of the Am-Be source) create photoelectrons with energies around 50 keV¹³ that locally ionizes many atoms before leaving the detector with its remaining energy (see Flierl [2014]).

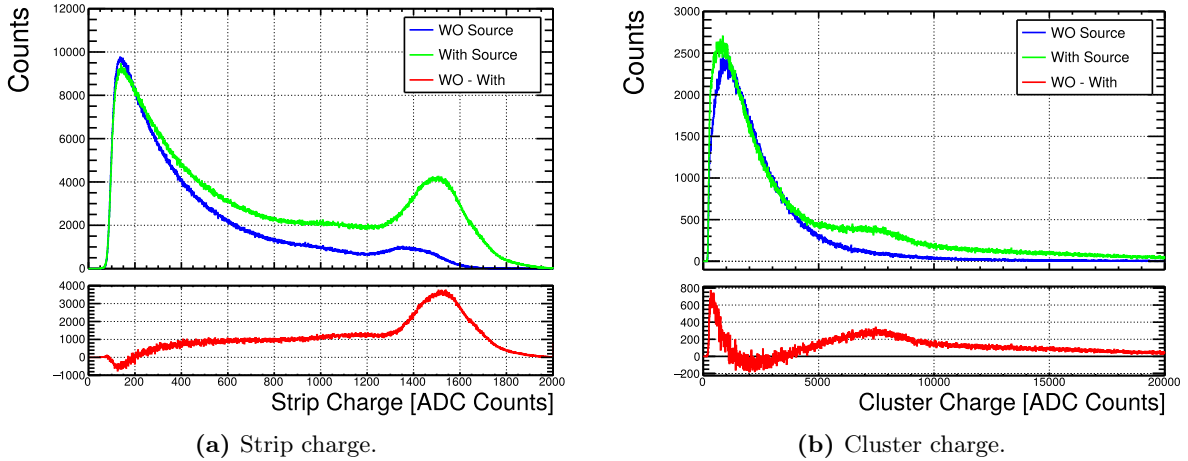


Figure 8.21: Influence of the Am-Be source on the measured strip and cluster charge.

More strips show saturation and the overall strip charge is higher if the source is present. Subtracting the two cluster charge distributions (red) shows more clusters with smaller cluster charges but also a local maximum at cluster charges of approximately 7500 ADC Counts with a long tail to very high values for the installed source.

The following equation 8.9 this maximum possibly originates from the 60 keV photons.

$U_{\text{Amp}} = 520 \text{ V}$, Eta_{Out} , Ar:CO₂:iC₄H₁₀ 93:5:2 vol%.

The cluster charge shows an increased number for very small values (< 1000 ADC Counts) resulting from weaker ionizing particles like high energy electrons, that have a large mean free path (Perkins et al. [1991]).

A distinct wide bump at a cluster charge of 7500 ADC Counts with a long tail is observed. Clusters of that charge possibly originate from the low-energy photons ($\approx 60 \text{ keV}$) emitted from the source. A gain-dependent estimation of the deposited energy (E_{Depo}) is possible. With one ADC Count corresponding to 230 electrons¹⁴, a gain G and an ionization energy of Argon ($E_{\text{I}} = 15.7 \text{ eV}$) given in table 2.1 the deposited energy can be described by:

$$E_{\text{Depo}} = Q_{\text{Cluster}} \times \frac{230}{G} \times E_{\text{I}} = 7500 \times \frac{230}{G} \times 15.7 \text{ eV} = \frac{27 \times 10^6}{G} \text{ eV} \quad (8.9)$$

For typical gain values from $G = 4000$ - 7000 follow $E_{\text{Depo}} = 6.75 - 3.86 \text{ keV}$ respectively.

According to Perkins et al. [1991], a 51 keV electron deposits 7.58 keV cm^{-1} . With a given drift gap of 5 mm and assuming a non-straight trajectory of the photoelectron, is the 60 keV photon a good candidate for the bump at 7500 ADC Counts.

Reconstructed mean pulse heights for the previously discussed clusters are shown for all four readout layers in figure 8.22. An expected increase in all layers is observed. This increase is more pronounced for the layers closer to the source also following the expectations originating from inverse square dependence of the source intensity.

¹³During photoeffect almost the whole energy of 60 keV is given to the photoelectron. Material-dependent binding energies have to be considered. For the cathode material copper this is in the order of 9 keV.

¹⁴https://hallaweb.jlab.org/wiki/images/f/f3/APV25_readout_system_for_SBS_07_2014.pdf.

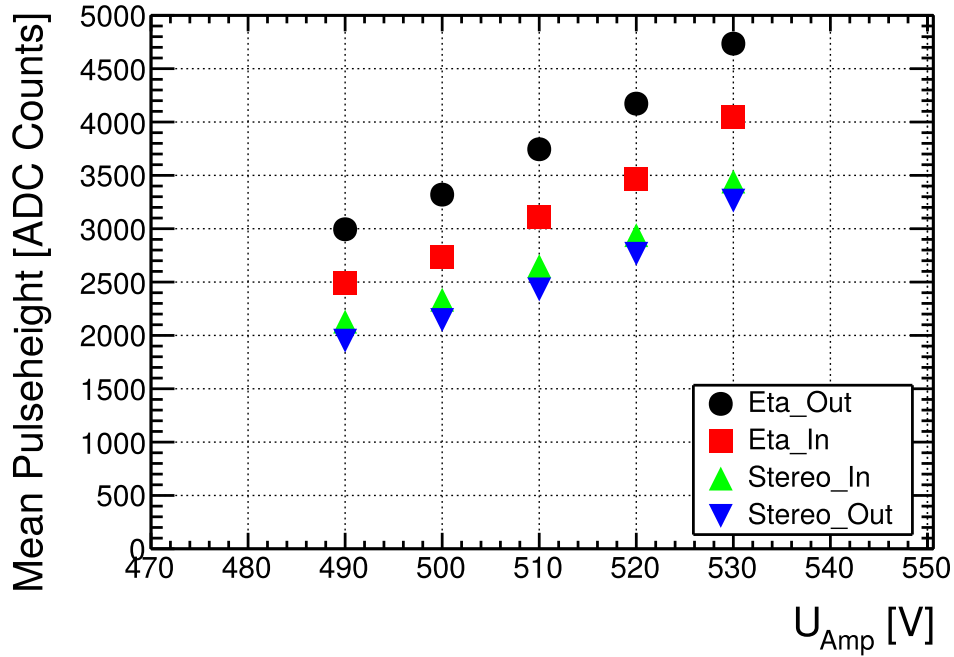


Figure 8.22: Mean pulse height of SM2 M03 with the Am-Be source as background. The effect of the source is clearly visible splitting up the individual layers and showing the highest pulse heights for the layers closer to the source (Eta_{Out} being closest). For all layers, the pulse height is still exponentially rising for increasing amplification voltages. Ar:CO₂:iC₄H₁₀ 93:5:2 vol%.

The influence of the source on the detector resolution is only minor with a decrease by 10 μm for the core (left) and weighted (right) resolutions as shown in figure 8.23. Since the source influence decreases strongly with distance (see figure 8.20), this effect on the overall resolution of the whole PCB is expected.

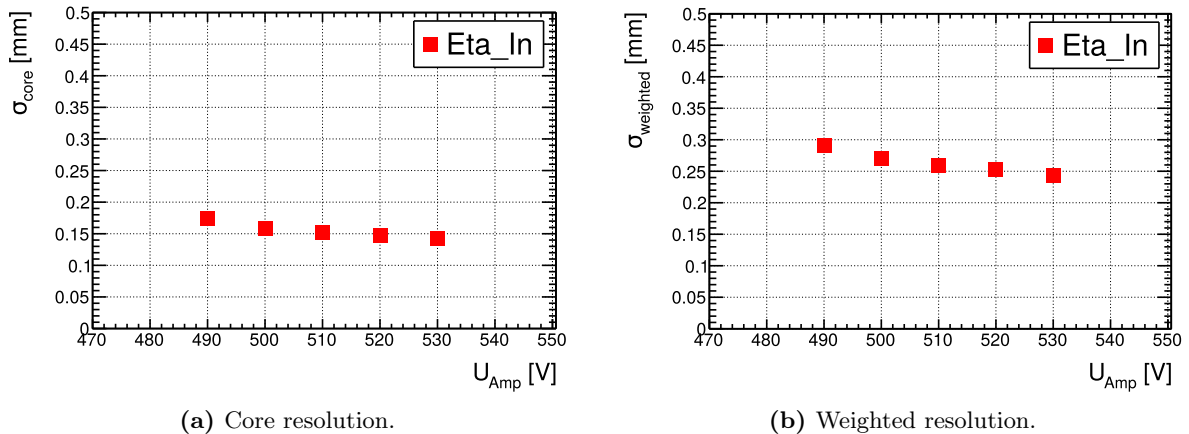


Figure 8.23: Cosmic muon detector resolutions with the Am-Be source as background. Core resolutions of $< 150 \mu\text{m}$ and weighted resolutions of $< 250 \mu\text{m}$ are reconstructed. In comparison with the resolutions without background (figure 8.17) a minor worsening of $< 10 \mu\text{m}$ is visible. Ar:CO₂:iC₄H₁₀ 93:5:2 vol%.

The same effect holds for the average detector efficiency that is depicted in figure 8.24. An overall decrease in the order of 5% compared to no background irradiation shown in figure 8.18, is observed. The position-dependent efficiency shows the local influence of the neutron source indicated by the black cross in figure 8.25.

While the efficiency in the upper part for $Y > 1100$ mm remains almost unaffected a clear worsening around the source center is observed. Since the readout is strip-based the source-induced readout problems as discussed in chapter 7.3 may occur and affect the efficiency along the whole X-axis.

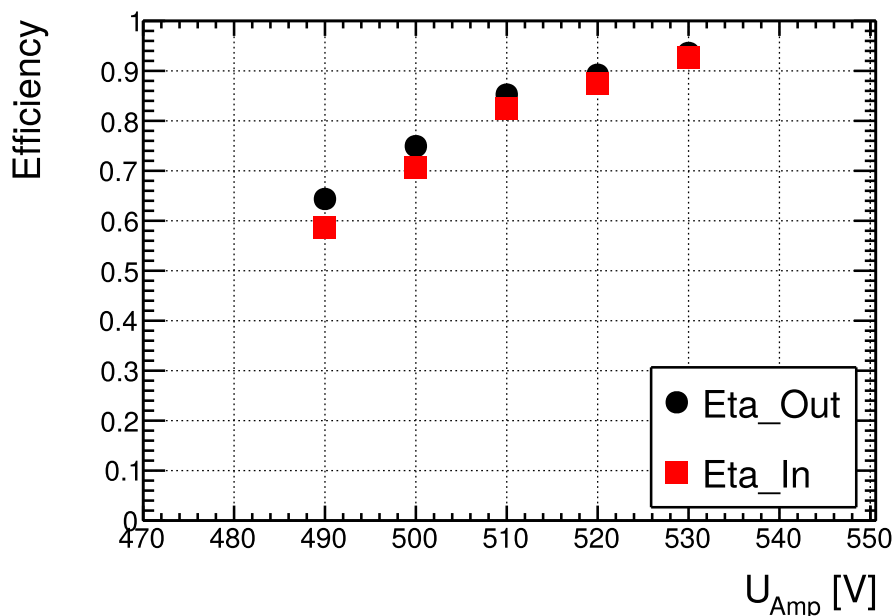


Figure 8.24: Efficiency for different values of U_{Amp} with the Am-Be source as background. An overall efficiency of $> 90\%$ can only be reached for the highest amplification voltage of 530 V showing similar decreases as seen in chapter 7. The foreseen working point is $U_{Amp} = 520$ V. Ar:CO₂:iC₄H₁₀ 93:5:2 vol%.

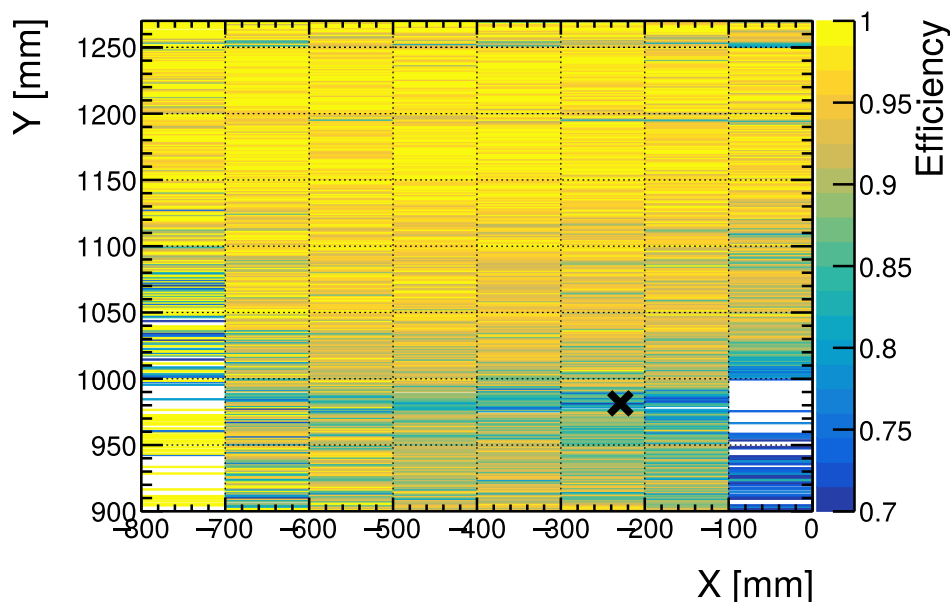


Figure 8.25: 2D efficiency distribution of η_{Out} with the neutron source as background (black cross).

A clear influence of the source is visible showing a local decrease of up to 20 % around the source. The source affects also the efficiency in the horizontal direction by inducing additional signals on the horizontal readout strips. Regions further away (above $Y=1150$ mm) remain unaffected with efficiencies $> 95\%$.

The region right of the source resembles the passivated area around the interconnection.

$U_{Amp} = 530$ V, Ar:CO₂:iC₄H₁₀ 93:5:2 vol%.

8.5 Conclusion Neutron Irradiation Studies

In this chapter the long-term irradiation of a NSW series Micromegas detector with an Am-Be neutron source was discussed.

The calibration of the source showed, that current densities similar to the expected HL-LHC background are achieved in an area with radius 50 mm around the source center.

Despite the highly ionizing neutron irradiation, no aging was observed. The detector efficiency after almost three years of irradiation still reaches 95%. Concerning the area facing the strongest irradiation, no decrease in efficiency compared to less irradiated areas was observed.

Cosmic muon measurements with the Am-Be source as additional background showed a similar influence of very high background rates on the detector efficiency as observed in the GIF++ (see chapter 7).

Combining the results for highly ionizing irradiation studies and the irradiation studies performed in the GIF++ no aging is observed in the NSW. No aging related issues are to be expected going into the HL-LHC era.

Chapter 9

Summary

In this thesis long-term irradiation studies of ATLAS NSW Micromegas detectors have been discussed.

Following the scaling from small Micromegas detectors to square-meter-sized detectors many challenges arose with the high-voltage stability being a central part. Many detectors operated with the legacy gas mixture, Ar:CO₂ 93:7 vol%, did not reach operating voltages or experienced constant discharges. Damages on the resistive anode resulting from these sparks were observed leading to possible deteriorations in terms of the long-term operation in the upcoming decade. A proposed solution was an adaptation of the operating gas to the ternary gas mixture Ar:CO₂iC₄H₁₀ 93:5:2 vol%.

Following the nature of hydrocarbon admixtures and experiences made in other large high-energy experiments, an extensive test of the new gas mixture on possible aging has been performed. Additionally, detector operation parameters like drift and amplification voltages are adapted. Two facilities, the GIF++ at CERN and the MLL in Munich, were chosen to carry out long-term irradiation tests accumulating charges on the detector equivalent to the expected values for HL-LHC.

Due to the different irradiation situation in the GIF++ compared to the operation at ATLAS a calibration of the irradiation strength provided by the 14 TBq GIF++ source was performed. The base of the rate calibration are the number of reconstructed clusters in the ATLAS sTGCs of the NSW and rate measurements in the GIF++ using a random trigger with the photon source at highest intensity. The hit rate at 1.8 m distance from the source is equal to the highest expected rate at the innermost part of the NSW closest to the LHC beam pipe.

Expected amounts of accumulated charges at HL-LHC are based on measured currents in the ATLAS detector, extrapolated to the operating voltage at GIF++ and accounting for the inhomogeneous irradiation intensity decreasing radially in the NSW. At the innermost part of the NSW charges of 0.068 C cm⁻²a⁻¹ at an amplification voltage of U_{Amp} = 520 V are expected at the HL-LHC operation with a luminosity of 7.5×10³⁴ cm⁻²s⁻¹. Charges equivalent to five years of operation are accumulated with the irradiation ongoing. No deteriorations of the high-voltage sectors or instabilities were observed.

Muon beams originating from the SPS are regularly delivered into the GIF++ allowing for performance tests with and without background provided from the GIF++ source during the irradiation period. For perpendicularly incident muons detector resolutions of $\sigma_{\text{core}} < 80 \mu\text{m}$ are achieved for no background. Including background rates equivalent and even higher than expected at HL-LHC the resolution worsens to $\approx 100 \mu\text{m}$.

Inclined tracks are reconstructed by two different methods. The μ TPC-like method is based on TPC detectors with the ionization position of the electrons being reconstructed inside the drift region exploiting the arrival time on the anode (see chapter 5.4.1). Resolutions of

$\sigma_{\text{core}} < 160 \mu\text{m}$ are achieved. This was the first time, that such good resolutions were obtained using large-area Micromegas detectors. An excellent timing calibration and the VMM readout ASIC were key to achieving this.

A second method utilizes the correlation between the charge-weighted cluster position and charge-weighted cluster time and corrects for it (see chapter 5.4.2), resulting in resolutions of $\sigma_{\text{core}} < 130 \mu\text{m}$ for $U_{\text{Amp}} = 530 \text{ V}$.

At background rates equivalent to $\approx 2 \times \text{HL-LHC}$ a saturation of the number of reconstructed clusters is observed originating from limitations of the readout electronics. Adaptation of the bias current of the VMM chip allows the recovery of many clusters. A remaining saturation at hit rates higher than HL-LHC equivalent values is observed.

The efficiency of the detectors reaches above 90% starting from $U_{\text{Amp}} = 500 \text{ V}$ for the ternary gas mixture. They reach a plateau of 98% at an amplification voltage of 520 V

Irradiation studies using an Am-Be source to provide a hadronic background were performed in Munich. Over the course of almost three years a series Micromegas detector was irradiated investigating the legacy Ar:CO₂ 93:7 vol% and the new ternary gas mixture showing an improvement in stability using the latter one. A calibration of the neutron source irradiation strength and intensity per area was performed showing an HL-LHC equivalent background rate in an area of radius 50 mm around the source center. Observed currents remained stable within environmental fluctuations that could be corrected for. Charges equivalent to multiple years of HL-LHC were accumulated in the central part around the source center. Performance tests after concluding the irradiation period using cosmic muons and internal tracking within the Micromegas detector showed no decrease in efficiency or spatial resolution compared to benchmark measurements carried out before irradiation. Overall a better performance using the new ternary gas mixture is observed resulting from the higher achievable pulse heights. No local decrease around the most strongly irradiated area was observed achieving a detector-wide efficiency $\epsilon > 95 \%$. Additional measurements including the Am-Be source as background showed the clear effect of the source with a local decrease in efficiency at the irradiated area ($\approx 75 \%$) similar to the GIF++ measurements with the background.

Concluding no sign of detector degradation and thus aging after the long-term irradiations are observed. In contrast, the detector performance improves concerning efficiency and resolution due to higher achievable gains using the new ternary gas mixture. According to the testbeam results, in the ATLAS NSW closest to the beam pipe small decreases in efficiency due to the strong background are expected at HL-LHC as a result of readout electronic limitations. This only holds for the innermost centimeters of the wheel, after that no decrease is expected. Over the whole HL-LHC period NSW Micromegas operated with a gas mixture of Ar:CO₂:iC₄H₁₀ 93:5:2 vol% are expected to perform well without deterioration providing the required efficiency and resolution.

Based on the results presented in this thesis the ATLAS collaboration decided to operate the NSW Micromegas under the ternary gas mixture of Ar:CO₂:iC₄H₁₀ 93:5:2 vol%.

List of Abbreviations

- ADC** Analog to Digital Converter
- ADDC** Address in Real Time Data Driver Card
- ALICE** A Large Ion Collider Experiment
- Am-Be** Americium-Beryllium
- ASIC** Application Specific Integrated Circuit
- ATLAS** A Toroidal LHC ApparatuS
- CDF** Collider Detector at Fermilab
- CERN** Conseil Européen pour la Recherche Nucléaire
- CA** Charge Amplifier
- CM** center-of-mass
- CMS** Compact Muon Solenoid
- CRF** Cosmic Ray Facility
- CSC** Cathode Strip Chambers
- CSDA** Continuous Slowing Down Approximation
- DAQ** Data AcQuisition
- FEC** Front-End Concentrator
- FELIX** Front End Link eXchange
- FPGA** Field-Programmable Gate Array
- GIF++** Gamma Irradiation Facility++
- HL-LHC** High-Luminosity LHC
- IBL** Insertable B-Layer
- L1DDC** Level 1 Data Driver Card
- LEP** Large Electron-Positron Collider
- LHC** Large Hadron Collider
- LHCb** Large Hadron Collider beauty

LINAC Linear Accelerator

LM1 Large Module 1

LM2 Large Module 2

MDT Monitored Drift Tube

MIPs Minimum Ionizing Particles

Micromegas MICRO-MEsh GAseous Structure

MLL Maier-Leibnitz-Laboratorium

MMFE8 MicroMegas Front-End with 8 VMM's

MPV Most Probable Value

NSW New Small Wheel

NIM Nuclear Instrumentation Standard

PCB Printed Circuit Board

PDO Peak Detector Output

PS Proton Synchrotron

ROC Read-Out Controller

RPC Resistive Plate Chambers

SCA Slow Control Adapter

SCT Semiconductor Tracker

SM1 Small Module 1

SM2 Small Module 2

SPS Super Proton Synchrotron

SRS Scalable Readout System

SRU Scalable Readout Unit

sTGCs Small-Strip Thin Gap Chambers

swROD SoftWare ReadOut Driver

TAC Time-to-Amplitude Converter

TDO Time Detector Output

TDR Technical Design Report

TGC Thin Gap Chambers

TPC Time Projection Chamber

TRT Transition Radiation Tracker

TTC Timing, Trigger and Control

Bibliography

- [Aberle et al.(2020)] Aberle, O., Béjar Alonso, I, Brüning, O, et al. *High-Luminosity Large Hadron Collider (HL-LHC): Technical design report*. CERN Yellow Reports: Monographs. CERN, Geneva, 2020. doi:10.23731/CYRM-2020-0010. URL <https://cds.cern.ch/record/2749422>.
- [Alexopoulos et al.(2015)] Alexopoulos, T., Amelung, C., Iakovidis, G., et al. Stereo Information in Micromegas Detectors. Technical report, CERN, Geneva, 2015. URL <https://cds.cern.ch/record/2052206>. All figures including auxiliary figures are available at <https://atlas.web.cern.ch/Atlas/GROUPS/PHYSICS/PUBNOTES/ATL-MUON-PUB-2015-001>.
- [Alexopoulos et al.(2011)] Alexopoulos, T., Burnens, J., de Oliveira, R., et al. A spark-resistant bulk-micromegas chamber for high-rate applications. *Nuclear Instruments and Methods in Physics Research Section A: Accelerators, Spectrometers, Detectors and Associated Equipment*, 640(1):110–118, 2011. ISSN 0168-9002. doi:<https://doi.org/10.1016/j.nima.2011.03.025>. URL <https://www.sciencedirect.com/science/article/pii/S0168900211005869>.
- [Arnison et al.(1983a)] Arnison, G., Astbury, A., Aubert, B., et al. Experimental observation of isolated large transverse energy electrons with associated missing energy at $s=540$ gev. *Physics Letters B*, 122(1):103–116, 1983a. ISSN 0370-2693. doi:[https://doi.org/10.1016/0370-2693\(83\)91177-2](https://doi.org/10.1016/0370-2693(83)91177-2). URL <https://www.sciencedirect.com/science/article/pii/0370269383911772>.
- [Arnison et al.(1983b)] Arnison, G., Astbury, A., Aubert, B., et al. Experimental observation of lepton pairs of invariant mass around 95 gev/c² at the cern sps collider. *Physics Letters B*, 126(5):398–410, 1983b. ISSN 0370-2693. doi:[https://doi.org/10.1016/0370-2693\(83\)90188-0](https://doi.org/10.1016/0370-2693(83)90188-0). URL <https://www.sciencedirect.com/science/article/pii/0370269383901880>.
- [Basiri and Tavakoli-Anbaran(2018)] Basiri, H. and Tavakoli-Anbaran, H. Investigation of some possible changes in am-be neutron source configuration in order to increase the thermal neutron flux using monte carlo code. *Journal of Physics: Conference Series*, 956(1):012010, 2018. doi:10.1088/1742-6596/956/1/012010. URL <https://dx.doi.org/10.1088/1742-6596/956/1/012010>.
- [Berger et al.(2010)] Berger, M.J., Hubbell, J.H., and Seltzer, S.M. Xcom: Photon cross sections database. 2010. doi:10.18434/T48G6X. URL <https://dx.doi.org/10.18434/T48G6X>.
- [Biagi(2023)] Biagi, S. Magboltz - transport of electrons in gas mixtures. 2023. URL <https://magboltz.web.cern.ch/magboltz/>.
- [Binkley et al.(2003)] Binkley, M., Wagner, R.L., Mukherjee, A., et al. Aging in large cdf tracking chambers. *Nuclear Instruments and Methods in Physics Research Section A: Accelerators, Spectrometers, Detectors and Associated Equipment*, 515(1):53–59, 2003. ISSN 0168-9002.

- doi:<https://doi.org/10.1016/j.nima.2003.08.130>. URL <https://www.sciencedirect.com/science/article/pii/S0168900203024513>. Proceedings of the International Workshop on Aging Phenomena in Gaseous Detectors.
- [Bortfeldt(2014)] Bortfeldt, J. Development of floating strip micromegas detectors. 2014. URL <http://nbn-resolving.de/urn:nbn:de:bvb:19-169727>.
- [Brice and Ordan(2021)] Brice, M. and Ordan, J. M. New Small Wheel (NSW) descent into ATLAS' "side A" of the experimental cavern. 2021. URL <https://cds.cern.ch/record/2775525>. General Photo.
- [Cai et al.(2017)] Cai, H., Koi, T., Martinez Outschoorn, V., et al. Sensitivity of micromegas to photons and neutrons in the atlas new small wheel. Technical report, CERN, Geneva, 2017. URL <https://cds.cern.ch/record/2281463>. Internal document (restricted access).
- [Capeans et al.(2010)] Capeans, M., Darbo, G., Einsweiler, K., et al. ATLAS Insertable B-Layer Technical Design Report. Technical report, 2010. URL <https://cds.cern.ch/record/1291633>.
- [Carnegie et al.(2005)] Carnegie, R.K., Dixit, M.S., Dubeau, J., et al. Resolution studies of cosmic-ray tracks in a tpc with gem readout. *Nuclear Instruments and Methods in Physics Research Section A: Accelerators, Spectrometers, Detectors and Associated Equipment*, 538(1):372–383, 2005. ISSN 0168-9002. doi:<https://doi.org/10.1016/j.nima.2004.08.132>. URL <https://www.sciencedirect.com/science/article/pii/S0168900204021023>.
- [Cecchetto et al.(2021)] Cecchetto, M., Alia, R., Wrobel, F., et al. 0.1-10 mev neutron soft error rate in accelerator and atmospheric environments. *IEEE Transactions on Nuclear Science*, PP:1–1, 2021. doi:10.1109/TNS.2021.3064666.
- [CERN(1996a)] CERN. *ATLAS liquid-argon calorimeter: Technical Design Report*. Technical design report. ATLAS. CERN, Geneva, 1996a. doi:10.17181/CERN.FWRW.FOOQ. URL <http://cds.cern.ch/record/331061>.
- [CERN(1996b)] CERN. *ATLAS tile calorimeter: Technical Design Report*. Technical design report. ATLAS. CERN, Geneva, 1996b. doi:10.17181/CERN.JRBJ.7O28. URL <http://cds.cern.ch/record/331062>.
- [CERN(1997a)] CERN. *ATLAS inner detector: Technical Design Report, 1*. Technical design report. ATLAS. CERN, Geneva, 1997a. URL <http://cds.cern.ch/record/331063>.
- [CERN(1997b)] CERN. *ATLAS magnet system: Technical Design Report, 1*. Technical design report. ATLAS. CERN, Geneva, 1997b. doi:10.17181/CERN.9O5C.VDTM. URL <http://cds.cern.ch/record/338080>.
- [CERN(1997c)] CERN. *ATLAS muon spectrometer: Technical Design Report*. Technical design report. ATLAS. CERN, Geneva, 1997c. URL <http://cds.cern.ch/record/331068>.
- [CERN(2012)] CERN. Cern experiments observe particle consistent with long-sought higgs boson. 2012. URL <https://home.cern/news/press-release/cern/cern-experiments-observe-particle-consistent-long-sought-higgs-boson>.
- [CERN(2017a)] CERN. ATLAS Liquid Argon Calorimeter Phase-II Upgrade: Technical Design Report. Technical report, CERN, Geneva, 2017a. doi:10.17181/CERN.6QJO.YGHO. URL <http://cds.cern.ch/record/2285582>.

- [CERN(2017b)] CERN. Technical Design Report for the ATLAS Inner Tracker Pixel Detector. Technical report, CERN, Geneva, 2017b. doi:10.17181/CERN.FOZZ.ZP3Q. URL <http://cds.cern.ch/record/2285585>.
- [CERN(2017c)] CERN. Technical Design Report for the ATLAS Inner Tracker Strip Detector. Technical report, CERN, Geneva, 2017c. URL <http://cds.cern.ch/record/2257755>.
- [CERN(2017d)] CERN. Technical Design Report for the Phase-II Upgrade of the ATLAS Muon Spectrometer. Technical report, CERN, Geneva, 2017d. URL <http://cds.cern.ch/record/2285580>.
- [CERN(2017e)] CERN. Technical Design Report for the Phase-II Upgrade of the ATLAS Tile Calorimeter. Technical report, CERN, Geneva, 2017e. URL <http://cds.cern.ch/record/2285583>.
- [CERN(2023a)] CERN. Alice. 2023a. URL <https://home.cern/science/experiments/alice>.
- [CERN(2023b)] CERN. High-luminosity lhc. 2023b. URL <https://home.cern/science/accelerators/high-luminosity-lhc>.
- [CERN(2023c)] CERN. Lhcb. 2023c. URL <https://home.cern/science/experiments/lhcb>.
- [Chiodini(2012)] Chiodini, G. ATLAS RPC time-of-flight performance. *PoS*, RPC2012:007, 2012. doi:10.22323/1.159.0007.
- [Costrell et al.(1990)] Costrell, L., Lenkszus, F. R., Rudnick, S. J., et al. Standard nim instrumentation system. 1990. doi:10.2172/7120327. URL <https://www.osti.gov/biblio/7120327>.
- [Cranberg et al.(1956)] Cranberg, L., Frye, G., Nereson, N., et al. Fission neutron spectrum of u^{235} . *Phys. Rev.*, 103:662–670, 1956. doi:10.1103/PhysRev.103.662. URL <https://link.aps.org/doi/10.1103/PhysRev.103.662>.
- [Croft(1989)] Croft, S. The use of neutron intensity calibrated $9\text{be}(\alpha, n)$ sources as 4438 keV gamma-ray reference standards. *Nuclear Instruments and Methods in Physics Research Section A: Accelerators, Spectrometers, Detectors and Associated Equipment*, 281(1):103–116, 1989. ISSN 0168-9002. doi:[https://doi.org/10.1016/0168-9002\(89\)91221-7](https://doi.org/10.1016/0168-9002(89)91221-7). URL <https://www.sciencedirect.com/science/article/pii/0168900289912217>.
- [de Geronimo et al.(2022)] de Geronimo, G., Iakovidis, G., Martoiu, S., et al. The vmm3a ASIC. *IEEE Transactions on Nuclear Science*, 69(4):976–985, 2022. doi:10.1109/TNS.2022.3155818.
- [Dupont(2023)] Dupont. Kapton® polyimide films. 2023. URL <https://www.dupont.com/electronics-industrial/kapton-polyimide-film.html>.
- [Egli(2023)] Egli, F. Upgrading the cosmic ray facility for tests of the phase-II upgrade of the ATLAS muon spectrometer. 2023. URL https://www.etp.physik.uni-muenchen.de/publications/theses/download/master_fegli.pdf.
- [Einstein(1905)] Einstein, A. Über einen die Erzeugung und Verwandlung des Lichtes betreffenden heuristischen Gesichtspunkt. *Annalen der Physik*, 322(6):132–148, 1905. doi:<https://doi.org/10.1002/andp.19053220607>. URL <https://onlinelibrary.wiley.com/doi/10.1002/andp.19053220607>.
- [Fallavollita and Iengo(2022)] Fallavollita, F. and Iengo, P. Transparency and ion backflow measurements on lm2-m40 chamber at the gif++ facility, 2022. (Unpublished).

- [Ferguson et al.(2002)] Ferguson, T., Gavrilov, G., Korytov, A., et al. Aging studies of cms muon chamber prototypes. *Nuclear Instruments and Methods in Physics Research Section A: Accelerators, Spectrometers, Detectors and Associated Equipment*, 488(1):240–257, 2002. ISSN 0168-9002. doi:[https://doi.org/10.1016/S0168-9002\(02\)00400-X](https://doi.org/10.1016/S0168-9002(02)00400-X). URL <https://www.sciencedirect.com/science/article/pii/S016890020200400X>.
- [Flierl(2018)] Flierl, B. Particle tracking with micro-pattern gaseous detectors. 2018. URL <http://nbn-resolving.de/urn:nbn:de:bvb:19-221980>.
- [Flierl(2014)] Flierl, B.M. Tracking of photons and detection of thermal neutrons with a gem-detector. 2014. URL https://www.etp.physik.uni-muenchen.de/publications/theses/download/master_bflierl.pdf.
- [Galilei(1638)] Galilei, G. *Dialogues Concerning Two New Sciences*. 1638. Translated by Crew, H. and de Salvio, Alfonso (1914) Macmillan, New York.
- [Giomataris et al.(1996)] Giomataris, Y., Rebourgeard, Ph., Robert, J.P., et al. Micromegas: a high-granularity position-sensitive gaseous detector for high particle-flux environments. *Nuclear Instruments and Methods in Physics Research Section A: Accelerators, Spectrometers, Detectors and Associated Equipment*, 376(1):29–35, 1996. ISSN 0168-9002. doi:[https://doi.org/10.1016/0168-9002\(96\)00175-1](https://doi.org/10.1016/0168-9002(96)00175-1). URL <https://www.sciencedirect.com/science/article/pii/0168900296001751>.
- [Herrmann(2019)] Herrmann, M. Series calibration of segmented and multi-layered micromegas modules for atlas. 2019. URL https://www.etp.physik.uni-muenchen.de/publications/theses/download/phd_mherrmann.pdf.
- [Hesse(1865)] Hesse, O. *Vorlesungen aus der analytischen Geometrie der geraden Linie, des Punktes und des Kreises in der Ebene*. Teubner, Leipzig, 1865. URL https://books.google.de/books?id=at6qA3g2YDwC&redir_esc=y.
- [Horvat(2005)] Horvat, S. Study of the Higgs Discovery Potential in the Process $pp \rightarrow H \rightarrow 4\mu$. 2005. URL <https://cds.cern.ch/record/858509>. Presented on 11 Apr 2005.
- [Hough(1959)] Hough, P. V. C. Machine Analysis of Bubble Chamber Pictures. *Conf. Proc. C*, 590914:554–558, 1959.
- [Iakovidis(2014)] Iakovidis, G. Research and Development in Micromegas Detector for the ATLAS Upgrade. 2014. URL <https://cds.cern.ch/record/1955475>. Presented 13 Oct 2014.
- [Iakovidis(2022)] Iakovidis, G. The VMM3a User’s Guide. Technical report, CERN, Geneva, 2022. URL <https://cds.cern.ch/record/2807691>. All figures including auxiliary figures are available at <https://atlas.web.cern.ch/Atlas/GROUPS/PHYSICS/PUBNOTES/ATL-MUON-PUB-2022-002>.
- [Iakovidis et al.(2023)] Iakovidis, G., Levinson, L., and Afik, Y. The new small wheel electronics. *Journal of Instrumentation*, 18(05):P05012, 2023. doi:10.1088/1748-0221/18/05/p05012. URL <https://doi.org/10.1088%2F1748-0221%2F18%2F05%2Fp05012>.
- [Iodice et al.(2023)] Iodice, M., Kabana, S., Rosati, S., et al. New Small Wheel Performance plots based on 2022 Data. Technical report, CERN, Geneva, 2023. URL <https://cds.cern.ch/record/2869618>.
- [Jaekel et al.(2015)] Jaekel, M. R., Capeans, M., Efthymiopoulos, I., et al. CERN-GIF++: a new irradiation facility to test large-area particle detectors for the high-luminosity LHC program. *PoS, TIPP2014:102*, 2015. doi:10.22323/1.213.0102.

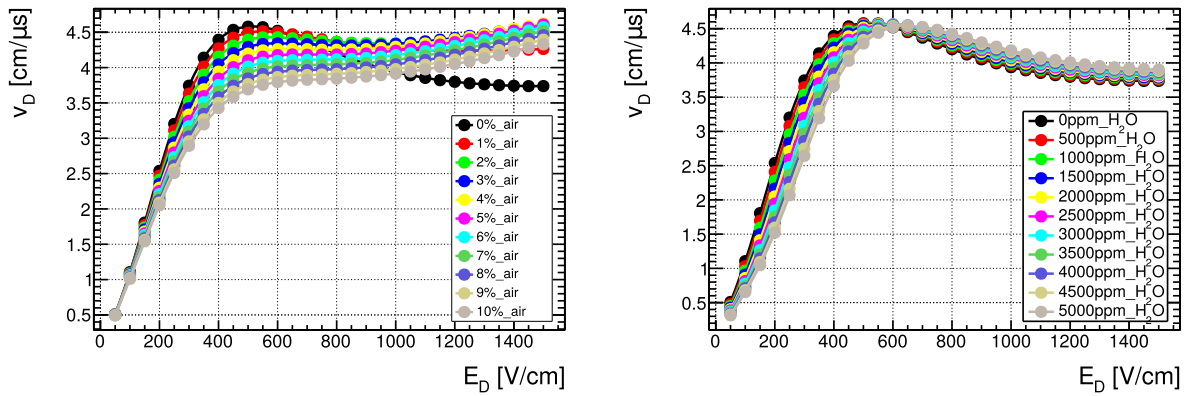
- [Jagfeld(2023)] Jagfeld, C. Research and development of a segmented gem readout detector. 2023. URL <http://nbn-resolving.de/urn:nbn:de:bvb:19-318945>.
- [Jones et al.(1999)] Jones, L. L., French, M. J., Morrissey, Q. R., et al. The APV25 deep submicron readout chip for CMS detectors. 1999. doi:10.5170/CERN-1999-009.162. URL <https://cds.cern.ch/record/432224>.
- [Kawamoto et al.(2013)] Kawamoto, T., Vlachos, S., Pontecorvo, L., et al. New small wheel technical design report. Technical report, 2013. URL <http://cds.cern.ch/record/1552862>. ATLAS New Small Wheel Technical Design Report.
- [Kleinknecht(1992)] Kleinknecht, K. *Detektoren für Teilchenstrahlung*. Vieweg+Teubner Verlag, Wiesbaden, 1992. ISBN 3-519-23058-5. doi:10.1007/978-3-322-94130-5.
- [Klitzner(2019)] Klitzner, F. Development of novel two-dimensional floating strip micromegas detectors with an in-depth insight into the strip signal formation. 2019. URL <http://nbn-resolving.de/urn:nbn:de:bvb:19-242860>.
- [Kolanoski and Wermes(2016)] Kolanoski, H. and Wermes, N. *Teilchendetektoren*. Springer, Berlin, Heidelberg, 2016. ISBN 978-3-662-45350-6. doi:<https://doi.org/10.1007/978-3-662-45350-6>. URL <https://link.springer.com/book/10.1007/978-3-662-45350-6>.
- [Kolitsi et al.(2023)] Kolitsi, F., Alexopoulos, T., D’Amico, V., et al. Performance of micromegas electronics in a high-radiation environment. In *2023 12th International Conference on Modern Circuits and Systems Technologies (MOCASST)*, pages 1–4. 2023. doi:10.1109/MOCASST57943.2023.10176380.
- [Korff(1946)] Korff, S. A. Electron and nuclear counters theory and use. 1946.
- [Koulouris(2019)] Koulouris, A. Performance characterization of the NSW Micromegas detector, services design and development of the Slow Control Adapter for the ATLAS upgrade. Μελέτη της απόδοσης των Ανιχνευτών NSW Micromegas, Σχεδιασμός των Υπηρεσιακών Συστημάτων και Ανάπτυξη του Slow Control Adapter για την αναβάθμιση του Πειράματος LHC-ATLAS. 2019. URL <https://cds.cern.ch/record/2675805>. Presented 21 May 2019.
- [Kuger(2017)] Kuger, F. *Signal Formation Processes in Micromegas Detectors and Quality Control for large size Detector Construction for the ATLAS New Small Wheel*. doctoralthesis, Universität Würzburg, 2017.
- [Kumar(2023)] Kumar, E. Cosmic muon tracking with micromegas detectors and neutron source characterisation. 2023. URL https://www.etp.physik.uni-muenchen.de/publications/theses/download/master_ekumar.pdf.
- [Landau and Lifshitz(1977)] Landau, L.D. and Lifshitz, E.M. Chapter xiii - polyatomic molecules. In L.D. Landau and E.M. Lifshitz, editors, *Quantum Mechanics (Third Edition)*, pages 396–430. Pergamon, third edition edition, 1977. ISBN 978-0-08-020940-1. doi:<https://doi.org/10.1016/B978-0-08-020940-1.50020-7>. URL <https://www.sciencedirect.com/science/article/pii/B9780080209401500207>.
- [Landua(2022)] Landua, F. The CERN accelerator complex layout in 2022. Complexe des accélérateurs du CERN en janvier 2022. 2022. URL <http://cds.cern.ch/record/2813716>. General Photo.
- [Leo(1994)] Leo, W. R. Techniques for nuclear and particle physics experiments. (2), 1994. doi:<https://doi.org/10.1007/978-3-642-57920-2>.

- [Lippert(2012)] Lippert, B. Studien zur signalentstehung undparametrisierung dergasverstärkung in einem micromegas detektor. 2012. URL https://www.etp.physik.uni-muenchen.de/publications/bachelor/download_auth_etp/bac12_blippert.pdf. (restricted access).
- [Lösel(2017)] Lösel, P. Precision calibration of large area micro pattern gaseous detectors. 2017. URL <http://nbn-resolving.de/urn:nbn:de:bvb:19-212513>.
- [Marion and Fowler(1960)] Marion, J.B. and Fowler, J.L. Fast neutron physics part 1. *Science*, 132(3427):613–614, 1960. doi:10.1126/science.132.3427.613. URL <https://www.science.org/doi/abs/10.1126/science.132.3427.613>.
- [Martoiu et al.(2013)] Martoiu, S., Muller, H., Tarazona, A., et al. Development of the scalable readout system for micro-pattern gas detectors and other applications. *Journal of Instrumentation*, 8(03):C03015, 2013. doi:10.1088/1748-0221/8/03/C03015. URL <https://dx.doi.org/10.1088/1748-0221/8/03/C03015>.
- [Newton(1687)] Newton, I. *Philosophiae naturalis principia mathematica*. J. Societatis Regiae ac Typis J. Streater, 1687. URL <https://books.google.de/books?id=-dVKAQAIAAJ>.
- [Pequenao(2008a)] Pequenao, J. Computer Generated image of the ATLAS calorimeter, 2008a. URL <http://cds.cern.ch/record/1095927>.
- [Pequenao(2008b)] Pequenao, J. Computer generated image of the ATLAS inner detector, 2008b. URL <https://cds.cern.ch/record/1095926>.
- [Pequenao(2008c)] Pequenao, J. Computer generated image of the whole ATLAS detector, 2008c. URL <https://cds.cern.ch/record/1095924>.
- [Perkins et al.(1991)] Perkins, S., Cullen, D., and Seltzer, S. Tables and graphs of electron-interaction cross sections from 10 ev to 100 gev derived from the lnl evaluated electron data library (eedl), $z = 1$ to 100. 1991. doi:10.2172/5691165.
- [Pfeiffer et al.(2017)] Pfeiffer, D., Gorine, G., Reithler, H., et al. The radiation field in the gamma irradiation facility gif++ at cern. *Nuclear Instruments and Methods in Physics Research Section A: Accelerators, Spectrometers, Detectors and Associated Equipment*, 866:91–103, 2017. ISSN 0168-9002. doi:<https://doi.org/10.1016/j.nima.2017.05.045>. URL <https://www.sciencedirect.com/science/article/pii/S0168900217306113>.
- [Raether(1964)] Raether, H. Electron avalanches and breakdown in gases. 1964.
- [Ramo(1939)] Ramo, S. Currents induced by electron motion. *Proceedings of the IRE*, 27(9):584–585, 1939. doi:10.1109/JRPROC.1939.228757.
- [Ramsauer and Kollath(1929)] Ramsauer, C. and Kollath, R. Über den wirkungsquerschnitt der edelgasmoleküle gegenüber elektronen unterhalb 1 volt. *Annalen der Physik*, 395(4):536–564, 1929. doi:<https://doi.org/10.1002/andp.19293950405>. URL <https://onlinelibrary.wiley.com/doi/abs/10.1002/andp.19293950405>.
- [Rossi and Brüning(2012)] Rossi, L. and Brüning, O. High Luminosity Large Hadron Collider: A description for the European Strategy Preparatory Group. Technical report, CERN, Geneva, 2012. URL <https://cds.cern.ch/record/1471000>.
- [Sauli(2023)] Sauli, F. Gas counters aging for dummies. 2023. URL <https://indico.cern.ch/event/1237829/contributions/5637193/attachments/2746235/4778596/AGING%20FOR%20DUMMIES.pdf>. Conference Talk (restricted access), not yet published.

- [Shockley(2004)] Shockley, W. Currents to Conductors Induced by a Moving Point Charge. *Journal of Applied Physics*, 9(10):635–636, 2004. ISSN 0021-8979. doi:10.1063/1.1710367. URL <https://doi.org/10.1063/1.1710367>.
- [Sidiropoulou(2018)] Sidiropoulou, O. Characterization of the ATLAS-type Micromegas Detectors. Charakterisierung von Micromegas-Detektoren des ATLAS-Typs. 2018. URL <https://cds.cern.ch/record/2636918>. Presented 03 Aug 2018.
- [Titov(2004)] Titov, M. Radiation Damage and Long-Term Aging in Gas Detectors. *ICFA Instrument. Bull.*, 26:002, 2004. doi:10.1142/9789812702951_0014. URL <https://cds.cern.ch/record/722642>.
- [Townsend(1910)] Townsend, J. The theory of ionization of gases by collision. 1910.
- [Vandenbroucke(2019)] Vandenbroucke, M. Optimisation of gas composition for micromegas of the atlas experiment. 2019. doi:10.13140/RG.2.2.16706.09926. URL https://www.researchgate.net/publication/349533057_OPTIMISATION_OF_GAS_COMPOSITION_FOR_MICROMEGAS_OF_THE_ATLAS_EXPERIMENT.
- [Vasil'Ev et al.(1958)] Vasil'Ev, S., Komarov, V., and Popova, A. Dissociation of c12 into three alpha particles induced by fast neutrons. *Journal of Experimental and Theoretical Physics - J EXP THEOR PHYS*, 6, 1958.
- [Veenhof(2010)] Veenhof, R. Garfield - simulation of gaseous detectors. 2010. URL <https://garfield.web.cern.ch/garfield/>.
- [Vogel(2021)] Vogel, F. Test of ATLAS Micromegas detectors with ternary gas mixture at the CERN GIF++ facility. Technical report, CERN, Geneva, 2021. URL <https://cds.cern.ch/record/2775631>. Internal document (restricted access).
- [Vogel et al.(2023)] Vogel, F., Biebel, O., Jagfeld, C., et al. Long term neutron irradiation studies of square meter sized resistive strip micromegas detectors. *Nuclear Instruments and Methods in Physics Research Section A: Accelerators, Spectrometers, Detectors and Associated Equipment*, 1045:167653, 2023. ISSN 0168-9002. doi:<https://doi.org/10.1016/j.nima.2022.167653>. URL <https://www.sciencedirect.com/science/article/pii/S0168900222009457>.
- [Vogel(2022)] Vogel, F. on behalf of the ATLAS Muon Collaboration. Test of ATLAS Micromegas detectors with ternary gas mixture at the CERN GIF++ facility. *PoS, EPS-HEP2021:757*, 2022. doi:10.22323/1.398.0757.
- [Winberg and Garcia(1995)] Winberg, M.R. and Garcia, R.S. National low-level waste management program radionuclide report series. 14: Americium-241, 1995. URL https://inis.iaea.org/collection/NCLCollectionStore/_Public/27/032/27032341.pdf.
- [Wirtz and Beckurts(1958)] Wirtz, K. and Beckurts, K.H. *Elementare Neutronenphysik*. Springer, Berlin, Heidelberg, 1958. ISBN 978-3-662-23764-9. doi:10.1007/978-3-662-25867-5.
- [Workman et al.(2022)] Workman, R. L., Burkert, V. D., Crede, V., et al. Review of Particle Physics. *Progress of Theoretical and Experimental Physics*, 2022(8):083C01, 2022. ISSN 2050-3911. doi:10.1093/ptep/ptac097. URL <https://doi.org/10.1093/ptep/ptac097>.

Appendix A

Simulated Electron Drift Velocity for Polluted Detector Gas



(a) Simulated drift velocity for different percentages of air pollution in the detector gas. With increased pollution, the drift velocity at operation voltage (480 V/cm) decreases.

(b) Simulated drift velocity for different contents of water pollution (given in units of ppm) in the detector gas. With increased pollution, the drift velocity at operation voltage (480 V/cm) decreases.

Figure A.1: Effect of different types of detector gas pollution on the electron drift velocity simulated using MAGBOLTZ (Biagi [2023] in Garfield++ (Veenhof [2010])). The operating gas is Ar:CO₂:iC₄H₁₀ 93:5:2 vol%.

Appendix B

VMM Registers

Global bits (defaults are 0)	Description
s32	skips channels 16-47 and makes 15 and 48 neighbors
stlc	enables mild tail cancellation (when enabled, overrides sbip)
srec	enables fast recovery from high charge
sbip	enables bipolar shape
srat	enables timing ramp at threshold
sfrst	enables fast reset at 6-b completion
slvsbc	enable slvs 100 Ω termination on ckbc
slvstp	enable slvs 100 Ω termination on cktp
slvstk	enable slvs 100 Ω termination on cktk
slvsdt	enable slvs 100 Ω termination on ckdt
slvsart	enable slvs 100 Ω termination on kart
slvstki	enable slvs 100 Ω termination on cktki
slvsena	enable slvs 100 Ω termination on kena
slvs6b	enable slvs 100 Ω termination on ck6b
sL0enaV	disable mixed signal functions when L0 enabled
reset reset	Hard reset when both high
sL0ena	enable L0 core / reset core & gate clk if 0
l0offset_i0:11	L0 BC offset
offset_i0:11	Channel tagging BC offset
rollover_i0:11	Channel tagging BC rollover
window_i0:2	Size of trigger window
truncate_i0:5	Max hits per L0
nskip_i0:6	Number of L0 triggers to skip on overflow
sL0cktest	enable clocks when L0 core disabled (test)
sL0ckinv	invert BCCLK
sL0dckinv	invert DCK
nskipm_i	magic number on BCID - 0xFE8
slh, slxh	increases bias current at input node from nominal 1nA to 15nA or 300nA respectively
stgc	extreme charge handling compensation

Figure B.1: Configuration registers of the VMM3a ASIC.

Adapting the slh register, a faster recovery of the baseline is possible improving the operation at very high backgrounds¹.

¹Taken from Iakovidis [2022].

Global bits (defaults are 0)	Description
sp	input charge polarity ([0] negative, [1] positive)
sdp	disable-at-peak
sbmx	routes analog monitor to PDO output
sbft [0 1], sbfp [0 1], sbfm [0 1]	analog output buffers, [1] enable (TDO, PDO, MO)
slg	leakage current disable ([0] enabled)
sm5-sm0, scmx	monitor multiplexing. <ul style="list-style-type: none"> • Common monitor: scmx, sm5-sm0 [0 000001 to 000100], pulser DAC (after pulser switch), threshold DAC, band-gap reference, temperature sensor) • channel monitor: scmx, sm5-sm0 [1 000000 to 111111], channels 0 to 63
sfa [0 1], sfam [0 1]	ART enable (sfa [1]) and mode (sfam [0] timing at threshold, [1] timing at peak)
st1,st0 [00 01 10 11]	peaktime (200, 100, 50, 25 ns)
sfm [0 1]	enables full-mirror (AC) and high-leakage operation (enables SLH)
sg2,sg1,sg0 [000:111]	gain (0.5, 1, 3, 4.5, 6, 9, 12, 16 mV/fC)
sng	neighbor (channel and chip) triggering enable
stot [0 1]	timing outputs control 1 (s6b must be disabled) <ul style="list-style-type: none"> • stpp,stot[00,01,10,11]: TtP,ToT,PtP,PtT • TtP: threshold-to-peak • ToT: time-over-threshold • PtP: pulse-at-peak (10ns) (not available with s10b) • PtT: peak-to-threshold (not available with s10b)
sttt [0 1]	enables direct-output logic (both timing and s6b)
ssh [0 1]	enables sub-hysteresis discrimination
stc1,stc0 [00 01 10 11]	TAC slope adjustment (60, 100, 350, 650 ns)
sdt9-sdt0 [0:0 through 1:1]	coarse threshold DAC
sdp9-sdp0 [0:0 through 1:1]	test pulse DAC
sc010b,sc110b	10-bit ADC conv. time (increase subtracts 60 ns)
sc08b,sc18b	8-bit ADC conv. time (increase subtracts 60 ns)
sc06b, sc16b, sc26b	6-bit ADC conversion time
s8b	8-bit ADC conversion mode
s6b	enables 6-bit ADC (requires sttt enabled)
s10b	enables high resolution ADCs (10/8-bit ADC enable)
sdcks	dual clock edge serialized data enable
sdcka	dual clock edge serialized ART enable
sdck6b	dual clock edge serialized 6-bit enable
sdrv	tristates analog outputs with token, used in analog mode
stpp [0 1]	timing outputs control 2
slvs	enables direct output IOs
stcr	enables auto-reset (at the end of the ramp, if no stop occurs)
ssart	enables ART flag synchronization (trail to next trail)

Figure B.2: see B.1.

Appendix C

Additional Beamtime Plots

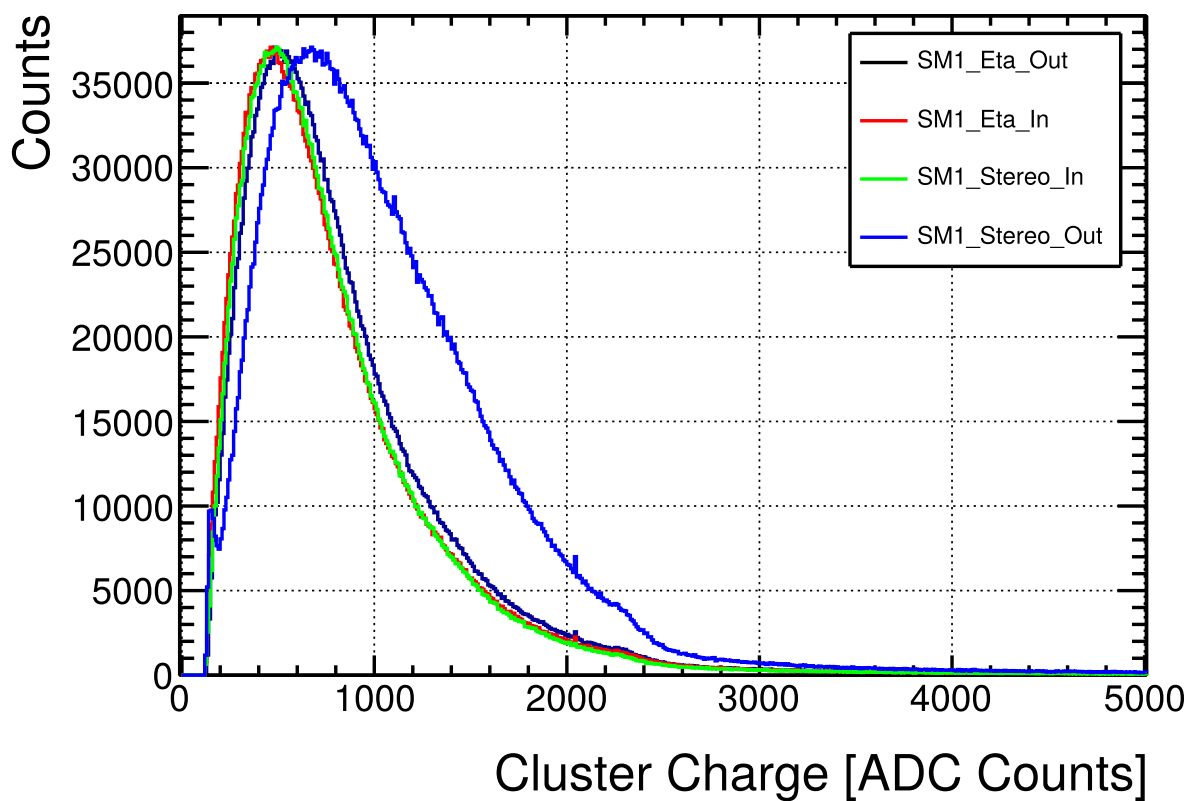


Figure C.1: Comparison of the cluster charge distributions for the four layers of SM1 M40. Stereo_{Out} shows higher cluster charges than the other three layers. This effect is visible in the higher current drawn by this sector suggesting a higher gain of this layer. $U_{\text{Amp}} = 520 \text{ V}$, $p_t = 200 \text{ ns}$, $VMM_{\text{RMS}} = 9\sigma$.

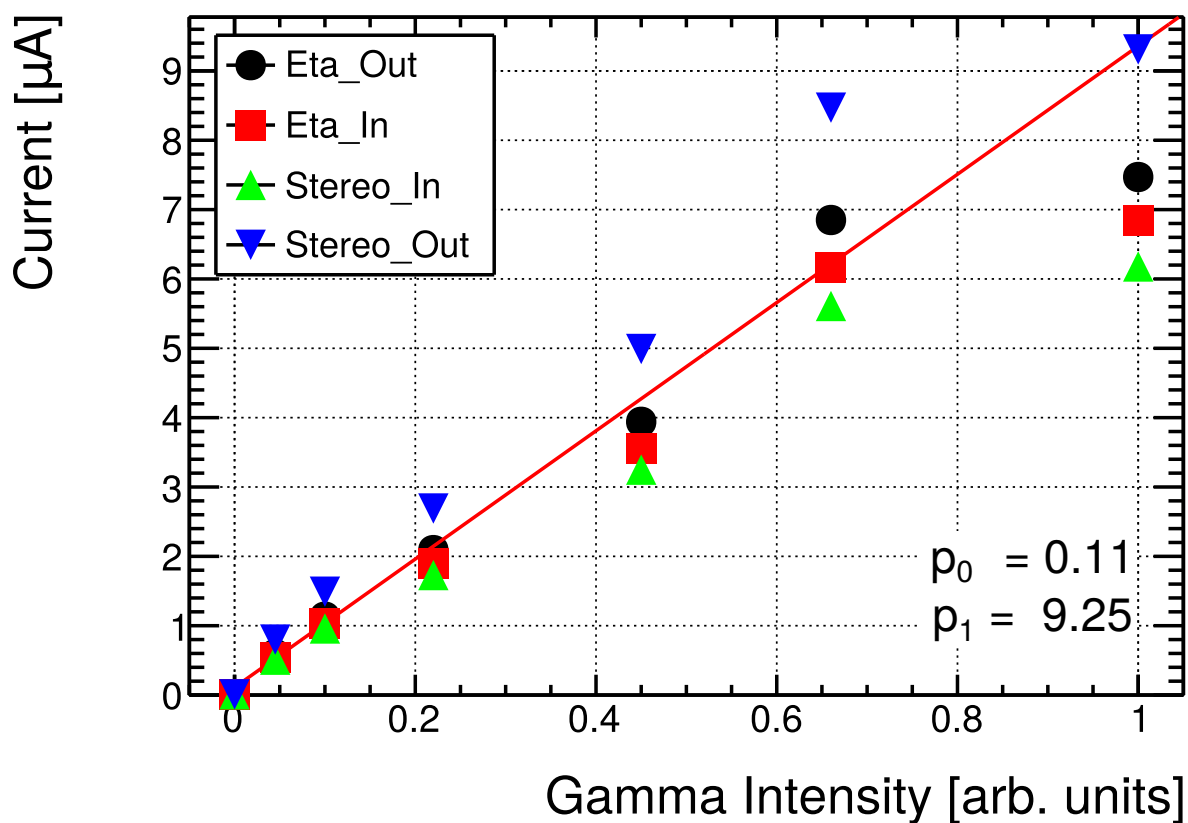


Figure C.2: Observed current for different values of gamma intensity at 1.8 m distance from the source.

The drop in current at gamma intensity 1 remains. From this, a non-perfect filter setting for some of the irradiation levels can be deduced.

Appendix D

Neutron Irradiation Studies

D.1 Neutron Interaction Cross-Sections

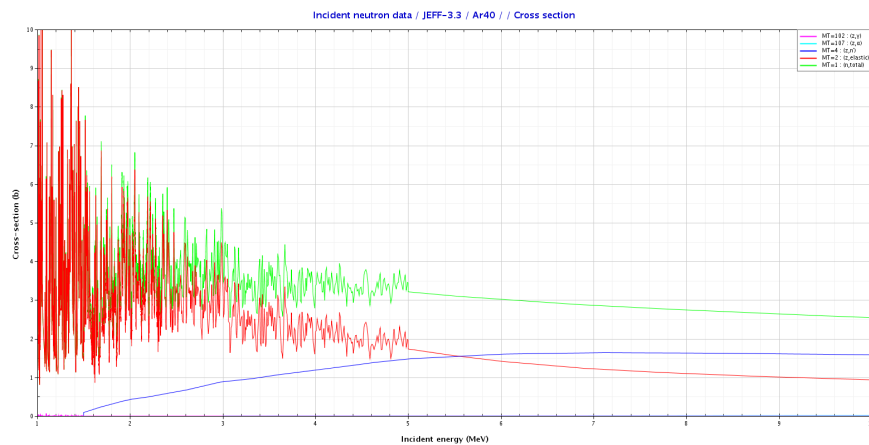


Figure D.1: Neutron cross-section in Argon. Graphic produced using a JAVA-based Nuclear Information Software (JANIS) and the JEFF-3.3 database¹.

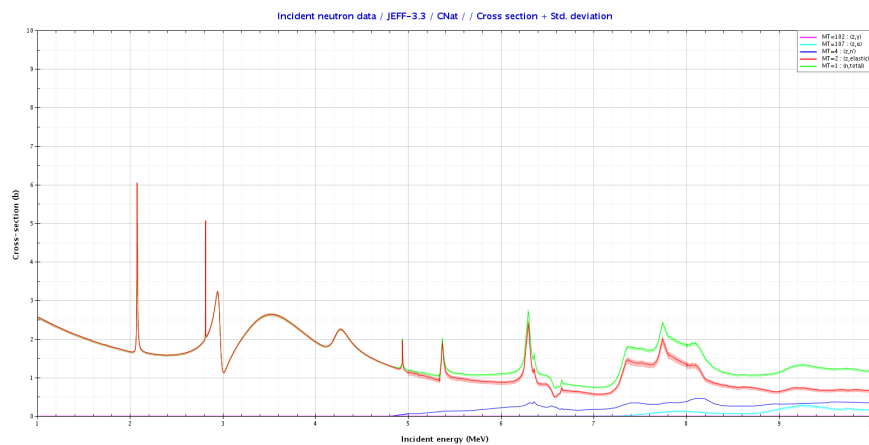


Figure D.2: Neutron cross-section in Carbon. Graphic produced using JANIS and the JEFF-3.3 database².

¹<https://www.oecd-nea.org/janisweb/>

²see footnote 1.

D.2 Asymmetric Irradiation

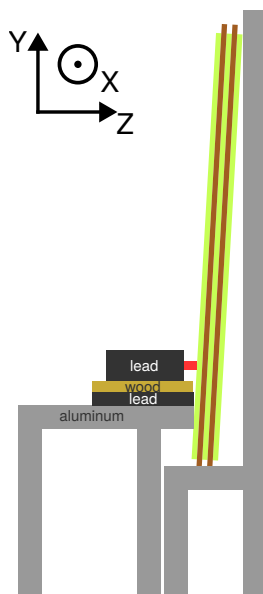


Figure D.3: Side view of the long-term irradiation setup with the Am-Be source.

The neutron source is placed against the outer side of the panel with the active material encapsulated on the tip (red square). For stabilization, the source is placed on top of a wood and lead block on an aluminum frame. The irradiated module is slightly tilted for better stability standing upwards resulting in a slightly inhomogeneous irradiation along Y. The lead is for shielding the 60 keV and MeV gammas. Borated plastic blocks, PVC plates, and water containers were used for neutron shielding.

Shielding material to the sides and the top is not shown.

D.3 Environmental Dependent Current Fluctuations

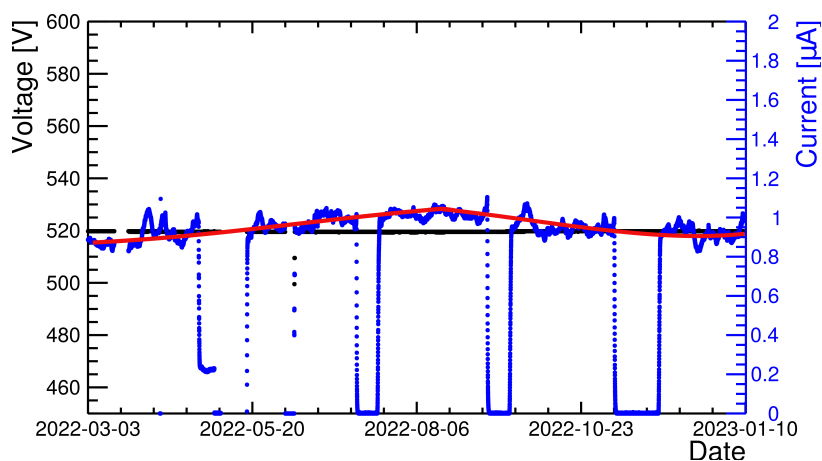


Figure D.4: Environmentally induced current fluctuations.

The faster fluctuations originate from the pressure fluctuations. The slow fluctuation with a frequency of approximately one year is temperature-induced.

The red line is purely for guiding the eye.

Periods with no current correspond to maintenance periods.

Danksagung

Diese Zeilen dienen dazu den Personen zu danken, die mich auf dem Weg begleitet haben, der schlussendlich in dieser Arbeit gemündet hat:

- Professor Otmar Biebel für sein Vertrauen in mich und der Möglichkeit diese Dissertation unter seiner Betreuung zu verfassen. Zusätzlich möchte ich mich für die vielen, interessanten Diskussionen an der Kaffeemaschine bedanken, die immer wieder zum Nachdenken angeregt haben.
- Professor Wolfgang Dünnweber für die Anfertigung des Zweitgutachtens dieser Arbeit.
- Dr. Ralf Hertenberg für die unzähligen konstruktiven Diskussionen und seine Ratschläge. Ich bin dankbar dafür, dass er sein Wissen mit mir geteilt hat und jederzeit ein offenes Ohr bei physikalischen Herausforderungen hatte.
- Dr. Christoph Jagfeld für das Korrekturlesen dieser Arbeit. Vielmehr jedoch für seine durchwegs positive Art die, die gemeinsamen Testmessungen oder Konferenzreisen zu unvergesslichen Erlebnissen machte. Auch für seine wahnsinnige Unterstützung in den Einarbeitungsphasen und die vielen konstruktiven Diskussionen möchte ich mich bedanken.
- Der Strahlzeitcrew, namentlich Prof. Theodoros Alexopoulos, Nikolaos Kanellos und Foteini Kolitsi die mit ihrem Wissen über die NSW Ausleseelektronik und Datennahme für erfolgreiche Strahlzeiten mit vielen interessanten Daten gesorgt haben.
- Dr. Francesco Fallavollita und allen Mitgliedern der Isobutan Arbeitsgruppe für ihre Arbeit vor Ort am CERN, ohne die keine Detektoren in der GIF++ bestrahlt worden wären die ich untersuchen konnte.
- Ein großes Dankeschön geht auch an alle weiteren (ehemaligen) Mitglieder der Arbeitsgruppe: Dr. Valerio D'Amico, Florian Egli, Dr. Bernhard Flierl, Stefanie Götz, Dr. Maximilian Herrmann, Dr. Felix Klitzner, Eshita Kumar, Dr. Alexander Lory, Katrin Penski, Dr. Maximilian Rinnagel, Nick Schneider, Dr. Chrysostomos Valderanis. Diese Personen haben für ein stets angenehmes Klima gesorgt, sodass jegliche Arbeit viel leichter von der Hand ging. Auch möchte ich mich bei Georg Holthoff für viele Diskussionen rund um die VMMs bedanken.
- Ein Riesendank geht im Besonderen an Karl-Heinz Lode und Patrick Baumli, die mich seit dem Gymnasium begleiten. Vor allem für die unzähligen schönen Unternehmungen und gemeinsamen Grillabende. Aber auch für ihr Verständnis dafür, dass meine Zeit in den letzten Monaten sehr begrenzt war und sie trotz allem immer hinter mir standen.
- Meinen Eltern Angela und Bernhard Vogel die mir diese Reise durch ihren unermüdlichen Einsatz, im Besonderen in jungen Jahren, ermöglicht haben. Meiner Cousine Maria Fleidl, die immer ein Fels in der Brandung war. Und meinen Großeltern Edeltraud und Josef Johann Kapsegger (†) die sich stets Zeit für mich genommen haben und einen großen Einfluss darauf hatten, wer ich heute bin.